Bournemouth University

Experimental Investigation and Mathematical Modelling of Dynamic Equilibrium of Novel Thermo-fluids for Renewable Technology Applications

Huseyin Utku Helvaci

The thesis is submitted in partial fulfilment of the requirements of Faculty of Science and Technology, Bournemouth University for the degree of Doctor of Philosophy (PhD)

January 2017

NanoCorr, Energy & Modelling Research Group (NCEM)
Faculty of Science and Technology, Bournemouth University, UK

Copyright Statement

Reprint permission

Reprints from published papers can be made subject to permission from the respective publishers.

Abstract

Environmental issues such as air and water pollutions and climate change can be linked to the fossil fuels being still the main source for human activities and therefore, its intensive consumption. As a result, there is a clear need to utilise alternative and clean energy sources to address these environmental problems. Solar thermal energy has a potential to diminish the dependency on fossil fuels and reduce CO_2 emissions in which solar radiation is converted to heat via a thermal fluid for power and heat generation. Medium and high-temperature solar thermal systems where concentrated collectors are employed have been utilised for power generation, whereas low-temperature solar systems where non-concentrated collectors such as flat plate are employed have been used for heat generation.

A review of the literature indicates that by using an appropriate thermal fluid, the generation of power and heat is possible via low-temperature solar thermal systems. It can also be revealed from the literature that when selecting a thermo-fluid to be utilised in such systems it is important to consider thermophysical, environmental and safety aspects all together.

This project is focused on the investigation of novel and environmentally friendly thermo-fluids that can be potentially utilised in low-temperature solar thermal systems for mechanical and heat energy generation. This was accomplished in three stages. Firstly, a low-temperature solar thermal system which consists of solar organic Rankine cycle and heat recovery units was designed, commissioned and tested experimentally. In the experiments, HFE 7000 refrigerant that has zero ozone depletion potential (ODP) and low global warming potential (GWP) was employed. The performance of the system was evaluated in terms of energy and exergy analyses. In the 2nd stage, the flat plate collector was mathematically modelled and simulated under various operating conditions. Then, the model was extended to the solar organic Rankine cycle to perform a simulation study where 24 organic compounds were examined according to their applicability in terms of the thermal performance of the cycle and environmental properties of the fluids such as flammability, toxicity and global warming potential. In the last stage, a numerical study of the laminar flow of HFE 7000 based nano-refrigerants at different Reynolds number and volume concentration ratio was conducted. The convective heat transfer coefficient, the pressure drop and the entropy generation of the each flow was investigated.

Publications resulting from this thesis

Refereed Journal Publications from PhD

I Helvaci H.U., Khan Z. A., (2016). Experimental study of thermodynamic assessment of a small scale solar thermal system. Energy Conversion and Management, 117, 567-576. Q1/IF: 4.80

II Helvaci H.U., Khan Z. A., (2015). Mathematical modelling and simulation of multiphase flow in a flat plate solar energy collector. Energy Conversion and Management, 106, 139-150. Q1/IF: 4.80

III Helvaci H.U., Khan Z. A., (2017). Thermodynamic modelling and analysis of a solar organic Rankine cycle employing thermofluids. Energy Conversion and Management (Accepted). Q1/IF: 4.80

IV Huseyin Utku, H., & Khan, Z. (2017). A theoretical and experimental study of HFE 7000 in a small scale solar organic Rankine cycle as a thermofluid. In International Conference on Power Engineering (ICOPE-17). Charlotte NC, USA (Accepted).

V Helvaci H.U., Khan Z. A., (2017). Heat transfer and entropy generation analysis of HFE 7000 based nanorefrigerants. International Journal of Heat and Mass Transfer, 104, 318-327. Q1/IF: 2.85

Presentations

I Helvaci H.U., Khan Z., Tabeshfar K., Camfield T., 2014. Simulation of Boiling Flow in a Horizontal Tube. 7th PGR Poster Conference, 21st May 2014, School of Design Engineering and Computing, Bournemouth University.

II Huseyin Utku, H., & Khan, Z. (2016). A theoretical and experimental study of HFE 7000 in a small scale solar organic Rankine cycle as a thermofluid. In International Conference on Power Engineering (ICOPE-17). Charlotte NC, USA (Accepted).

Table of content

List of figures

List of tables

Acknowledgements

I would like to thank to my supervisor Professor Zulfiqar Khan for his guidance and his encouragement. I will also like to express my gratitude to Mr. Tony Camfield and Mr. Brian Camfield for their kind assistance on setting up my experiments. I would also like to express my gratitude to Future Energy Source Ltd for fully funding this research. Finally, I would like to express my sincere gratitude to my family for their support.

Author’s Declaration

This thesis contains the original work of the author except otherwise indicated. This research is fully funded with laboratory facilities by Future Energy Source Ltd. Research, the content and this report is subject to confidentiality agreement subject to BU and Future Energy Source Ltd confidentiality and commercialisation contract.

Nomenclature

A	Area, m^2
C_p	Specific heat, J/kgK
d	Radius of the stator to the centre of the rotor, m
D	Diameter, m
e	Specific exergy, J/kg
$\dot{E}x$	Exergy rate, W
f	Friction factor
F	Collector heat removal factor
F_R	Heat removal factor
G	Mass flux, $kg/m^2/s$
h	Enthalpy, J/kg
h_f	Fluid heat transfer coefficient, W/m^2K
h_{fg}	Heat of vaporisation, J/kg
h_w	Wind heat transfer coefficient, W/m^2K
k	Thermal conductivity, W/mK
k_{ratio}	Heat capacity ratio
L	Length, m
m	Mass, kg
$\dot{m}$	Mass flow rate, kg/s
N_c	Number of glass cover
$\dot{Q}$	Heat transfer rate, W
$\dot{Q}_u$	Useful heat gain, W
P	Pressure, bar
r	Radius, m
$r_{v,built\text{-}in}$	Built-in ratio of the expander
S_{in}	Incoming solar radiation, W/m^2
s	Entropy, J/kg K
t	Time, s
T	Temperature, ºC
U	Heat loss coefficient, W/m^2K
v	Velocity, m/s
V	Volume, m^3
$\dot{W}$	Work rate, W
W	Tube spacing
x	Vapour quality
Subscripts	
amb	ambient
ave	average
bf	base fluid
c	convective
col	collector
cond	condenser
crit	critical
cw	cooling water
cyc	cycle
dest	destruction
dsg	designed

exp	expander
f	fluid
g	gas, vapour
gen	generation
in	inlet
ins	insulation
int	Initial, intake
l	liquid
lat	latent
m	mean
mec	mechanical
mp	multiphase
n	number of vanes
nbp	normal boiling point
nc	nucleate
nf	nanofluid
o	reference (dead) state
out	outlet
ov	over
p	plate
pp	pinch point
rec	recovery
rot	rotor
s	isentropic, particle
sat	saturation
snb	sensible
sp	single phase
st	storage
stat	stator
T	total
ud	under
w	water
wf	working fluid
Greek symbols	
$\tau\alpha$	transmittance- absorbance product
ρ	density, kg/m^3
η	first law efficiency
ε	exergy efficiency
ε_p	plate emissivity
ε_c	glass cover emissivity
δ	absorber plate thickness
υ	kinematic viscosity, m^2/s
Φ	heat flux, W/m^2
μ	dynamic viscosity, kg/ms
β	collector tilt angle
σ	Stefan-Boltzmann constant
θ	angle of a specific vane from the origin
v	specific volume, m^3/kg
γ	angle between the vanes, deg
ϕ	particle volume concentration (%)

Abbreviations

Following abbreviations are used in this thesis.

Abbreviations	Description
Bo	Boiling number
CFC	Chlorofluorocarbon
CSP	Concentrated solar power
Co	Convection number
CO_2	Carbon dioxide
Fr	Froude number
GWP	Global warming potential
HC	Hydrocarbon
HCFC	Hydroclorofluorocarbon
HFC	Hydrofluorocarbon
HFE	Hydrofluoroether
HFO	Hydrofluoroolefin
LFR	Linear Fresnel reflector
MWCNT	Multiwall carbon nanotubes
Nu	Nusselt number
ODP	Ozone depletion potential
ORC	Organic Rankine cycle
PFC	Perfluorocarbon
Pr	Prandtl number
PR	Pressure ratio
PTC	Parabolic trough collector
PV	Photovoltaic
Re	Reynolds number
RO	Reverse osmosis
SORC	Solar organic Rankine cycle

Chapter 1 Introduction

1.1. Research outline

Energy is the capacity to do work and it is crucially required for people to meet their activities in industrial, transportation and residential sectors throughout the World. Energy can be classified as non-renewable such as fossil and nuclear fuels and renewable including hydropower, biofuels, solar, wind, geothermal and wave power. Fossil fuels are also called hydrocarbons and they are formed mainly carbon and hydrogen atoms. Because fossil fuels are abundant and provide large amounts of energy to be stored they are still the most used energy sources in the World. Coal, oil and natural gas which are various forms of fossil fuels supply the great majority of World's energy demand (Boyle, G. et al., 2003). Figure 1-1 represents the energy consumption of the World by renewable and non-renewable sources.

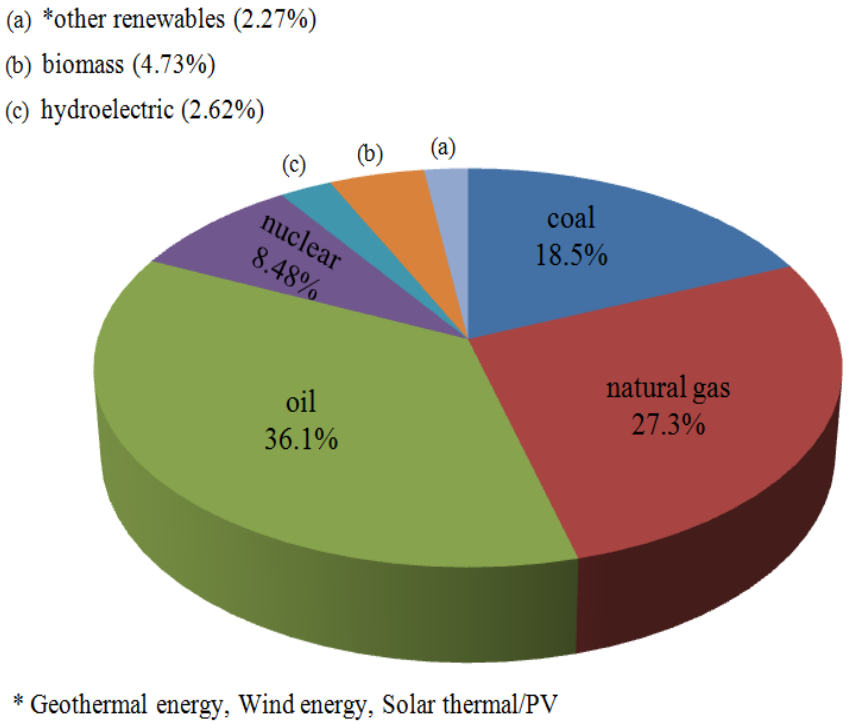

Figure 1-1 World energy consumption by sources (EIA 2014)

However, the use of fossil fuels has many adverse effects on the environment. For instance, large quantities of CO_2 (a major greenhouse gas) is generated and is released to the atmosphere which subsequently causes a rise in the Earth's temperature and makes significant changes in the World's climate system (Reddy, V. S. et al., 2013). Table 1-1 shows the atmospheric CO_2 levels in parts per million in the World from 1995

to 2005. It can be seen from the table that the level of CO_2 was 360 ppm in 1995 and this value increased to 400 ppm in 2015.

Furthermore, extracting fossil fuels in the future will become gradually challenging and it seems to be unlikely to keep the pace with their consumption and reproduce them to meet the demand. In this regard, since the nuclear energy still has some limitations and currently available only in large scale power generations, using renewable energy sources as an alternative energy source has become very important and the best choice for domestic heating and electricity generation (Boyle, G. et al., 2003; Mekhilef, S. et al., 2011).

Table 1-1 CO_2 levels in the World between 1995 and 2015 (NASA 2015)

Year	**CO_2 (ppm)**	**Year**	**CO_2 (ppm)**
01-1996	362.04	01-2006	381.35
01-1997	363.04	01-2007	382.93
01-1998	365.18	01-2008	385.44
01-1999	368.12	01-2009	386.94
01-2000	369.25	01-2010	388.5
01-2001	370.52	01-2011	391.25
01-2002	372.45	01-2012	393.12
01-2003	374.87	01-2013	395.54
01-2004	377	01-2014	397.8
01-2005	378.47	01-2015	399.96

Renewable energy sources such as solar, wind, biomass, geothermal, i.e. which are produced by both direct and indirect effects of the Sun's energy on the earth can be utilised for heat and electricity production (Boyle, G. et al., 2003). Figure 1-2 depicts the renewable energy consumption by source from 2005 to 2011 in terms of trillion Btu. It can be seen that the general trend for all sources was upward. The most used renewable energy source was biomass during the 7 year period. It was followed by hydro and wind energy respectively. Yet the consumption of solar energy for domestic heating and electricity generation is below among the other energy sources, available solar energy for use is much higher than the amount of utilising of other energy sources.

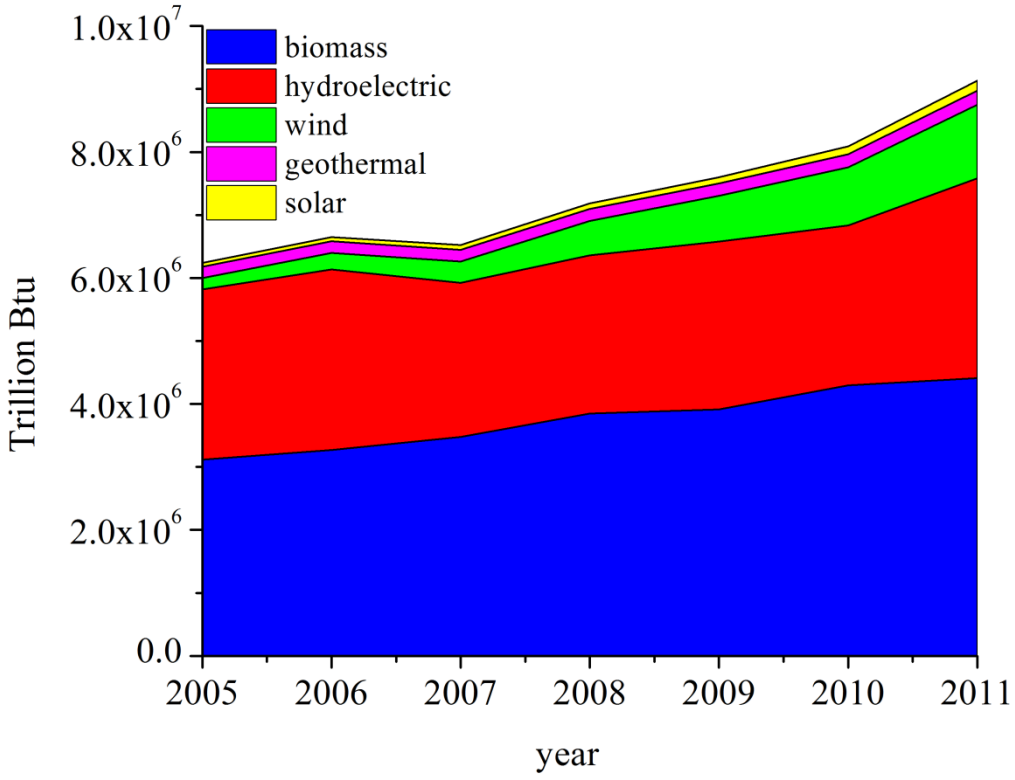

Figure 1-2 Renewable energy consumption by source (EIA 2014)

Solar energy is abundant and free renewable energy source that can be supplied without making any kind of pollution to the atmosphere. It has been utilised for drying, space heating and cooling, water heating, steam generating, desalination, refrigeration, mechanical energy and electricity generation applications. There are two ways of utilising solar energy which are solar photovoltaic (PV) and solar thermal systems (Mekhilef, S. et al., 2011).

Photovoltaic systems consist of silicon or selenium based semiconductors and they absorb the solar energy and convert it to the electricity directly. Solar PVs have become popular for electricity generation recently. However, these panels have some drawbacks. For instance, PV panels are more expensive compared to the panels for solar thermal energy and PV panels have limited efficiency levels ranging from 12 to 20%. Moreover, conversion of direct electric current (DC) generated from solar PVs to alternating current (AC) requires inverters and expensive electronic equipment (Green Energy Saving Tips 2015; Green Power Technology 2015). Another way of utilising solar energy is '*solar thermal*' where the solar energy is converted into heat and

transferred to a thermal fluid in solar collectors. Solar thermal technology can be utilised for generating electricity and heat. (Mekhilef, S. et al., 2011).

Solar thermal technology can be categorised as law temperature, medium and high temperature thermal systems depending on the solar collector that is utilised. Concentrated collectors such as parabolic trough, parabolic dish and power tower can generate heat at medium and high temperature whereas non-concentrated collectors such as flat plate can provide heat at low-temperature (Reddy, V. S. et al., 2013).

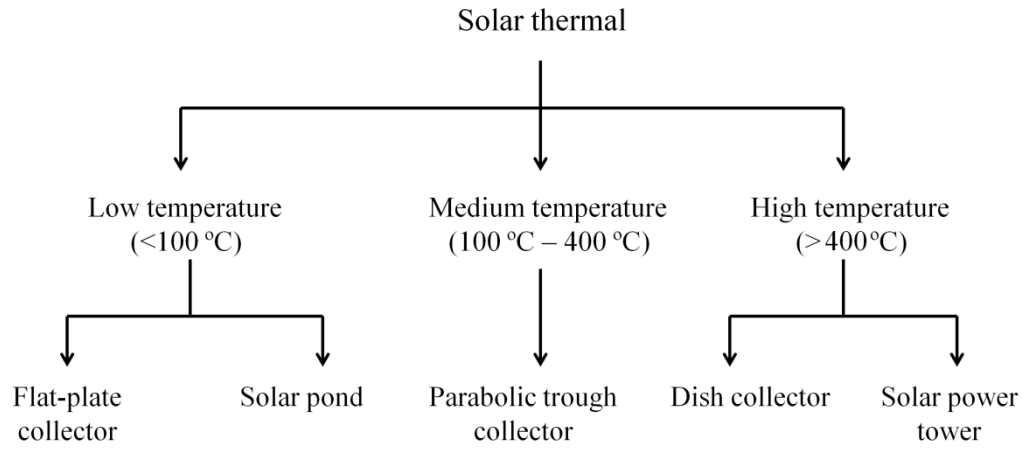

Figure 1-3 Solar thermal technology classification according to temperature (Reddy, V. S. et al., 2013)

However, medium and high temperature solar thermal systems where the concentrated collectors are utilised have some obstacles. For instance, concentrated collectors require complex technologies and high investment costs. Furthermore, high temperature and high pressure operating conditions are necessary to make these systems profitable (Kalogirou, S. A., 2004; Mekhilef, S. et al., 2011; Romero, M. and González-Aguilar, J., 2014).

Alternatively, non-concentrated flat plate collectors and solar ponds can be used to generate power and heat. Utilising working fluids with lower boiling temperature than water allows low-temperature solar thermal systems to operate on organic Rankine cycle (ORC) and generate heat and electricity at lower temperatures (Reddy, V. S. et al., 2013).

The choice of thermo-fluids has a great effect both on the system performance and the environment (Bao, J. and Zhao, L., 2013). Chlorofluorocarbons (CFCs) and Hydrofluorocarbons (HCFCs) are conventional thermo-fluids and they are recognised as ozone depleting substances by Montreal Protocol. Due to their high ODP and GWP,

CFCs have been phased out already and complete phase out of HCFCs has been projected in 2030 (Husband, W. and Beyene, A., 2008). Hydrofluorocarbons (HFCs) have been used as substitutes for CFCs and HCFCs. Although HFCs have zero ODP value, they present high global warming potential. (Shahinfard, S. and Beyene, A., 2013). Other alternative thermo-fluids which can be utilised in solar thermal systems are hydrocarbons (HCs), yet they have flammability issues (Granryd, E., 2001). Hydrofluoroethers (HFEs) and hydrofluoroolefins (HFOs) also have zero ODP and relatively low GWP which make them alternative thermo-fluids for solar thermal systems (Invernizzi, C. M. et al., 2016; Tsai, W.-T., 2005). Furthermore, nanofluids which are a suspension of solid particles in a base fluid can be utilised in solar thermal applications (Daungthongsuk, W. and Wongwises, S., 2007; Saadatfar, B. et al., 2014). Nanofluids present enhanced heat transfer characteristics as dispersed solid particles have thermal conductivity much more than that of base fluids. Therefore, nanofluids have the potential to provide higher efficiency and better performance when they are used in heat transfer applications (Duangthongsuk, W. and Wongwises, S., 2009; Khanafer, K. and Vafai, K., 2011).

1.2. Research question

Considering the environmental problems such as global warming and climate change the utilisation of clean and alternative renewable energy sources has become a vital concern for the World. Therefore, the research question being addressed in this project is to determine if novel and environmentally friendly thermofluids can be utilised in renewable energy applications such as solar thermal systems for mechanical and heat energy generation efficiently.

1.3. Novelty

In this work, a low-temperature solar thermal system which generates mechanical and heat energy was designed and tested experimentally. Firstly, a non-concentrated flat plate collector was utilised as the direct heat source of the proposed system. In other words, additional heat exchanger such as an evaporator was eliminated from the system which implies lower installation cost and less thermal loss from the system boundaries. Secondly, instead of complex and expensive conventional turbines, an air motor which is a positive displacement machine was used as an expander of the system. This will address the issue of utilising and adopting appropriate positive displacement expanders

such as rotary vane expander for low-temperature solar thermal systems. Furthermore, this study will demonstrate the feasibility of utilisation an environmentally friendly thermo-fluid (HFE 7000) in a low-temperature solar thermal system for mechanical energy and heat generation. In the literature, in solar organic Rankine cycle modelling and thermo-fluid selection studies, the collector and expander efficiencies are set constant. In the developed steady-state, mathematical model of the cycle, the collector and the expander efficiencies were varied according to operating conditions of the cycle and thermo physical properties of investigated fluids. Therefore, their effects on the solar ORC performance were taken into the consideration. Furthermore, rather than conventional thermofluids such as Chlorofluorocarbons (CFCs) and Hydrochlorofluorocarbons (HCFCs), only thermofluids that have zero-ozone depletion potential (ODP) such as Hydrocarbons (HCs), Hydrofluorocarbons (HFCs), Perfluorocarbons (PFCs), Hydrofluoroethers (HFEs) and Hydrofluoroolefins (HFOs) are considered in this research. Lastly, the laminar flow of environmentally friendly novel refrigerant HFE 7000 based nanofluids including Al_2O_3, CuO, SiO_2 and MgO nanoparticles at various Reynolds numbers and particle volume concentration ratios was numerically investigated. The flow characteristics as well as the performance of the HFE 7000 based nanofluids were studied through the exergy analysis method. This study will bring a significant contribution to the knowledge of nano-refrigerants which can be utilised in solar thermal applications for thermal efficiency enhancement.

1.4. Aims and objectives of the thesis

The first main aim of this thesis is to evaluate the thermodynamic performance of a low-temperature solar thermal system, utilising a new generation, environmentally friendly thermo-fluid for mechanical energy and heat generation. The second main aim of the thesis is to develop a mathematical model of the solar thermal cycle to simulate the system using various novel thermo-fluids and to determine the optimal fluids in terms of thermodynamic and environmental aspects. The last aim of this thesis is to examine the feasibility and heat transfer characteristics of various nano-refrigerants by performing numerical simulations.

The following objectives have been set to attain the project aims mentioned above:

1) To design and construct an experimental test rig of a low-temperature solar thermal system with the selection of a novel and environmentally friendly

thermo-fluid to be utilised in the proposed system as the working fluid for mechanical energy and heat generation. Then, design and conduct experiments to collect data. As a part of this study, evaluate the thermodynamic performance of the system in terms of energy and exergy analysis methods based on the data obtained from the experiments,

2) To develop a mathematical model of the flat plate collector and the proposed solar ORC. Furthermore, validate the mathematical model of the system components such as collector and expander against the obtained experimental data
3) To simulate the flat plate collector under various operating conditions (mass flow rate and operating pressure) to understand the collector efficiency behaviour.
4) To perform a simulation study of the solar ORC, using twenty four thermo-fluids including hydrocarbons, hydrofluorocarbons, perfluorocarbons, hydrofluoroethers and hydrofluoroolefins. As a part of this study, determine the potential thermo-fluid candidates that can be utilised in the considered application in terms of thermodynamic performance such as net work output and cycle efficiency and environmental and safety criteria such as global warming potential, flammability and toxicity.
5) Determine the potential HFE 7000 based nano-refrigerants that can be utilised in the proposed solar thermal application. Then, design and perform numerical simulations of HFE 7000 based nano-refrigerants in a horizontal tube using single-phase model to understand the hydrodynamic and thermal behaviour of the considered nano-refrigerants. Furthermore, analyse the effect of Reynolds number, nano particle and nanoparticle volumetric concentration ratio on the convective heat transfer coefficient, pressure drop and exergy generation of the flow.

1.5. Research methodology

The research methodology followed in this thesis has been two kinds: experimental and numerical. The first section represents the experimental methodology whereas the rest indicates the numerical methodology as:

1) A low-temperature solar thermal system was designed and commissioned, employing an environmentally friendly thermo-fluid HFE 7000. Furthermore, an experimental study of thermodynamic analysis of the system was conducted.
2) A mathematical model of the flat plate collector, as well as the whole system was developed using MATLAB programme.
3) The modelled flat plate collector was numerically simulated employing the developed code via MATLAB software.
4) The numerical simulations were extended to the modelled solar ORC in MATLAB environment.
5) CFD analysis of HFE 7000 based nano-refrigerants was performed by using ANSYS Fluent software.

1.6. Thesis outline

This thesis consists of the material from five published papers by the author (primary). In Chapter 2, a literature review which covers the related topics regarding to this research is presented. The state of the art of both experimental and numerical solar thermal applications has been discussed in this chapter. Furthermore, experimental and numerical analysis of forced convection flow of nanofluids including single and multi-phase approaches has been presented.

Chapter 3 provides the description of the system components that make up the low-temperature solar thermal system. The measurement devices, the working fluid and experimental methodology are also presented in this section. *(Papers I and II)*.

The fourth chapter reports the experimental results in terms of the performance analysis of the system. The experimental data is discussed through energy and exergy methods *(Paper I)*.

In Chapter 5, the detailed mathematical modelling of the proposed system is presented including each component such as the flat plate collector, expander, condenser and pump *(Papers II and III)*.

Chapter 6 shows the simulation analysis of the modelled flat plate collector that has been used in the experiments. The collector thermal analysis which includes the collector heat loss and collector efficiency using two refrigerants (HFC-134a and HFE 7000) in single-phase and two-phase flow regimes is analysed and the simulation results are discussed in this chapter *(Paper II)*.

Chapter 7 presents a simulation study of the proposed system using 24 thermo-fluids fluids. This chapter focuses on the thermodynamic and environmental properties of each fluid and their effects on the system performance *(Papers III and IV)*.

In Chapter 8, numerical analysis of HFE 7000 based nano-refrigerants are presented based on the *(Paper V)*. The convective heat transfer characteristics, pressure drop and entropy generation analysis of investigated nano-refrigerants have been investigated.

Chapter 9 presents the discussion of the findings obtained from this research. Recommendations for future work are presented in Chapter 10. References and appendices are provided at the end of the thesis.

Chapter 2 Literature review

2.1. Solar Energy

Solar energy, which is a clean renewable energy source can be utilised to address many environmental problems such as pollution and global warming by diminishing the dependency on fossil fuel consumption (Baharoon, D. A. et al., 2015; Reddy, V. S. et al., 2013). Solar energy can be harvested in two ways which are solar photovoltaics and solar thermal.

2.2. Solar photovoltaics (PVs)

The term *'photovoltaic'* stands for the direct conversion of sunlight into electricity. Photovoltaic cells, which are made of layers of semiconductor materials (e.g. silicon) are used to convert photons of sunlight into electricity. Photovoltaic cells are generated in modules comprising a large number of cells interconnected in series as a low voltage can be produced from each cell (Boyle, G. et al., 2003). Figure 2-1 demonstrates the schematic of a cell, module and array respectively.

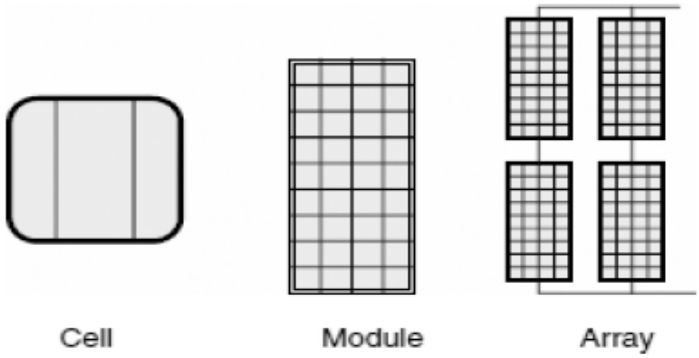

Figure 2-1 The photovoltaic hierarchy (Zobaa, A. F. and Bansal, R. C., 2011)

Most of the PV systems are mounted on the roofs and facades of domestic and industrial buildings and the generated electricity is fed into a grid system. However, these systems need an inverter to convert the direct voltage (DC) electricity produced from the PV into alternating voltage (AC) before it is exported to the grid. Photovoltaic systems can also be used without being connected to an electricity grid. This system is called *'Solar island systems'* and they are rather used in the areas which are far from an electricity grid. Figure 2-2 and Figure 2-3 represent grid-connected and off grid PV systems respectively.

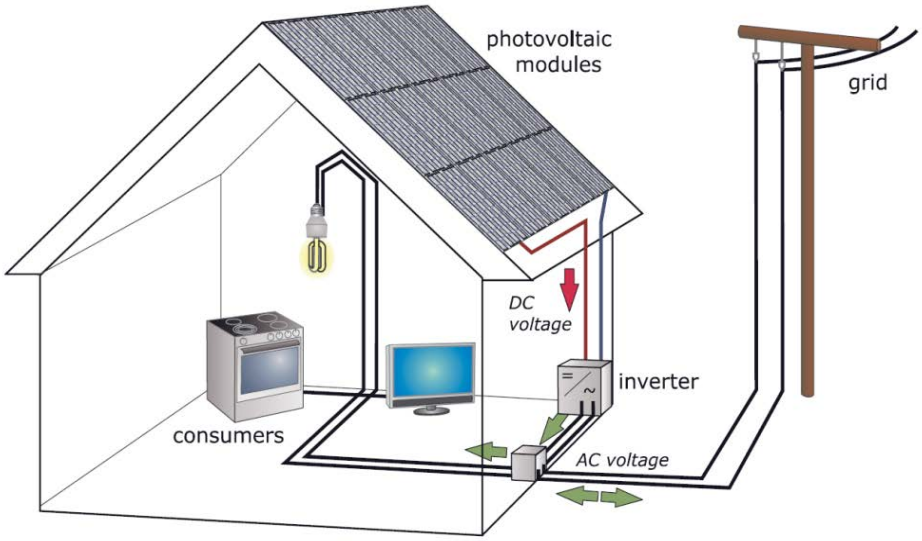

Figure 2-2 Grid-connected solar PV system as an example (Quaschning, V., 2009)

One of the major drawbacks of solar PV systems is that the manufacturing of the silicon for a cell is an energy-intensive process. However, it is also projected that the amount of material that is used for PV generation will decrease, therefore, the amount of energy that is necessary for PV production will diminish in the future (Quaschning, V., 2009).

Figure 2-3 An example of a solar island system (Quaschning, V., 2009)

2.3. Solar thermal energy

Solar thermal energy is a technology which indicates the conversion of the solar radiation into heat in solar collectors. Solar thermal energy applications can range from domestic heating, cooking, drying, cooling, and mechanical energy generation.

Various types of collectors can be used depending on the application and desired temperatures. Solar collectors that are used in solar thermal applications can be divided into two categories as concentrating and non-concentrating (stationary) collectors (Kalogirou, S. A., 2004). The properties of various types of collectors are given in Table 2-1.

Table 2-1 Properties of various types of solar energy collectors (Kalogirou, S. A., 2013)

Collector type	Concentration ratio	Absorber type	Temperature (ºC)
Flat plate collector (FPC)	1	Flat	30-80
Evacuated tube collector (ETC)	1	Flat	50-200
Parabolic trough collector (PTC)	10-85	Tubular	60-400
Linear Fresnel reflector (LFR)	10-40	Tubular	60-250
Parabolic dish reflector (PDR)	600-2000	Point	100-1500
Heliostat field reflector (HFC)	300-1500	Point	150-2000

2.3.1. Concentrating solar collectors

Concentrating solar collectors contain a concave reflecting surface which is used to concentrate the solar radiation onto a receiving area. In concentrating solar collector applications, the radiation heat flux that is directed to the receiver is increased, therefore higher temperatures can be achieved. Utilisation of concentrating solar collectors in solar thermal systems is also called as *'concentrating solar power'*. Concentrating solar power (CSP) is more appropriate in the areas, where there is a high percentage of clear sky days as it is able to capture only the direct beam radiation. There are four concentrating solar collectors that are used in CSP applications in the World (Figure 2-4). The concentrating solar collectors can be listed as parabolic trough collectors (PTC), linear Fresnel reflector (LFR), solar power tower and parabolic dish collector. (Kalogirou, S. A., 2013).

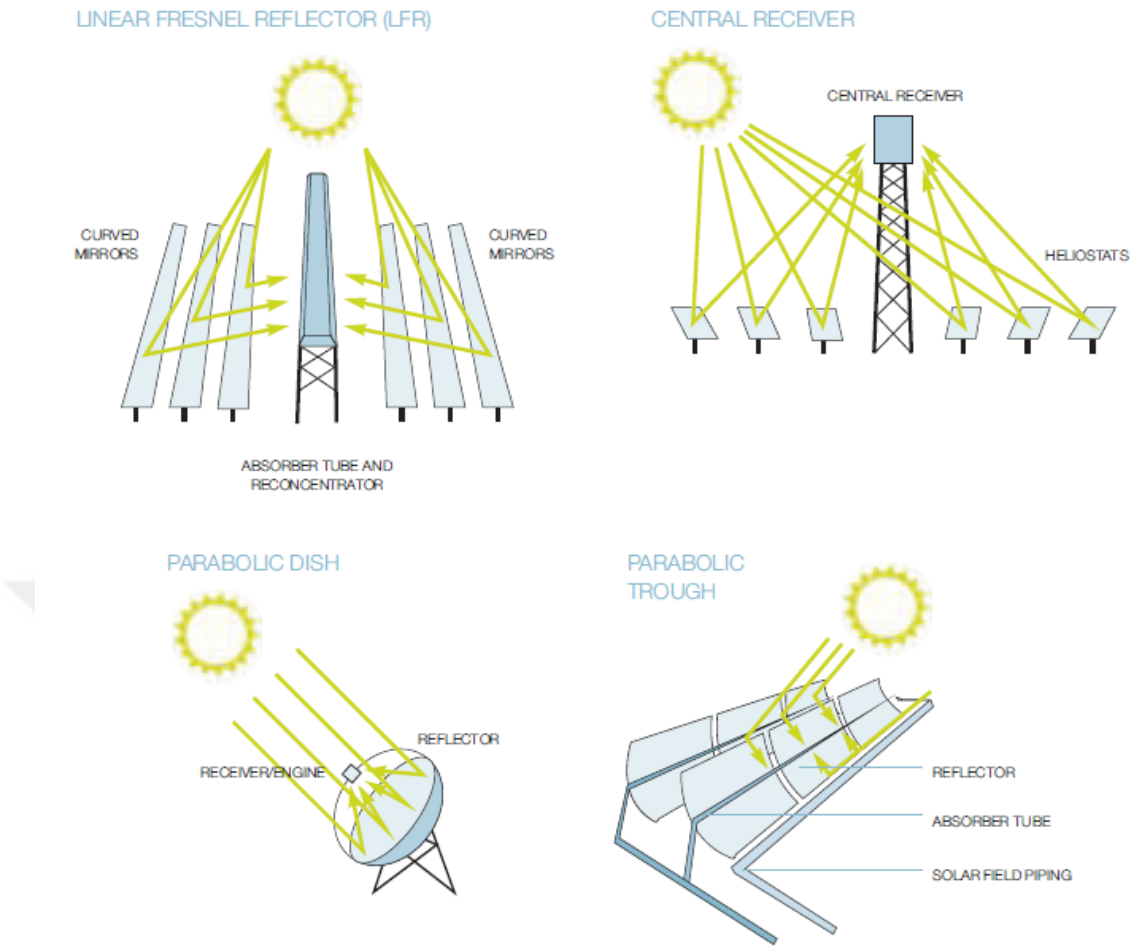

Figure 2-4 Schematic representation of four different CSP technologies (Richter, C. et al., 2009)

2.3.1.1 Parabolic trough collector

A parabolic-trough collector (PTC) systems consists of a parabolic trough shaped, long mirrors and a conduit that is positioned on the focal line of the trough. The sunlight is concentrated by the parabolic mirrors onto the conduit (receiver tube) where the heat transfer fluid is circulated. Then, the heated heat transfer fluid is directed to a heat exchanger to transfer its heat to water and generate vapour in a water-steam cycle. In the water-steam cycle, the vapour expands in a steam turbine that is coupled to a generator and produces electricity. The water-steam cycle, which is coupled with parabolic trough collectors, is also called the Clausius-Rankine cycle. In parabolic trough collectors, receiver comprises two concentric tubes. The inner tube which is separated from the outer tube by vacuum carries the heat transfer fluid. This is to prevent convection heat losses from the receiver. Water, oil and water-ethylene-glycol mixture can be utilised as a heat transfer fluid in the receiver tube (Quaschning, V., 2009; Zobaa, A. F. and

Bansal, R. C., 2011). A schematic representation of a parabolic tower system is shown in Figure 2-5.

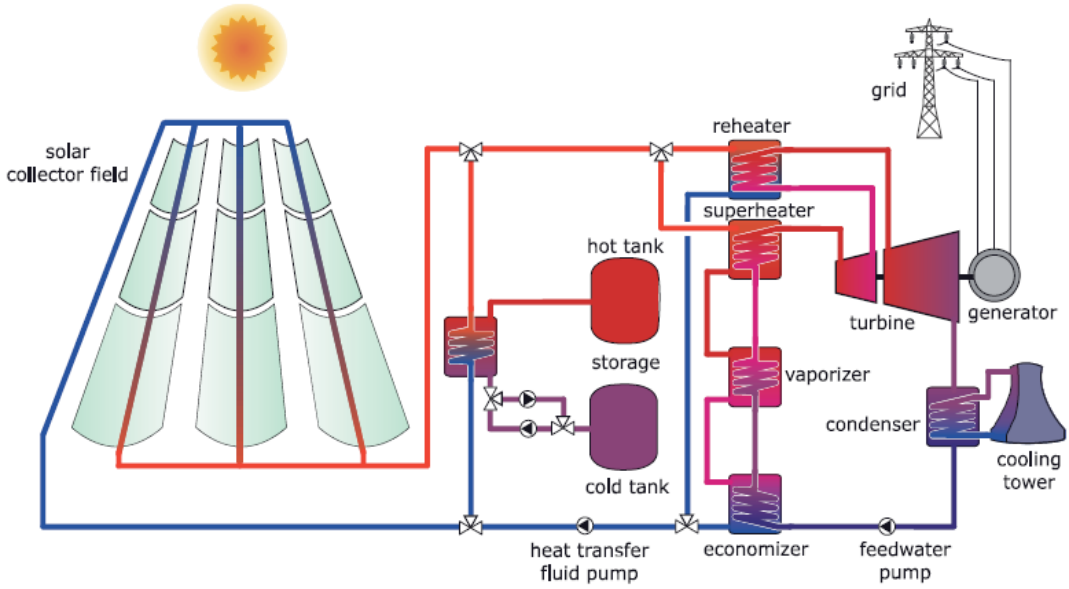

Figure 2-5 Parabolic trough power system coupled with thermal storage (Quaschning, V., 2009)

2.3.1.2 Linear Fresnel Reflector

In Linear Fresnel reflectors (LFR), multiple long and narrow mirrors are oriented close to the ground to reflect the sunlight to the fixed and linear receivers (Figure 2-6). As it is mentioned previously large mirrors as a reflector are used in PTC. However, eliminating the large reflectors in LFRs allows an easier cleaning and repair. Furthermore, fixed position of the receiver in LFR makes these systems cheaper compared to the PTCs (Chen, C. J., 2011; Zobaa, A. F. and Bansal, R. C., 2011).

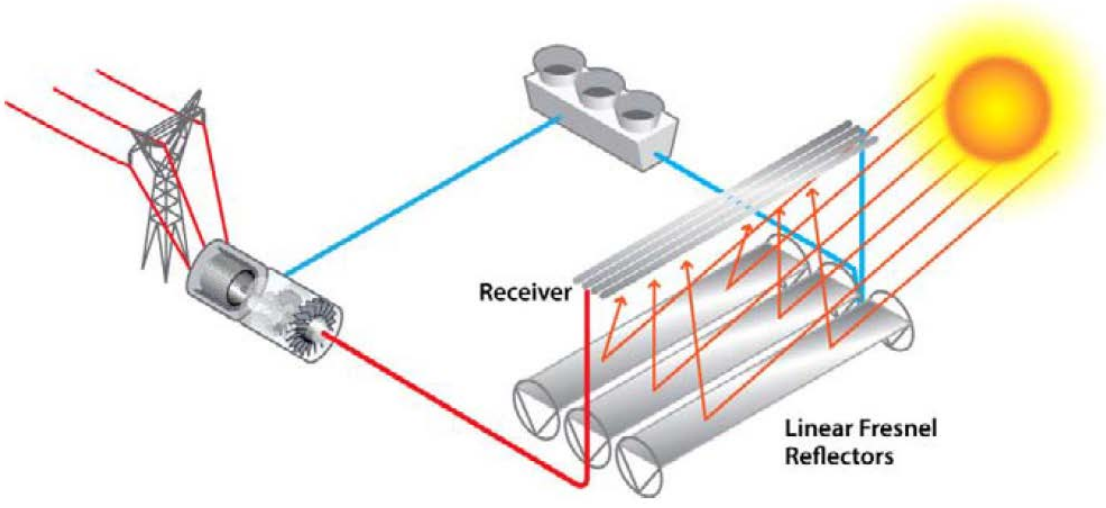

Figure 2-6 Linear Fresnel reflector system (Zobaa, A. F. and Bansal, R. C., 2011)

2.3.1.3 Solar Power Tower

This system consists of thousands of individual sun-tracking mirrors (heliostats) and a receiver that is located on the top of a tower. The heliostats which reflect the solar radiation onto the receiver are controlled by a computer to track the sunlight. Molten salt, which is mostly used as a heat transfer fluid in the receiver gains the solar heat and transfer its heat to a secondary fluid. Then the secondary fluid, for instance, water that turns into a steam in the receiver drives a steam turbine in a Rankine cycle to generate electricity (Chen, C. J., 2011; Quaschning, V., 2009; Zobaa, A. F. and Bansal, R. C., 2011). Figure 2-7 represents a schematic of a solar power tower system.

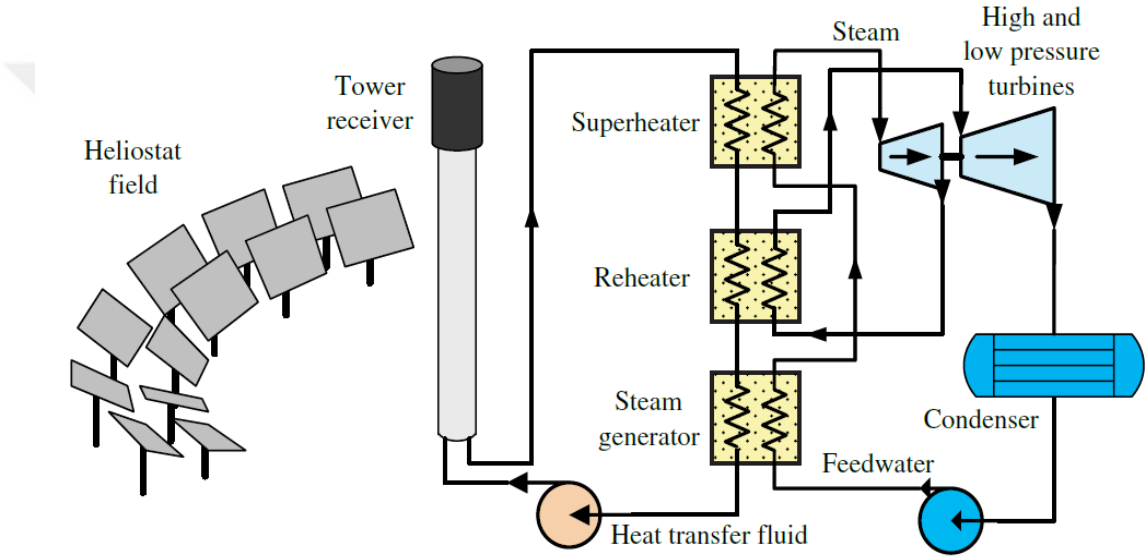

Figure 2-7 Solar power tower system (Zobaa, A. F. and Bansal, R. C., 2011)

2.3.1.4 Parabolic Dish Collector

Parabolic dish technology utilises a convex mirror in the form of a big dish to concentrate the sunlight onto a receiver which is sited at the dish's focal point. The sunlight is converted to heat in the receiver and the heat is directed to the Stirling engine to generate electricity (Kalogirou, S. A., 2013; Quaschning, V., 2009).

Figure 2-8 A representation of a parabolic dish system (Zobaa, A. F. and Bansal, R. C., 2011)

2.3.2. Non-concentrating solar collectors

Non-concentrating solar collectors such as flat plate and evacuated tube collectors have the same area for intercepting and absorbing the sunlight. Compared to the concentrating collectors, flat plate and evacuated tube collectors can operate at lower temperatures (Kalogirou, S. A., 2013).

2.3.2.1 Flat plate collector

Flat plate collector which is classified as stationary collectors is used for low-temperature applications. Flat plate collectors which can harness both diffuse and direct (beam) radiation mainly consist of a glass, an absorber plate, collector tubes, insulation and a casing (Figure 2-9).

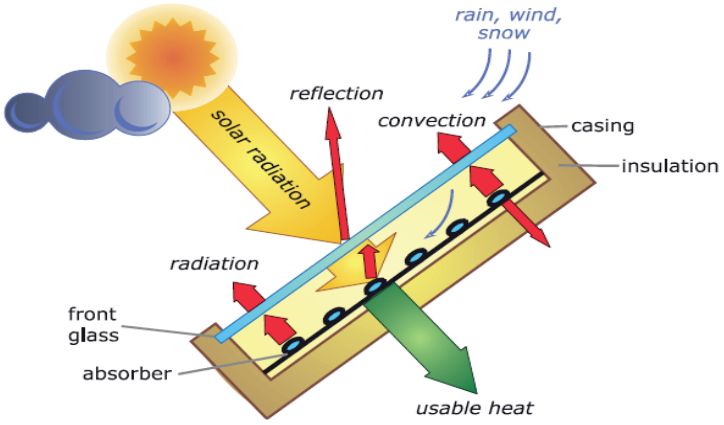

Figure 2-9 Schematic diagram of a flat plate collector (Quaschning, V., 2004)

Glazing which is normally formed by glass or other diathermanous material is used to reduce convection and radiation losses from the collector. As the solar radiation is transmitted from glazing it falls on the absorber plate surface. Absorber plate which can be flat, corrugated or grooved is a blackened material with a high absorptivity. A large portion of the energy is absorbed on the plate and transferred to the fluid (e.g. water, air). The fluid circulates in the collector tubes to carry away the energy to be stored or used. Collector tubes can be designed in two arrangements. The first one is header/riser arrangement and the other alternative is serpentine tube arrangement. The latter is preferred for the lower flow rates since the header/riser design can result in poor flow distribution and performance. The casing which stands the underside of the absorber plate is well insulated on the sides (Duffie, J. A. and Beckman, W. A., 2013; Kalogirou, S. A., 2004).

2.3.2.2 Evacuated tube collectors

Evacuated tube collector comprises a heat pipe inside a vacuum-sealed tube which decreases conduction and convection losses. Similar to flat plate collectors, evacuated tube collectors can also absorb both beam and direct radiation. They can operate at higher temperatures compared to flat plate collectors whereas they are relatively expensive (Kalogirou, S. A., 2013).

Figure 2-10 Evacuated tube collector with heat pipe (Quaschning, V., 2009)

2.3.3. Non-concentrating solar collector thermal applications

Stationary collectors, namely flat plate and evacuated tube collectors are mainly used in water heating systems. In these systems, collectors absorb the solar radiation and convert it into heat. Then, the heat is transferred to water that is circulated through the collector. The heated water can be stored in a storage tank or used directly. In water

heating systems, water is circulated by natural convection (thermospihoning) through the collector. Alternatively, a fan or pump can be used to circulate the water through the collector (Kalogirou, S. A., 2013). Figure 2-11 indicates solar water heating systems with and without pump.

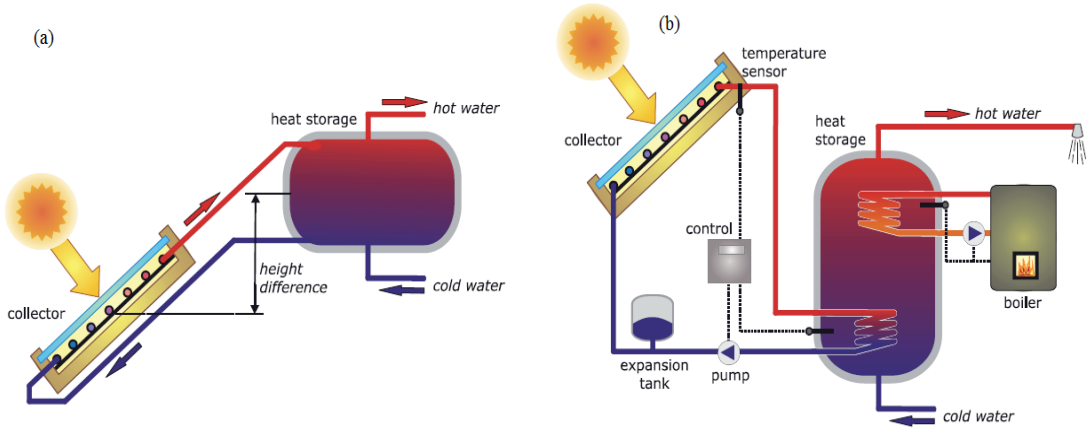

Figure 2-11 Solar water heating systems a) thermo-syphon b) pumped (Quaschning, V., 2009)

Stationary collectors can also be utilised for both water and domestic heating where the collector and the storage tank is connected to the heating cycle (Figure 2-12).

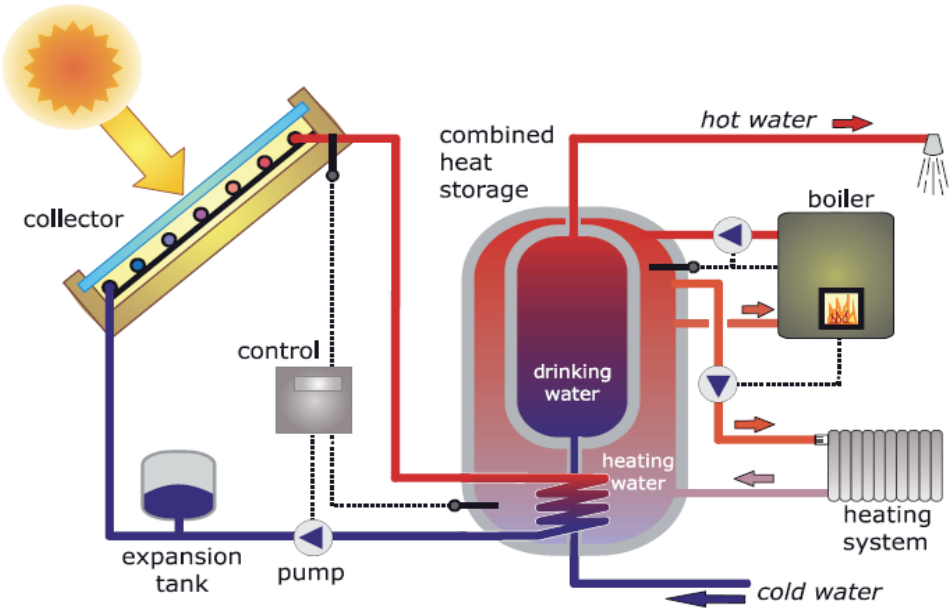

Figure 2-12 Solar thermal system for hot water and heating applications (Quaschning, V., 2009)

In addition to water and space heating applications, non-concentrating (stationary) collectors can be utilised for mechanical and electricity generation. The system working principle relies on the conversion of sunlight into heat in the collector and storing the heat (if appropriate) and utilising the converted heat to operate a heat engine (Figure

2-13). However, the system efficiency is low in comparison to the concentrating power systems as the stationary collectors can provide heat to operate an heat engine at lower temperatures than concentrating collectors (Duffie, J. A. and Beckman, W. A., 2013).

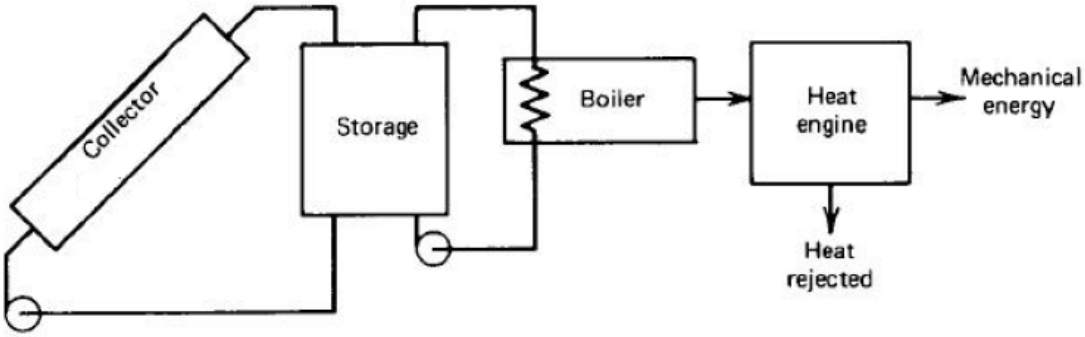

Figure 2-13 Schematic of solar thermal power generation system using a flat plate collector
Modified from: (Duffie, J. A. and Beckman, W. A., 2013)

2.4. Steam (Rankine) cycle

Steam cycle, in other words, conventional Rankine cycle is the most used thermodynamic cycle in CSP applications.

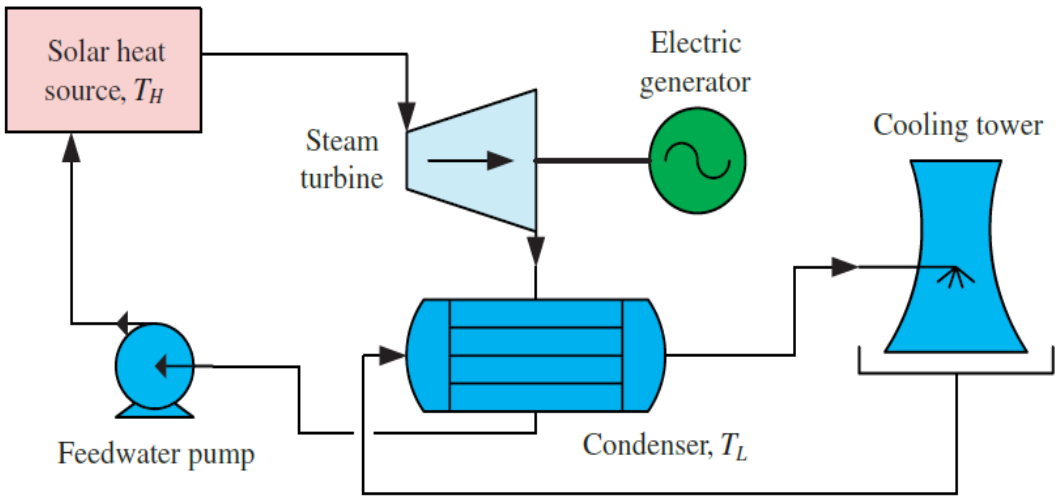

Figure 2-14 Solar thermal power plant utilising the Rankine cycle (Holbert, K. E., 2011)

The Rankine cycle mainly consists of four components which are a boiler, a steam turbine, a condenser and a pump (Figure 2-15).

It comprises of the following processes:

Process 1-2: Reversible adiabatic pumping process in the pump

Process 2-3: Constant pressure heat transfer in the boiler

Process 3-4: Reversible adiabatic expansion in the turbine

Process 4-1: Constant pressure heat transfer in the condenser

Water is used in conventional steam Rankine cycles as the working fluid. Rankine cycle efficiency is highly related to the boiler pressure and super heating of the fluid. Also, reducing the condenser efficiency has a positive impact on the efficiency of the system (Cengel, Y. A. et al., 2011).

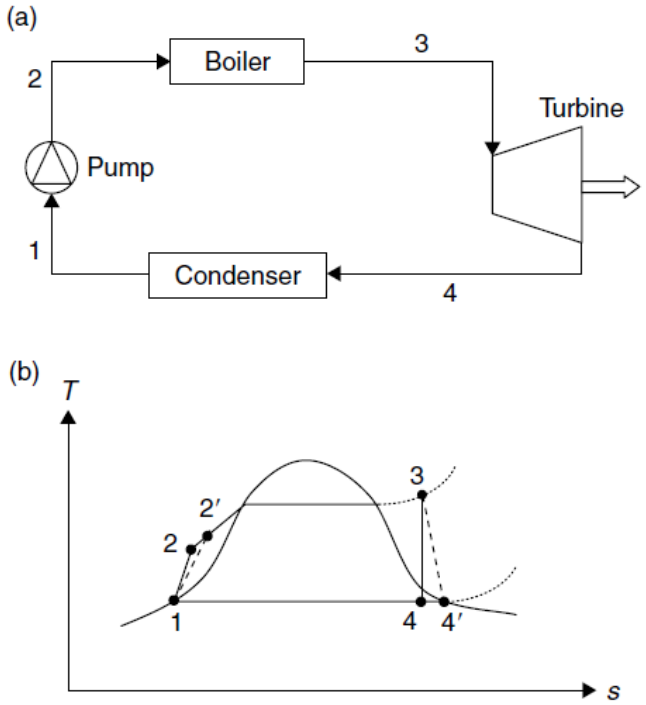

Figure 2-15 (a) Configuration of the cycle (b) T-s diagram of the cycle (Kalogirou, S. A., 2013)

2.5. Organic Rankine cycle

An organic Rankine cycle, which utilises organic compounds instead of water yet it has the same system configuration as conventional Rankine Cycle. Using organic substances in the system eliminates many problems such as the need of superheating to avoid condensation during expansion and corrosion risk. Also, it brings the benefits of requiring single-stage expander instead of complex and expensive turbines. Simple structure, less costly design and easy maintenance are the other advantages of the Organic Rankine cycle over conventional Rankine cycle (Andersen, W. C. and Bruno, T. J., 2005; Tchanche, B. F. et al., 2011; Vélez, F. et al., 2012).

2.6. Thermofluids of an ORC

Hydrocarbons (HCs), ethers, Perfluorocarbons (PFCs), Chlorofluorocarbons (CFCs), Hydrofluorocarbons (HFCs), hydrochlorofluorocarbons (HCFCs), hydrofluoroolefins (HFOs), hydrofluoroethers (HFEs), alcohols, siloxanes and inorganics are the substances which can be used in ORCs with the exception of some fluids whose critical temperatures are too high or too low (Bao, J. and Zhao, L., 2013).

2.6.1. Thermodynamic and Physical Properties of Working Fluids

Working fluids can be categorised as dry, isentropic and wet according to their saturation vapour curve on a T-s diagram. $\xi=ds/dT$ is the inverse of the slope of the vapour curve (dT/ds) and it is defined to express the type of a fluid if it is "dry" or "wet". For instance, a dry fluid has a positive slope ($\xi>0$), wet fluid has a negative slope ($\xi<0$) whereas isentropic fluid has a large infinite slope ($\xi=0$), (Figure 2-16). Since wet fluids have negative slope of the saturation vapour curve such as water, the fluid will contain some liquid droplets after isentropic expansion at the turbine stages. This causes damage in turbine blades and also it decreases the turbine isentropic efficiency. Thus, it is necessary to superheat wet fluids before it enters the turbine. Also, dry fluids leave the turbine as superheated vapour which is a waste of energy and this increases the cooling load and the necessary heat transfer area of the condenser. Alternatively, a regenerator can be added at the end of turbine to regain superheated vapour. Although this would raise the system's initial cost and complexity, dry fluids are good alternative to be used in such cycles. On the other hand, isentropic fluids have a vertical saturation line so the fluid remains saturated at the outlet of the turbine without any liquid droplet occurrence. It also eliminates the need for adding additional heat exchanger (regenerator) in the system. Therefore, isentropic fluids are ideal working fluids for ORC applications (Hung, T.-C., 2001; Hung, T. C. et al., 1997).

2.6.1.1 Vaporisation latent heat

Fluids with a higher latent heat of vaporization lead most of the heat to be added to the fluid during the phase change process in the heat exchanger. This also means that the fluid remains in the phase change region and absorbs more energy from the heat source (Chen, H. et al., 2010; Maizza, V. and Maizza, A., 2001).

2.6.1.2 Density

Fluids with low density results higher volume flow rate and this increases the pressure drop in the heat exchangers. Subsequently, pressure drop causes higher pump work input. Also, lower density enlarges the size of the equipment in the cycle, such as expander, condenser and evaporator (Nouman, J., 2012).

2.6.1.3 Boiling temperature

According to the study of Qiu (2012), working fluids which have boiling temperature between 0 to 100°C is easier to handle at ambient environment (Qiu, G., 2012).

2.6.1.4 Freezing point

Freezing point of the fluids should be below than the lowest temperature point in the cycle (Bao, J. and Zhao, L., 2013).

2.6.1.5 Viscosity

Both liquid and vapour viscosities of the fluid should be low to avoid friction losses in the heat exchangers and maximize convective heat transfer coefficients (Bao, J. and Zhao, L., 2013; Panesar, A. S., 2012).

2.6.1.6 Thermal conductivity

Heat transfer process between the heat source, heat sink and working fluid are highly related to the thermal conductivity. The higher thermal conductivity the higher heat transfer coefficients of the fluid. This increases the amount of heat that can be transferred to the fluid (Nouman, J., 2012; Panesar, A. S., 2012).

2.6.1.7 Environmental properties of thermofluids

ODP and GWP are the vital criteria which state substance's potential to further to ozone degradation and global warming respectively. CFC (CCl_mF_{4-m} and $C_2Cl_mF_{6-m}$) m is different from zero are banned in 1995 and HCFC ($CCl_mF_nH_{4-m-n}$ and $C_2Cl_xF_yH_{6-x-y}$) m, n, x, y are different from zero will be banned by 2030 in some countries due to their high ODP and GWP values (Chen, H. et al., 2010; Shahinfard, S. and Beyene, A., 2013).

2.6.1.8 Safety properties of thermofluids

Although, all fluids are inevitably toxic, fluids with lower flammability and lower toxicity should be considered in ORCs (Nouman, J., 2012; Panesar, A. S., 2012).

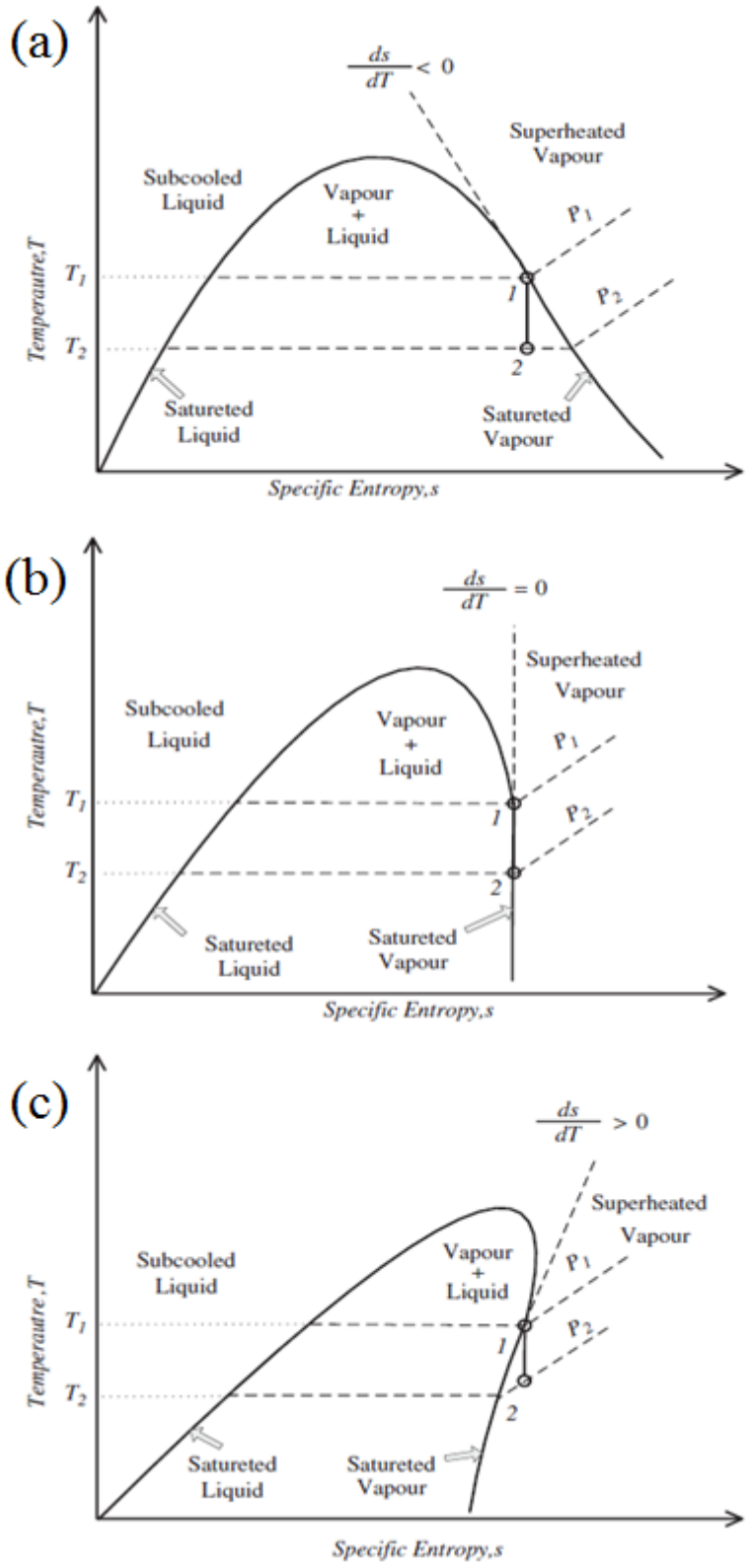

Figure 2-16 T-s diagram of three types of fluids (a) wet, (b) isentropic, (c) dry (Bao, J. and Zhao, L., 2013)

2.6.1.9 Economical properties of thermofluids

Working fluids which are easily available and have low cost are preferred in ORCs (Quoilin, S. and Lemort, V., 2009).

2.7. Solar sourced organic Rankine cycle

Higher temperature and pressure conditions must be ensured to increase the Rankine cycle efficiency and to avoid water droplet formation during the expansion. However, these requirements increase the system complexity and the cost. The maximum amount of solar radiation and heat must be captured in the collectors to achieve these conditions. Therefore, optical concentration devices have been used in many solar thermal power applications. Additionally, flat plate or evacuated tube collectors can be utilised in solar thermal power generation to avoid the disadvantages of the concentrated solar collectors (Duffie, J. A. and Beckman, W. A., 2013; Quoilin, S. and Lemort, V., 2009; Romero, M. and González-Aguilar, J., 2014). Employing flat plate collectors as a heat source of an ORC for mechanical and heat generation, utilising HFCs and CO_2 has been of interest to many researchers. A small-scale solar ORC was designed and tested to derive a reverse osmosis (RO) desalination system in (Manolakos, D. et al., 2009; Manolakos, D. et al., 2007; Manolakos, D. et al., 2005). The design system consists of a vacuum tube collector, a heat engine unit, including pre-heater, evaporator, expanders, condenser, a pump and RO unit (Figure 2-17). HFC-134a was used as the working fluid of the cycle in this study.

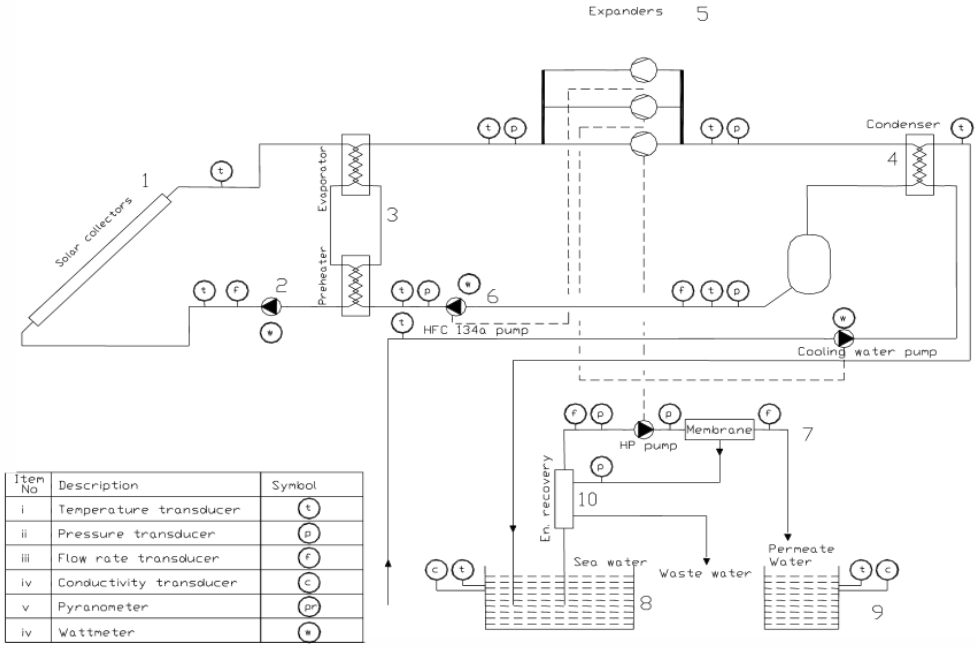

Figure 2-17 Schematic representation of solar ORC (Manolakos, D. et al., 2007)

Wang et al. (2010) conducted an experimental study of a solar thermal system utilizing HFC-245fa. In this study, a prototype of the system was designed and tested. Also, new rolling-piston expander was mounted in the system. Flat plate and evacuated tube collectors were utilised in the tests and the collector efficiencies of 55.2% and 71.6% were found for the flat plate and the evacuated tube collectors respectively. They reported that the system has a power generation efficiency of 4.2% for evacuated tube and 3.2% for the flat plate solar collector. They also concluded that 1.64 kW average shaft output was obtained from the new designed R245fa expander (Wang, X. et al., 2010).

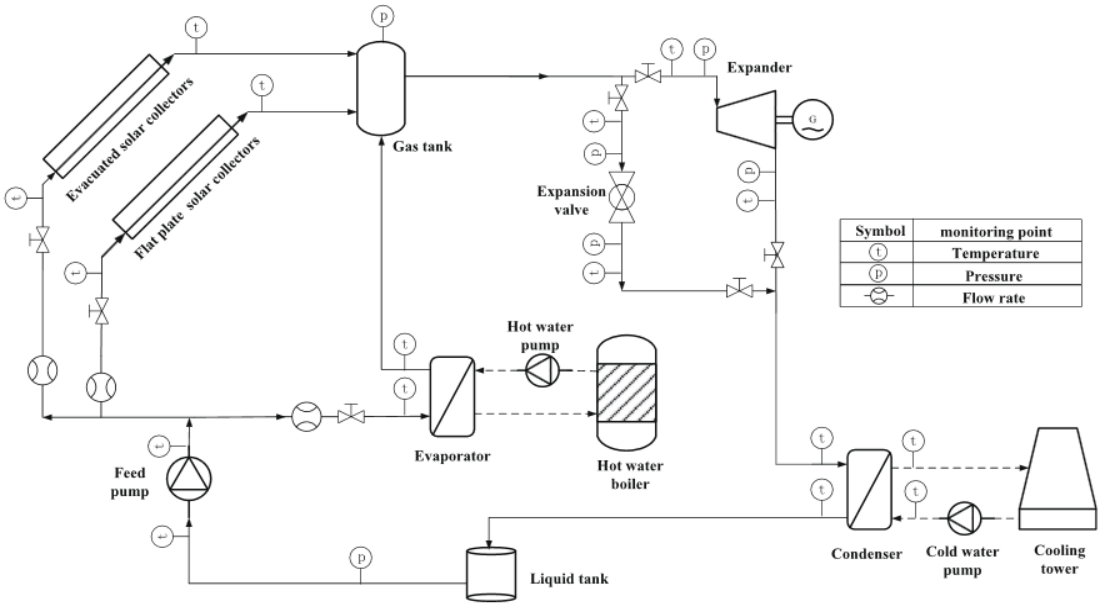

Figure 2-18 Schematic representation of the experimental system (Wang, X. et al., 2010)

Bryszewska-Mazurek et al. (2011) carried out a performance study of solar sourced organic Rankine cycle where HFC-245fa was used as a working fluid of the cycle. The cycle with an internal heat exchanger was built and tested experimentally. The system consists of flat plate collectors, evaporator, multi vane volume expander, condenser, internal heat exchanger, pump and cooling tower. The solar collectors supply heat to the evaporator where HFC-245fa is evaporated and it turns the turbine to generate mechanical work. After expansion the fluid goes to the internal heat exchanger where the fluid is preheated. Then it condenses in the condenser and is compressed by the pump. They obtained maximum thermal efficiency of 9% with heat regeneration (Bryszewska-Mazurek, A. et al., 2011). Wang et al. (2012) carried out an experimental investigation of an recuperative solar thermal cycle, using HFC-245fa. As it can be seen

from Figure 2-19, the evaporator was eliminated from the system and the flat plate collector was utilised as the direct heat source of the cycle where the working fluid undergoes phase change. It was reported that the thermal efficiency of the cycle was found to be 3.67% and there was no positive impact observed on the system thermal efficiency due to the use of a regenerator (Wang, J. et al., 2012).

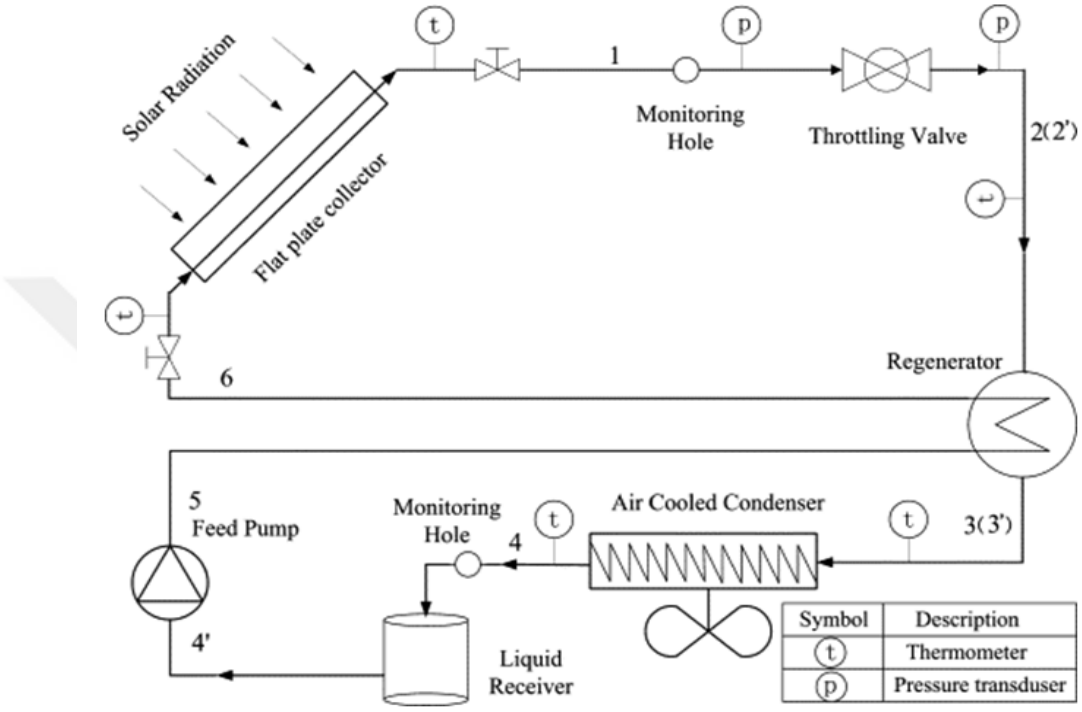

Figure 2-19 Schematic layout of the recuperative solar ORC (Wang, J. et al., 2012)

Additionally, CO_2 was used as a working fluid in solar thermal power applications. Yamaguchi et al. (2006) conducted an experimental study of solar energy powered organic Rankine cycle using CO_2. Experimental prototype which is comprised of solar collector, throttling valve, heat exchanger, CO_2 pump and cooling tower was designed and tested. The system not only generates mechanical work, but also provides heat energy. To simulate pressure drop in the turbine a throttling valve was used in the experiments. They concluded that the solar collector can be utilised for heating of CO_2 in the cycle up to 165ºC. The power generation efficiency of the cycle was estimated 25% and the heat recovery efficiency was 65% (Yamaguchi, H. et al., 2006). Zhang et al. (2007) examined the performance of a solar thermal cycle where supercritical CO_2 is used as a working fluid. The system consists of evacuated solar collector, turbine, heat exchanger and feed pump. They concluded that the heat collection efficiency of the

collector reached 70% and the system achieved 8.78-9.45% power generation efficiency (Zhang, X.-R. et al., 2007).

2.8. Thermofluid selection for solar ORC

Working fluid selection is a crucial task in the ORC design since it affects the efficiency of the system, operating conditions, the size of the system components, expansion machine design, environmental concerns and economic viability of the cycle (Bao, J. and Zhao, L., 2013). Many researchers performed fluid selection studies for solar powered Organic Rankine cycle. Delgado-Torres and García-Rodríguez (2010) analysed and conducted an optimization study of a solar ORC. They considered three collectors which were flat plate, evacuated tube and parabolic collector. Two types of cycle configurations which were a direct vapour generation (DVG) and heat transfer fluid (HTF) configurations were considered in the study (Figure 2-20).

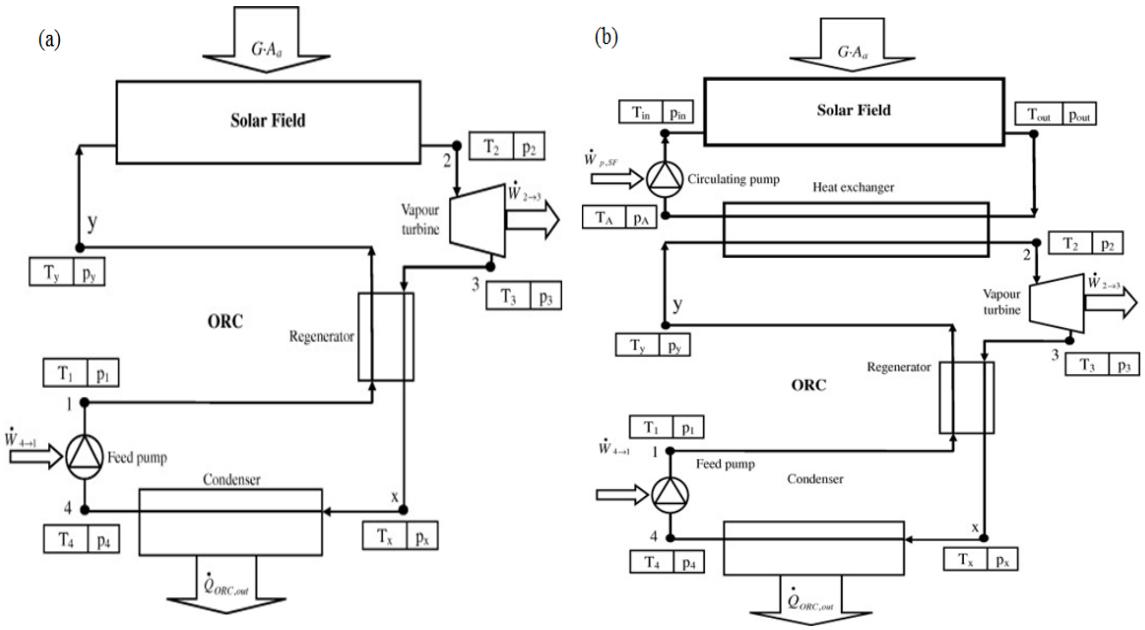

Figure 2-20 Layout of the regenerative solar organic Rankine cycle a) DVG configuration b) HTF configuration (Delgado-Torres, A. M. and García-Rodríguez, L., 2010)

In DVG configuration, the working fluid is heated directly in the solar collector where as it is heated in a heat exchanger in HTF configuration. In HTF design, solar collector supplies the heat source of the evaporator and this heat is transferred to the working fluid in the evaporator. Dry, wet and isentropic fluids were considered as working fluids of the system and aperture area needed per unit of mechanical power output of the cycle was taken into account as a comparison criterion for different operating conditions of

ORC. They concluded that, in general, wet fluids need higher values of the unit aperture area than dry fluids with the exception of ammonia. Unit aperture area values for the flat plate collector were found 17-18 m^2/kW in DVG and 22-23 m^2/kW in HFT. For other type of flat plate collector unit aperture area was found 15 m^2/kW in DVG and 18 m^2/kW in HTF. A unit aperture area of 10 m^2/kW in DVG and 12 m^2/kW in the HTF was found for evacuated tube collector. Finally, for parabolic collector unit aperture area was found 19-20 m^2/kW in DVG and 25-26 m^2/kW in HTF configuration (Delgado-Torres, A. M. and García-Rodríguez, L., 2010). Tchanche et al. (2009) investigated a fluid selection study for a low-temperature solar thermal cycle. Twenty fluids were compared in the study and the thermodynamic performance of the cycle based on the first and second laws was evaluated. They reported that HFC-134a is the most appropriate working fluid for low-temperature solar applications. This is followed by HFC-152a, HC-600a, HC-600 and HC-290 (Tchanche, B. F. et al., 2009). Various working fluids for solar organic Rankine cycle, according to their molecular components, temperature-entropy diagram and their effects on the thermal efficiency, net power output and the exergy efficiency of the cycle was analysed by Rayegan and Tao (2011). Thermal/exergy efficiency and net power output were selected as the main criteria to choice the best working fluid. They concluded that fluids with higher critical temperature have better performance in ORCs. They also claimed that thermal efficiency, higher than 25% and exergy efficiency, higher than 20% is possible to achieve in ORCs (Rayegan, R. and Tao, Y., 2011). Marion et al. (2012) modelled and simulated and ORC, combined with a single-glazed flat plate collector (Figure 2-21). The system thermal performance was investigated by using HFC-134a, HFC-227ea and R365mfc compounds. The simulation results were validated by experiments. Parametric optimisation was also performed to evaluate the optimum operating conditions in terms of mass flow rate of the working fluid. The results revealed that the working fluid mass flow rate has a significant effect on the generated net mechanical power. The results also showed that R365mfc was found to be the best fluid and it was followed by HFC-134a and HFC-227ea.

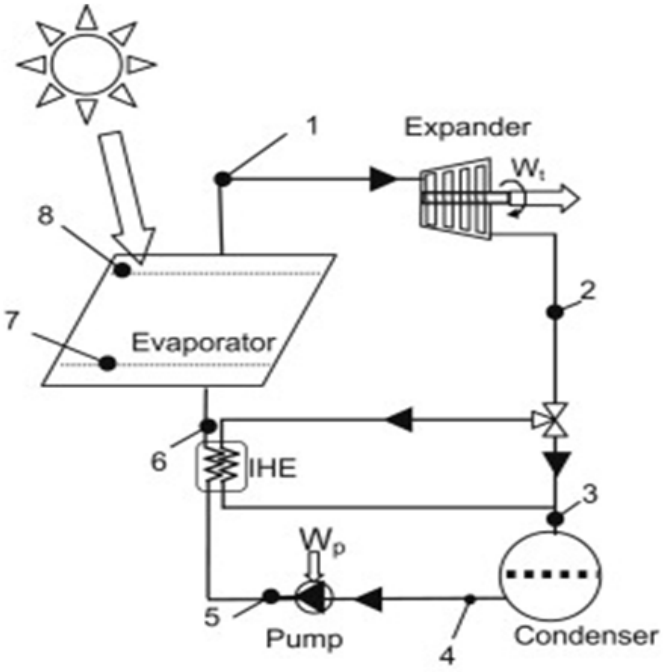

Figure 2-21 Solar organic Rankine cycle with an internal heat exchanger (Marion, M. et al., 2012)

It can be concluded that several solar ORC studies have been conducted employing flat plate and evacuated tube collectors and promising thermal efficiency and mechanical work values were obtained. It can be seen from the above studies that organic compounds such as HFCs and HCs and inorganic compound such as CO_2 are the most used thermofluids that have been examined in solar thermal power cycles. However, yet the above compounds have desirable thermodynamic and thermophysical properties, they bring several environmental and safety issues. For instance, HFCs such as R-134a and R-227ea have high global warming potential. HC-600 and HC-600a are classified as highly flammable compounds and demanding operating conditions of CO_2 (supercritical cycle). Therefore, it is important to investigate thermofluids which can be safely utilised in solar thermal power cycles and provide promising thermophysical properties.

2.9. Nanofluids

Nanofluids which are constituted of dispersing solid particles (10-50 nm) in a conventional fluid are a novel class of heat transfer fluids. Because of the enhancement in thermal conductivity, nanofluids have the potential to improve the heat transfer mechanism and provide a higher efficiency and a better performance. (Khanafer, K. and Vafai, K., 2011).

Metallic or non-metallic particles with high thermal conductivity which have been suspended in various base fluids are represented in Table 2-2.

Table 2-2 Thermal conductivities of metallic and non-metallic particles

Particle	Thermal conductivity (W/mK)	Reference
Al	237	(Murshed, S. S. and De Castro, C. N., 2011)
Cu	397.5	(Heris, S. Z. et al., 2007)
Ag	429	(Murshed, S. S. and De Castro, C. N., 2011)
Al_2O_3	40	(Pathipakka, G. and Sivashanmugam, P., 2010)
SiO_2	1.2	(Salman, B. et al., 2014)
MgO	45	(Davarnejad, R. and Jamshidzadeh, M., 2015)
CuO	20	(Nasrin, R. and Alim, M., 2013)
TiO_2	8.4	(Purohit, N. et al., 2016)
ZrO_2	2.8	(Purohit, N. et al., 2016)
Boron carbide	90	(CES, 2014)
Boron nitride	2000	(CES, 2014)
Beryllium oxide	265	(CES, 2014)
Graphite	388	(CES, 2014)
Silicon	150	(CES, 2014)
Aluminium nitride	200	(CES, 2014)
Silicon carbide	130	(CES, 2014)

2.10. Previous research on convective heat transfer behaviours of nanofluids

There have been several studies conducted on the convective heat transfer behaviours of various nanofluids both experimentally and numerically.

2.10.1. Experimental studies

Experimental research on forced convective heat transfer analysis of nanofluids mainly focuses on the effect of Reynolds number, particle volume concentration ratio and particle diameter on

the local and average heat transfer coefficient of nanofluids. Table 2-3 summaries the conducted experimental work, including various nanoparticles at various volumetric concentration ratios. It can be concluded from the obtained results that the heat transfer coefficient of nanofluids is dependent on Reynolds number of flow, particle volume concentration and particle diameter. Furthermore, higher heat transfer coefficients obtained for nanofluids compared to base fluid. On the other hand, the experimental studies also showed that the friction coefficient, as well as, pressure drop is higher for nanofluids than base fluids and this also increased with increasing Re and particle volumetric concentration ratio.

Table 2-3 Summary of experimental nanofluid studies

Nanofluid	Volumetric concentration ratio	Regime	Findings	Reference
γAl_2O_3/water	0.6, 1, 1.6%	L	A considerable amount of increase in the heat transfer coefficient was obtained	(Wen, D. and Ding, Y., 2004)
Al_2O_3/water CuO/water	0.2, 1, 2, 2.5, 3%	L	The heat transfer coefficient enhances with increasing nanoparticle concentration	(Heris, S. Z. et al., 2007)
TiO_2/water	0.2%	T	The heat transfer coefficient rose by 6-11%	(Duangthongsuk, W. and Wongwises, S., 2009)
Al_2O_3/water	0.1, 0.15, 0.2%	L/T	The heat transfer coefficient rose by 34% at 0.2% Al_2O_3/water	(Chandrasekar, M. and Suresh, S., 2011)
TiO_2/water	0.1, 0.5, 1, 1.5, 2%	T	Re does not have any significance effect on heat transfer coefficient	(Kayhani, M. et al., 2012)
MWCNT/water-ethylene glycol	0.15, 0.3, 0.45%	L/T	Nu increases with increasing MWCNT concentration ratio and decreasing Re	(Kumaresan, V. et al., 2013)
Al_2O_3/water	0.1-2%	L	The heat transfer coefficient rose with increasing Re and particle concentration	(Heyhat, M. et al., 2013)
GO/water	0.02, 0.07, 0.12%	L/T	0.12% GO/water increased the heat transfer coefficient by 77%	(Mirzaei, M. and Azimi, A., 2016)

L: Laminar T: Turbulent

2.10.2. Numerical studies

Numerical studies on nanofluids where the convective heat transfer of nanofluids is evaluated can be considered in two parts; single phase and two-phase modelling. In the single phase modelling, base fluid and nanoparticles are treated as a single, homogeneous fluid instead of liquid-solid mixture and it is accepted that fluid and particles are in thermal equilibrium. The calculated or measured nanofluid properties are applied to the governing equations (continuity, motion and energy). Therefore, it is crucial to utilise the most suitable correlations for investigation of nanofluid properties. Some authors also considered the thermal dispersion effect of the chaotic movements of particles in single phase modelling (Heris, S. Z. et al., 2007; Zeinali Heris, S. et al., 2012).

Two-phase models consist of two general approaches which are Lagrangian-Eulerian and Eulerian- Eulerian. Lagrangian-Eulerian approach is more appropriate for low solid volume fractions. Eulerian, mixture and VOF (volume of fluid) models which belong to Eulerian- Eulerian approach has been used for nanofluid analysis.

The slip velocity between base fluid and particles which occurs due to the several factors such as friction between the fluid and particles, gravity and dispersion can be considered in these two approaches. The performed numerical studies including both single and two phase models are summarised in Table 2-4.

Table 2-4 Summary of numerical nanofluid studies

Model	Nanofluid	Regime	Findings	Reference
SP/TP	Al_2O_3/water	L	Two-phase models over predict the heat transfer coefficient.	(Akbari, M. et al., 2011)
SP/TP	Cu/water	L	Two-phase models provide better predictions than single phase model	(Fard, M. H. et al., 2010)
SP	γAl_2O_3/water γAl_2O_3/ethylene glycol	L/T	γAl_2O_3/ethylene glycol gives higher heat transfer rate than γAl_2O_3/water	(MaïGa, S. E. B. et al., 2004)
SP/TP	MgO/water	T	Nanofluid heat transfer rate augmented with increasing volume fraction	(Davarnejad, R. and Jamshidzadeh, M., 2015)
SP	TiO_2/water Al_2O_3/water	L	Nanofluid with higher volume fraction provide higher heat transfer rate	(Demir, H. et al., 2011)
SP	Al_2O_3/water	L	The heat transfer rate increases with rising Re for each nanoparticle concentration	(Pathipakka, G. and Sivashanmugam, P., 2010)
SP/TP	Cu/water	T	An increase higher than 15% in Nu was obtained by 1% Cu-water nanofluid	(Behzadmehr, A. et al., 2007)
SP	Al_2O_3/water CuO/water Cu/water	L	Increasing nanoparticle concentration and decreasing particle size enhances heat transfer coefficient	(Heris, S. Z. et al., 2007)
SP	Al_2O_3/water	L	Increased heat transfer and pressure loss with increasing nanoparticle volume concentration	(Zhao, N. et al., 2016)
SP	Fe_3O_4/water	T	Increase in Re and volume concentration enhanced the Nu and heat transfer rate	(Moraveji, M. K. and Hejazian, M., 2012)
SP/TP	Al_2O_3/water	L	Nanoparticle concentration has an positive effect on the increase in Nu	(Moraveji, M. K. and Ardehali, R. M., 2013)
TP	Al_2O_3/water	T	The greater Re and particle volumetric concentration ratio the more heat transfer rate	(Hejazian, M. et al., 2014)
SP	Al_2O_3/water SiO_2/water	L	SiO_2/water with 1% volumetric concentration ratio provided the highest heat transfer rate	(Salman, B. et al., 2014)
SP/TP	Al_2O_3/water	L	Increase in Re increased the heat transfer rate and shear stress	(Bianco, V. et al., 2014)
TP	TiO_2/water	T	Optimum conditions obtained with 4% TiO_2/water nanofluid at Re of 5000	(Siavashi, M. and Jamali, M., 2016)
TP	Al_2O_3/water TiO_2/water	T	Re of 60×10^3, volume concentration of 6% and particle diameter of 10 nm provided the optimum flow conditions	(Saha, G. and Paul, M. C., 2015)
SP	Al_2O_3/water TiO_2/water ZrO_2/water	L	Lower entropy generation for the nanofluids compared to the base fluid	(Purohit, N. et al., 2016)
SP	Al_2O_3/water	T	Low concentration of nanoparticles is crucial for minimising the entropy generation	(Bianco, V. et al., 2014)

SP: Single phase TP: Two phase L: Laminar T: Turbulent

It can be concluded from the studies in the literature that two-phase models can predict flow behaviours of nanofluids more accurately than single-phase models. On the other hand, it was also claimed by several researchers that two-phase models generally over predict heat transfer coefficient of nanofluids.

Nanofluids can be utilised in solar thermal applications such as in solar collectors, solar stills, solar cells and solar cooling systems to increase the heat transfer rate. Several studies have been conducted on nanofluid utilisation in flat plate collectors and the results indicated that nanofluids improved the thermal efficiency of flat plate collectors (Chaji, H. et al., 2013; Colangelo, G. et al., 2013; Yousefi, T. et al., 2012a; Yousefi, T. et al., 2012b). Furthermore, nanofluids can be utilised in solar thermal power applications as a working fluid. For instance, Saadatfar et al. (2014), used silver-nano pentane in solar organic Rankine cycle for power, heating and cooling applications. It was reported that the achieved performance of the cycle when using nanofluids was higher than that of the base fluid (n-pentane) (Saadatfar, B. et al., 2014).

Chapter 3 Experimental methodology

Low-temperature solar thermal systems utilising novel thermo-fluids has been an important subject to several researchers since many years. Therefore, a practical experience is vital to understand solar thermal systems under real operating conditions. In this context, a low-temperature solar thermal system prototype was developed and the experimental tests of the prototype, employing a new generation thermo-fluid (HFE 7000) were conducted. The experimental set-up and the experimental methodology are comprehensively described in this section. This chapter is summarised and represented in *Papers I* and *II*.

3.1. Testing room

The solar thermal power test bench was placed in a testing room where the system tests were conducted. The testing room consists of four insulated walls and an inner wall which separates the collector and heat engine unit. The schematic layout of the testing room is shown in Figure 3-1.

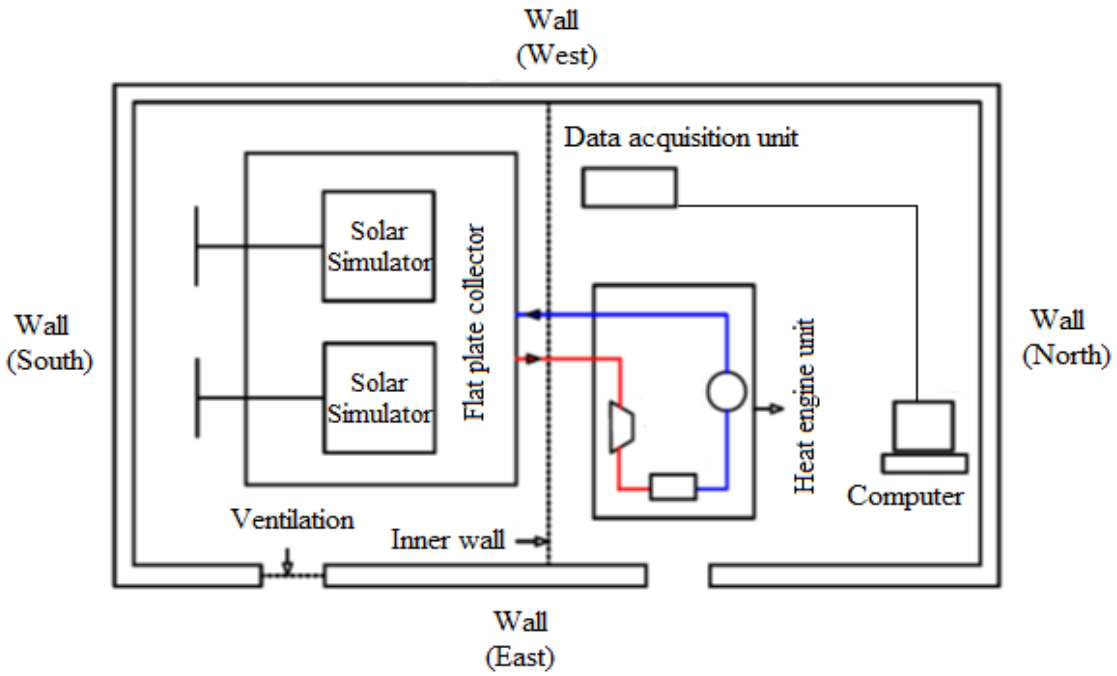

Figure 3-1 Schematic illustration of the experimental test bench

The experimental test bench is comprised of two units connected to each other. The first unit is the solar organic Rankine cycle. This is where the working fluid is utilised in order to generate mechanical work and heat simultaneously. The second unit is the heat

recovery section where the rejected heat coming from the first unit via condenser is recovered. The solar ORC unit consists of a flat plate collector, an expander, a water cooled condenser, a circulation pump, a liquid reservoir and other additional components. There is a domestic hot water tank which is connected to solar ORC through the condenser in the heat recovery unit. A schematic diagram of the test bench is represented in Figure 3-2.

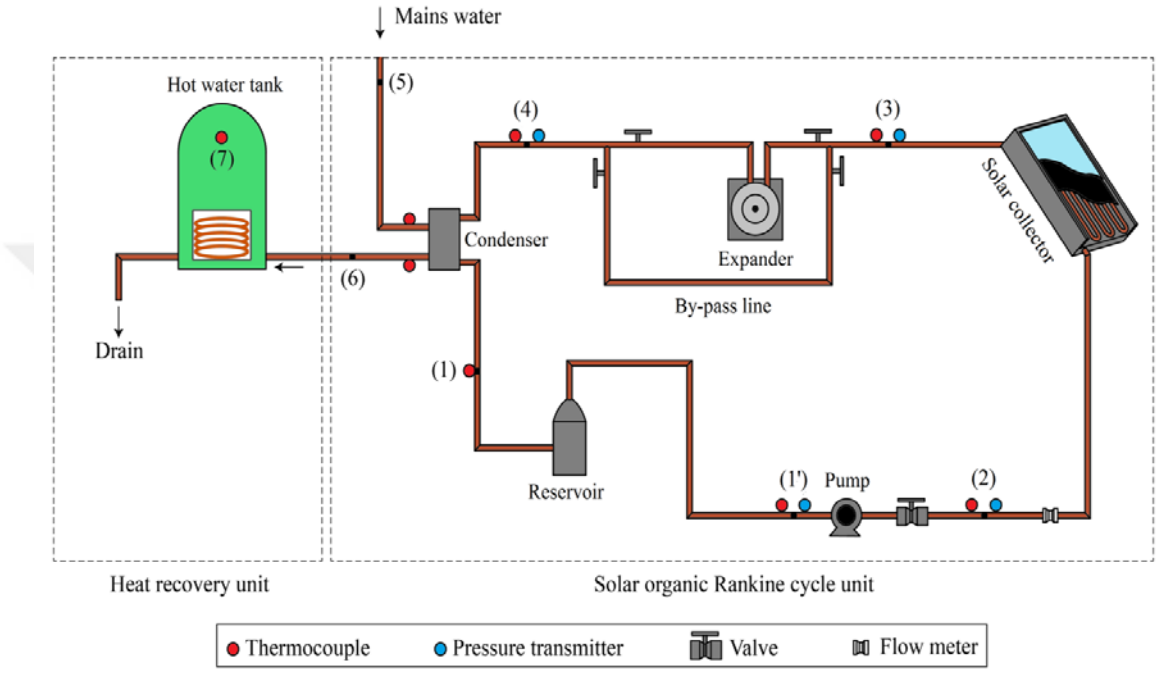

Figure 3-2 Schematic layout of the solar thermal system (Helvaci, H. and Khan, Z. A., 2016)

The solar ORC unit operates on a basic ORC principle where the liquid coming from the reservoir is pumped into the solar collector to gain heat energy. As the liquid gathers energy, its temperature increases and turns into vapour. Then, the vapour expands in the vane expander and rotates the expander shaft. This is where the mechanical energy is generated. Post the expander, the fluid is sent to the condenser to decrease its temperature and reject some heat from the system. Finally, the condensed thermo-fluid is pressurised by the pump and is sent back to the collector to complete the cycle. The rejected heat coming from the solar ORC unit is directed to the hot water tank in the heat recovery unit. This is to utilise the waste heat in terms of increasing the temperature of the stagnant and stored water in the tank *(Paper I; section 3.1*).

3.2. System components

The components which constitute the solar thermal test rig are described in this section *(Paper I; section 3.1 and Paper II; section 2)*.

3.2.1. Flat plate solar collector

Flat plate collector consists of a cover (1), absorber (2), copper tube (3) and insulation (4) in the back and the edges of the collector (Figure 3-3).

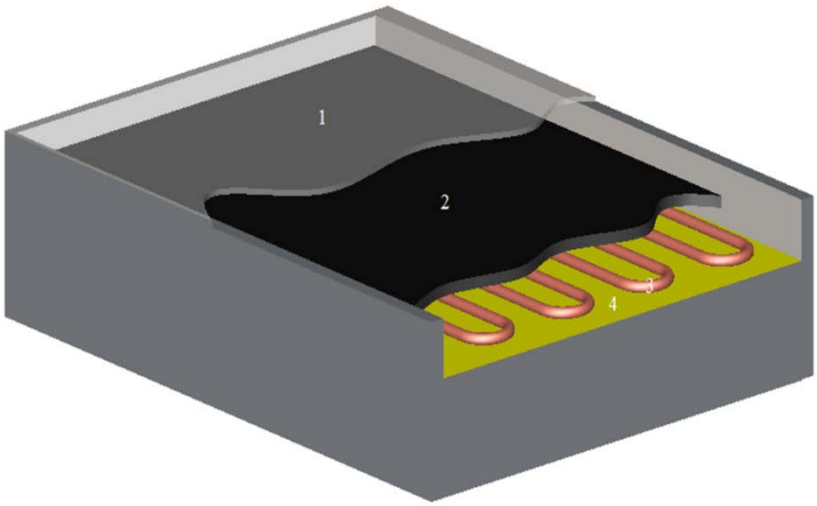

Figure 3-3 Schematic of the flat plate collector (Helvaci, H. and Khan, Z. A., 2015)

The cover is a transparent glass and it is used to reduce radiation, as well as convection losses from the collector. The absorber is a stainless-steel plate with high absorption property. The collector has a serpentine tube configuration. The collector tube is composed of 3 smaller tubes welded together and the total length of the collector tube is 56 m. The joints were sealed by using suitable sealants. The fluid circulates in the copper tubes where the heat is transferred from the absorber to the fluid. Conduction and convection loss from the back end edges of the collector is reduced by the insulation. The flat plate collector specifications are given in Table 3-1.

Table 3-1 The flat plate collector specifications (Helvaci, H. and Khan, Z. A., 2015)

Absorber plate thermal conductivity (W/m-K)	50
Absorber plate thickness (m)	0.001
Total length of tube (m)	56
Tube inner diameter (m)	0.008
Tube outer diameter (m)	0.01
Effective transmittance-absorbance product (-)	0.81

3.2.2. Pump

Based on the way that pumps transmit energy to the media, they are divided into two types; kinetic and positive displacement pumps. Kinetic energy is impelled to the fluid

by impellers in kinetic pumps. However, reciprocating actions of pistons, gears, lobes or other moving bodies are used to displace fluid in positive displacement pumps. Selection criteria of the pump can vary from flow rate, differential pressure, operating temperature and fluid viscosity. Positive displacement pumps are better options in ORC applications due to their ability to operate at lower flow rates and desired pressure ratios (Panesar, A. S., 2012).

Figure 3-4 Photograph of the diaphragm pump

In this study, a diaphragm pump which is a positive displacement pump was employed to pressurise the system. The technical specifications of the pump are given in Table 3-2.

Table 3-2 Technical specifications of the diaphragm pump

Pump type	**Diaphragm**
Maximum flow rate (L/min)	3
Maximum pressure (bar)	20
Maximum head (m)	89
Motor output (W)	55

It is important to note that a flow control valve was mounted on the discharge side of the pump to adjust the flow rate of the working fluid in the cycle (Figure 3-2).

3.2.3. Expander

The efficiency of an Organic Rankine cycle is highly related to the selected expander. Expanders can be divided into two groups as: velocity type and volumetric type

expanders. Velocity type expanders refer axial and radial turbines, volumetric types, in other words, positive displacement types refer scroll and screw expanders, reciprocating piston expanders and rotary vane expanders. All of these expanders have their own advantages and disadvantages when they are used in ORCs. However, positive displacement expanders are more appropriate for ORC applications due to their lower rotational speeds, ability to operate under large pressure ratios and their good performance (Bao, J. and Zhao, L., 2013; Lemort, V. et al., 2013). Table 3-3 compares 5 different types of expanders which have been used in ORCs previously.

Table 3-3 Comparison of various expander types (Bao, J. and Zhao, L., 2013; Lemort, V. et al., 2013)

Type	**Capacity range (kW)**	**Rotational speed (rpm)**	**Cost**
Radial turbine	50-500	8000-80000	High
Scroll expander	1-10	<6000	Low
Screw expander	15-200	<6000	Medium
Reciprocating piston expander	20-100	-	Medium
Rotary vane expander	1-10	<6000	Low

It can be seen from the Table 3-3 that radial turbines, screw expanders and reciprocating piston expanders are more appropriate for larger applications where as a scroll and rotary vane expanders are appropriate for medium and small scale applications. Air motors are rotary vane expanders and they have simpler structure, easier manufacturing and lower cost in comparison to the other expander types (Bao, J. and Zhao, L., 2013). In this study, a rotary vane air motor is used as an expander of the cycle (Figure 3-5) and the technical specifications of the air motor are provided in Table 3-4.

Table 3-4 Technical specifications of the air motor

Model	**Globe -VA2J**
Maximum power (kW)	0.8
Torque at maximum power (Nm)	2
Minimum starting torque (Nm)	2.3
Maximum speed (rpm)	4000

Figure 3-5 Photograph of the air motor

3.2.4. Condenser

A brazed type plate heat exchanger is selected for the experimental study (Figure 3-6). Plate heat exchangers consist of a stack of thin plates and they have major advantages over conventional heat exchangers.

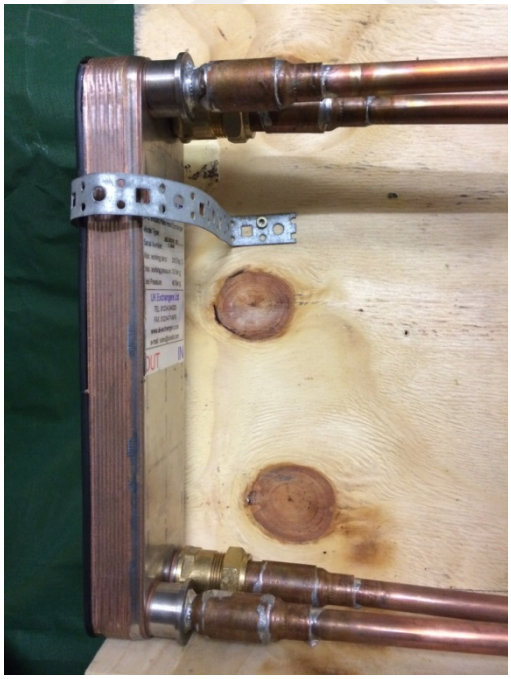

Figure 3-6 Brazed type plate condenser

Corrugated thin plates are brazed together and let the fluid exposure to larger surface area. Plate heat exchangers are suitable for any type of gas, liquid and two-phase flows (Yang, B. et al., 2009). Technical specifications of the condenser which was utilised in this research are given in Table 3-5.

Table 3-5 Technical specifications of the condenser

Type	**Brazed plate heat exchanger**
Model	UKE-BRO40
Number of plates	10
Plate material	316 Stainless steel
Braze material	Copper
Maximum working pressure (bar)	30

3.2.5. Liquid reservoir

Liquid reservoir where the fluid is charged into the system allows a steady supply of working fluid. In this study, 12 litre vertical liquid reservoir was selected and it was placed after the condenser to avoid any vapour flowing to the pump which might cause a cavitation in the pump (Figure 3-7).

Figure 3-7 Twelve litre liquid reservoir

3.2.6. Hot water tank

The hot water tank was connected to the condenser in order to utilise the waste heat coming from the solar ORC unit. In this study, a copper-coiled, 118 L hot water tank was utilised to collect the rejected heat from the condenser (Figure 3-8).

Figure 3-8 Photograph of the hot water tank

3.3. Measurement devices

In this section, all the measuring instruments which enabled data acquisition from different points of the system are described *(Paper I; section 3.2 and Paper II; section 6)*.

3.3.1. Thermocouples

For temperature measurements, K-type thermocouples with stainless steel sheath were used in the experiments (Figure 3-9).

Figure 3-9 K-type thermocouple (Source: LABFACILITY)

Eight thermocouples with a diameter of 4.5 mm were mounted in the test bench at various locations (Figure 3-2) to collect the temperature data.

3.3.2. Pressure transmitters

Four industrial pressure transmitters which provide a 4-20mA output signal were used to measure pressures of the system at the inlet of the collector, expander, condenser and the pump. Pressure drop in the condenser was neglected during the experiments. The pressure transmitter is represented in Figure 3-10.

Figure 3-10 Photograph of the pressure transmitter (Source: TC Direct)

3.3.3. Flow meter

The liquid flow meter which was installed in the system is a multi-range turbine meter with a flow range between from 0.05 to 0.5 L/min. The flow meter has a linearity of 2% of full scale deflection (Figure 3-11).

Figure 3-11 Photograph of the flow meter (Source: Titan enterprise Ltd.)

3.3.4. Pyranometer

Pyranometer was used to measure the irradiance on the flat plate collector surface. The pyranometer which has a spectral range between 300 and 2800 nm can measure solar irradiance up to 2000 W/m^2. The pyranometer is represented in Figure 3-12.

Figure 3-12 Photograph of the pyranometer (Source: Kipp & Zonen)

3.3.5. Data taker

Agilent 34972A data acquisition unit with 34901A multiplexer was used in the experiments for the collection of data. The acquisition unit can measure and convert various signals such as DC/AC volts, DC/AC currents, frequency, period and temperature with thermocouples.

Figure 3-13 Photograph of the data taker (Source: Agilent)

3.4. Heat source

It is difficult to obtain stable solar radiation in UK weather conditions. Therefore, a solar simulator, which consists of two lighting machines, was used to provide steady energy on the surface of the solar collector during the experiments. Each machine consists of 6 glare lamps and each lamp can provide 1kW heat energy.

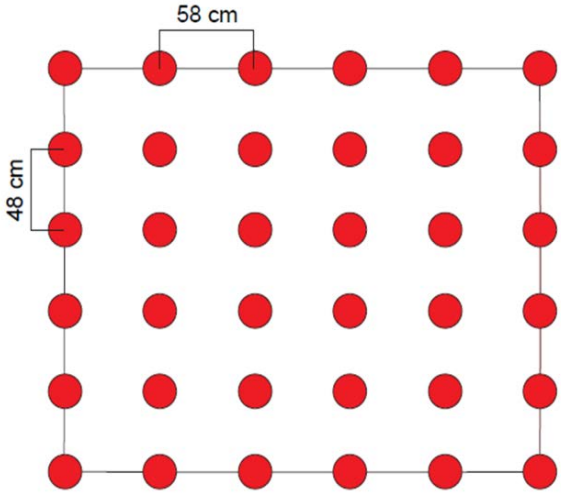

Figure 3-14 Marked points on the flat plate collector surface

It is also crucial to measure the amount of the incoming radiation on the collector surface for understanding and interpreting the collector and the whole system performance. Therefore, measurements were conducted to investigate the incoming solar radiation under two operating conditions. Initially, the collector was marked to specify the points where the pyranometer was placed (Figure 3-14). Then, the solar simulator was placed 2 m away from the flat plate collector and initially 6 lights were

turn on. This means 6 kW heat was supplied on the collector surface. Measured irradiation data at each marked point was recorded. After the first measurement, another 4 lights were also switched on so 10 kW heat was supplied on the collector surface. The measurement procedure was followed and the measured data at each point was recorded. According to the measurement results, an average of 550 W/m^2 and average of 890 W/m^2 solar radiation was provided in the first and second conditions respectively. Figure 3-15 demonstrates the irradiation distribution on collector surface.

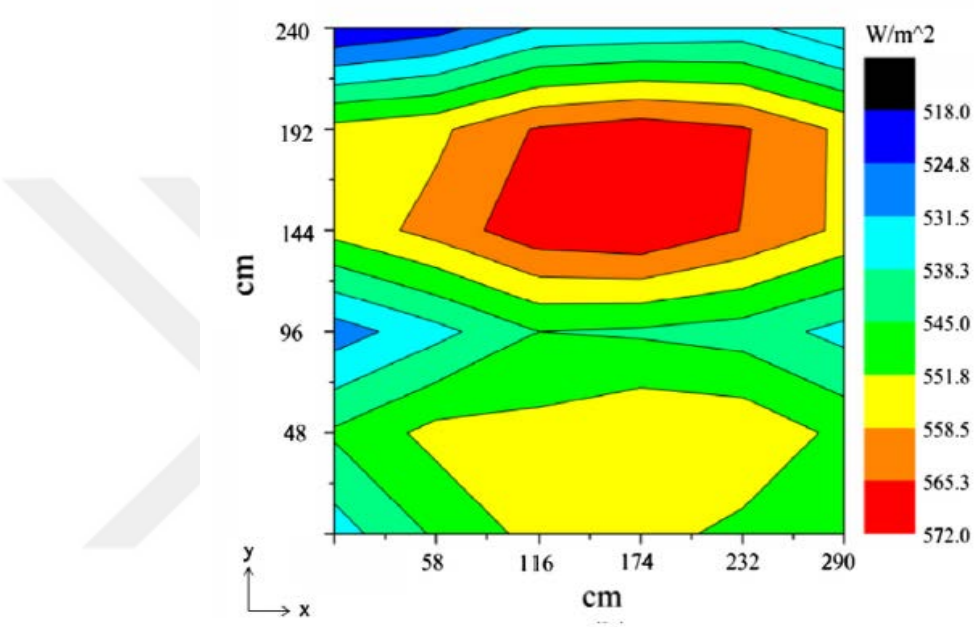

Figure 3-15 Measured irradiation distribution on the collector surface (Helvaci, H. and Khan, Z. A., 2015)

3.5. Working fluid

Hydrofluoroether (HFE) 7000 ($C_3F_7OCH_3$) which was selected as the working fluid of the system has zero ODP and GWP of 450 (Tsai, W.-T., 2005). Compared to the water, it has a lower boiling point temperature and higher latent heat of vaporization, density and molecular weight. HFE 7000 is compatible with many materials such as stainless steel, brass, copper, aluminium, polypropylene, polyethylene and nylon. It is also a non-flammable and non-corrosive compound.

3.6. Test procedure

The procedure followed before and during the each test is represented in this section (*Paper I; section 3.2).*

3.6.1. Leak test of the system

Leak test of the system is one of the most important tasks since it affects the overall system efficiency and the safety of the system. The system leak tests were conducted to examine if there was a leakage somewhere in the system. Special attention was given to couplings, joints and the components of the system. Initially, the system was pressurized with a compressor up to 8 bars via compressor line which was connected to the system. Then, a stream of a foamy liquid leak detector was applied to the parts of the system mentioned above. Unfortunately, a formation of bubbles was observed in the expander and in the joint (Figure 3-16).

Figure 3-16 Bubble formation in the expander and the joint

Once the leakage was detected the air was released from the system. Then the expander and the joint were taken apart. The point where the leakage was coming out of the joint was sealed properly. The expander was also disassembled and modified to stop leaking (Figure 3-16).

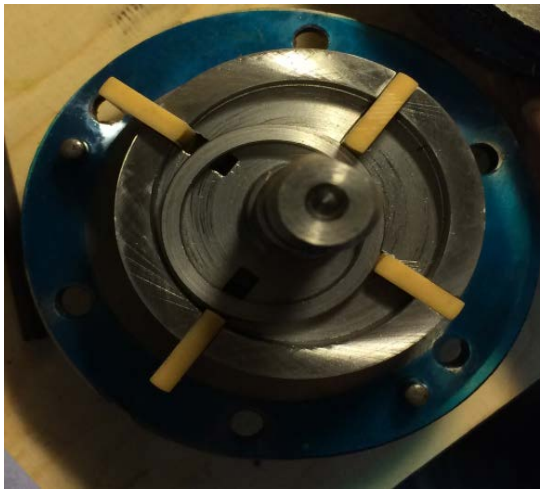

Figure 3-17 Internal view of the expander

Subsequently, the same procedure was followed to detect any leakage in the system. Once there was no leak observed in the system, the compressor was turned off and the air was released from the system. Instantly, a vacuum pump was connected to the system via vacuum line to pull a vacuum in the cycle. Vacuum gauge was mounted to the system to read and record the vacuum pressure. The system was vacuumed to -0.56 bar and left for 24 hours to observe for any leakage through changes in the system's pressure. After 24 hours the vacuum gauge checked again and it remained in the same position as where it was.

3.6.2. Working fluid charging

The amount of the working fluid (HFE 7000) which is charged into the system must be evaluated before any test is carried out. The procedure relies on the calculation of the volume of each element. Since the vapour density is relatively smaller compared to the liquid density, the regions in the components and the pipe where the fluid turns into vapour was not taken into account in the calculations (Quoilin 2007). The volumes of the components such as pump, collector, condenser and also the tube in the system were evaluated. Collector volume was calculated by determining the total length of the pipe in the collector (56m) and it was assumed that vapour region occupies 20% of the total length of the pipe. Table 3-6 represents the calculated volumes of each component and the tube.

Table 3-6 Volumes of each component

Component	**Volume (L)**
Pump	2.84×10^{-1}
Collector	3.45
Condenser	0.645
Piping	1.08
Total volume	5.45

Then, the total volume was multiplied by the fluid density to calculate the amount of the mass of the fluid. The total amount of working fluid that needs to be charged into the system was found 7.64 kg. Considering the possible fluid losses in the system 8 kg (5.7 L) of HFE 7000 was introduced to the system. Initially, the vacuum line was shut off and the vacuum pump was disconnected. Then, the vacuum line connected to the working fluid cylinder and the valve was turned on. Subsequently, the fluid flowed into

the system via the pressure difference between the system and the working fluid cylinder. Finally, the vacuum line valve was shut off after 8 kg (5.7 L) of fluid was charged into the system.

3.7. Experimental procedure

Initially, the expander by-pass line was opened and the valve on the discharge side of the pump was set to the desired position. The data taker was turned on to monitor and record the temperature, pressure and flow rate data. The pump was turned on and let the fluid circulate through the system without turning any lights on for half an hour. This was to check the system consistency and safety. Then, the lights were turned on in a way that 890 W/m^2 radiation was supplied to the collector surface. As it was mentioned previously, the solar thermal system consists of two parts which are solar organic Rankine cycle and heat recovery unit. In the ORC unit, the pump sucked the fluid and moved it along the system by consuming some work. Subsequently, the fluid reached the collector as pressurized liquid. The flat plate collector was used as an evaporator of the cycle and there was a heat addition into the system in the collector. This heat was used to heat and vaporize the fluid in the collector. The fluid might leave the collector as a mixture of saturated liquid and vapour, saturated vapour or superheated vapour depending on the amount of the heat transferred to the fluid, inlet pressure and the flow rate of the fluid. If the fluid did not reach vapour conditions, then it was by-passed via the by-pass line and it went to the condenser. Once the fluid reached the vapour conditions then the by-pass line was closed and let the fluid pass through the expander. The fluid expanded in the expander and produced shaft work. In other words, the mechanical work was generated in the expander. The lower pressure exhaust vapour at the end of the expander was directed to the condenser where heat rejection of the system took place. The fluid was cooled down and turned into the liquid state in the condenser. It was also sub-cooled in the liquid reservoir depending on the level of the liquid and it was pumped again into high pressure to complete the system. In the condenser, the cooling water condenses the HFE 7000 by gaining some energy from it. This increases the temperature of the cooling water. Therefore, in the heat recovery unit, the cooling water was directed to the domestic hot water tank to recover its energy. Measured points of temperature, pressure and flow rate of the fluid is shown in Figure 3-2. (Paper I; section 3.2).

3.8. Thermodynamic analysis

This section indicates the thermodynamic analysis of the solar thermal system and it is taken from section 4 of Paper I. The proposed low-temperature solar ORC represents a closed loop cycle. Therefore, the performance analysis can be conducted through energy and exergy analysis methods which base on the mass, energy and exergy balance equations. The following assumptions were made to derive the balance equations:

- The system is in steady-state conditions
- Kinetic and potential energy changes are neglected
- Pressure of P_0= 1 bar and temperature of T_0= 15 °C is taken as reference-dead state

The balance equations which were applied to each component of the system are defined as follows:

$$\sum \dot{m}_{in} = \sum \dot{m}_{out} \tag{3-1}$$

$$\dot{Q} - \dot{W} = \sum \dot{m}_{out} h_{out} - \sum \dot{m}_{in} h_{in} \tag{3-2}$$

Equation (3-1) and Equation (3-2) indicates the mass balance and energy budget equations respectively. $\dot{m}$ is the mass flow rate of the fluid, $\dot{Q}$ and $\dot{W}$ are the heat transfer and work rate respectively and h indicates the enthalpy of the fluid.

$$\dot{E}x_{heat} - \dot{W} + \sum \dot{E}x_{in} - \sum \dot{E}x_{out} = \sum \dot{E}x_{dest} \tag{3-3}$$

Equation (3-3) indicates the exergy budget equation where $\dot{E}x_{heat}$ and $\dot{E}x_{dest}$ are the exergy transfer rate by heat and exergy destruction rate respectively. Exergy transfer rate by heat can be derived as;

$$\dot{E}x_{heat} = \sum 1 - \left(\frac{T_0}{T}\right) \dot{Q}_j \tag{3-4}$$

Exergy rate is calculated by multiplying the mass flow rate by specific exergy (e).

$$e = (h - h_0) - T_0(s - s_0) \tag{3-5}$$

3.8.1. Energy analysis

In the energy analysis, the mass and energy budget equations were applied to each component of the solar ORC unit. Table 3-7 shows the mass and energy budget equations for each component (for each state refer to Figure 3-2).

Table 3-7 Mass and energy budget equations for each component (Helvaci, H. and Khan, Z. A., 2016)

Component	Mass balance equations		Energy budget equations	
Collector	$\dot{m}_2 = \dot{m}_3 = \dot{m}_{wf}$	*(3-6)*	$\dot{Q}_{gain} = \dot{m}_{wf} \times (h_3 - h_2)$	*(3-7)*
Expander	$\dot{m}_3 = \dot{m}_4 = \dot{m}_{wf}$	*(3-8)*	$\dot{W}_{exp} = \dot{m}_{wf} \times (h_3 - h_4)$	*(3-9)*
Condenser	$\dot{m}_4 = \dot{m}_1 = \dot{m}_{wf}$ $\dot{m}_5 = \dot{m}_6 = \dot{m}_w$	*(3-10)*	$\dot{Q}_{cond} = \dot{m}_{wf} \times (h_4 - h_1)$ $\dot{Q}_{cond} = \dot{m}_w \times (h_{cw,out} - h_{cw,in})$	*(3-11)*
Pump	$\dot{m}_{1'} = \dot{m}_2 = \dot{m}_{wf}$	*(3-12)*	$\dot{W}_{pump} = \dot{m}_{wf} \times (h_2 - h_{1'})$	*(3-13)*

In Eq. (3-11), flow rate of the cooling water was calculated via the energy budget of the condenser with the assumption of steady state conditions as:

$$\dot{Q}_{cond} = \dot{m}_{wf} \times (h_4 - h_1) = \dot{m}_w \times (h_{cw,out} - h_{cw,in}) \quad (3\text{-}14)$$

$$\dot{m}_w = \frac{\dot{Q}_{cond}}{(h_{cw,out} - h_{cw,in})} \quad (3\text{-}15)$$

where $\dot{Q}_{cond}$ is the heat rate discarded from the condenser and $h_{w,in}$ and $h_{w,out}$ are the inlet and outlet enthalpy of water respectively. Furthermore, the amount of the stored energy in the hot water tank during the experiment can be evaluated as:

$$\dot{Q}_{st} = \frac{m_{cw,st} \times C_{p,cw} \times (T_{cw,st,final} - T_{cw,st,initial})}{t_{exp}} \quad (3\text{-}16)$$

$$m_{w,st} = V_{st} \times \rho_{cw} \quad (3\text{-}17)$$

where $\dot{Q}_{st}$ is the amount of heat that is transferred to the cold water in the hot water tank from condenser. $T_{w,st,initial}$ and $T_{w,st,final}$ indicate the cold water temperature in the tank at the beginning and at the end of the experiment. $m_{w,st}$ is the mass of the water in the hot water tank.

3.8.2. Exergy analysis

Exergy balance equations were applied to each component of the solar ORC unit and represented in Table 3-8.

Table 3-8 Exergy balance equations for each component (Helvaci, H. and Khan, Z. A., 2016)

Component	Exergy balance equations	
Collector	$\dot{E}x_{dest,col} = (\dot{E}x_2 - \dot{E}x_3) + S_{in}\, A_{col}\left[1 - \frac{T_0}{T_p}\right]$	*(3-18)*
Expander	$\dot{E}x_{dest,exp} = (\dot{E}x_3 - \dot{E}x_4)$ - $\dot{W}_{exp}$	*(3-19)*
Condenser	$\dot{E}x_{dest,cond} = (\dot{E}x_4 - \dot{E}x_1) + \dot{m}_w \times (\dot{E}x_5 - \dot{E}x_6)$	*(3-20)*
Pump	$\dot{E}x_{dest,pump} = (\dot{E}x_{1'} - \dot{E}x_2) + \dot{W}_{pump}$	*(3-21)*

In Eq. (3-18), the term "$S_{in}\, A_{col}\left[1 - \frac{T_0}{T_p}\right]$" indicates the solar radiation exergy rate which was absorbed on the surface of the collector (Dikici, A. and Akbulut, A., 2008). S_{in} and A_{col} are the incoming solar radiation and the collector area respectively. T_p and T_0 represent the collector plate temperature and dead state temperature respectively.

3.8.3. Efficiency calculations

Energy efficiency can be defined as the ratio of the output energy to the input energy, whereas exergy efficiency is the ratio of the exergy output to the exergy input (Gupta, M. and Kaushik, S., 2010). Efficiency analysis of each component was evaluated through first and second law efficiencies of each component and was given in Table 3-9.

Table 3-9 Energy and exergy efficiency calculations of the components (Helvaci, H. and Khan, Z. A., 2016)

Component	Energy efficiency		Exergy efficiency	
Flat plate collector	$\eta_{col} = \frac{\dot{Q}_{gain}}{S_{in} A_{col}}$	*(3-22)*	$\varepsilon_{col} = \frac{\dot{E}x_3 - \dot{E}x_2}{S_{in}\, A_{col}\left(1 - \frac{T_0}{T_p}\right)}$	*(3-23)*
Expander	$\eta_{exp} = \frac{h_3 - h_4}{h_3 - h_{4,s}}$	*(3-24)*	$\varepsilon_{exp} = \frac{\dot{W}_{exp}}{(\dot{E}x_3 - \dot{E}x_4)}$	*(3-25)*
Condenser	-		$\varepsilon_{pump} = \frac{\dot{E}x_2 - \dot{E}x_{1'}}{\dot{W}_{pump}}$	*(3-26)*
Pump	-		$\varepsilon_{cond} = \frac{\dot{E}x_6 - \dot{E}x_5}{(\dot{E}x_4 - \dot{E}x_1)}$	*(3-27)*

The energy and exergy efficiency of the proposed solar ORC was calculated as follows:

$$\eta_{sorc} = \frac{\dot{W}_{net}}{\dot{Q}_{gain}} = \frac{\dot{W}_{exp} - \dot{W}_{pump}}{\dot{Q}_{gain}} \qquad (3\text{-}28)$$

$$\varepsilon_{sorc} = \frac{\dot{W}_{net}}{\dot{E}x_{in}} = \varepsilon_{sorc} = \frac{\dot{W}_{net}}{S_{in}A_{col}\left(1-\frac{T_0}{T_p}\right)} \quad (3\text{-}29)$$

Furthermore, the energy efficiency of the heat recovery unit was calculated as follows:

$$\eta_{rec} = \frac{\dot{Q}_{st}}{\dot{Q}_{cond}} \quad (3\text{-}30)$$

Eq. (3-30) indicates the ratio of heat, which was utilised by the cold water in the hot water tank to the available heat that can be transferred from the condenser. Finally, the following equation was utilised to calculate the ratio of the relative exergy destruction of each component to the total destruction.

$$RI_j = \frac{\dot{E}x_{dest,j}}{\dot{E}x_{dest,tot}} \quad (3\text{-}31)$$

Chapter 4 Experimental test results and discussion

The performance analysis of the system is explained in two sections; energy analysis and exergy analysis results in section 4.1 and section 4.2 respectively. Experimental test results were taken from section 5of *Paper I.*

The experimental data of temperature (ºC), pressure (bar) and flow rate (kg/s) were collected to evaluate the fluid states at the defined points (Table 4-1). The collected data of HFE 7000 is also represented in the T-s diagram in Figure 4-1.

Table 4-1 Thermodynamic state properties of HFE 7000 at various points (Helvaci, H. and Khan, Z. A., 2016)

State (No)	Fluid type	Phase	T (^oC)	P (bar)	$\dot{m}$ (kg/s)	h (kJ/kg)	e (kJ/kg)	$\dot{E}x$ (W)
0	HFE 7000	Dead state	15	1	-	218.05	-	-
0	Water	Dead state	15	1	-	63.076	-	-
1	HFE 7000	Liquid	19.54	0.66	0.022	223.56	0.038	0.83
1’	HFE 7000	Liquid	18.73	0.57	0.022	222.57	0.084	1.86
2	HFE 7000	Liquid	19.1	1.86	0.022	223.06	0.402	8.84
3	HFE 7000	Gas	45.41	1.32	0.022	385.07	15.532	341.7
4	HFE 7000	Gas	36.36	0.66	0.022	378.4	4.542	99.98
5	Water	Liquid	13.47	0.66	0.06	56.63	-0.11	-6.6
6	Water	Liquid	26.88	0.66	0.06	112.75	1.002	60.12

As it was mentioned in chapter 3, the measured solar radiation on the collector surface (condition two) was found to be 890 W/m^2. In the experiments, constant flow rate conditions were supplied with an average value of 0.022 kg/s. Furthermore, the-reference dead state conditions were assumed to be 288 K and 1 bar for the temperature and pressure respectively. Lastly, the thermodynamic properties of HFE 7000 were taken from REFPROP software (Lemmon, E. et al., 2013).

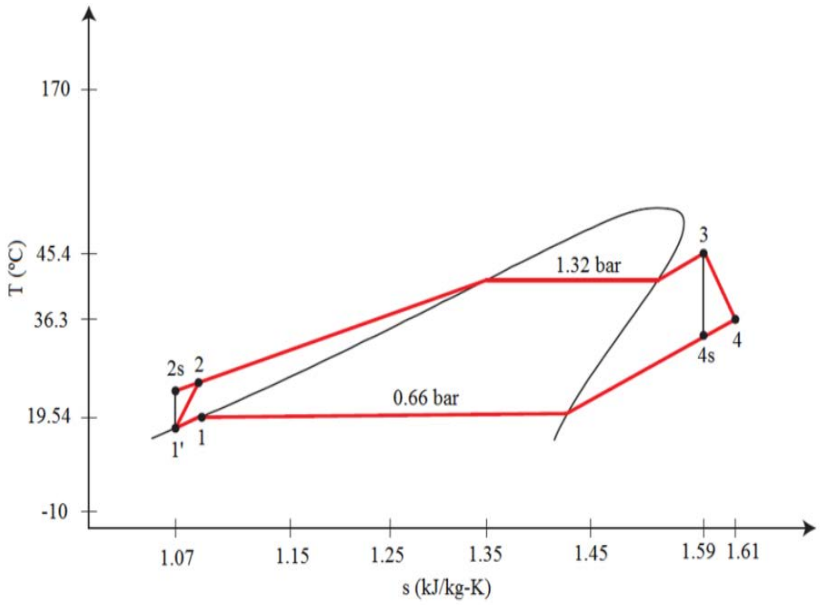

Figure 4-1 T-s diagram of the experimental results (Helvaci, H. and Khan, Z. A., 2016)

4.1. Energy analysis results

This section presents the energy analysis results of the system and it was taken from section 5.1 of *Paper I*.

4.1.1. Flat plate collector results

The calculated energy on the flat plate collector surface was found to be 6194.4 W by using Eq. (3-7). Then, 57.53% of this energy was transferred to the working fluid in the collector which resulted in a increase in the fluid temperature from 19.1 ºC to 45.41 ºC. The fluid left the collector as a superheated vapour as the fluid corresponding saturation temperature was 41 ºC at the pressure of 1.86 bar. It is worth mentioning that the chosen flow rate of the working fluid (0.022 kg/s) was sufficient enough for the fluid to reach saturated vapour, even superheated vapour conditions.

Table 4-2 Energy analysis of the solar collector (Helvaci, H. and Khan, Z. A., 2016)

Parameters	Value	Unit
Energy received by the collector ($S_{in}A_{col}$)	6194.4	W
Useful heat gain of the fluid (Q_{gain})	3564.2	W
Collector energy loss[a]	2907.8	W
Collector efficiency (η_{exp})	57.53	%

[a] $= S_{in}A_{col} - Q_{gain}$

As it can be seen from Figure 4-1 that HFE 7000 is a dry fluid and even small degree of superheating should not present any risk of encountering some portion of liquid in the expander. On the other hand, the higher degree of superheating the higher temperature

in the collector in other words, the greater heat loss from the collector to the ambient. Energy analysis of the solar collector is represented in Table 4-2.

4.1.2. Expander results

The generated mechanical work of the expander was calculated as 146.74 W with the help of Eq. (3-9). Furthermore, with the assumption of the expander is adiabatic, the isentropic efficiency of the expander was found to be 58.66%. Similar efficiency of vane expander was obtained in the literature by (Qiu, G. et al., 2012).

4.1.3. Condenser results

The pressure at the outlet of the expander also indicates the condensing pressure (0.66 bar) as the pressure loss through the condenser was assumed to be zero. The fluid entered the condenser with the temperature of 36.36 ºC and left the condenser at 19.54 ºC. Post condenser, its temperature and pressure decreased to 18.73 ºC and 0.57 bar. It is important to note that at this temperature and pressure conditions the fluid was sub-cooled liquid at the outlet of the liquid reservoir. In other words, there was no risk of saturate vapour of the fluid entering the pump which might have resulted in cavitation otherwise.

4.1.4. Heat recovery unit analysis

It was mentioned in the condenser results sectioned that the working fluid temperature was diminished from 36.36 ºC to 19.54 ºC. This means that 3406.48 W heat was transferred from the working fluid to the water and as a result the water temperature rose from 13.47 ºC to 26.88 ºC. As it was shown in Figure 3-2, the cooling water outlet was connected to the hot water tank to utilise this rejected heat from the cycle. The cooling water, which was preheated at the outlet of the condenser was directed to the storage tank and transferred some portion of its heat to the stagnant, cold water by circulating within the coil of the tank.

Table 4-3 Energy analysis of the heat recovery unit (Helvaci, H. and Khan, Z. A., 2016)

Parameters	Value	Unit
Testing time	3600	s
Initial water temperature ($T_{7,int}$)	16.65	ºC
Final water temperature ($T_{7,fin}$)	22.41	ºC
Total mass of water in the tank ($m_{w,st}$)	118	kg
Water specific heat capacity ($C_{p,w}$)	4.187	kJ/kg K
Total energy gain rate in the tank	2845.82	kJ
Average energy gain rate throughout the test ($\dot{Q}_{st}$)	0.79	kW
Average rejected heat rate in the condenser ($\dot{Q}_{cond}$)	3.406	kW
Heat recovery efficiency in the hot water tank (η_{rec})	23.2	%

4.2. Exergy analysis results

This section presents the exergy analysis results of the system and it was taken from section 5.2 of *Paper I*.

The exergy destruction rate and the exergetic efficiency values of each component was calculated by using Equations (3-23) to (3-27) and is represented in this section. The heat recovery unit was not considered in the exergy analysis. Table 4-4 shows the exergy destruction rate and exergy efficiency of each component.

Table 4-4 Exergy analysis of each component (Helvaci, H. and Khan, Z. A., 2016)

Component	$\dot{E}x_{dest}$ (W)	ε (%)
Solar collector	431	43.57
Expander	95	60.7
Condenser	32.3	67.3
Pump	3.8	64.73

The greatest amount of exergy destruction took place in the flat plate collector (431 W) (Table 4-4). Similar findings where the solar collector was found to be the highest source of exergy destruction in solar thermal systems were reported by (Al-Sulaiman, F. A., 2014; Elsafi, A. M., 2015; Freeman, J. et al., 2015). It can be stated that the high difference in quality between solar radiation and the working fluid at the collector operating temperature could be the source of this amount of exergy destruction rate in the solar collector. The collector was followed by the expander (95 W), condenser (32.3 W) and the pump (3.8 W) respectively. Friction and thermal loss which causes

irreversibility can be stated as the source of the expander exergy destruction (Tchanche, B. et al., 2010).

Table 4-4 also indicates that due to the large exergy destruction rate of the collector, it has the lowest exergy efficiency which was accounted for 43.57%. The exergy efficiency of the expander was the second lowest among the other components (60.7%). Then, the expander was followed by the pump (64.73%) and the condenser (67.3%) respectively.

The relative irreversibility of the components was evaluated according to Eq. (3-31) and was demonstrated in Figure 4-2. As it was expected, the collector showed the highest relative irreversibility which was accounted for 76.68 %.

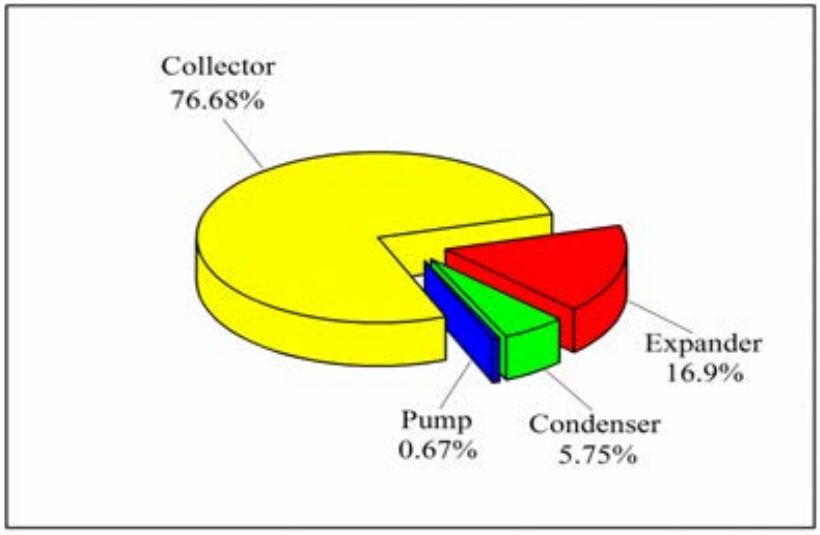

Figure 4-2 Relative irreversibility of each component (Helvaci, H. and Khan, Z. A., 2016)

Consequently, the energy and exergy analysis results shows that the proposed system was able to transfer 3564.2 W heat to the HFE 7000 in the collector and converted 146.74 W of this heat to the mechanical work in the expander. Furthermore, the solar ORC unit generated 135.96 W net work output ($\dot{W}_{pump}$= 10.78 W) with the first law efficiency of 3.81 and the exergy efficiency of 17.8%.

4.3. Parametric analysis of the solar ORC

This section presents the parametric analysis results of the system. It is taken from section 5.3 of *Paper I*. In order to investigate how the thermal and exergy efficiency of the solar ORC vary with expander inlet pressure and temperature, the parametric analysis was performed. It is important to note that in the analysis, the incoming solar

radiation (890 W/m^2), the efficiency of the collector (57.53%) and the condenser pressure (0.66 bar) were kept constant, whereas the expander inlet pressure was ranged from 2 bar to 5 bar and the degree of superheating at the expander inlet was changed from 5 to 35K. The pressure loss in the collector was also neglected which make the expander inlet pressure and collector inlet pressure equal.

The analysis shows that the mass flow rate of the fluid and the net work output of the cycle, which are highly related to the first and exergy efficiency of the cycle were influenced by the change in the expander inlet pressure and temperature (Figure 4-3).

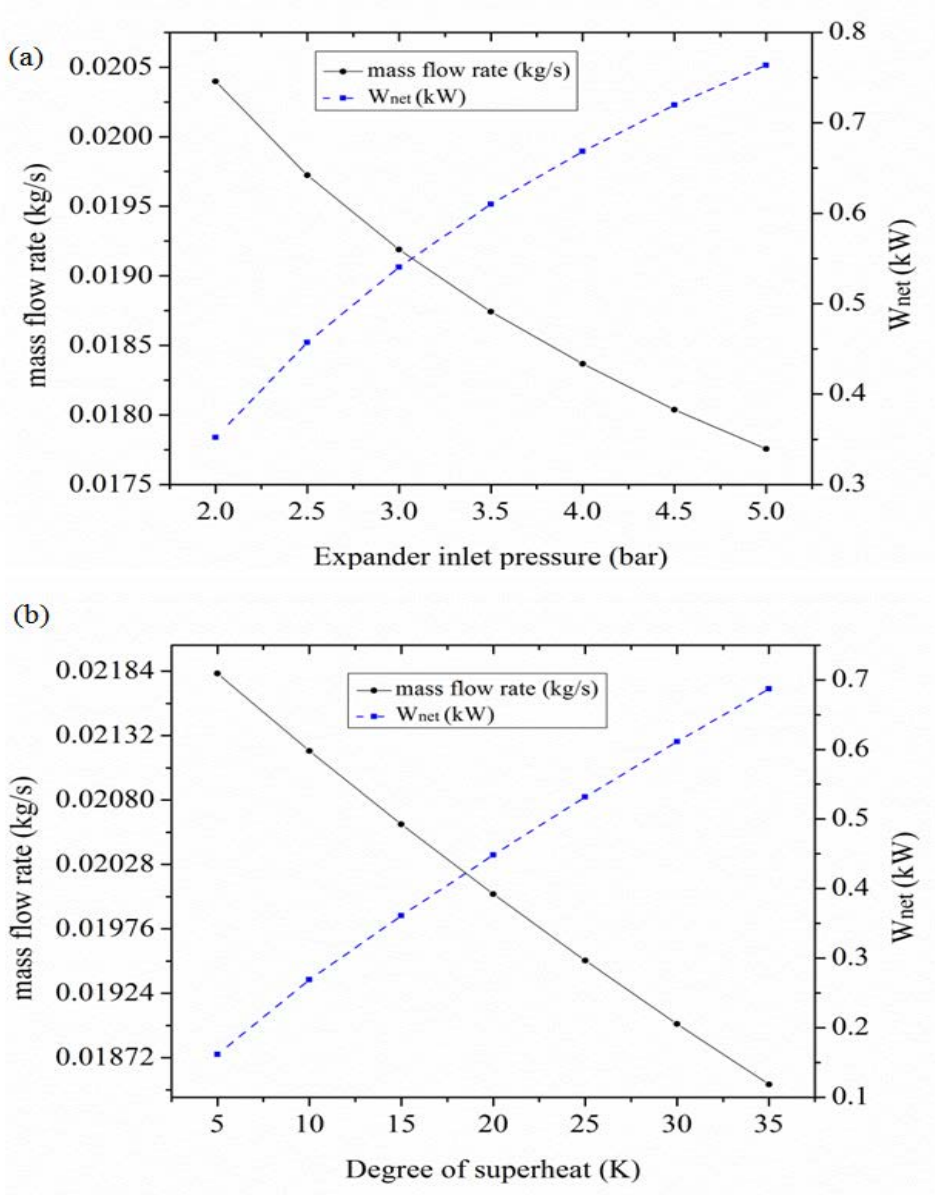

Figure 4-3 Mass flow rate and net work output versus a) expander inlet pressure b) degree of superheat

As the incoming solar radiation and the collector efficiency were kept constant, the increase in the expander inlet pressure which also equals to the flat plate collector

pressure enhanced the corresponding saturation pressure, as well as the saturation temperature of the fluid. This caused a decrease in the mass flow rate of the fluid to reach the specified conditions. The same effect was observed with the expander inlet temperature on the mass flow rate of the fluid. On the other hand, with the constant condenser pressure conditions, the increase in the expander inlet pressure and temperature enhanced the enthalpy gradient between the highest (expander) and the lowest (condenser) points of the cycle which subsequently increased the net mechanical work output of the cycle.

Figure 4-4 shows the first law and exergy efficiencies of the cycle versus expander inlet pressure. As it can be seen from Figure 4-4 that the thermal efficiency rose from 9.96% to 21.63% and the exergy efficiency augmented from 36.95% to 54.07% respectively.

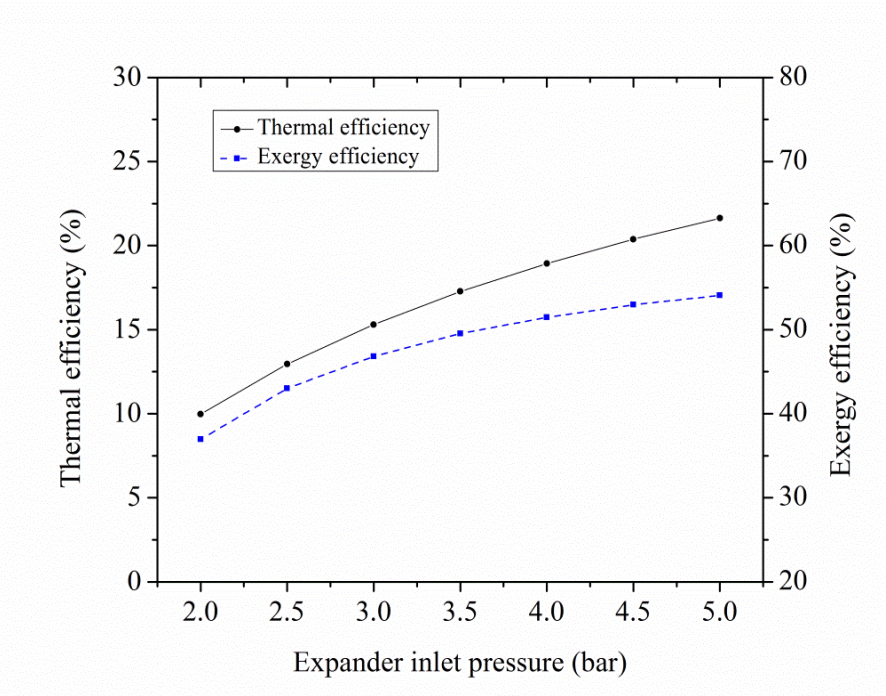

Figure 4-4 Variation of the energy and exergy efficiencies of the solar ORC for various expander inlet pressure

This trend shows that the higher pressure ratio of the cycle the more increase in the first and exergy efficiency of the cycle (Baral, S. and Kim, K. C., 2014). A similar trend was obtained when the degree of superheating rose from 5K to 35K the first and exergy efficiency of the cycle reached 19.29% and 56.9% respectively (Figure 4-5). Although the mass flow rate decreased with the increasing expander pressure and temperature, the enhancement in the net work output was superior to the reduce in the mass flow rate. Therefore, the first and the exergy efficiency of the cycle increased with expander inlet pressure and temperature.

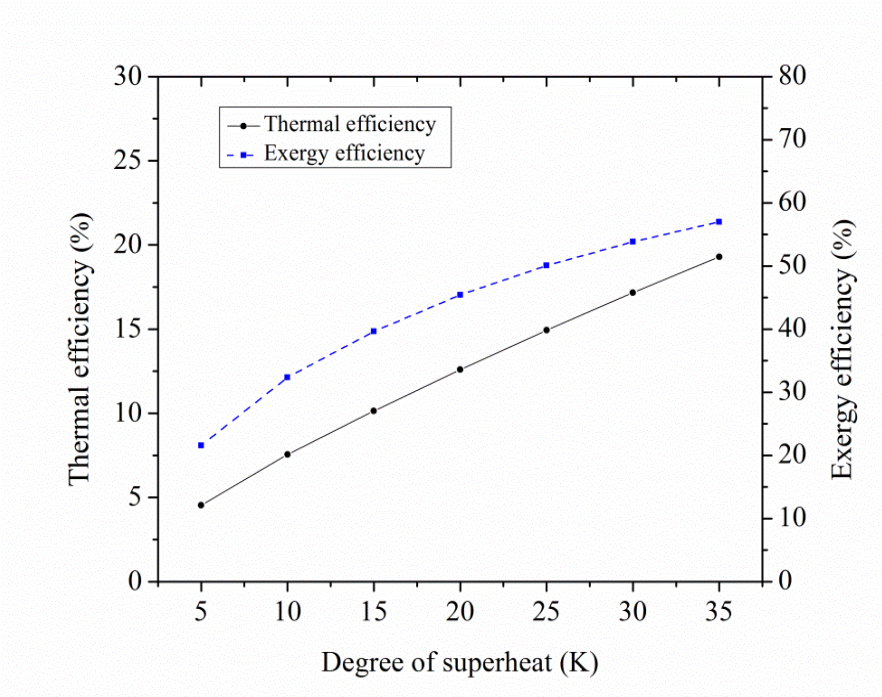

Figure 4-5 Variation of the energy and exergy efficiencies of the solar ORC for various degree of superheat

It should be noted that in reality, as the degree of superheating increases, in other words, the collector temperature increases the heat loss from the collector to the atmosphere rises. Therefore, the collector efficiency should vary with the degree of superheating. Furthermore, there should be a practical pressure ratio limit of the system due to the leakage and structural concerns of the expander. Tchance et al. suggested pressure ratio value of 3.5 for positive displacement expanders (Tchanche, B. F. et al., 2009). It is also important to take the effect of designed pressure ratio of the expander into consideration when evaluating the expander efficiency. In conclusion, it is crucial to conduct a parametric study considering a variable collector and expander efficiency in the analysis.

Chapter 5 Modelling of the proposed solar ORC

This chapter covers the modelling of the proposed solar ORC which then will be used for simulation of the components, as well as the whole cycle. The modelling methodology and the equations are taken from *Paper II*, *Paper III* and *Paper IV*. The schematic diagram of the modelled solar ORC is shown in Figure 5-1.

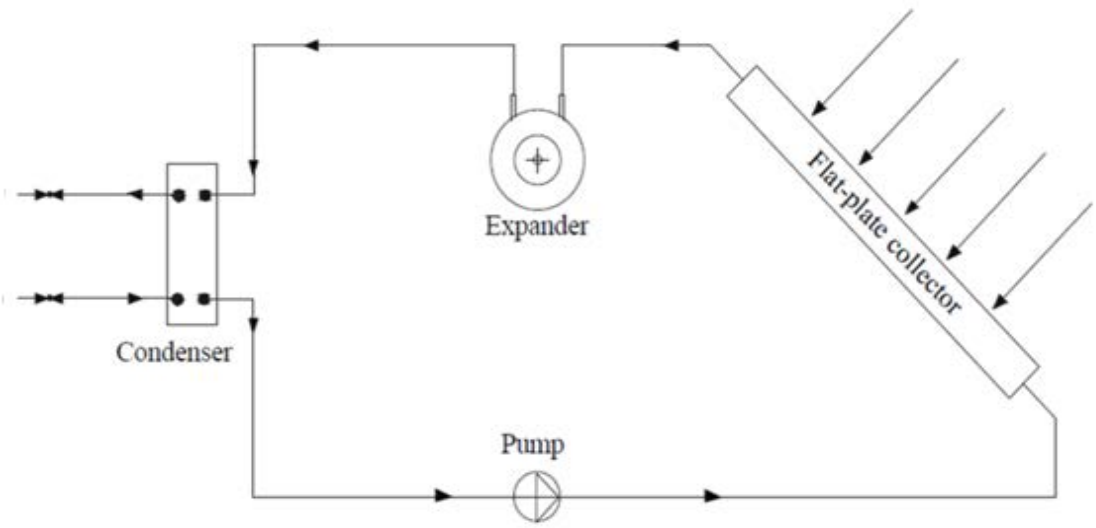

Figure 5-1 Schematic representation of the modelled solar ORC

5.1. Model assumptions

The solar ORC consists of the flat plate collector, the vane expander, the condenser and the pump and it is modelled based on the following assumptions:

- All the components of the solar ORC is considered as steady-state
- Pressure drop in the collector and the condenser are assumed to be zero
- Heat losses in the expander, the condenser and the pump are neglected
- The collector tube is modelled as one flat tube when determining the heat transfer coefficient of the fluid
- The thermal and radiation properties of the absorber and the glass cover are set to be constant
- In the collector, the working fluid undergoes a phase-change when its average temperature reaches the corresponding boiling temperature
- The heat transfer coefficient of the fluid both in single and multiphase flow conditions varies along the tube
- The pinch point temperature difference in the condenser was assumed to be 5 °C

5.2. Flat plate collector

The equations of the collector modelling are taken from sections 3 of *Paper II*, section 2.2 of *Paper III and 'THEORY'* section of *Paper IV*. The collector consists of a glass cover, absorber plate, copper tube and insulation as it is shown in Figure 5-2. The flat plate collector model is divided into two sections which are the determination of losses and the convective heat transfer calculations. The energy budget of the collector is represented in Figure 5-2.

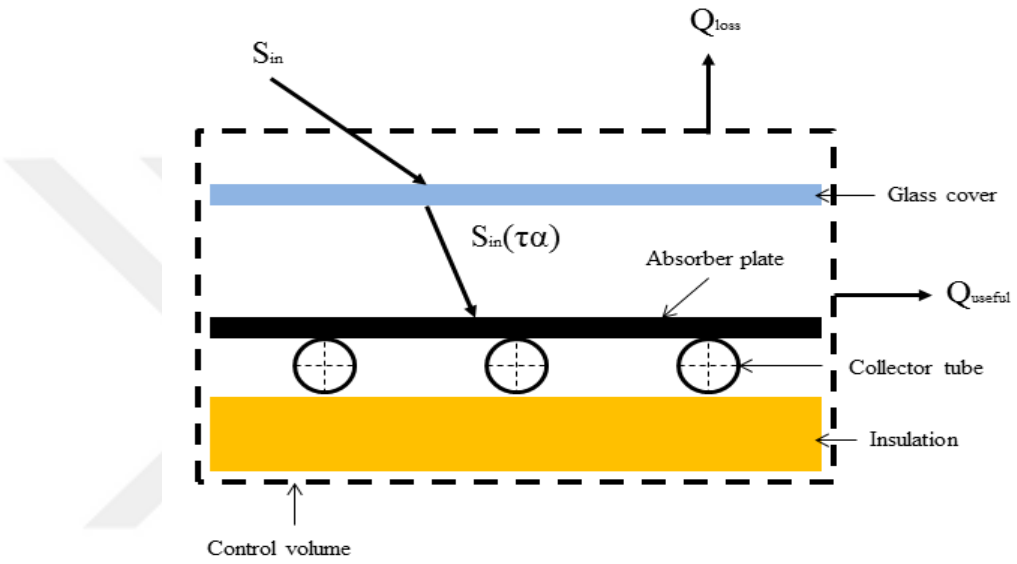

Figure 5-2 Flat plate collector energy budget representation

5.2.1. Determination of losses

There are two types of losses occur in the flat plate collector which are heat optical loss and thermal loss.

5.2.1.1 Optical losses of the collector

The optical loss represents the amount of the heat which is lost to the atmosphere when the incoming solar radiation is travelling through the glass cover. Optical loss is represented as S_{in} ($\boldsymbol{\tau}\alpha$), where ($\boldsymbol{\tau}\alpha$) indicates the transmittance-absorbance of the glass cover (Figure 5-2).

5.2.1.2 Heat losses of the collector

Heat losses can take place from the top, the edge and the back of the collector. It is important to note that the heat losses from the edge of the collector were neglected in the flat plate collector modelling. At the top of the collector, heat losses occur through

convection and radiation mechanism from the glass cover and the absorber plate to the ambient. The formula which was generalised by Klein (1975) was used to evaluate the top heat loss coefficient as (Klein, S., 1975):

$$U_{top} = \left(\frac{N_c}{\frac{C}{T_p}\left[\frac{T_p - T_a}{N_c + f}\right]^e} + \frac{1}{h_w} \right)^{-1} + \frac{\sigma\left(T_p + T_a\right)\left(T_p^{\,2} + T_a^{\,2}\right)}{\left(\varepsilon_p + 0.00591 N_c h_w\right)^{-1} + \frac{2N_c + f - 1 + 0.133\varepsilon_p}{\varepsilon_c} - N_c} \qquad (5\text{-}1)$$

where

$$h_w = 2.8 + (3V_w)$$

$$f = \left(1 + 0.0889 h_w - 0.1166 h_w \varepsilon_p\right)\left(1 + 0.07866 N_c\right)$$

$C = 520\left(1 - 0.000051\beta^2\right)$ where $0^o<\beta<70^o$ and if $70^o<\beta<90^o$ apply β=70º

$$e = 0.430\left(1 - 100 / T_p\right)$$

Heat losses at the back of the collector were calculated as:

$$U_{back} = \frac{k_{ins}}{L_{ins}} \qquad (5\text{-}2)$$

Thus, the total heat loss coefficient was evaluated as:

$$U_T = U_{top} + U_{back} \qquad (5\text{-}3)$$

5.2.2. Convective heat transfer calculations

The remaining absorbed heat energy on the collector surface now can be calculated as:

$$\dot{Q}_p = A_p\left[S_{in}(\tau\alpha) - U_T\left(T_p - T_a\right)\right] \qquad (5\text{-}4)$$

Then, some portion of this heat is transferred to the working fluid via heat transfer convection as the fluid is circulated along the collector. The amount of the heat that is transferred by the fluid is estimated as:

$$\dot{Q}_u = A_p F_R\left[S_{in}(\tau\alpha) - U_T\left(T_{f,in} - T_a\right)\right] \qquad (5\text{-}5)$$

where F_R is the collector heat removal factor and $T_{f,in}$ is the working fluid temperature at the collector inlet.

$$F_R = \frac{\dot{m}C_p}{A_p U_T}\left[1 - exp\left(-\frac{A_p U_T F'}{\dot{m}C_p}\right)\right] \qquad (5\text{-}6)$$

In Eq. (5-6), F′ indicates the collector efficiency factor and it was determined as:

$$F' = \frac{(U_T)^{-1}}{W[U_T(D_0+(W-D_0)F)]^{-1}+(C_b)^{-1}+(\pi D_i h_f)^{-1}} \quad (5\text{-}7)$$

where W indicates tube spacing, D_o and D_i represent the outer and inner tube diameter respectively. C_b is the bond conductance and it was not considered ($1/C_b=0$) in the calculation.

F represents the fin efficiency and it is estimated by Eq. (5-8).

$$F = \frac{tanh[m(W-D_0/2)]}{m(W-D_0/2)} \quad (5\text{-}8)$$

where $m = \sqrt{\frac{U_T}{k\delta}}$

In Eq. (5-7), h_f represents the convective heat transfer coefficient of the fluid. As it can be seen from Figure 5-1, the flat plate collector is used as an evaporator of the solar ORC. Therefore, the phase change of the fluid takes place in the collector and the convective heat transfer coefficient (h_f) should be evaluated for single and two phase flows individually in the model.

5.2.2.1 Single-phase flow

The heat transfer coefficient in the single phase region was evaluated based on the flow regime of the fluid. For constant heat flux, under a laminar flow regime (*Re<2300*) and under a turbulent flow regime (*0.5<Pr<2000, 3×10^3<Re<5×10^6*) Nusselt number is represented as follows:

$$Nu = 4.36 \quad (5\text{-}9)$$

$$Nu = \frac{\left(\frac{f}{8}\right)(Re-1000)Pr}{1+12.7\left(\frac{f}{8}\right)^{0.5}(Pr^{2/3}-1)} \quad (5\text{-}10)$$

In Eq. (5-10), Re and Pr are the Reynolds and Prandtl numbers and they were determined as:

$$Re = \frac{vD}{\upsilon} \quad (5\text{-}11)$$

$$Pr = \frac{\rho \upsilon C_p}{k} \quad (5\text{-}12)$$

where V is the velocity of the fluid, D is the tube diameter, υ represents the kinematic viscosity of the fluid, k and C_p are the thermal conductivity and specific heat of the fluid.

Then the heat transfer coefficient was calculated as:

$$h_{sp} = Nu\frac{k_{sp}}{D} \quad (5\text{-}13)$$

5.2.2.2 Two phase flow

In order to calculate the two phase heat transfer coefficient the model which was proposed by Shah (1982) is utilised (Shah, M., 1982). The model includes two different boiling mechanism which are nucleate and convective boiling. Initially, the dimensionless parameter (N) is estimated based on the Froude number conditions;

$N = 0.38(Fr_l)^{-0.3}Co$ if $Fr_l < 0.04$ *(5-14)*

$N = Co$ if $Fr_l < 0.04$ *(5-15)*

and Froude number was determined as follows:

$$Fr_l = Froude\ number = \frac{G^2}{\rho^2 gD} \quad (5\text{-}16)$$

The other important dimensionless parameter which should be evaluated is the convection number (Co). The convection number was(Incropera, F. P., 2011) calculated as:

$$Co = \text{Convection number} = \left(\frac{1}{x} - 1\right)^{0.8}\left(\frac{\rho_g}{\rho_l}\right)^{0.5} \quad (5\text{-}17)$$

Then, two boiling mechanisms nucleate and convective are determined under three cases as:

Case I : (N > 1)

$h_{nc,B} = (230Bo^{0.5}) \times h_l$ if $Bo > 0.0003$ *(5-18)*

$h_{nc,B} = (1 + 46Bo^{0.5}) \times h_l$ if $Bo < 0.0003$ *(5-19)*

$h_{c,B} = (1..8N^{0.8}) \times h_l$ *(5-20)*

Case II : (1>N >0.1)

$h_{nc,B} = (CBo^{0.5}) \times \exp(0.47N^{-0.1}) \times h_l$ *(5-21)*

$h_{c,B} = (1..8N^{0.8}) \times h_l$ *(5-22)*

Case III : (N < 0.1)

$h_{nc,B} = (CBo^{0.5}) \times \exp(2.47N^{-0.15}) \times h_l$ *(5-23)*

$h_{c,B} = (1..8N^{0.8}) \times h_l$ *(5-24)*

In the above equations h_l and Bo are the liquid phase heat transfer coefficient and boiling number respectively. Dittus-Boelter equation (Incropera, F. P., 2011) was used

to calculate the liquid phase heat transfer coefficient. Boiling factor was estimated by using the formula below:

$$Bo = Boiling\ number = \frac{\phi}{Gh_{fg}} \quad (5\text{-}25)$$

Thus, constant C can be determined as follows:

$$C = 14.7 \quad \text{if} \quad Bo > 0.0011 \quad (5\text{-}26)$$

$$C = 15.43 \quad \text{if} \quad Bo < 0.0011 \quad (5\text{-}27)$$

Finally, both the convective boiling and nucleate boiling factor were calculated at the appropriate case and the one which is larger than the other one was considered as two phase heat transfer coefficient.

5.3. Vane expander

This section was taken from section 2.3 of *Paper III*. The vane expander was modelled under two parts: geometry of the expander and thermodynamic analysis of the expander. The modelled expander which comprises a rotor, a stator and four vanes is represented in Figure 5-3.

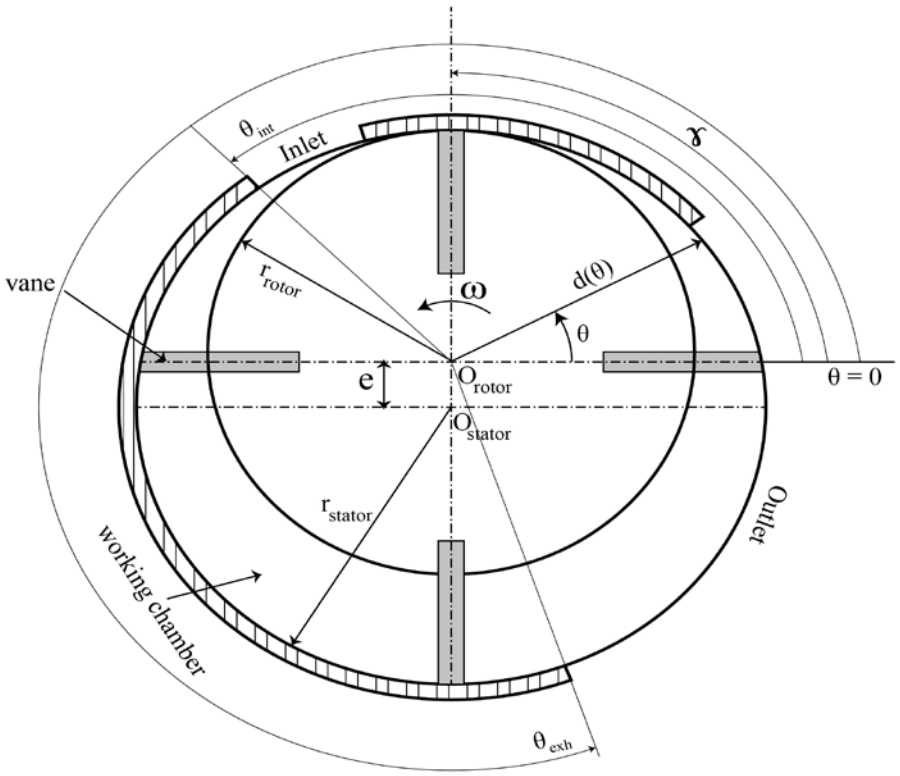

Figure 5-3 Schematic of the vane expander

The working principle of the expander is discussed comprehensively in section 2.3 of *Paper III*.

In the geometrical part of the modelling, initially, the radius of the stator to the centre of the rotor was calculated according to angular displacement as follows:

$$d(\theta) = -e \times sin\theta + \sqrt{(r_{stat})^2 - (e \times cos\theta)^2} \quad (5\text{-}28)$$

where $d(\theta)$ is the radius of the stator to the centre of the rotor. e and r_{stat} indicates the eccentricity and radius of the stator respectively.

Then, the area of the working chamber was evaluated as:

$$A(\theta) = \frac{1}{2}\int_{\theta}^{\theta+\frac{2\pi}{n}} (d^2 - {r_{rot}}^2)\, d\theta \quad (5\text{-}29)$$

The volume of the working chamber was determined according to the below equation.

$$V(\theta) = A \times L_{stat} \quad (5\text{-}30)$$

where L_{stat} is the length of the stator.

The calculation of the volume of the working chamber is crucial to determine the built-in ratio of the expander and it was calculated by using the formula below;

$$r_{v,built-in} = \frac{V_{out}}{V_{in}} \quad (5\text{-}31)$$

V_{out} and V_{in} can be evaluated by introducing the intake (θ_{int}) and the exhaust (θ_{exh}) angles into the Eq. (5-30).

Then, the expander design pressure ratio was evaluated by using the calculated built-in ratio as (Gnutek, Z. and Kolasiński, P., 2013):

$$PR_{dsg} = \frac{P_{exp,in}}{P_{exp,out,dsg}} = \left(r_{v,built-in}\right)^{k_{ratio}} \quad (5\text{-}32)$$

where $P_{exp,in}$ and $P_{exp,\ out,dsg}$ demonstrates the expander inlet and expander designed outlet pressure respectively.

During the expander operation, if the expander design pressure ratio is higher than the cycle operating pressure ratio over-expansion, otherwise under-expansion takes place (Quoilin, S. et al., 2011).

The cycle operating pressure ratio can be calculated as:

$$PR_{cyc} = \frac{P_{exp,in}}{P_{exp,out}} \quad (5\text{-}33)$$

The under and over expansion process in an isentropic expansion is demonstrated in Figure 5-4

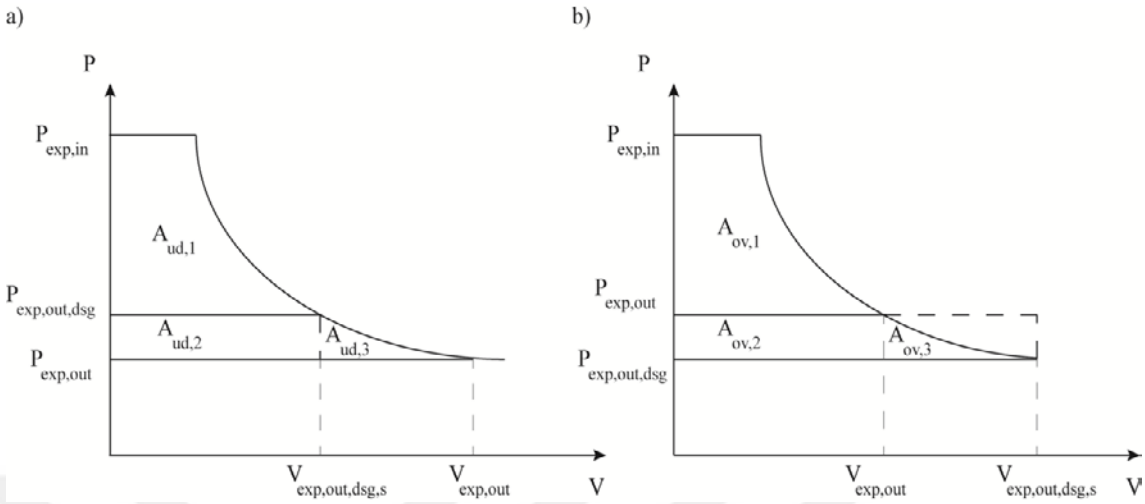

Figure 5-4 Isentropic expansion process a) under expansion b) over expansion

As the expander design pressure and the cycle pressure ratios are defined, the work that is generated in the expander can be evaluated as:

Under-expansion case

$$\dot{W}_{exp,ud} = \dot{m}_{wf} \times \left(\left(h_{exp,in} - h_{\substack{exp,out \\ dsg,s}} \right) \times 10^{-3} + \left(v_{\substack{exp,out \\ dsg,s}} \times \left(P_{exp,out} - P_{\substack{exp,out \\ dsg}} \right) \right) \times 10^{-2} \right) \times \eta_{mec}$$

(5-34)

Over-expansion case

$$\dot{W}_{exp,ov} = \dot{m}_{wf} \times \left(\left(h_{exp,in} - h_{\substack{exp,out \\ dsg,s}} \right) \times 10^{-3} - \left(v_{\substack{exp,out \\ dsg,s}} \times \left(P_{exp,out} - P_{\substack{exp,out \\ dsg}} \right) \right) \times 10^{-2} \right) \times \eta_{mec}$$

(5-35)

5.4. Condenser

The condenser modelling was taken from the section 2.4 of *Paper III*. In the condenser modelling, it was assumed that the working fluid which is coming from the expander condenses in the condenser and leaves it as a saturated liquid. Therefore, the condenser was divided into two sections as sensible heat and latent heat.

The total amount of condensation heat equals to the summation of the sensible and latent heat and it was evaluated as follows:

$$\dot{Q}_{cond} = \dot{m}_{wf} \times \left(h_{exp,out} - h_{\substack{g@cond \\ temp}} \right) + \dot{m}_{wf} \times \left(h_{\substack{g@cond \\ temp.}} - h_{\substack{l@cond \\ temp.}} \right) \quad (5\text{-}36)$$

In Eq. (5-36), the first term of the right hand side of the equation indicates the sensible heat, whereas the second term of the right hand side of the equation represents the latent heat.

As the considered condenser is a water-cooled heat exchanger, the smallest difference between the working fluid and cooling water temperature which is called *'the pinch point temperature (ΔT_{pp})'* should be considered in the condenser modelling. The pinch point (point pp) was taken as 5 ºC in the modelling and it is represented in Figure 5-5.

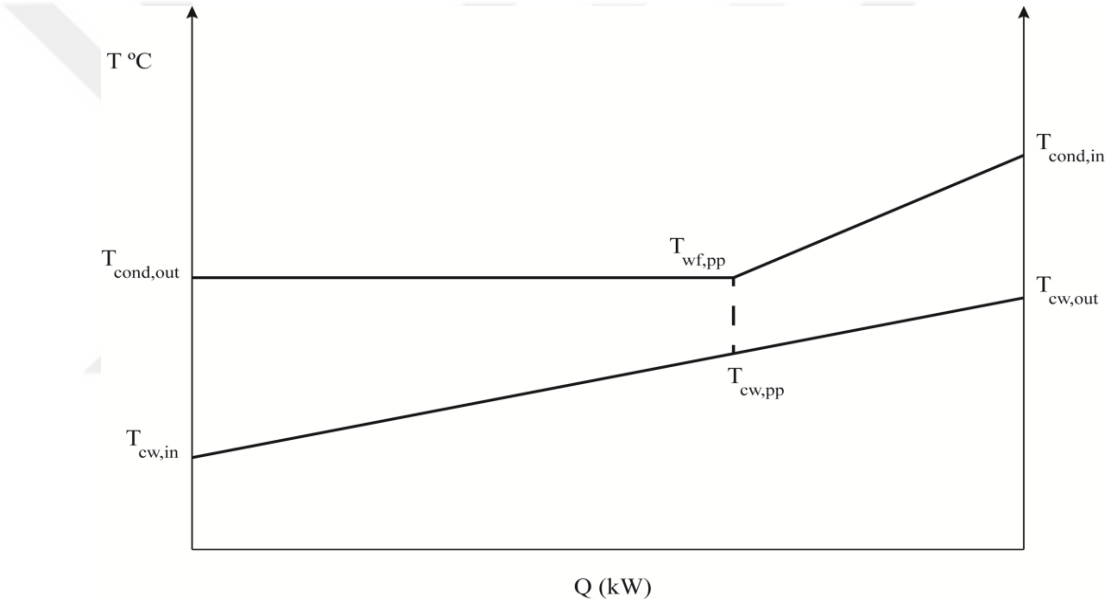

Figure 5-5 Temperature profiles and the pinch point temperature in the condenser

As it can be seen from Figure 5-5, the amount of the latent heat which is transferred to the cooling water increases the cooling water temperature from its inlet temperature to pinch point temperature. This heat balance can be represented as follows:

$$\dot{m}_{wf} \times \left(h_{\substack{g@cond \\ temp}} - \mathrm{h}_{\substack{l@cond \\ temp}} \right) = \dot{m}_{cw} \times C_{p,cw} \times (T_{cw,pp} - T_{cw,in}) \quad (5\text{-}37)$$

In Eq. (5-37), both $\dot{m}_{cw}$ and $T_{cw,pp}$ are unknown. Therefore, the equation should be solved iteratively. The procedure is explained in section 7.2.3 of Chapter 7.

Then, the cooling water outlet temperature was calculated by the use of the following:

$$\dot{Q}_{cond} = \dot{m}_{cw} \times C_{p,cw} \times (T_{cw,out} - T_{cw,in}) \quad (5\text{-}38)$$

5.5. Pump

The pump modelling section was taken from the section 2.5 of *Paper III*. The consumed work by the pump was calculated from:

$$\dot{W}_{pump} = \frac{\dot{m}_{wf}(\nu_{pump,in})\times(P_{evap}-P_{cond})\times 10^{-2}}{\eta_{pump,s}} \quad (5\text{-}39)$$

where ν and P represents the specific volume of the working fluid and the pressure respectively. $\eta_{pump,is}$ is the pump isentropic efficiency.

Chapter 6 Simulation study of the flat plate collector

This chapter covers the simulation analysis of the flat plate collector based on the mathematical model of the collector which was proposed in chapter 5, section 5.2. The simulation methodology and the results are taken from sections 4, 5 and 6 of *Paper II*.

6.1. Background of the simulation study

As previously discussed (see section 4.3), the collector operating temperature and pressure should have an effect on the efficiency of the collector. Therefore, special attention should be given to the collector to understand its behaviour under various operating conditions. A numerical model of the flat plate collector was developed to analyse the collector performance under three different operating pressures (4, 6 and 8 bar) and working fluid mass flow rates (0.001, 0.005 and 0.01 kg/s) which consequently influences the collector operating temperature as well as, the collector efficiency. In this study, due to its promising thermal properties HFC-134a was selected as the working fluid of the collector. The operating conditions of the simulations are given in Table 6-1.

Table 6-1 Simulation operating conditions (Helvaci, H. and Khan, Z. A., 2015)

Fluid inlet temperature (K)	278
Fluid mass flow rate (kg/s)	0.001-0.005-0.01
Collector operating pressure (bar)	4-6-8
Incoming solar radiation (W/m^2)	500
Ambient temperature (K)	275
Wind velocity (m/s)	2

6.2. Numerical procedure

In this study, the collector tube was considered as a single, flat tube and it was divided into small elements. The collector outlet temperature, plate temperature, collector heat loss, fluid heat transfer coefficient and heat gain were calculated at the outlet of each element. These output conditions also represent the input conditions of the next element as each element is connected to the next one (Figure 6-1).

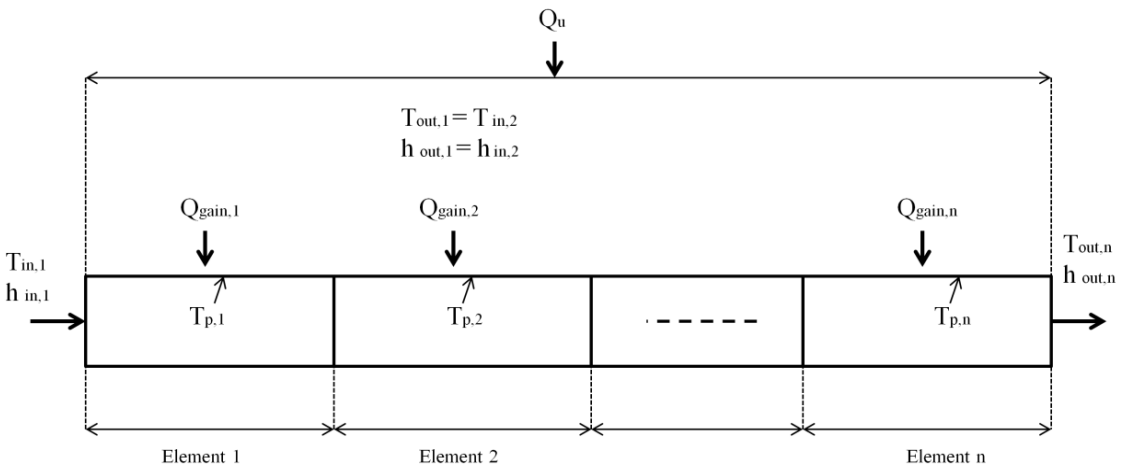

Figure 6-1 Schematic of collector elements (Helvaci, H. and Khan, Z. A., 2015)

The model begins with calculating the heat loss coefficient by using equations from (5-1) to (5-3). As it can be seen from Eq. (5-1), the collector plate temperature was needed to calculate the top heat loss coefficient. Therefore, an arbitrary value which is 5 ºC higher than the fluid temperature at the collector inlet was given. Then, the flow regime was evaluated whether it was laminar or turbulent in order to calculate the heat transfer coefficient of the fluid (equations from (5-9) to (5-13)). However, the fluid properties (thermal conductivity (k), density (ρ), specific heat (C_p), viscosity (μ)) were needed to utilise the equations from (5-9) to (5-13). The developed regression equations were employed to determine the fluid thermal properties by introducing the data which was taken from REFPROP 9.1 programme (Lemmon, E. et al., 2013). The fluid mean temperature which was introduced to the regression equations was calculated by using the formula below:

$$T_{f,m} = \frac{T_{f,in}+T_p}{2} \qquad (6\text{-}1)$$

Once the heat transfer coefficient and heat loss coefficient was calculated, the useful heat gain of the collector was evaluated by using Eq. (5-5). As stated previously, the collector tube was divided into small elements and therefore, the calculated useful heat of the fluid can be expressed as follows:

$$\dot{Q}_u = Q''_u \pi D_{in} L_{tube} \qquad (6\text{-}2)$$

where Q''_u indicates the useful heat rate and πD_{in} represents the surface perimeter. Therefore, the useful heat gain of each element can be calculated by multiplying the useful heat rate by the surface perimeter and the length of each element.

$$\dot{Q}_{gain} = Q''_u \pi D_{in} \int_0^{L_{tube}} dx \qquad (6\text{-}3)$$

As the amount of the heat gained by the first element is known now, the fluid outlet temperature can be evaluated by introducing Q_{gain} into the following equation.

$$T_{f,out} = T_{f,in} + \frac{\dot{Q}_{gain}}{\dot{m}_{wf} \times C_{p,f}} \qquad (6\text{-}4)$$

The fluid mean temperature was previously estimated by using Eq. (6-1) where the plate temperature was used in the equation. Now, by using the calculated $T_{f,out}$, the new value of the fluid mean temperature can be determined by the use of the following:

$$T_{f,m}{}^{new} = \frac{T_{f,in} + T_{f,out}}{2} \qquad (6\text{-}5)$$

The new calculated fluid mean temperature was utilised in the regression equations to obtain the fluid properties and the new value of $\dot{Q}_u$. Then, the new plate temperature was evaluated as follows:

$$T_p{}^{new} = T_{f,in} + \frac{\frac{\dot{Q}_u}{A_p}}{F_R \times U_T}(1 - F_R) \qquad (6\text{-}6)$$

The inner loop re-calculates the U_T, $\dot{Q}_u$ and $\dot{Q}_{gain}$ by employing the new plate and fluid mean temperature till the convergence criteria which represents 0.01ºC difference between plate temperatures (T_p) at n^{th} and $(n+1)^{th}$ iteration is satisfied. Once the convergence is satisfied, the outer loop checks if the fluid outlet temperature reaches its corresponding saturation temperature. If the fluid temperature at the outlet of an element is lower than the corresponding fluid saturation temperature, the outer loop increases the number of element till its temperature reaches the saturation point. When, the fluid temperature reaches the corresponding saturation temperature, the fluid enters the multi-phase region. In the multi-phase region, in other words in the flow boiling region the fluid temperature remains constant. Therefore, instead of calculating the fluid outlet temperature as it was represented in Eq. (6-4), the fluid outlet enthalpy was evaluated from the following equation:

$$h_{f,out} = h_{f,in} + \frac{\dot{Q}_{gain}}{\dot{m}_{wf}} \qquad (6\text{-}7)$$

Furthermore, instead of single phase heat transfer coefficient, as it was represented in section 5.2.2.2 of Chapter 5, the two phase heat transfer coefficient was calculated by using the equations from (5-14) to (5-27).

Vapour quality of the fluid was calculated at each element by the use of the following:

$$x = \frac{h_{f,out} - h_l}{h_g - h_l} \qquad (6\text{-}8)$$

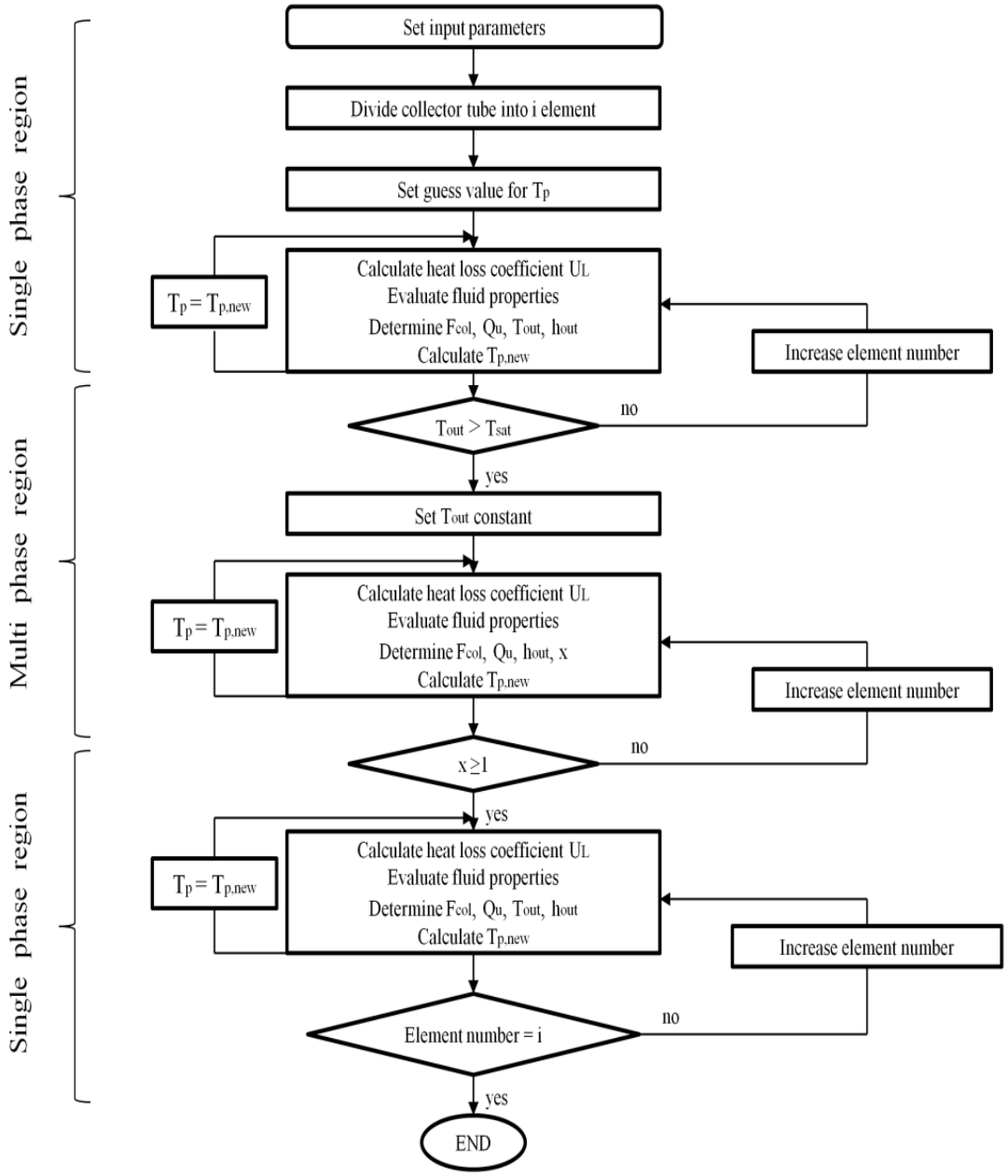

Figure 6-2 Flow chart of the simulation process (Helvaci, H. and Khan, Z. A., 2015)

Then, the outer loop increases the number of elements if the vapour quality of the fluid does not exceed 1. This means that the fluid is still not in the superheated region and the two -phase region calculations are valid. Once the fluid enters the superheated region, the same calculations which were used in the single phase regions were performed (with superheated vapour properties). The outer code increases the element number till the end of the tube. The flow chart of the simulation model is represented in Figure 6-2.

6.3. Simulation results and discussion of the flat plate collector

The results of the proposed simulation model are taken from section 5 of *Paper II*. Figure 6-3 represents the simulated fluid mean temperature and fluid heat gain along the collector tube at the pressure of 6 bar and mass flow rate of 0.005 kg/s. As it can be seen from Figure 6-3, the fluid entered the collector at 278 K (5 °C) and its temperature rose till the fluid corresponding saturation temperature at 6 bar (22.2°C). Then, its temperature remained constant until it reached the superheated region. In the superheated region the temperature of the fluid increased till the end of the tube where it was a superheated vapour at the temperature of 26.3°C.

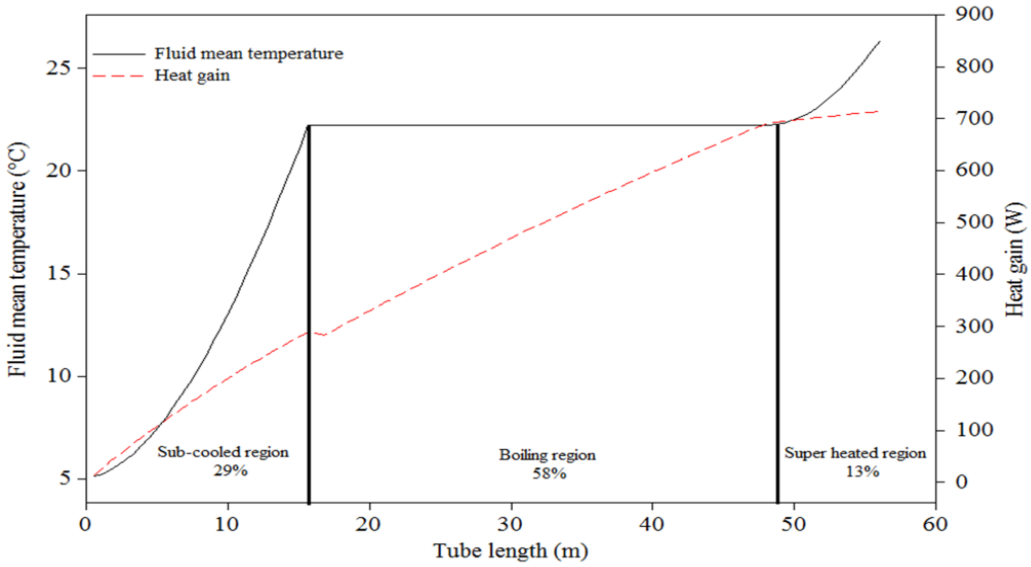

Figure 6-3 Fluid mean temperature and heat gain variation along the collector tube (P=6 bar, m=0.005 kg/s) (Helvaci, H. and Khan, Z. A., 2015)

As it was previously stated the heat transfer coefficient of the fluid varies in single phase and multi-phase regions. The heat transfer coefficient showed a slight increase in the single phase flow region where it was rising from 153.54 W/m^{2}K to 173.93 W/m^{2}K. In the multi phase region, it increased gradually to 610.27 W/m^{2}K and reached a peak.

This point represents the fluid vapour quality of 0.8. Then, it started to decrease drastically to 498.23 W/m^{2}K before it entered the single phase (vapour) region (Figure 6-4). This phenomenon is called *'dry out'* and it is due to the lower conductivity property of dry steam (Odeh, S. et al., 1998).

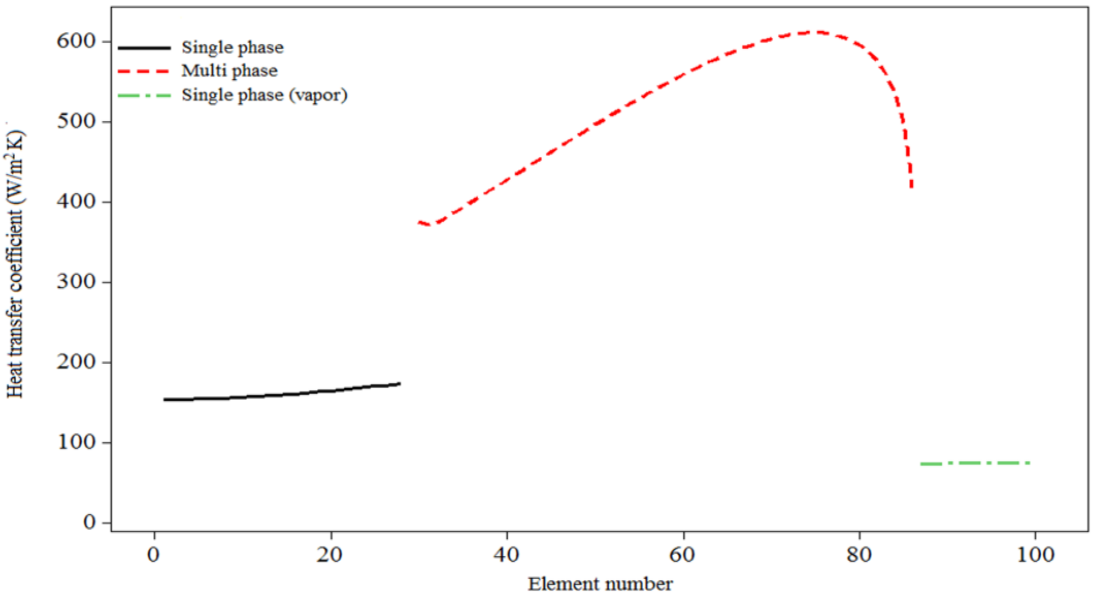

Figure 6-4 Fluid heat transfer coefficient in various flow regions (P=6 bar, m=0.005 kg/s) (Helvaci, H. and Khan, Z. A., 2015)

It was previously mentioned that the collector efficiency vary with the parameters such as the collector temperature, the collector pressure and the mass flow rate (see section 4.3). Therefore, the collector efficiency was evaluated by the use of the following equation:

$$\eta_{col} = \frac{Q_p}{S_{in} A_p} \qquad (6\text{-}9)$$

In Eq. (6-9), the collector efficiency was defined in terms of the collector plate temperature in order to determine the effect of the collector pressure and the fluid mass flow rate on the plate temperature and its subsequent effect on the efficiency. Figure 6-5 and Figure 6-6 represents the collector efficiency and collector plate temperature versus collector operating pressure and fluid mass flow rate.

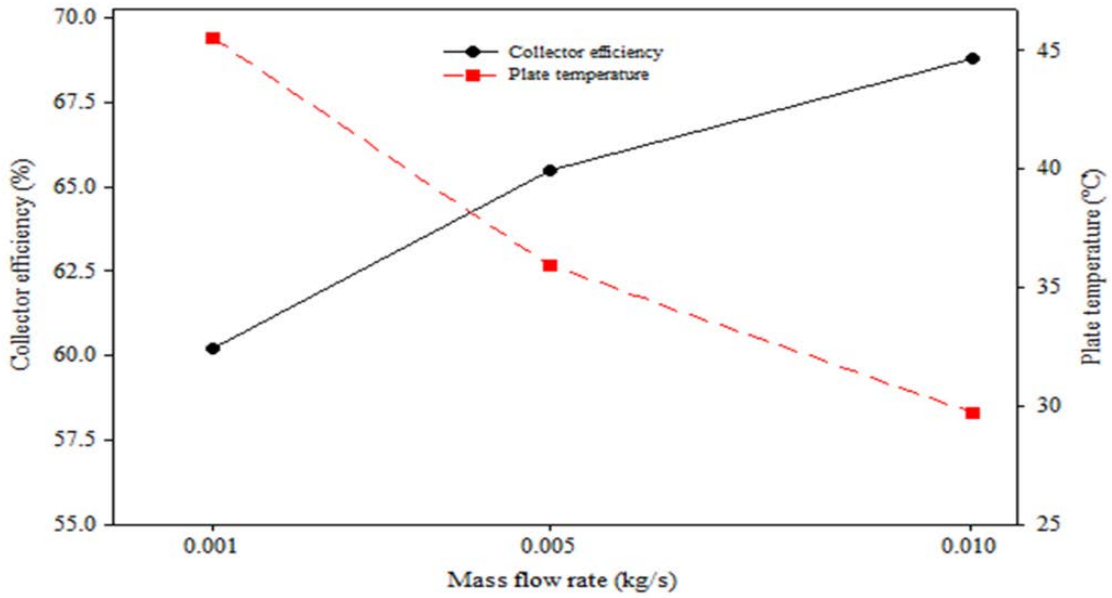

Figure 6-5 Collector efficiency and plate temperature at various mass flow rates (P=6 bar) (Helvaci, H. and Khan, Z. A., 2015)

Collector efficiency increased from 60.2% to 68.8% as the fluid mass flow rate rose from 0.001 kg/s to 0.01 kg/s. This is due to the fact that at the higher mass flow rate, a higher amount of the heat which is available on the collector plate was transferred to the fluid. Therefore, the collector plate temperature decreases with the increasing mass flow rate and less amount of heat was transferred from the collector to the ambient (Figure 6-5). Similarly, the collector efficiency varied with the collector operating pressure. As the collector operating pressure increased from 4 bar to 8 bar, the fluid saturation temperature rose from 9.6 °C to 31.9 °C. The increase in the saturation temperature of the fluid caused the collector operate at higher temperatures, in other words, at higher collector plate temperatures. For instance, the collector plate temperature increased from 22.1°C to 41.8°C where the collector pressure increased from 4 bar to 8 bar. Therefore, a higher amount of heat was lost from the collector to the surroundings at a higher plate temperature which resulted in a decrease in the collector efficiency (Figure 6-6). Furthermore, the working fluid which is utilised in the collector has also an effect on the collector efficiency due to the different thermal properties of fluids. Figure 6-7 demonstrates the collector efficiency for HFC-134a and HFE 7000. Because each fluid has a different saturation temperature characteristic, HFC-134a and HFE 7000 entered the collector at 8.6 bar and 1 bar respectively. Thus, the same saturation conditions were obtained which is 15°C higher than the fluid temperatures at the collector inlet (20 °C).

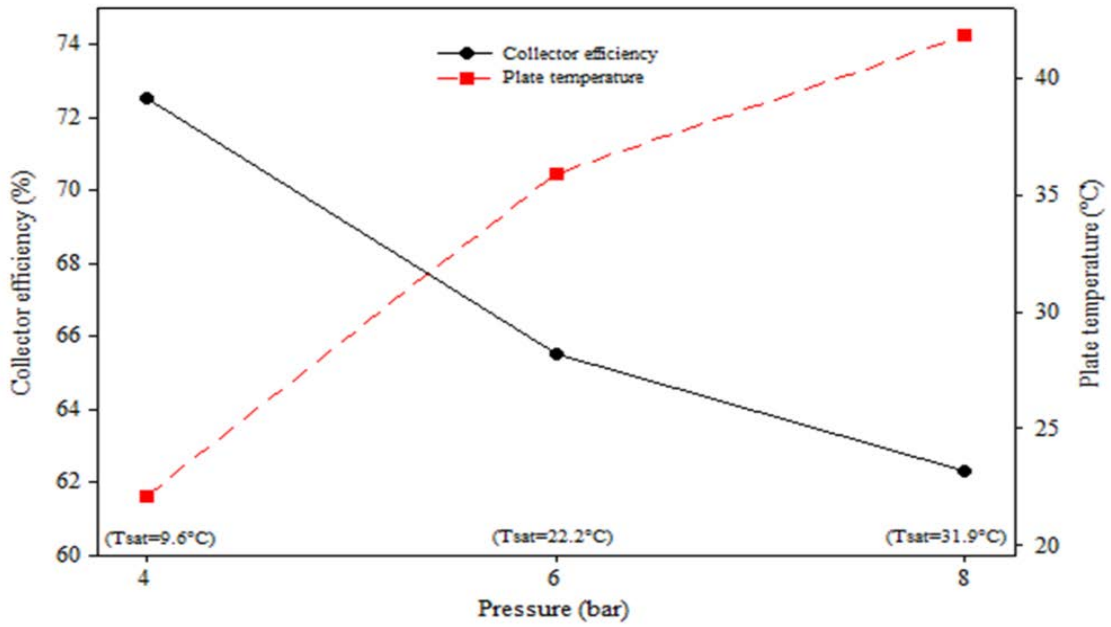

Figure 6-6 Collector efficiency and plate temperature at various operating pressure (m=0.005 kg/s) (Helvaci, H. and Khan, Z. A., 2015)

The mass flow rate of each fluid and the incoming solar radiation was the same in the simulations. As it can be seen from Figure 6-7, higher collector efficiency was obtained when utilising HFC-134a rather than HFE 7000. One of the reasons for this issue is that HFC-134a has a higher thermal conductivity (0.083 W/m-K) than HFE 7000 (0.0757 W/m-K).

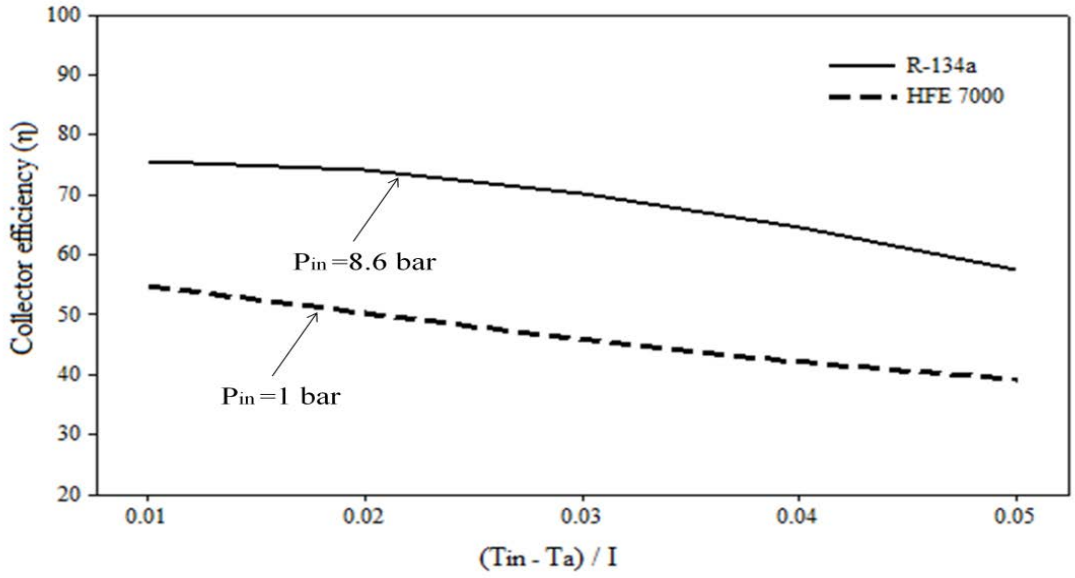

Figure 6-7 Collector efficiency as a function of $(T_{in} - T_a)$ /I for R-134a and HFE 7000 (Helvaci, H. and Khan, Z. A., 2015)

It is worth mentioning that although, HFC-134a provides a higher collector efficiency than HFE 7000, it has a higher global warming potential (1370) compared to HFE 7000 (450). The effects of thermal properties of various working fluids on the solar ORC efficiency, as well as their environmental impacts in terms of global warming potential, toxicity and flammability are discussed in Chapter 7.

Chapter 7 Fluid selection study of the solar ORC

This chapter presents the simulation analysis of the proposed solar ORC based on the model which was proposed in Chapter 5. The simulation methodology and the results are taken from *Paper III* and *Paper IV*.

7.1. Background of the study

The mathematical model of the solar ORC was developed and demonstrated in Chapter 5 and the simulation study of the flat plate collector where the effects of the operating conditions on the collector heat loss, the collector heat gain and the collector efficiency was evaluated was represented in Chapter 6. It was also mentioned that not only the operating conditions but also the working fluid that is used in the collector has an effect on the thermal performance of the collector (see section 6.3). Therefore, the simulation of the collector was extended to the whole solar ORC in order to evaluate the cycle behaviour under various operating conditions with utilising different thermo-fluids. The simulations of the cycle were performed where the condenser temperature/pressure was set constant and the cycle operating pressure ratio, in other words the ratio of evaporating pressure to condenser pressure varied from 1.5 to 6. In the simulations, twenty four organic compounds including Hydrofluorocarbons (HFCs), Perfluorocarbons (PFCs), Hydrocarbons (HCs), Hydrofluoroethers (HFEs) and Hydrofluoroolefins (HFOs) were considered. The proposed cycle was considered as saturated, in other words the working fluid left the collector and the condenser as saturated vapour and saturated liquid respectively. In this study, the effect of the cycle operating pressure on the collector, the vane expander, the cycle net work output and the cycle efficiency was discussed. Furthermore, the investigated working fluids suitability in terms of the fluids' thermophysical effects on the cycle and the fluids' environmental characteristics such as global warming potential, flammability and toxicity was examined.

7.2. Numerical procedure

The numerical methodology of each element, as well as the whole cycle is taken from section 3 of *Paper III*. The simulation model of the cycle comprises sub-codes which represents the calculation of output variables of each component based on the given input and fixed variables. Calculated output variables from one component were

transmitted to the next component as input variables as each component was connected to the other one. The followings were kept constant during the simulations.

- Component specifications
- The condensing, the ambient and the cooling water temperatures
- Pump isentropic efficiency
- Expander mechanical efficiency
- Incoming solar radiation

The operating conditions of the cycle are given in Table 7-1.

Table 7-1 Operating conditions of the saturated solar ORC

Parameter	Unit	Value
Incoming solar radiation	W/m^2	800
Condensation temperature	ºC	25
Ambient temperature	ºC	15
Cooling water inlet temperature	ºC	12
Pump isentropic efficiency	-	0.6
Expander mechanical efficiency	-	0.7
Pressure ratio of the cycle	-	1.5 - 6

The REFPROP 9.1 software where the fluid properties at various conditions were taken from was run in parallel with the code.

Initially, the condensing pressure at saturated conditions was determined for each fluid as the condensing temperature was set constant at 25 °C (Table 7-1). Then, the evaporating pressure was calculated as the condensing pressure and the cycle pressure ratio are known. By use of the calculated condensing and evaporating pressures of the cycle, the followings were read from REFPROP as:

- Fluid evaporation temperature at corresponding P_{evap}
- Fluid sat. liquid density at corresponding P_{evap}
- Fluid sat. liquid density at corresponding P_{evap}
- Fluid sat. vapour density at corresponding P_{evap}
- Fluid sat. liquid conductivity at corresponding P_{evap}
- Fluid sat. liquid viscosity at corresponding P_{evap}
- Fluid sat. vapour viscosity at corresponding P_{evap}
- Fluid sat. liquid enthalpy at corresponding P_{evap}
- Fluid sat. vapour enthalpy at corresponding P_{evap}
- Fluid saturated liquid enthalpy at 25 ºC

- Fluid saturated vapour enthalpy at 25 ºC
- Fluid saturated liquid specific volume at 25 ºC

Before the collector code was activated the specific pump work and the collector inlet enthalpy was determined as:

$$\dot{w}_{pump} = \frac{v_{pump,in} \times (P_{evap} - P_{cond}) \times 10^{-2}}{\eta_{pump,s}} \quad (7\text{-}1)$$

$$h_{col,in} = (\dot{w}_{pump} \times 10^{3}) + h_{pump,in} \quad (7\text{-}2)$$

As the collector inlet enthalpy was calculated by using equations (7-1) and (7-2), the collector inlet temperature was read with the use of known fluid enthalpy at the collector inlet and collector pressure, in other words evaporating pressure.

7.2.1. Flat plate collector

The numerical simulation of the collector was represented previously in section 6.2. The same approach was followed in this study. However, the only difference was the mass flow rate for given collector inlet and collector outlet temperature (as the cycle is saturated) was calculated in the current study whereas the collector outlet temperature was evaluated for the given collector inlet temperature and the mass flow rate in section 6.2. The simulation continues until the difference between $\dot{m}_{wf,sp}$ and $\dot{m}_{wf,tp}$ is less than 0.0001. If the condition does not meet the convergence criterion (0.0001), the model increases the number of elements for the single phase part region until the condition satisfies the convergence.

The flow chart of the collector simulation is represented in Figure 7-1 and the details of the collector simulation procedure can be found in section 3.1 of *Paper III*.

As the evaporation pressure of the cycle represents the collector outlet temperature, the collector efficiency was calculated as follows:

$$\eta_{col} = \frac{\dot{m}_{wf} \times \left[\left(C_p (T_{evap} - T_{col,in}) + (h_g - h_l) \right) \right]}{S_{in} \times A_{col}} \quad (7\text{-}3)$$

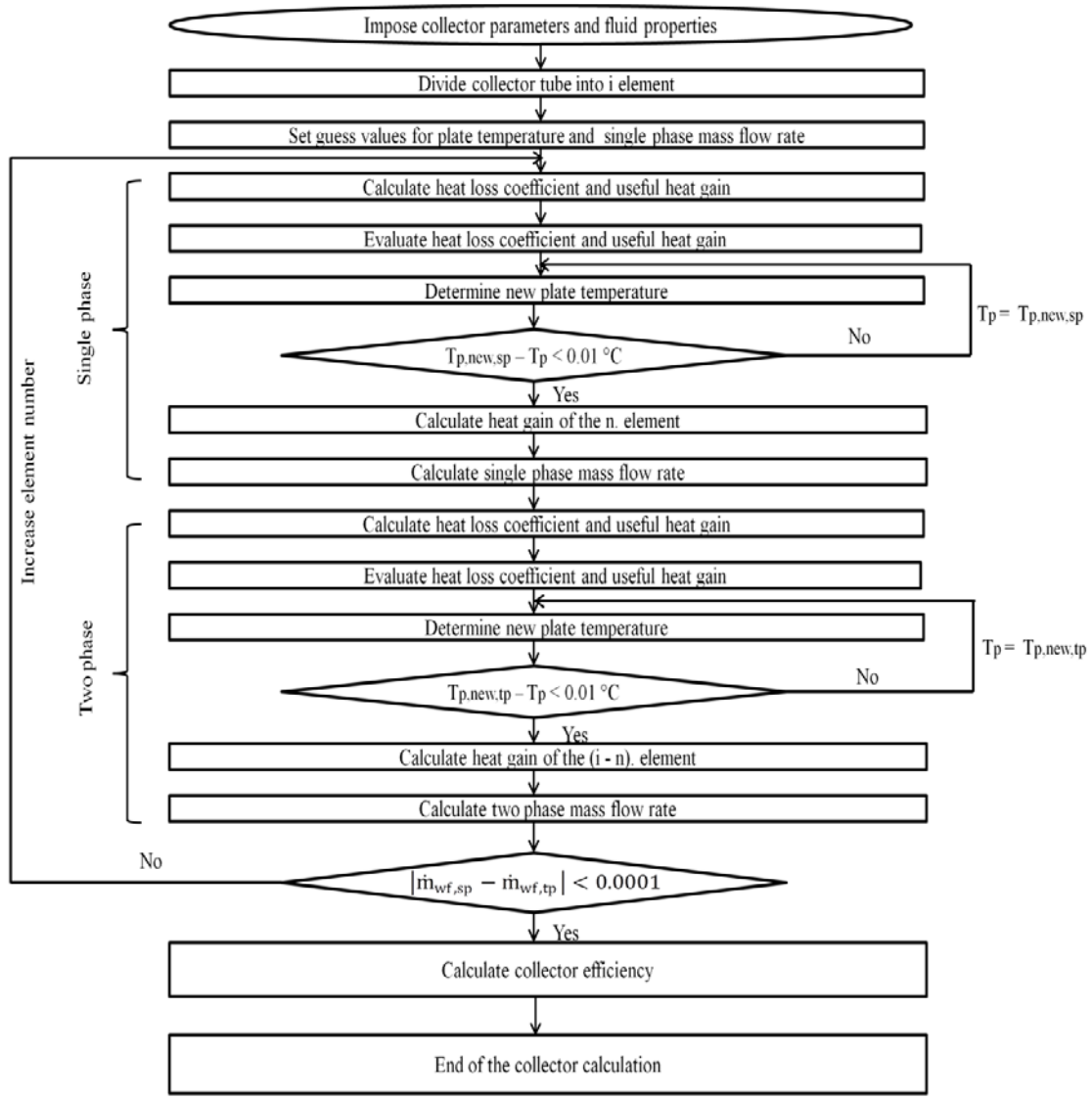

Figure 7-1 Flow chart of the collector simulation model

7.2.2. Expander

Initially, the parameters of the expander including the input parameters which were calculated from the collector sub-code and transferred to the expander and the fixed parameters such as expander specifications were introduced into the expander code. The parameters were given as follows:

- Expander inlet pressure ($P_{exp,in}$)
- Expander outlet pressure, ($P_{exp.out}$)
- Rotor radius, (r_{rot})
- Stator radius, (r_{stat})
- Eccentricity, (e)

- Intake angle, (θ_{int})
- Exhaust angle, (θ_{exh})
- Expander mechanical efficiency, (η_{mec})

Then, by the use of equations from (5-28) to (5-32), the expander built-in ratio and the expander designed outlet pressure were calculated. Based on the expander designed pressure ratio and the cycle operating pressure ratio, the mechanical work generated in the expander were calculated by using the equations from (5-34) to (5-35). The efficiency of the expander for under-expansion and over expansion were calculated with the use of equation below as:

$$\eta_{exp,ud} = \frac{\dot{W}_{exp,ud} \times 10^3}{\dot{m}_{wf} \times (h_{exp,in} - h_{exp,out,s})} \quad (7\text{-}4)$$

$$\eta_{exp,ov} = \frac{\dot{W}_{exp,ov} \times 10^3}{\dot{m}_{wf} \times (h_{exp,in} - h_{exp,out,s})} \quad (7\text{-}5)$$

The flow chart of the expander simulation model is shown in Figure 7-2.

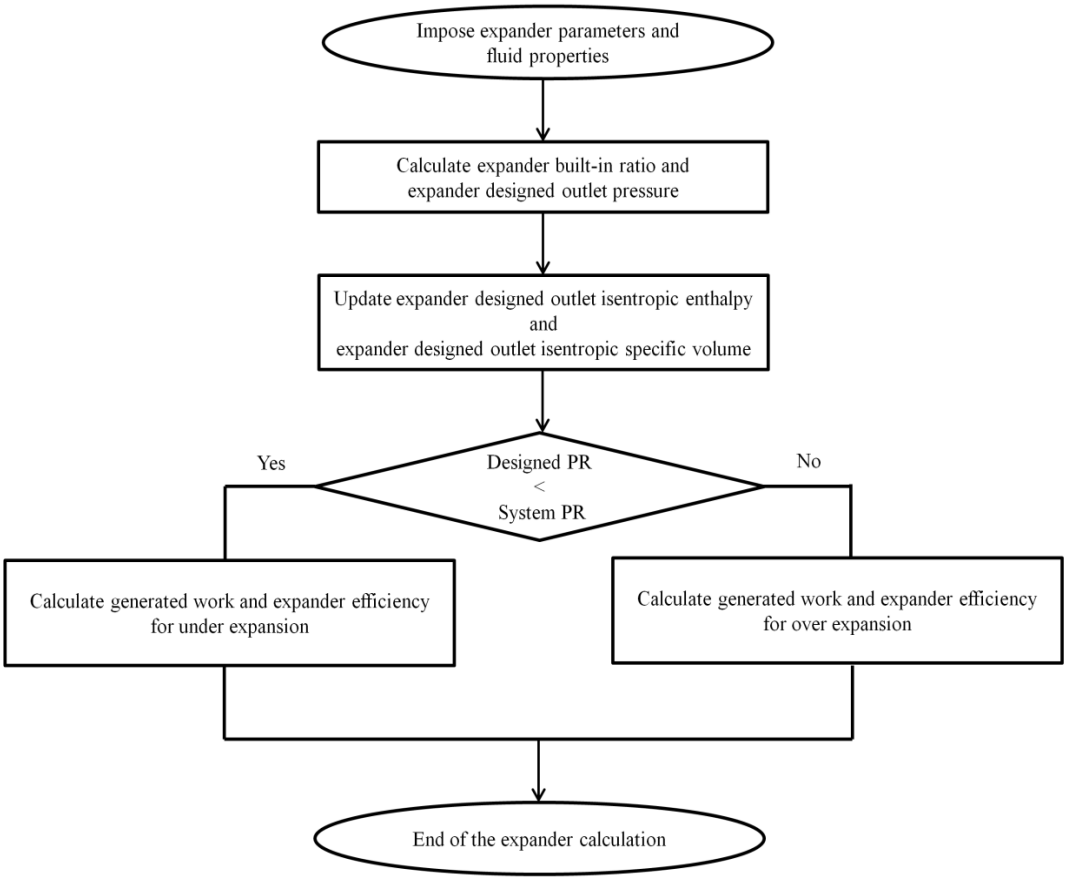

Figure 7-2 Flow chart of the expander simulation model

7.2.3. Condenser

In the condenser sub-code, the pinch point was defined as follows:

$$25 - T_{cw,pp} \geq 5\ °C \tag{7-6}$$

Then, by using an arbitrary value of cooling water mass flow rate (0.001 kg/s), Eq. (5-37) was solved iteratively until the condition in Eq. (7-6) is satisfied. Thereafter, according to Eq. (5-38), the cooling water outlet temperature was evaluated.

7.2.4. Pump

The amount of the work that is spent in the pump was evaluated by multiplying the calculated specific pump work (see Eq. (7-1)) by the cycle mass flow rate.

7.3. Performance parameters of the solar ORC

The following parameters were used to evaluate the performance of the cycle at each performed simulation to make a comparison of cycle operating conditions and each considered fluid. The following equations which calculate the net work output and the efficiency of the cycle were evaluated as follows:

$$\dot{W}_{net} = \dot{W}_{exp} - \dot{W}_{pump} \tag{7-7}$$

$$\eta_{SORC} = \frac{\dot{W}_{net} \times 10^3}{\dot{Q}_{gain}} \tag{7-8}$$

7.4. Boundary conditions of the simulation model

The followings represent the constraints of the simulations as:

- Because of the leakage and safety concerns of the flat plate collector pressure in domestic applications the maximum pressure of the cycle is limited to 1.5MPa (15 bar).
- Minimum condenser pressure should not be lower than 0.05 bar
- Pump isentropic efficiency is 0.6

7.5. Pre-selection of working fluids

In order to limit the number of the working fluids to be considered in the analysis, some working fluids were omitted from the analysis based on their environmental properties and saturation pressure values. For instance Table 7-2 represents the fluids which show a condensing pressure less that 0.05 bar at 25 °C. Furthermore, Chlorofluorocarbons (CFCs) and hydrochlorofluorocarbons (HCFCs) which have ozone depletion potential

were eliminated from the analysis. Consequently, fluids with zero ozone depletion potential and a saturation pressure greater than 0.05 bar at 25 °C were considered in this analysis. The considered twenty four fluids can be categorised as Hydrocarbons (HCs), Hydrofluorocarbons (HFCs), Perfluorocarbons (PFCs), Hydrofluoroolefins (HFOs) and Hydrofluoroethers (HFEs). Properties of the considered fluids are represented in Appendix B.

Table 7-2 Fluids with a condensation pressure less than 0.05 bar

Fluid	**Condensation pressure at 25 ºC (bar)**
D4	0.0012
Decane	0.001
Dodecane	0.0001
Ethyl benzene	0.012
MDM	0.004
MD2M	0.0005
MD3M	0.00006
m-xylene	0.011
Nonane	0.005
Octane	0.018
p-xylene	0.011
Toluene	0.037

Table 7-3 List of the considered fluids

Fluid	**Alt. Name**	**Type**
Trans-2-butene		HC
Cis-2-butene		HC
1-butene		HC
Isobutane	R600a	HC
Butane	R600	HC
Neopentane		HC
Isopentane	R601a	HC
Pentane	R601	HC
Isohexane		HC
Hexane		HC
Cyclohexane		HC
1,1,1,2-tetrafluoroethane	R134a	HFC
1,1-difluoroethane	R152a	HFC
1,1,1,2,3,3,3-heptafluoropropane	R227ea	HFC
1,1,1,2,3,3-hexafluoropropane	R236ea	HFC
1,1,1,3,3,3-hexafluoropropane	R236fa	HFC
1,1,1,3,3-pentafluoropropane	R245fa	HFC
1,1,2,2,3-pentafluoropropane	R245ca	HFC
Octafluorocyclobutane	RC318	PFC
Methyl-heptafluoropropyl-ether	RE347mcc	HFE
2,2,2-trifluoroethyl-difluoromethyl-ether	RE245fa2	HFE
2,3,3,3-Tetrafluoropropene	R1234yf	HFO
Trans-1,3,3,3-tetrafluoropropene	R1234ze	HFO
Trans-1-chloro-3,3,3-trifluoropropene	R1233zd	HFO

7.6. Simulation results and discussion of the solar ORC

The results of the proposed simulation study of the solar ORC are taken from section 4 of *Paper III*. The considered fluids in this study are given in Table 7-3.

It is worth mentioning that some of the considered fluids showed pressure values higher than 15 bars at some cycle pressure ratio points. As the allowable maximum pressure in the collector was set to 15 bar, the cases where fluid exceeded the limit were not taken into account (Table 7-4).

Table 7-4 List of the fluids which showed a saturation pressure higher than 15 bar at various pressure ratio values

Fluid	**Pressure Ratio**										
	P_{cond} at 25 °C (bar)	1.5	2	2.5	3	3.5	4	4.5	5	5.5	6
1-butene	2.95	4.43	5.91	7.39	8.87	10.35	11.83	13.31	14.79	**16.27**	**17.75**
R-600a	3.49	5.23	6.98	8.72	10.47	12.21	13.96	15.71	**17.45**	**19.20**	**20.94**
R-134a	6.62	9.93	13.2	**16.56**	**19.87**	**23.18**	**26.49**	**29.80**	**33.12**	**36.43**	**39.74**
R-152a	5.93	8.90	11.8	14.84	**17.81**	**20.78**	**23.75**	**26.71**	**29.68**	**32.65**	**35.62**
R-227ea	4.52	6.78	9.05	11.31	13.57	15.84	**18.10**	**20.36**	**22.63**	**24.89**	**27.15**
R-236fa	2.7	4.05	5.41	6.76	8.11	9.47	10.82	12.17	13.52	14.88	**16.23**
RC-318	3.11	4.66	6.22	7.77	9.33	10.88	12.44	13.99	15.55	**17.10**	**18.66**
R1234yf	6.79	10.1	13.5	**16.9**	**20.3**	**23.78**	**27.18**	**30.5**	-	-	-
R1234ze	4.96	7.44	9.92	12.4	14.88	**17.36**	**19.85**	**22.33**	**24.81**	**27.29**	**29.77**

7.7. Collector analysis

This section analyses the effect of cycle pressure ratio and the fluid thermophysical properties such as saturation temperature on the collector heat loss and collector efficiency.

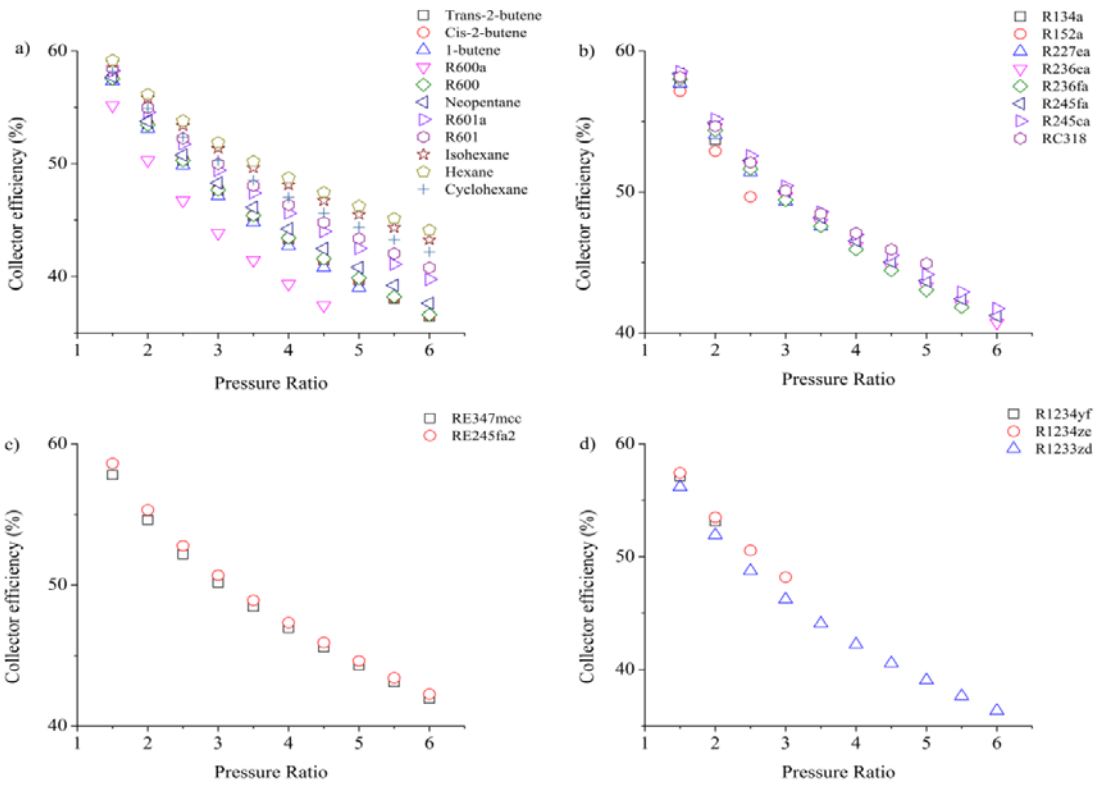

Figure 7-3 Collector efficiency versus cycle pressure ratio for a) HCs b) HFC-PFCs c) HFEs d) HFOs

The simulation results indicates that the collector efficiency varied between 59.19% and 37.44% where the cycle pressure ratio increased from 1.5 to 6 considering all the investigated fluids. Furthermore, the collector efficiency decreased with the increasing pressure ratio of the cycle for each fluid including HCs, HFCs, PFCs, HFEs and HFOs (Figure 7-3). This is due to the higher saturation temperature points of the fluids at higher collector, in other words evaporation pressure points. As the collector pressure increased with the increasing cycle pressure ratio, the collector temperature rose and this caused a higher amount of heat to be transferred to the atmosphere (Marion, M. et al., 2012). For instance, Figure 7-4 indicates the relation between the saturation temperature and the amount of the heat loss from the collector. As it can be seen these results are in agreement with the proposed findings in section 6.3.

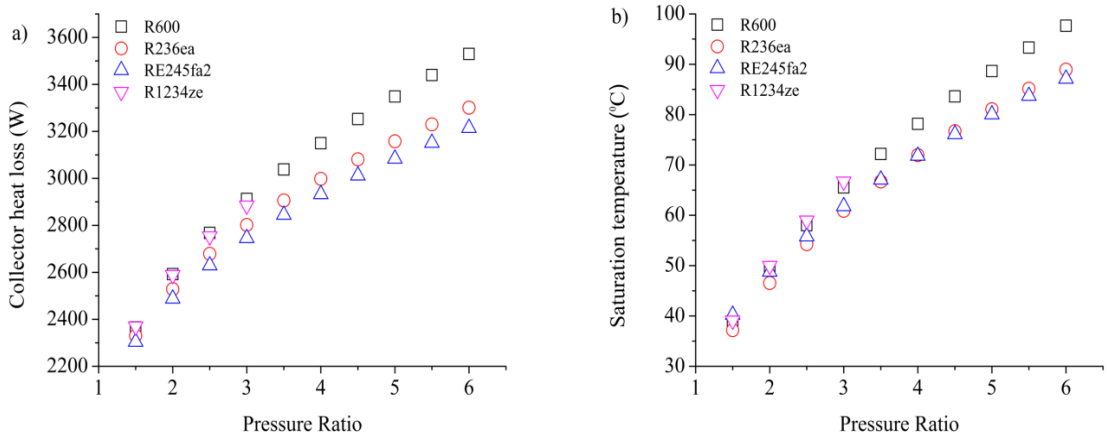

Figure 7-4 Collector heat loss and saturation temperature versus pressure ratio

7.8. Expander analysis

Figure 7-5 represents the expander efficiency values for each considered fluid with the increasing pressure ratio values. The expander efficiency increased when the cycle pressure ratio rose from 1.5 to 2.5 and reached its maximum at the pressure ratio of 2.5. Then, the expander efficiency decreased as the pressure ratio increased from 2.5 to 6. This behaviour shows that when the expander pressure ratio was lower than its designed pressure ratio which was calculated as 2.5, the expander operated under over-expansion. As the pressure ratio approached to 2.5 which indicates the ideal operating conditions for the proposed expander, the efficiency increased. However, as the expander pressure ratio became distant from 2.5, the expander operated under under-expansion and its efficiency decreased. This shows that the expander design characteristics such as built-in volume ratio has an effect on the operating conditions of the expander, as well as its efficiency due to the presenting different expander losses under different operating conditions (under and over-expansion) (Kim, Y. M. et al., 2014; Kolasiński, P., 2015). For example, when utilising R600, the expander efficiency increased from 49.26% to 69.98% when the cycle operating pressure rose from 1.5 to 2.5. Then, its efficiency decreased to 59.94 when the pressure ratio reached 6.

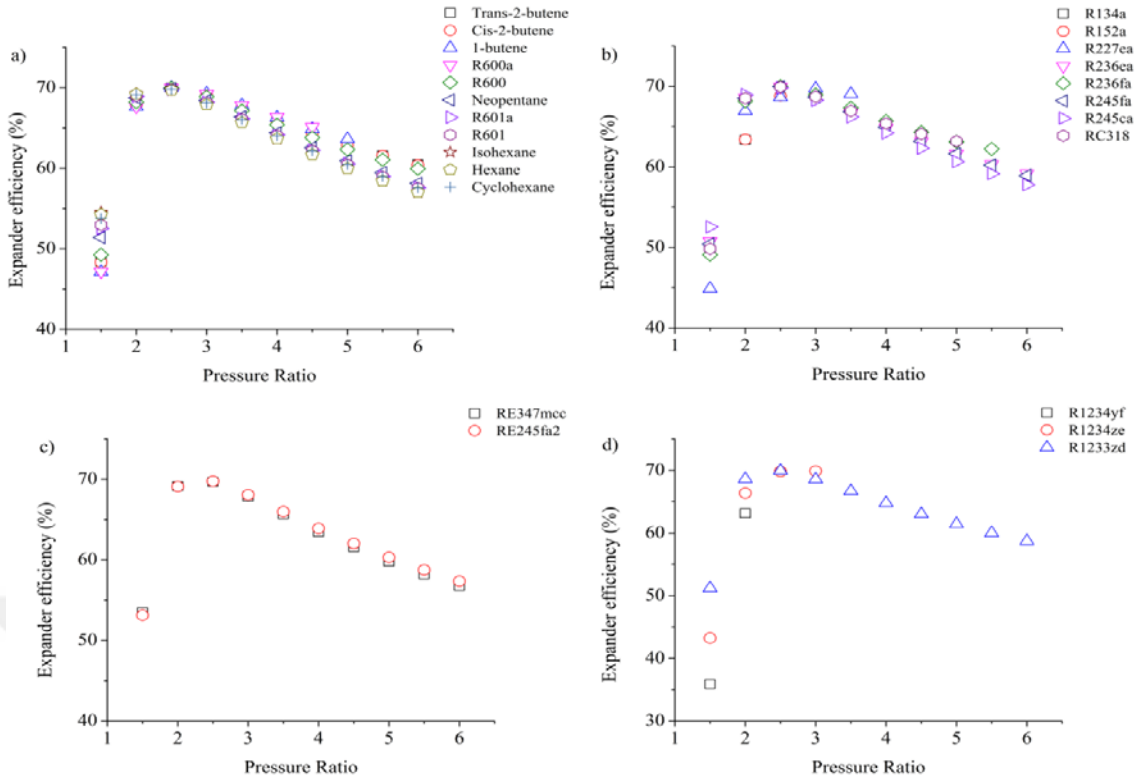

Figure 7-5 Expander efficiency under various pressure ratio a) HCs b) HFC-PFCs c) HFEs d) HFOs

It is worth mentioning that the maximum expander efficiency did not occurred at the pressure ratio of 2.5 for the fluids such as R134a and R1234yf because of their saturation pressure limitation. The simulation results reveal that 1-butene showed the highest expander efficiency (70.1%) among all the investigated fluids.

7.9. Condenser analysis

Based on the Eq. (5-36), the amount of the heat that was rejected from the condenser varied between 1729 W and 3223.96 W. That is to say that this amount of heat was transferred to the cooling water in the condenser and subsequently, increased its temperature at the outlet of the condenser. The mass flow rate of the cooling water and the cooling water temperature at the outlet of the condenser was calculated according to the equations from (5-37) to (5-38) for each considered fluid and the results are given in Table 7-5.

Table 7-5 Investigated cooling water mass flow rate and outlet temperature at pressure ratio of 1.5

Fluid	Cooling water mass flow rate (kg/s)	Cooling water inlet temperature (°C)	Cooling water outlet temperature (°C)
Trans-2-butene	0.091	12	20.21
Cis-2-butene	0.092	12	20.11
1-butene	0.091	12	20.16
R600a	0.087	12	20.25
R600	0.091	12	20.14
Neopentane	0.09	12	20.33
R601a	0.092	12	20.16
R601	0.093	12	20.14
Isohexane	0.094	12	20.18
Hexane	0.094	12	20.2
Cyclohexane	0.094	12	19.99
R134a	0.093	12	20.13
R152a	0.093	12	20
R227ea	0.09	12	20.39
R236ea	0.092	12	20.22
R236fa	0.092	12	20.23
R245fa	0.093	12	20.18
R245ca	0.093	12	20.18
RC318	0.09	12	20.45
RE347mcc	0.091	12	20.43
RE245fa2	0.093	12	20.23
R1234yf	0.091	12	19.01
R1234ze	0.091	12	20.24
R1233zd	0.09	12	18.65

For each investigated fluid, the cooling water temperature at the condenser outlet was approximately 6-8 °C higher than that of the inlet temperature. Although, the cooling water outlet temperature is not high enough to cover hot water needs of a household, it can be directed to a hot water tank to supply some pre-heated water as it was represented in section 4.1.4 of the thesis.

7.10. Solar ORC analysis

The net work output and the thermal efficiency of the solar ORC is discussed in this section. The generated net work output initially rose, then it reached a peak and remained almost constant with the increasing pressure ratio for 1-butene, R600a, hexane, Isohexane, Cyclohexane, R236fa, R245fa and RE245fa2. This trend in the net work output is due to the three mains factors which are a decrease in the working fluids mass flow rate and an increase in the pump work and an enthalpy drop. Namely, the enthalpy drop within the expander for each fluid augmented as the cycle operating pressure ratio increased which enhanced the generated mechanical work in the expander, as well as the net mechanical work of the cycle. However, at the same time with the increasing pressure ratio of the cycle, the mass flow rate of the working fluids

decreased and the pump work increased which have a negative effect on the net mechanical work. The cycle net mechanical work increased when the enthalpy drop was dominant compared to the effects of the mass flow rate and the pump work. After a certain point, the negative effects of the mass flow rate and the pump work compensated the positive effect of the enthalpy drop in the expander. Then, the net mechanical work of the cycle did not show any further increase. Similar finding were reported in (Wang, M. et al., 2013). This negative effects were even more profound for the fluids such as trans-2-butene, cis-2-butene, R600, neo-pentane, R601a, R236ea, R245ca, RE347mcc and R1233zd where the net mechanical work started to decrease after a certain point of pressure ratio.

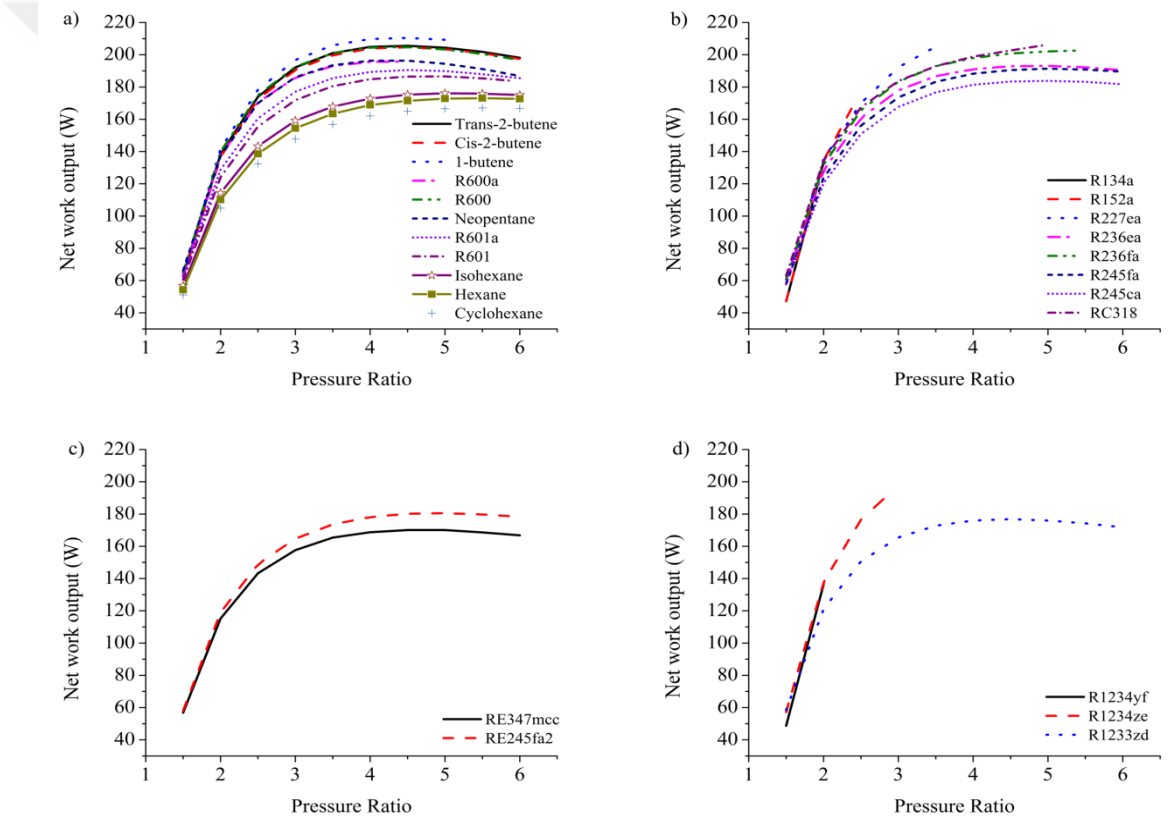

Figure 7-6 Net work output versus pressure ratios of the cycle for a) HCs b) HFC-PFCs c) HFEs d) HFOs

On the other hand, the thermal efficiency of the cycle presented a different behaviour than the net work output. Namely, the cycle efficiency increased gradually with the increasing cycle pressure ratio (Figure 7-7) whereas the net work output showed a maximum point (Figure 7-6). The upward trend of cycle efficiency is due to the combined effects of the collector efficiency which is related to the cycle heat input and the net mechanical work of the cycle. That is to say that although, the net work output of the cycle remained constant or decreased after a certain point of the cycle pressure

ratio, the decreasing trend of the collector efficiency, in other words the cycle heat input as the collector was utilised as an evaporator of the cycle led the cycle efficiency increase gradually (see Eq. (7-8)). Similar trend was reported in (Zhai, H. et al., 2014).

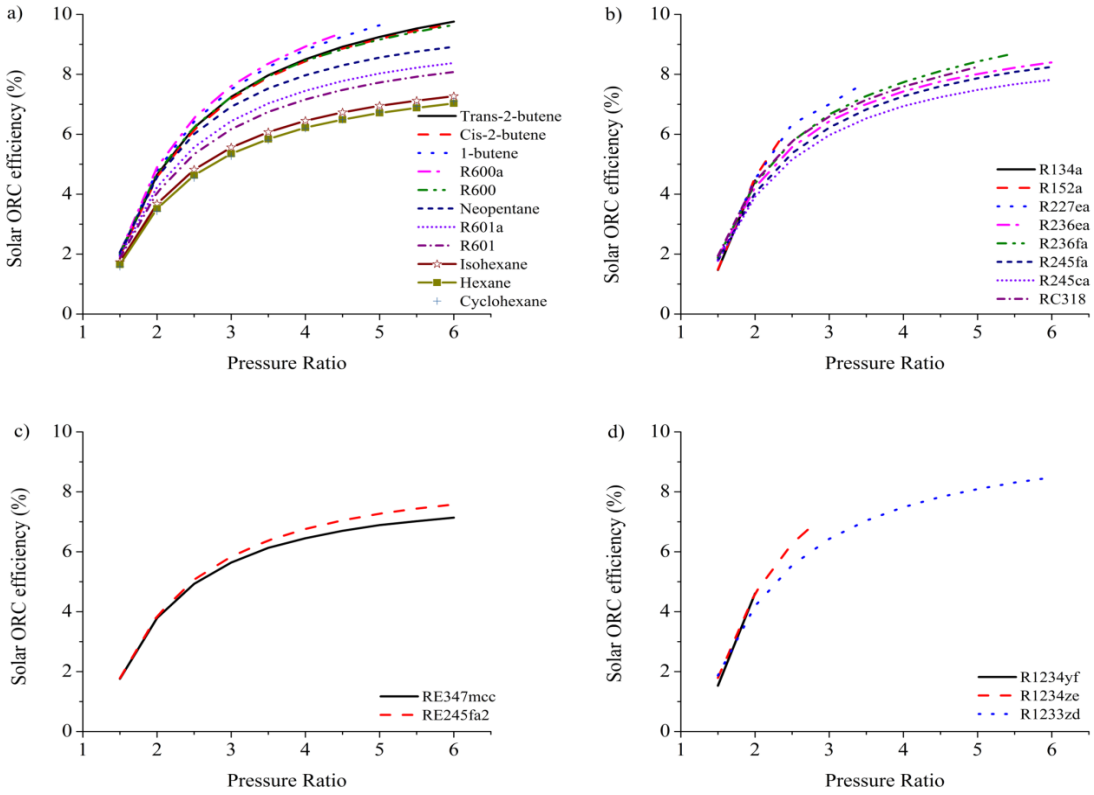

Figure 7-7 Solar ORC efficiency versus various pressure ratio for a) HCs b) HFC-PFCs c) HFEs d) HFOs

In general, hydrocarbons such as trans-2-butene, cis-2-butene, 1-butene, R600 and R600a provided the highest net work output of the cycle and the highest cycle efficiency was obtained by trans-2-butene (9.76%) and cis-2-butene (9.69%) among the investigated fluids. The operating conditions and efficiency values of the collector, the expander and the cycle efficiency at the maximum net work output for each investigated fluid is represented in Appendix C

7.11. Environmental and safety aspects of the considered fluids

Previously, in section 6.3 it was stated that although R134a provides higher collector efficiency than HFE 7000, the former has a higher global warming potential than the latter and it would be crucial to discuss the environmental effects together with their thermophysical properties. Table 7-6 shows the global warming potential and safety properties of the investigated fluid. Generally, the fluids which belong to HFCs and

PFC have high global warming potential. Furthermore, hydrocarbons are more flammable than HFCs, HFEs and HFOs.

Table 7-6 Environmental and safety properties of the considered fluids

Fluid	Alt. Name	Type	GWP	Safety
Trans-2-butene		HC	~20	-
Cis-2-butene		HC	~20	-
1-butene		HC	~20	-
Isobutane	R600a	HC	~20	A3
Butane	R600	HC	~20	A3
Neopentane		HC	~20	-
Isopentane	R601a	HC	~20	A3
Pentane	R601	HC	~20	A3
Isohexane		HC	~20	-
Hexane		HC	~20	-
Cyclohexane		HC	~20	A3
1,1,1,2-tetrafluoroethane	R134a	HFC	1370	A1
1,1-difluoroethane	R152a	HFC	133	A2
1,1,1,2,3,3,3-heptafluoropropane	R227ea	HFC	3500	A1
1,1,1,2,3,3-hexafluoropropane	R236ea	HFC	1410	-
1,1,1,3,3,3-hexafluoropropane	R236fa	HFC	6300	A1
1,1,1,3,3-pentafluoropropane	R245fa	HFC	1050	B1
1,1,2,2,3-pentafluoropropane	R245ca	HFC	726	-
Octafluorocyclobutane	RC318	PFC	10300	A1
Methyl-heptafluoropropyl-ether	RE347mcc	HFE	450	Non-flammable
2,2,2-trifluoroethyl-difluoromethyl-ether	RE245fa2	HFE	659	-
2,3,3,3-Tetrafluoropropene	R1234yf	HFO	4	A2L
Trans-1,3,3,3-tetrafluoropropene	R1234ze	HFO	6	A2L
Trans-1-chloro-3,3,3-trifluoropropene	R1233zd	HFO	7	A1

A: Lower toxicity, B: Higher toxicity, 1: Non-flammable, 2: Lower flammability 3: Higher flammability

7.12. Overall analysis of the considered thermo-fluids

It is worth mentioning that there is no one specific fluid that can satisfy all the criteria for the proposed low-temperature solar thermal system. The decision should be made based on the desired criteria. For instance, hydrocarbons such as R600a, R600 and cyclohexane provide net work output and high thermal efficiency yet they have flammability problems. Secondly, R236fa, R227ea and R134a have high GWP. Lastly, fluids such as R134a, R152a, R1234yf, R1234ze represents high saturation pressure at condensation temperature of 25 °C and this limits the cycle operating pressure ratio, as well as the system performance. It is also important to note that fluid mixtures, in other words blending a compound with other compounds that have lower flammability and

GWP could restrain the flammability and GWP issues (Wang, J. et al., 2010). This is discussed in Chapter 10 in detail.

Chapter 8 CFD analysis of HFE 7000 based nano-refrigerants

This chapter covers the CFD analysis of HFE 7000 based various nano-refrigerants under four different Reynolds number and four different particle volume concentration ratios. The detailed analysis of HFE 7000 based Al_2O_3, SiO_2, CuO and MgO nano-refrigerants which is taken from *Paper V* is discussed. In addition to that, further analysis results of HFE 7000 based 8 nano-refrigerants where the increase in the heat transfer coefficient is represented in this chapter.

8.1. Background of the study

It was previously mentioned that nanofluids where various nanoparticles are dispersed in water and ethylene glycol have been used in solar thermal applications as a working fluid. It was concluded from both experimental and theoretical studies that utilising nanofluids which have better thermal-properties than that of a base fluid provide a higher heat transfer mechanism. On the other hand, nano-particles could be suspended in refrigerants and utilised in applications such as refrigeration, heat pump, air conditioning and solar thermal. However, in the literature there are limited numbers of numerical and experimental studies on nano-refrigerants heat transfer characteristics, particularly convective flow characteristics of nano-refrigerants.

Table 8-1 The considered parameters of the simulation study

Base fluid	HFE 7000, water
Particle	Al_2O_3, SiO_2, CuO , MgO
Reynolds number	400, 800, 1200, 1600
Volume concentration ratio (%)	0%, 2%, 4%, 6%
Heat flux (W/m^2)	1000

Therefore, the laminar forced convection flow characteristics of HFE 7000 based Al_2O_3, SiO_2, CuO and MgO nano-refrigerants in a horizontal tube under constant heat flux is numerically analysed and represented in this section. The effects of Reynolds number and particle volume concentration ratio on both the heat transfer coefficient and the pressure drop of each nanofluid was investigated. Furthermore, the entropy generation analysis is provided for each nanofluid flow to specify the most beneficial nanofluid with optimum working conditions that minimises the total entropy generation of the flow. The considered parameters in the simulations study is given in Table 8-1.

8.2. Nano-refrigerant thermophysical properties

The thermophysical properties of the considered nano-refrigerants were discussed in section 3.2 of *Paper V*.

Thermal and physical properties such as the thermal conductivity, density, specific heat and viscosity of the considered nano-refrigerants were evaluated by using the formulas below:

Thermal conductivity

$$k_{nf} = k_{bf}\frac{[k_s+(n-1)k_{bf}+(n-1)\phi(k_s-k_{bf})]}{[k_s+(n-1)k_{bf}-\phi(k_s-k_{bf})]} \quad (8\text{-}1)$$

In Eq. (8-1), k_{bf} and k_{nf} indicates the thermal conductivity of the base fluid which is HFE 7000 and the thermal conductivity of the nanoparticles which are Al_2O_3, SiO_2, CuO and MgO in this study. The nanoparticles were assumed to be spherical and therefore, n was taken as 3 in the calculations (Hamilton, R. and Crosser, O., 1962).

Viscosity

Dynamic viscosity of the nano-refrigerants were calculated by using the equation which was developed by Einstein depending on the kinetic theory (Einstein, A., 1906).

$$\mu_{nf} = \mu_{bf}(1 + 2.5\phi) \quad (8\text{-}2)$$

where μ_{bf} is the dynamic viscosity of the HFE 7000.

Density

Pak and Chao developed a correlation utilising densities of base fluid and particle (Pak, B. C. and Cho, Y. I., 1998).

$$\rho_{nf} = \phi\rho_s + (1-\phi)\rho_{bf} \quad (8\text{-}3)$$

Specific heat

$$C_{p,nf} = \frac{\phi(\rho C_p)_s+(1-\phi)(\rho C_p)_{bf}}{\phi\rho_s+(1-\phi)\rho_{bf}} \quad (8\text{-}4)$$

8.3. Numerical analysis

8.3.1. Flow domain

This section is taken from section 2 of *Paper V*. The schematic of the flow domain is demonstrated in Figure 8-1. The tube which has a length of 1.2 m and a diameter of

0.00475 m was subjected to 1000 W/m^2 constant heat. Furthermore, the flow was assumed to be symmetrical and the investigated nano-refrigerants and pure HFE 7000 goes into the tube at 283 K.

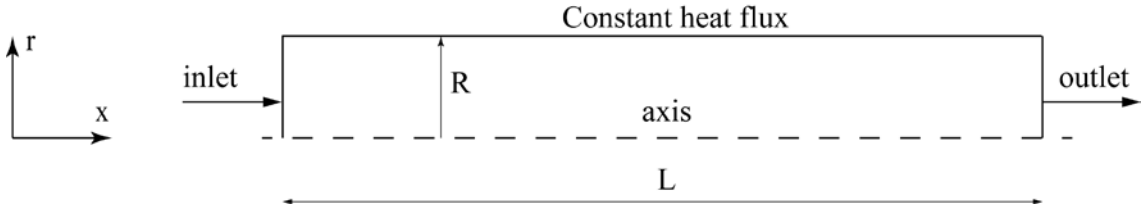

Figure 8-1 Schematic of the flow domain under consideration (Helvaci, H. U. and Khan, Z. A., 2017)

8.3.2. Mathematical modelling

This section is taken from section 3.1 of *Paper V*. The continuity, momentum and energy equations for laminar, incompressible flow are expressed as:

Continuity equation

$$\nabla.\left(\rho_{nf} v\right) = 0 \tag{8-5}$$

Momentum equation

$$\nabla.\left(\rho_{nf} vv\right) = -\nabla P + \nabla.\left(\mu_{nf} \nabla v\right) \tag{8-6}$$

Energy equation

$$\nabla\left(\rho_{nf} v C_p T\right) = \nabla\left(k_{nf} \nabla T\right) \tag{8-7}$$

8.3.3. Boundary conditions

This section is taken from section 3.3 of *Paper V*. The boundary conditions which were applied in the analysis are given in Table 8-2.

Table 8-2 Boundary conditions of the problem

Component	v_x (m/s)	v_r (m/s)	P (bar)	T (K)
Inlet	u	0	1	283
Outlet	?	0	?	?
Wall	0	0	?	$-k_{nf}\left.\frac{\partial T}{\partial r}\right\|_{r=R} = q''$

u indicates the velocity component in the x direction and it was calculated for each nano-refrigerant according to the defined Reynolds number of the flow (400, 800, 1200, 1600). The velocity at the wall was zero as no-slip boundary conditions were applied. Finally, constant heat flux (q'') boundary conditions were utilised at the upper wall of the tube.

8.4. Numerical method

In this study, the single phase homogeneous model was applied in order to investigate flow characteristics of the investigated nano-refrigerants. The finite volume solver Fluent 6.3.26 was utilised to solve the continuity, momentum and energy equations, with the defined boundary conditions. The convective and diffusive terms were solved by employing the second order upwind scheme and pressure-velocity coupling was modelled by utilising the SIMPLE algorithm.

8.5. Data reduction

The calculation of heat transfer coefficient, Nusselt number and entropy generation was discussed in detail in section 4.1 of *Paper V*. The convective heat transfer coefficient (local and average) was calculated as follows:

$$h\,(x) = \frac{q''}{T(x)_{wall} - T(x)_f} \tag{8-8}$$

$$h_{ave} = \frac{1}{L}\int_0^L h(x)dx \tag{8-9}$$

The entropy generation of the flow was represented as the summation of thermal and frictional entropy generation by the use of the following as:

$$S_{tot} = \frac{(q'')^2 \pi D^2 L}{Nu_{ave} k {T_{ave}}^2} + \frac{32\dot{m}^3 f L}{\pi^2 \rho^2 T_{ave} D^5} \tag{8-10}$$

where Nu_{ave}, T_{ave} and f represents the Nusselt number, fluid average temperature and friction factor and they can be calculated from:

$$Nu_{ave} = \frac{h_{ave} D}{k} \tag{8-11}$$

$$T_{ave} = \frac{T_{in} - T_{out}}{ln\left(\frac{T_{in}}{T_{out}}\right)} \tag{8-12}$$

$$f = \frac{2 \cdot \Delta P \cdot D}{\rho \cdot V^2 \cdot L} \tag{8-13}$$

8.6. Simulation results and discussion

This section discusses the effect of the Reynolds number, particle type and particle concentration ratio on the heat transfer coefficient, pressure drop and entropy generation analysis of the flow. All the results were taken from sections 4.2 and 4.3 and section 5 of *Paper V*.

8.6.1. Grid independency test

It is important to perform a grid independency analysis to guarantee the precision of the results. Thus, a grid independency test with various sets of uniform grids was conducted considering both water and HFE 7000 at Reynolds number of 800 and 1600. The analysis results are represented in Table 8-3. Grid 4 which has 2000 cells in x and 40 cell in y direction was used in the simulations as it provides satisfactory results (Table 8-3).

Table 8-3 Grid independency analysis results (Helvaci, H. U. and Khan, Z. A., 2017)

Grid number	**Number of cells in x direction**	**Number of cells in y direction**	**h (pure water)**	**h (pure HFE 7000)**
		Re = 800		
1	250	5	755.384	125.05
2	500	10	728.2	116.41
3	1000	20	720.32	114.63
4	**2000**	**40**	**718.47**	**114.16**
5	3000	40	719.26	114.21
		Re = 1600		
1	250	5	1120.64	158.05
2	500	10	1032.7	146.14
3	1000	20	1011.44	142.68
4	**2000**	**40**	**1006.25**	**141.86**
5	3000	40	1007.34	142

8.6.2. Validation of the model

The experimental analysis of Al_2O_3/water nanofluid conducted by Anoop (2009) was used to validate the model accuracy as there is no experimental and theoretical study of HFE 7000 based nanofluids in the literature (Anoop, K. et al., 2009). The numerical model results for utilising water and Al_2O_3/water nanofluid (ϕ = 4%) were compared with the experimental results. The simulation results of the heat transfer coefficient in the axial direction showed a good agreement between the experimental results where the maximum discrepancy was found to be 12% (Figure 8-2).

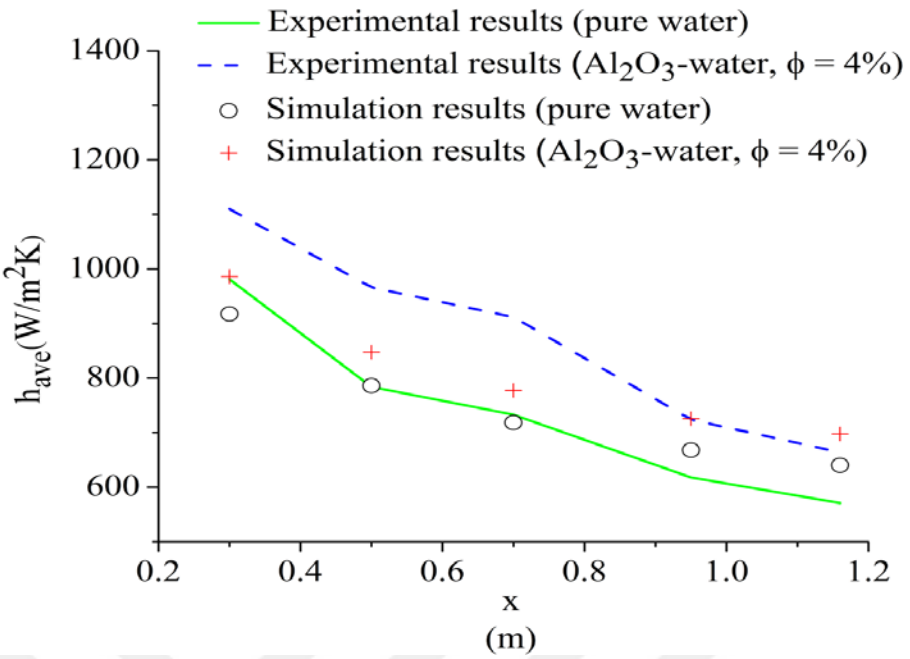

Figure 8-2 Comparison between the simulated and experimental results (Helvaci, H. U. and Khan, Z. A., 2017)

8.6.3. Temperature analysis

The temperature of Al_2O_3-HFE 7000 (ϕ = 0, 1, 4, 6%) and the wall temperature in axial direction is represented in Figure 8-3. It can be observed from Figure 8-3 that the higher nanoparticle volume concentration ratio the lower temperature difference between the wall and bulk temperature. This can be explained by the fact that a higher heat transfer rate occurred when the particle concentration ratio increased which is due to the superior thermophysical characteristics of Al_2O_3-HFE 7000 nano-refrigerant at higher concentration ratio. Similar findings were reported in (Bergman, T., 2009).

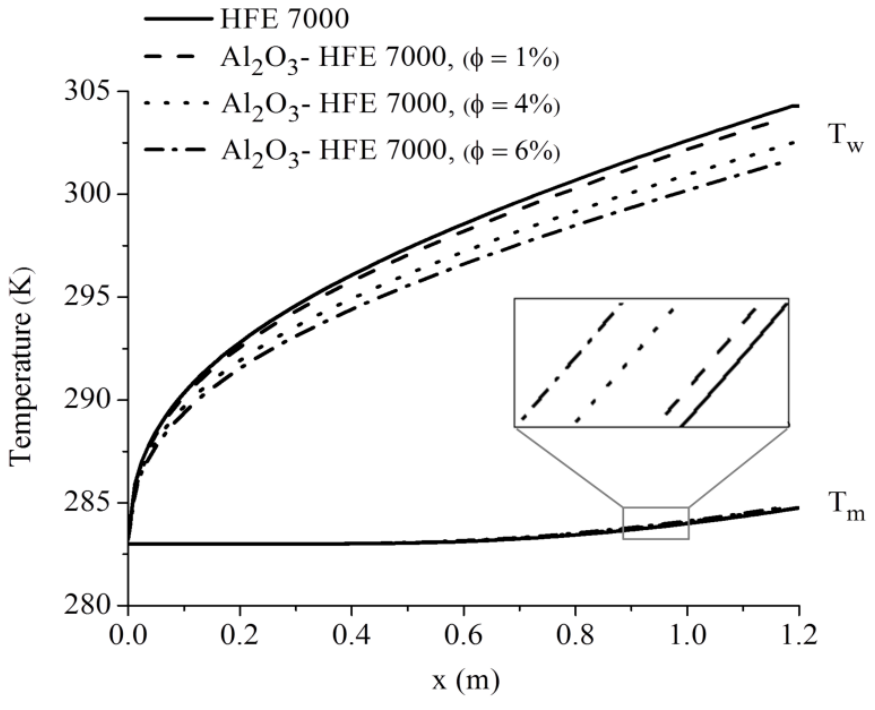

Figure 8-3 Axial distribution of wall and fluid temperature of Al_2O_3 nanofluid at various volume concentrations (Helvaci, H. U. and Khan, Z. A., 2017)

8.6.4. Convective heat transfer analysis

The heat transfer coefficients of the investigated nano-refrigerants at Reynolds number of 400, 800, 1200 and 1600 and particle volume concentration of 0%, 1%, 4% and 6% are demonstrated in Figure 8-4. The heat transfer coefficients of each nano-refrigerant increased with the increasing volume concentration ratio and the Reynolds number (Figure 8-4). This can be explained by the fact that the higher concentration ratio, the greater enhancement in the thermal conductivity of a nanofluid. Similar results were reported in various studies (Moraveji, M. K. and Ardehali, R. M., 2013; Moraveji, M. K. et al., 2011; Purohit, N. et al., 2016). The highest increase in the heat transfer coefficient was observed for MgO-HFE 7000 nano-refrigerant. For instance, the increase in the heat transfer coefficient at Reynolds number of 400 and concentration ratio of 6% was found to be 17.5% for MgO-HFE 7000, 16.9% for Al_2O_3-HFE 7000, 15.1% and 14.6% for CuO-HFE 7000 and SiO_2-HFE 7000 respectively. The increase in the heat transfer coefficient is proportional to the thermal conductivity of the nanoparticles. In other words, the increase in the heat transfer coefficient of a nanofluid is highly dependent of the enhancement in the thermal conductivity of a nanofluid when utilising the single phase model in laminar flow region (Bianco, V. et al., 2009).

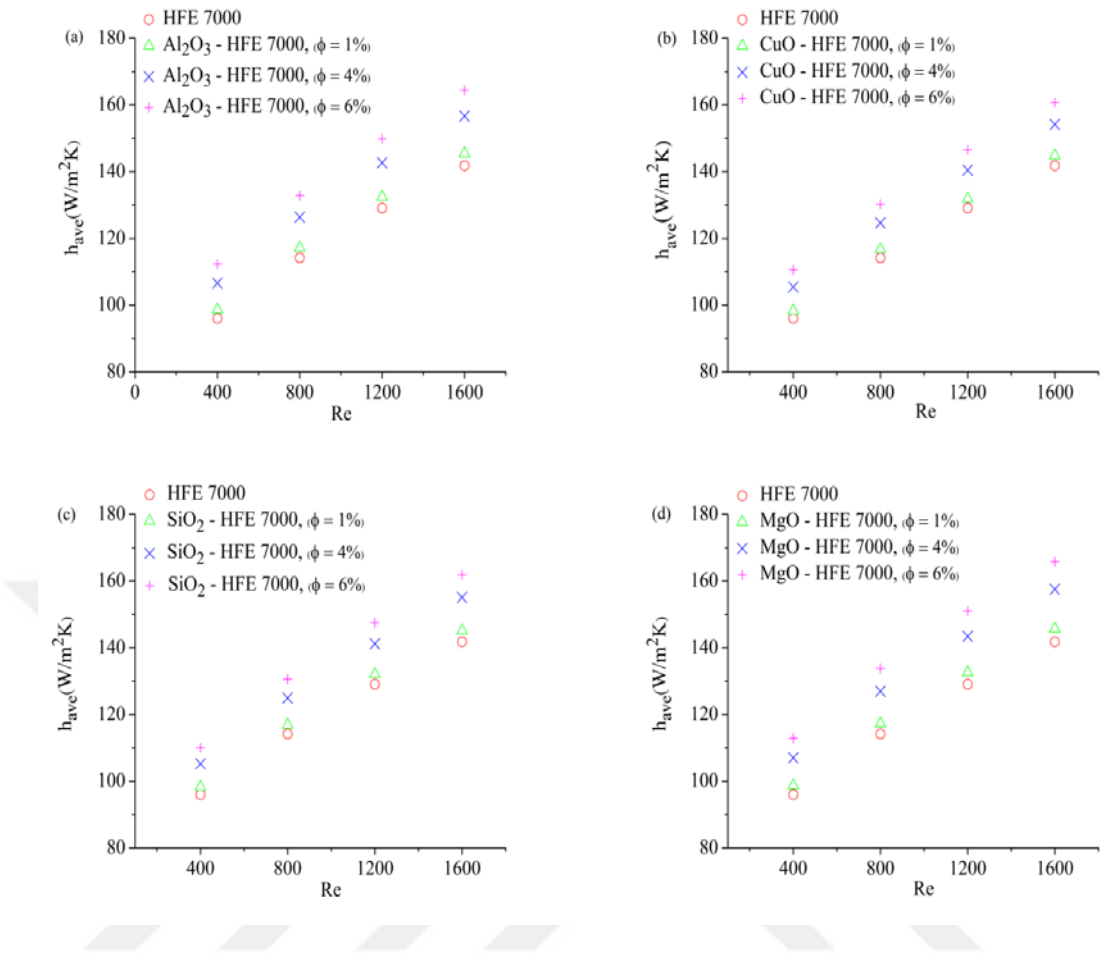

Figure 8-4 Variation of the heat transfer coefficients at different Reynolds number for (a) Al_2O_3-HFE 7000, (b) CuO-HFE 7000, (c) SiO_2-HFE 7000, (d) MgO-HFE 7000 (Helvaci, H. U. and Khan, Z. A., 2017)

8.6.5. Pressure drop analysis

Pressure drop of each nano-refrigerant at various Reynolds number and concentration ratio is shown in Figure 8-5. The increase in the Reynolds number and concentration ratio caused an enhancement in the pressure drop of each nano-refrigerant flow (Figure 8-5). The highest amount of pressure drop was found in SiO_2-HFE 7000 nanofluid (28.2%) and it was followed by MgO-HFE 7000 which accounts for 21.5%. It can be concluded that nano-refrigerants cause a higher pressure drop compared to that of base fluid. Because the nano-refrigerants have a higher viscosity and they become even more viscous as the volume concentration ratio increases (Figure 8-5) (Demir, H. et al., 2011).

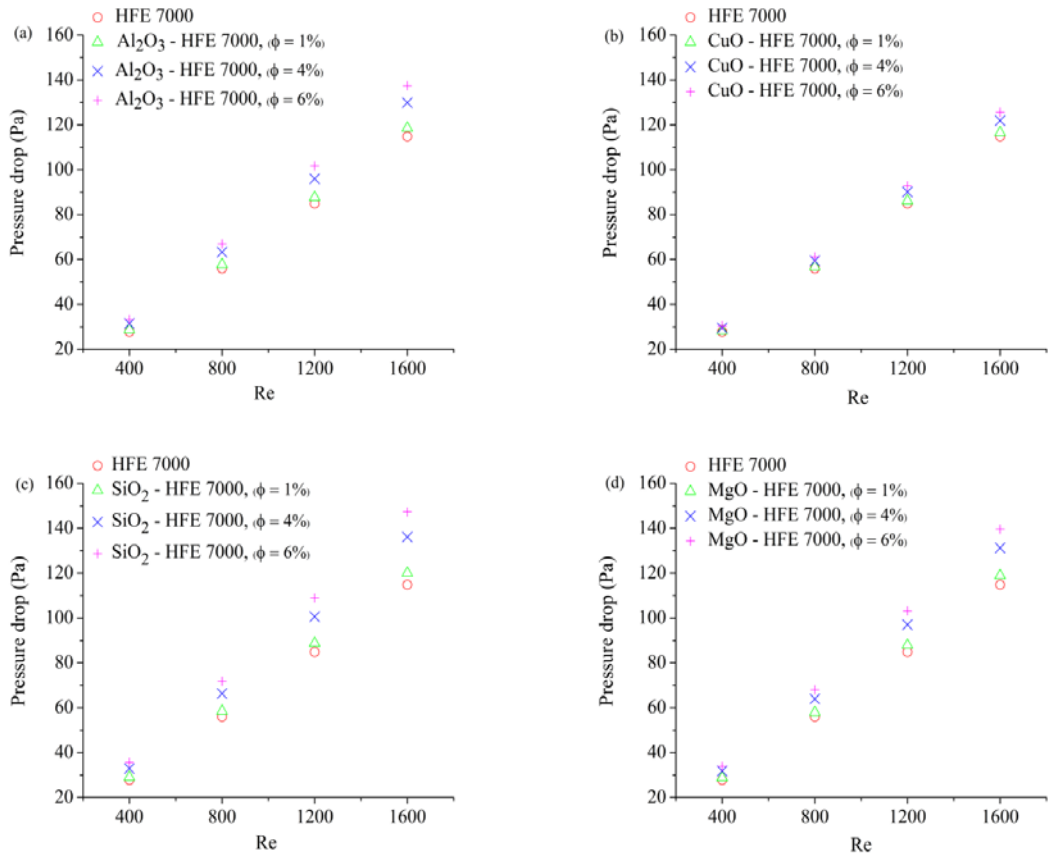

Figure 8-5 Variation of pressure drop at different Reynolds number for (a) Al_2O_3-HFE 7000, (b) CuO-HFE 7000, (c) SiO_2-HFE 7000, (d) MgO-HFE 7000 (Helvaci, H. U. and Khan, Z. A., 2017)

8.6.6. Entropy generation analysis

The entropy generation of each nano-refrigerant which is caused by the thermal and frictional irreversibilities at various Reynolds numbers (400-1200) and concentration ratios (0%-6%) are discussed in this section. Figure 8-6 and Figure 8-7 indicates the frictional and thermal entropy generation of the nano-refrigerants. It can be observed from Figure 8-6 and Figure 8-7 that the increase in the Reynolds number enhanced the frictional irreversibility whereas decreased the thermal irreversibility for each nano-refrigerant and base fluid. The decrease in the thermal entropy generation can be explained by the fact that the heat transfer coefficient, as well as the heat transfer mechanism increased in parallel with the increasing Reynolds number (Figure 8-4). On the other hand, the higher Reynolds number caused higher velocity profiles which resulted in a greater frictional irreversibility (Saha, G. and Paul, M. C., 2015). Similarly, the increase in the volumetric concentration ratio resulted in a decrease in the thermal entropy generation whereas an increase in the frictional entropy generation. This is due to the fact that a higher thermal conductivity obtained for nano-refrigerants with a higher volumetric concentration ratio. In other words, a higher thermal conductivity

resulted in a decrease in the thermal dissipation between the nano-refrigerants and the wall due to the increase in the heat transfer mechanism.

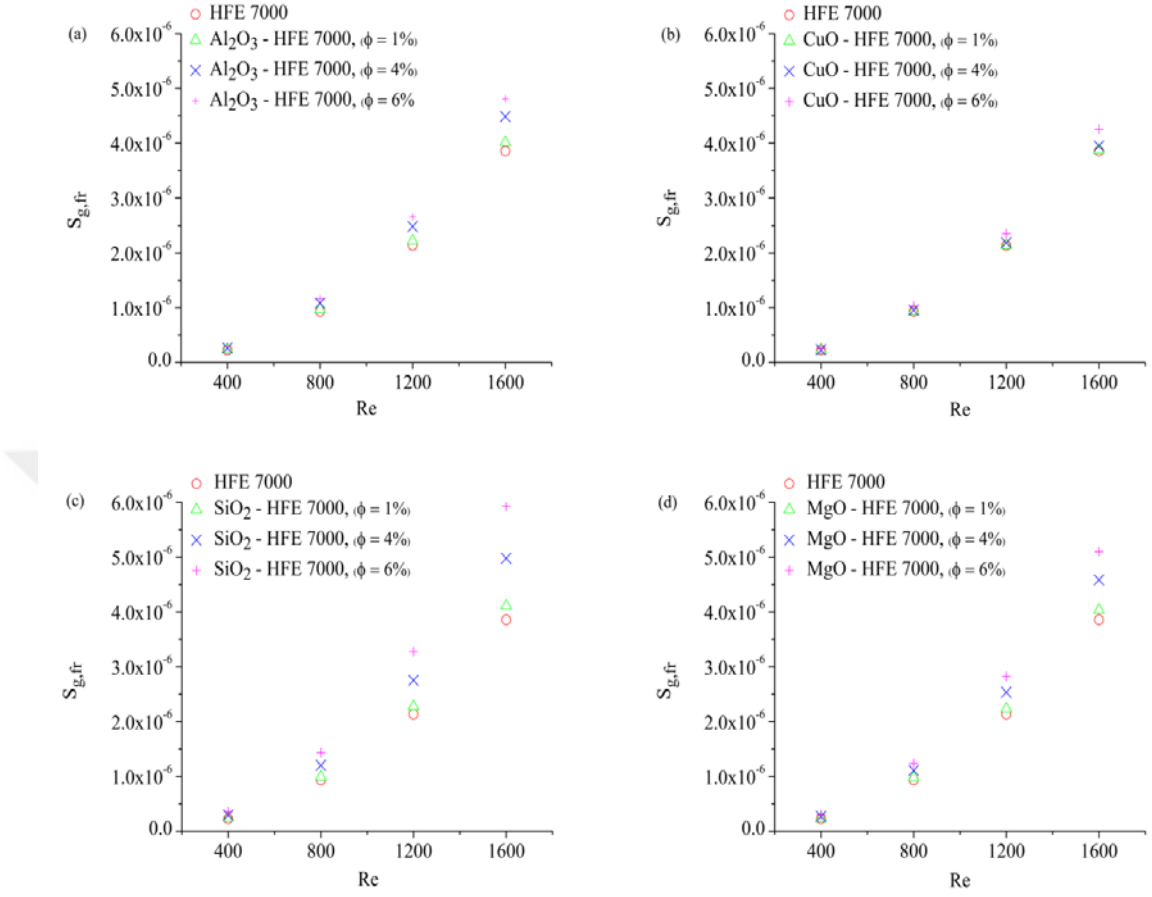

Figure 8-6 Variation of frictional entropy generation at different Reynolds number for (a) Al_2O_3-HFE 7000, (b) CuO-HFE 7000, (c) SiO_2-HFE 7000, (d) MgO-HFE 7000 (Helvaci, H. U. and Khan, Z. A., 2017)

However, the viscosity of nanofluids rose with the increasing volume concentration ratio which caused a higher frictional entropy generation (Bianco, V. et al., 2014).

Furthermore, the total entropy generation of each nano-refrigerant was divided by the entropy generation of the base fluid in order to define the thermodynamic performance of the flows. This is called exergy efficiency ratio of a flow and it was evaluated by the following equation:

$$S_{gen,ratio} = \frac{S_{gen,tot,nf}}{S_{gen,tot,bf}} \tag{8-14}$$

where $S_{gen,tot,nf}$ and $S_{gen,tot,bf}$ are the nanofluid and the base fluid total entropy generation respectively. As it is expected from Eq. (8-14), $S_{gen,ratio}$ is 1for pure HFE 7000 which shows there is no contribution to the flow. Thus, the $S_{gen,ratio}$ values close to zero shows great amount of contribution of nano particles to the flow.

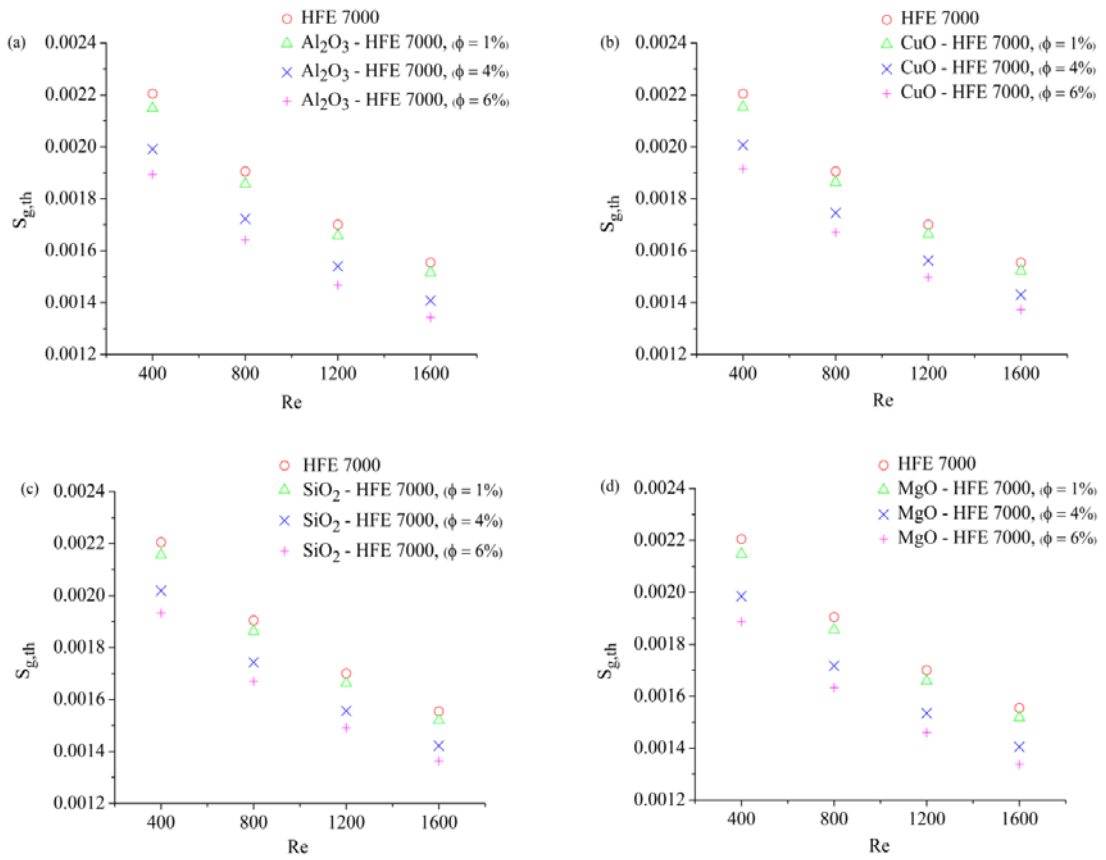

Figure 8-7 Variation of thermal entropy generation at different Reynolds number for (a) Al_2O_3-HFE 7000, (b) CuO-HFE 7000, (c) SiO_2-HFE 7000, (d) MgO-HFE 7000 (Helvaci, H. U. and Khan, Z. A., 2017)

At Reynolds number of 800, the $S_{gen,ratio}$ of each nanofluid is represented in Figure 8-8. For each investigated nano-refrigerant, the addition of nanoparticles has a beneficial effect on the entropy generation reduction and this effect was more pronounced at higher volumetric concentration ratios.

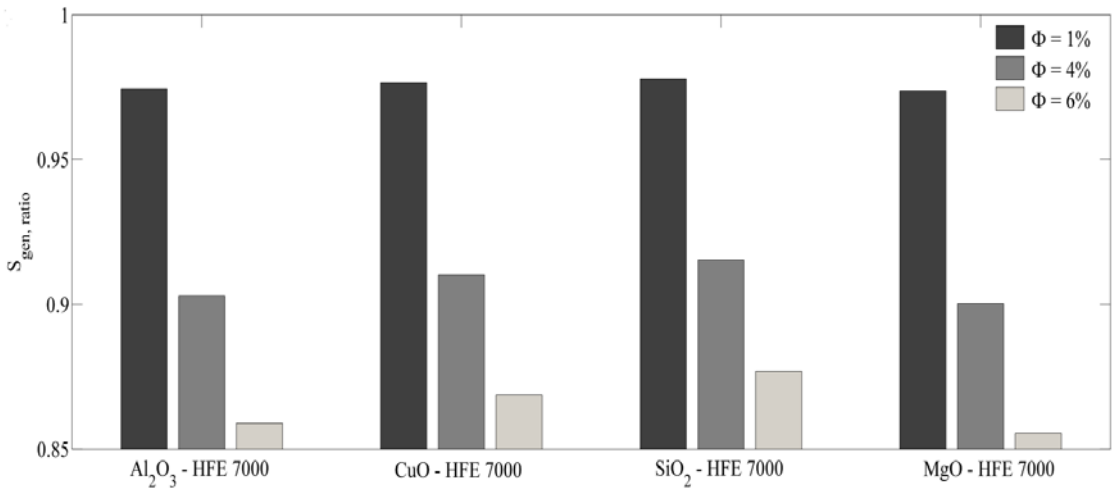

Figure 8-8 Entropy generation ratio of the nanofluids at Re = 800

For instance, the $S_{gen,ratio}$ at concentration ratio of 1% was found to be 0.97 where as it decreased to 0.85 as the concentration ratio rose to 6% for MgO-HFE 7000 nano-refrigerant. Furthermore, for SiO_2-HFE 7000, entropy generation ratio decreased from 0.97 to 0.87 as the concentration ratio increased from 1% to 6%. It is important to note that as it was previously mentioned and also represented in Figure 8-6 and Figure 8-7, the frictional entropy generation and thermal entropy generation showed an opposite trend with the increasing concentration ratio. However, the total entropy generation decreased with the rising volumetric concentration ratio. Therefore, it can be concluded that the thermal entropy generation dominated the total entropy generation as the entropy generation due to the friction is smaller compared to the thermal entropy generation (Moghaddami, M. et al., 2012; Zhao, N. et al., 2016).

In conclusion, the dispersion of the nanoparticles such as Al_2O_3, CuO, SiO_2 and MgO in HFE 7000 resulted in an increase in the heat transfer coefficient of HFE 7000 which enhanced the heat transfer mechanism and decreased the total entropy generation of the flow. It can be also concluded that the HFE 7000 based Al_2O_3, CuO, SiO_2 and MgO nano-refrigerants with the volumetric concentration ratio up to 6% offers a promising alternative to be utilised as a working fluid in the proposed solar thermal system.

8.7. Analysis of further HFE 7000 based nano-refrigerants

In addition to the considered particles (Al_2O_3, MgO, CuO and SiO_2), eight nanoparticles which were studied in several nano fluid applications in the literature were analysed and represented in this section. Table 8-4 shows the increase in the average heat transfer coefficient of HFE 7000 based twelve nano-refrigerants including (Al_2O_3, MgO, CuO and SiO_2) at 1%, 4% and 6% volumetric concentration ratio and Reynolds number of 1200. It can be observed that in general, all the investigated nano-refrigerants show a beneficial effect on the average heat transfer coefficient. For instance, heat transfer coefficient of boron carbide (B_4C) + HFE 7000 nano-refrigerant increased by 18.17% at particle volumetric concentration of 6%. Furthermore, HFE 7000 based boron nitride (BN) and beryllium oxide (BeO) nano-refrigerants could also be considered as potential thermo-fluids.

Table 8-4 Heat transfer coefficient augmentation at Re = 1200

Particle	**1%**	**4%**	**6%**
	h_{ave} (%)	**h_{ave} (%)**	**h_{ave} (%)**
Boron carbide (B_4C) + HFE 7000	2.912	11.923	18.170
Boron nitride (BN) + HFE 7000	2.861	11.708	17.834
Beryllium oxide (BeO) + HFE 7000	2.761	11.293	17.193
Magnesium oxide (MgO) + HFE 7000	2.723	11.130	16.950
Graphite + HFE 7000	2.712	11.068	16.831
Silicon (Si) + HFE 7000	2.690	10.969	16.679
Aluminium nitride (AIN) + HFE 7000	2.671	10.915	16.609
Silicon carbide (SiC) + HFE 7000	2.663	10.876	16.548
Aluminium oxide (Al_2O_3) + HFE 7000	2.580	10.543	16.051
Titanium dioxide (TiO_2) + HFE 7000	2.461	10.056	15.305
Silicon dioxide (SiO_2) + HFE 7000	2.315	9.396	14.240
Copper (II) oxide (CuO) + HFE 7000	2.149	8.858	13.555

8.8. Analysis of the proposed solar ORC employing twelve nano-refrigerants

Previously, the solar ORC was mathematically modelled and simulated with 24 zero-ODP refrigerants including HFE 7000. Furthermore, CFD simulations of HFE-7000 based 12 nano-refrigerants were conducted and the particles effect on the heat transfer characteristics of HFE 7000

discussed in section 8.7. As it can be seen from Table 8-4, addition of the particles into pure HFE 7000 increased the heat transfer coefficient. Previously, it was mentioned that nano-refrigerants can be used in ORC application such as working fluid and higher performance values can be obtained thanks to the improved thermo-physical properties of nano-refrigerants such as thermal conductivity compared to the that of base refrigerant. Therefore, it is important to evaluate the effect of nano-refrigerants on the net mechanical work of the solar ORC when they are used as working fluid of the cycle.

This section reports the simulation analysis of the proposed ORC employing 12 HFE 7000 based nano-refrigerants and their effect on the net generated mechanical work output. Operating conditions of the cycle simulation is given in Table 8-5.

Table 8-5 Operating conditions of the simulation

Parameter	**Description**
Cycle	Saturated
Working fluid	12 HFE-7000 based nano-refrigerants
Incoming solar radiation	800 W/m^2
Pressure ratio	5

It is worth mentioning that the enhancement in the thermal properties of pure HFE 7000 such as thermal conductivity, density, specific heat and viscosity only considered when the fluid is liquid, in other words when it is not saturated. Secondly, to make a benchmark analysis the fluid collector inlet temperature and fluid saturation temperature were assumed to be the same for each investigated nano-refrigerant, in other words the temperature difference between fluid saturation temperature in the collector and collector inlet temperature were the same for each nano-refrigerant.

It can be seen from Table 8-6 that all the investigated nano-refrigerants lead a higher net work output compared to the pure HFE 7000. The highest improvement was obtained by TiO2 + HFE 7000 where the net work output increased from 170.08 W to 180.33 W. It was followed by SiO2 + HFE 7000 and Silicon (Si) + HFE 7000. This could be explained by the fact that all the considered nano-refrigerants have superior thermal conductivity values compared to pure HFE 7000. Consequently, this leads a higher heat transfer mechanism in the proposed cycle. However, it is important to note that thermal conductivity is not the only source of the enhancement in the net mechanical work output. Namely, a higher net work output was obtained with SiO2 + HFE 7000 (180.33 W) than MgO + HFE 7000 (176.44 W) although, the thermal conductivity of MgO (45 W/m K) particle is higher than SiO2 (1.2 W/m K). The reason for that could be the combined effect of thermal conductivity and specific heat of the nano-refrigerants.

For instance, higher thermal conductivity of nano-refrigerants resulted in higher heat gained by the fluid in the collector. On the other hand, the nanoparticles have lower specific heat values compared to the pure HFE 7000. Thus, the increased heat gain of the fluid and the decreased specific heat of the nano-refrigerants resulted in higher mass flow rate values of the cycle as the temperature difference was kept constant in the collector (see Eq. 8.15). The heat balance of the collector in the single phase liquid region is calculated by the equation given below;

$$\dot{Q}_{qain} = \dot{m}_{wf} \times C_p \times \Delta T \tag{8-15}$$

Therefore, it can be concluded that the increased thermal conductivity and decreased specific heat characteristics of the nano-refrigerants showed a beneficial effect on the cycle. It is also important to mention that the proposed simulation only considers the thermo-physical properties in the single phase flow. Therefore, in reality higher beneficial effects of the nano particles should be observed.

Table 8-6 Simulation results of the solar ORC

Fluid	**Net work output of the cycle (W)**
Pure HFE 7000	170.08
Boron carbide (B_4C) + HFE 7000	178.22
Boron nitride (BN) + HFE 7000	179.32
Beryllium oxide (BeO) + HFE 7000	176.23
Magnesium oxide (MgO) + HFE 7000	176.44
Graphite + HFE 7000	179.6
Silicon (Si) + HFE 7000	180.19
Aluminium nitride (AIN) + HFE 7000	178.53
Silicon carbide (SiC) + HFE 7000	178.85
Aluminium oxide (Al_2O_3) + HFE 7000	179.9
Titanium dioxide (TiO_2) + HFE 7000	180.66
Silicon dioxide (SiO_2) + HFE 7000	180.33
Copper (II) oxide (CuO) + HFE 7000	183.1

Chapter 9 Conclusions

9.1. Fulfilling the objectives of the thesis

9.1.1. To conduct an experimental analysis of the low-temperature solar thermal system

These conclusions are based on the work conducted in Chapter 3 and Chapter 4. Initially, a low-temperature solar thermal system which consists of a solar ORC and heat recovery units were designed commissioned and tested experimentally. A novel and environmentally friendly thermal fluid HFE 7000 was employed in the ORC unit. The flat plate collector was utilised as an evaporator in the ORC unit to provide sufficient heat to the fluid. Therefore, the collector was used as a vapour generator of the cycle. Then, the generated vapour in the collector expanded in the expander and generated mechanical work. A heat recovery unit was connected to the ORC unit to recover some portions of the rejected heat from the condenser. The experimental data was analysed through the first and second law analysis of thermodynamics. The experimental results showed that the collector with a thermal efficiency of 57.53% was able to provide a superheated vapour at 45.41ºC to the expander. In the expander 146.74 W of mechanical energy was generated and the expander efficiency was calculated to be 58.66%. An average amount of 3406 W heat was transferred to the cooling water in condenser and 23.2% of this heat was recovered in the hot water storage tank for further uses. The second law analysis results indicated that the highest amount of exergy destruction was observed in the collector (431W) and this was followed by the expander (95W). The solar ORC was able to generate 135.96 W of net mechanical work with a thermal and exergy efficiency of 3.81% and 17.8% respectively. Furthermore, it was highlighted in the parametric analysis of the solar ORC that the cycle operating pressure ratio and the degree of superheat play an important role on the first and second law of the cycle. In conclusion, this experimental work demonstrated that the proposed low-temperature solar thermal cycle, employing new generation and environmentally friendly thermo-fluid HFE 7000 is a feasible option for mechanical and heat energy generation.

9.1.2. To mathematical model the solar ORC

These conclusions are based on the work conducted in Chapter 5. The proposed solar ORC was mathematically modelled where the flat plate solar energy collector and the vane expander were utilised as the heat source and the prime mover of the cycle similar

to the work which was represented in Chapter 3 and Chapter 4. In accordance with the findings of section 4.3, both the collector and the expander efficiencies are varied according to the fluid thermophysical properties and cycle operating conditions. This was done to take these effects into consideration when analysing the performance of the solar ORC.

9.1.3. To conduct a simulation study of the flat plate collector and the solar ORC

These conclusions are based on the work conducted in Chapter 6 and Chapter 7. The numerical analysis of the modelled collector was conducted to analyse the collector performance under various operating conditions by determining the fluid mean temperature, fluid heat gain and the collector heat loss. In the analysis, HFC-134a which was utilised as the working fluid of the collector entered the collector as a sub-cooled liquid and left the collector as a superheated vapour. The simulation results showed that a higher heat transfer coefficient of the fluid was obtained in the flow boiling region compared to the single phase (liquid and vapour) region. Furthermore, it was highlighted in the study that collector operating conditions such as the collector pressure, the fluid mass flow rate and the fluid thermal properties have an effect on the collector performance. In Chapter 7, the solar ORC was simulated under various operating conditions with twenty four thermo-fluids. In the simulations, the effect of each fluid's thermophysical property and cycle operating conditions were discussed. In addition to that the environmental impacts of the considered fluids were also considered in the analysis. A significant effect of the cycle pressure ratio on the collector, expander efficiency, as well as the cycle efficiency was observed from the analysis. In general, similar findings were reported in this study where the cycle pressure and the physical properties of the fluids play an important role on the component efficiencies, therefore the cycle performance.

The simulation results revealed that among the investigated fluids trans-2-butene, cis-2-butene, 1-butene, R600a, R600, R601, R601a, neopentane, R227ea, R236fa, RC318 and R1234ze provided higher values of net work output of the cycle. However, fluids such as trans-2-butene, cis-2-butene, 1-butene, R600a, R600, R601, R601a are hydrocarbons and they have flammability issues. Having a high global warming potential is also the disadvantages of RC 318and R236fa. Furthermore, R134a, R152a, R227ea, R1234yf, and R1234ze have a considerably high saturation pressure at the designed condenser temperature which limits their utilisation at higher cycle operating pressure conditions.

On the other hand, HFEs such as RE347mcc and RE245fa2 and HFOs such as R1234yf andR1233zd are environmentally friendly fluids in terms of global warming potential and have reliable safety characteristics such as flammability and toxicity yet they offer a moderate system performance and could be considered in low-temperature solar thermal systems.

9.1.4. To perform a CFD analysis of HFE 7000 based various nano-refrigerants

These conclusions are based on the work conducted in Chapter 8. CFD analysis where the convective heat transfer, pressure drop and entropy generation characteristics of HFE 7000 based Al_2O_3, CuO, SiO_2 and MgO nanofluids were discussed. In addition to the considered nanorefrigerants, eight nano-refrigerants where boron carbide (B_4C), boron nitride (BN), beryllium oxide (BeO), graphite, silicon, aluminium nitride (AIN), silicon carbide (SiC), titanium dioxide (TiO_2) were dispersed in HFE 7000 was analysed in terms of the augmentation in the heat transfer coefficient of the nano-refrigerants compared to HFE 7000 base fluid. The simulation results showed that all the investigated nano-refrigerants showed an increased value of heat transfer coefficient and a decreased value of total entropy generation. This indicates that adding the above nano particles in HFE 7000 enhanced its thermophysical properties. Furthermore, increasing Reynolds number and particle volume concentration ratio has a positive effect on the heat transfer coefficient, as well as the thermal entropy generation of the flows. However, these effects also increase the pressure drop and frictional entropy generation of the flow. Because the thermal entropy generation effect was more pronounced compared to the frictional entropy generation, as a result the total entropy generation of the nano-refrigerant was diminished compared to the base fluid, therefore, it was observed that addition of the considered nanoparticles into the HFE 7000 was beneficial.

This study also showed that the considered nano particles could be added into a thermo-fluid which is environmentally friendly but has moderate thermophysical properties such as HFE 7000 to enhance its heat transfer properties that could be utilised in low-temperature solar thermal systems.

Chapter 10 Future work

In undertaking the present work a number of recommendations have become apparent for further research. These are briefly summarised here:

10.1. A theoretical and experimental study of potential working fluid mixtures for the proposed solar thermal system

The proposed solar thermal system was modelled in Chapter 5 and a simulation study of the system employing twenty four pure thermal fluids was conducted in Chapter 7. The current simulation study with the appropriate modifications in the mathematical model of the system should be extended for the investigation of working fluid mixtures (azeotropes, near-azeotropes and zeotropoes). This could demonstrate the potential advantages of utilising mixtures as a working fluid such as an increase in the system efficiency, a decrease in the condenser duty and obtaining a working fluid mixture which has negligible global warming potential.

Furthermore, based on the simulation results, experimental study should be conducted to support the theoretical findings and investigate the possible disadvantages of fluid mixtures such as high temperature glide and leakage due to the possessing different vapour pressures.

10.2. Numerical analysis of HFE 7000 based nano-refrigerants using two phase models

CFD analysis of HFE 7000 based various nano-refrigerants was investigated and the results were discussed in Chapter 8. In the performed study, the single phase (homogeneous) model was utilised for the convective flow analysis of the considered refrigerants. However, the accuracy of the single phase model highly depends on the calculated effective thermophysical properties of the nanofluids. Furthermore, in the single phase model the slip velocity between the base fluid and the particles were assumed to be zero. Therefore, the convective flow analysis of the investigated nanorefrigerants should be investigated considering the two-phase models such as Eulerian and Langerian models and the results should be compared with the current findings.

Furthermore, considering that turbulent flow regime is more desired in heat transfer applications, the analysis of the nano-refrigerants should also be considered under turbulent flow to investigate different mechanism for heat transfer augmentation.

10.3. Experimental investigation of the considered nano-refrigerants

Experimental study should be performed in order to support the findings which were obtained from the CFD analysis. This would show if the nanorefrigerants are practically beneficial in heat transfer applications such as the proposed solar thermal system. Furthermore, it is also important to analyse the considered nanorefrigerants experimentally in multi-phase, in other words flow boiling conditions. This would demonstrate if the considered particles cause clogging due to the depositions of the particles especially when evaporation arises.

References

Akbari, M., Galanis, N., and Behzadmehr, A., 2011. Comparative analysis of single and two-phase models for cfd studies of nanofluid heat transfer. *International Journal of Thermal Sciences,* 50 (8), 1343-1354.

Al-Sulaiman, F. A., 2014. Exergy analysis of parabolic trough solar collectors integrated with combined steam and organic rankine cycles. *Energy Conversion and Management,* 77 (0), 441-449.

Andersen, W. C., and Bruno, T. J., 2005. Rapid screening of fluids for chemical stability in organic rankine cycle applications. *Industrial & engineering chemistry research,* 44 (15), 5560-5566.

Anoop, K., Sundararajan, T., and Das, S. K., 2009. Effect of particle size on the convective heat transfer in nanofluid in the developing region. *International journal of heat and mass transfer,* 52 (9), 2189-2195.

Baharoon, D. A., Rahman, H. A., Omar, W. Z. W., and Fadhl, S. O., 2015. Historical development of concentrating solar power technologies to generate clean electricity efficiently–a review. *Renewable and Sustainable Energy Reviews,* 41, 996-1027.

Bao, J., and Zhao, L., 2013. A review of working fluid and expander selections for organic rankine cycle. *Renewable and Sustainable Energy Reviews*, 24, 325-342.

Baral, S., and Kim, K. C., 2014. Thermodynamic modeling of the solar organic rankine cycle with selected organic working fluids for cogeneration. *Distributed Generation & Alternative Energy Journal,* 29 (3), 7-34.

Behzadmehr, A., Saffar-Avval, M., and Galanis, N., 2007. Prediction of turbulent forced convection of a nanofluid in a tube with uniform heat flux using a two phase approach. *International Journal of Heat and Fluid Flow,* 28 (2), 211-219.

Bergman, T., 2009. Effect of reduced specific heats of nanofluids on single phase, laminar internal forced convection. *International Journal of heat and mass Transfer,* 52 (5), 1240-1244.

Bianco, V., Chiacchio, F., Manca, O., and Nardini, S., 2009. Numerical investigation of nanofluids forced convection in circular tubes. *Applied Thermal Engineering,* 29 (17), 3632-3642.

Bianco, V., Manca, O., and Nardini, S., 2014. Entropy generation analysis of turbulent convection flow of al 2 o 3–water nanofluid in a circular tube subjected to constant wall heat flux. *Energy Conversion and Management,* 77, 306-314.

Boyle, G., Everett, B., Ramage, J., and University, T. O., 2003. *Energy systems and sustainability.* Oxford University Press Oxford.

Bryszewska-Mazurek, A., Świeboda, T., and Mazurek, W., 2011. Performance analysis of a solar-powered organic rankine cycle engine. *Journal of the Air & Waste Management Association,* 61 (1), 3-6.

Cengel, Y. A., Boles, M. A., and Kanoğlu, M., 2011. *Thermodynamics: An engineering approach.* Vol. 5: McGraw-Hill New York.

Chaji, H., Ajabshirchi, Y., Esmaeilzadeh, E., Heris, S. Z., Hedayatizadeh, M., and Kahani, M., 2013. Experimental study on thermal efficiency of flat plate solar collector using tio2/water nanofluid. *Modern Applied Science,* 7 (10), 60-69.

Chandrasekar, M., and Suresh, S., 2011. Experiments to explore the mechanisms of heat transfer in nanocrystalline alumina/water nanofluid under laminar and turbulent flow conditions. *Experimental Heat Transfer,* 24 (3), 234-256.

Chen, C. J., 2011. *Physics of solar energy.* John Wiley & Sons.

Chen, H., Goswami, D. Y., and Stefanakos, E. K., 2010. A review of thermodynamic cycles and working fluids for the conversion of low-grade heat. *Renewable and sustainable energy reviews,* 14 (9), 3059-3067.

Colangelo, G., Favale, E., De Risi, A., and Laforgia, D., 2013. A new solution for reduced sedimentation flat panel solar thermal collector using nanofluids. *Applied energy,* 111, 80-93.

Daungthongsuk, W., and Wongwises, S., 2007. A critical review of convective heat transfer of nanofluids. *Renewable and Sustainable Energy Reviews,* 11 (5), 797-817.

Davarnejad, R., and Jamshidzadeh, M., 2015. Cfd modeling of heat transfer performance of mgo-water nanofluid under turbulent flow. *Engineering Science and Technology, an International Journal,* 18 (4), 536-542.

Delgado-Torres, A. M., and García-Rodríguez, L., 2010. Analysis and optimization of the low-temperature solar organic rankine cycle (orc). *Energy Conversion and Management,* 51 (12), 2846-2856.

Demir, H., Dalkilic, A., Kürekci, N., Duangthongsuk, W., and Wongwises, S., 2011. Numerical investigation on the single phase forced convection heat transfer characteristics of tio 2 nanofluids in a double-tube counter flow heat exchanger. *International Communications in Heat and Mass Transfer,* 38 (2), 218-228.

Dikici, A., and Akbulut, A., 2008. Performance characteristics and energy–exergy analysis of solar-assisted heat pump system. *Building and Environment,* 43 (11), 1961-1972.

Duangthongsuk, W., and Wongwises, S., 2009. Heat transfer enhancement and pressure drop characteristics of tio 2–water nanofluid in a double-tube counter flow heat exchanger. *International Journal of Heat and Mass Transfer,* 52 (7), 2059-2067.

Duffie, J. A., and Beckman, W. A., 2013. *Solar engineering of thermal processes.* John Wiley & Sons.

Einstein, A., 1906. Eine neue bestimmung der moleküldimensionen. *Annalen der Physik,* 324 (2), 289-306.

Elsafi, A. M., 2015. Exergy and exergoeconomic analysis of sustainable direct steam generation solar power plants. *Energy Conversion and Management,* 103, 338-347.

Fard, M. H., Esfahany, M. N., and Talaie, M., 2010. Numerical study of convective heat transfer of nanofluids in a circular tube two-phase model versus single-phase model. *International Communications in Heat and Mass Transfer,* 37 (1), 91-97.

Freeman, J., Hellgardt, K., and Markides, C. N., 2015. An assessment of solar-powered organic rankine cycle systems for combined heating and power in uk domestic applications. *Applied Energy,* 138, 605-620.

Gnutek, Z., and Kolasiński, P., 2013. The application of rotary vane expanders in organic rankine cycle systems—thermodynamic description and experimental results. *Journal of Engineering for Gas Turbines and Power,* 135 (6), 061901.

Granryd, E., 2001. Hydrocarbons as refrigerants—an overview. *International journal of refrigeration,* 24 (1), 15-24.

Gupta, M., and Kaushik, S., 2010. Exergy analysis and investigation for various feed water heaters of direct steam generation solar–thermal power plant. *Renewable Energy,* 35 (6), 1228-1235.

Hamilton, R., and Crosser, O., 1962. Thermal conductivity of heterogeneous two-component systems. *Industrial & Engineering chemistry fundamentals,* 1 (3), 187-191.

Hejazian, M., Moraveji, M. K., and Beheshti, A., 2014. Comparative study of euler and mixture models for turbulent flow of al 2 o 3 nanofluid inside a horizontal tube. *International Communications in Heat and Mass Transfer*, 52, 152-158.

Helvaci, H., and Khan, Z. A., 2015. Mathematical modelling and simulation of multiphase flow in a flat plate solar energy collector. *Energy Conversion and Management*, 106, 139-150.

Helvaci, H., and Khan, Z. A., 2016. Experimental study of thermodynamic assessment of a small scale solar thermal system. *Energy Conversion and Management*, 117, 567-576.

Helvaci, H. U., and Khan, Z. A., 2017. Heat transfer and entropy generation analysis of hfe 7000 based nanorefrigerants. *International Journal of Heat and Mass Transfer*, 104, 318-327.

Heris, S. Z., Esfahany, M. N., and Etemad, G., 2007. Numerical investigation of nanofluid laminar convective heat transfer through a circular tube. *Numerical Heat Transfer, Part A: Applications*, 52 (11), 1043-1058.

Heyhat, M., Kowsary, F., Rashidi, A., Momenpour, M., and Amrollahi, A., 2013. Experimental investigation of laminar convective heat transfer and pressure drop of water-based al 2 o 3 nanofluids in fully developed flow regime. *Experimental Thermal and Fluid Science*, 44, 483-489.

Holbert, K. E., 2011. Solar thermal electric power plants. *Handbook of Renewable Energy Technology*, 225.

Hung, T.-C., 2001. Waste heat recovery of organic rankine cycle using dry fluids. *Energy Conversion and Management*, 42 (5), 539-553.

Hung, T. C., Shai, T. Y., and Wang, S. K., 1997. A review of organic rankine cycles (orcs) for the recovery of low-grade waste heat. *Energy*, 22 (7), 661-667.

Husband, W., and Beyene, A., 2008. Low-grade heat-driven rankine cycle, a feasibility study. *International Journal of Energy Research*, 32 (15), 1373-1382.

Incropera, F. P., 2011. *Fundamentals of heat and mass transfer*. John Wiley & Sons.

Invernizzi, C. M., Iora, P., Preßinger, M., and Manzolini, G., 2016. Hfos as substitute for r-134a as working fluids in orc power plants: A thermodynamic assessment and thermal stability analysis. *Applied Thermal Engineering*, 103, 790-797.

Kalogirou, S. A., 2004. Solar thermal collectors and applications. *Progress in energy and combustion science*, 30 (3), 231-295.

Kalogirou, S. A., 2013. *Solar energy engineering: Processes and systems*. Academic Press.

Kayhani, M., Soltanzadeh, H., Heyhat, M., Nazari, M., and Kowsary, F., 2012. Experimental study of convective heat transfer and pressure drop of tio 2/water nanofluid. *International Communications in Heat and Mass Transfer*, 39 (3), 456-462.

Khanafer, K., and Vafai, K., 2011. A critical synthesis of thermophysical characteristics of nanofluids. *International Journal of Heat and Mass Transfer*, 54 (19), 4410-4428.

Kim, Y. M., Shin, D. G., and Kim, C. G., 2014. Optimization of design pressure ratio of positive displacement expander for vehicle engine waste heat recovery. *Energies*, 7 (9), 6105-6117.

Klein, S., 1975. Calculation of flat-plate collector loss coefficients. *Solar Energy*, 17 (1), 79-80.

Kolasiński, P., 2015. The influence of the heat source temperature on the multivane expander output power in an organic rankine cycle (orc) system. *Energies*, 8 (5), 3351-3369.

Kumaresan, V., Khader, S. M. A., Karthikeyan, S., and Velraj, R., 2013. Convective heat transfer characteristics of cnt nanofluids in a tubular heat exchanger of various lengths for energy efficient cooling/heating system. *International Journal of Heat and Mass Transfer*, 60, 413-421.

Lemmon, E., Huber, M., and Mclinden, M., 2013. Nist reference database 23: Reference fluid thermodynamic and transport properties-refprop, version 9.1. *Standard Reference Data Program*.

Lemort, V., Guillaume, L., Legros, A., Declaye, S., and Quoilin, S., 2013. *A comparison of piston, screw and scroll expanders for small scale rankine cycle systems.* Paper presented at the Proceedings of the 3rd International Conference on Microgeneration and Related Technologies.

MaïGa, S. E. B., Nguyen, C. T., Galanis, N., and Roy, G., 2004. Heat transfer behaviours of nanofluids in a uniformly heated tube. *Superlattices and Microstructures*, 35 (3), 543-557.

Maizza, V., and Maizza, A., 2001. Unconventional working fluids in organic rankine-cycles for waste energy recovery systems. *Applied Thermal Engineering*, 21 (3), 381-390.

Manolakos, D., Kosmadakis, G., Kyritsis, S., and Papadakis, G., 2009. On site experimental evaluation of a low-temperature solar organic rankine cycle system for ro desalination. *Solar Energy*, 83 (5), 646-656.

Manolakos, D., Papadakis, G., Kyritsis, S., and Bouzianas, K., 2007. Experimental evaluation of an autonomous low-temperature solar rankine cycle system for reverse osmosis desalination. *Desalination*, 203 (1), 366-374.

Manolakos, D., Papadakis, G., Mohamed, E. S., Kyritsis, S., and Bouzianas, K., 2005. Design of an autonomous low-temperature solar rankine cycle system for reverse osmosis desalination. *Desalination*, 183 (1), 73-80.

Marion, M., Voicu, I., and Tiffonnet, A.-L., 2012. Study and optimization of a solar subcritical organic rankine cycle. *Renewable Energy*, 48, 100-109.

Mekhilef, S., Saidur, R., and Safari, A., 2011. A review on solar energy use in industries. *Renewable and Sustainable Energy Reviews*, 15 (4), 1777-1790.

Mirzaei, M., and Azimi, A., 2016. Heat transfer and pressure drop characteristics of graphene oxide/water nanofluid in a circular tube fitted with wire coil insert. *Experimental Heat Transfer*, 29 (2), 173-187.

Moghaddami, M., Shahidi, S., and Siavashi, M., 2012. Entropy generation analysis of nanofluid flow in turbulent and laminar regimes. *Journal of Computational and Theoretical Nanoscience*, 9 (10), 1586-1595.

Moraveji, M. K., and Ardehali, R. M., 2013. Cfd modeling (comparing single and two-phase approaches) on thermal performance of al 2 o 3/water nanofluid in mini-channel heat sink. *International Communications in Heat and Mass Transfer*, 44, 157-164.

Moraveji, M. K., Darabi, M., Haddad, S. M. H., and Davarnejad, R., 2011. Modeling of convective heat transfer of a nanofluid in the developing region of tube flow with computational fluid dynamics. *International Communications in Heat and Mass Transfer*, 38 (9), 1291-1295.

Moraveji, M. K., and Hejazian, M., 2012. Modeling of turbulent forced convective heat transfer and friction factor in a tube for fe 3 o 4 magnetic nanofluid with computational fluid dynamics. *International Communications in Heat and Mass Transfer*, 39 (8), 1293-1296.

Murshed, S. S., and De Castro, C. N., 2011. *Forced convective heat transfer of nanofluids in minichannels.* INTECH Open Access Publisher.

Nasrin, R., and Alim, M., 2013. Performance of nanofluids on heat transfer in a wavy solar collector. *International Journal of Engineering, Science and Technology,* 5 (3), 58-77.

Nouman, J., 2012. Comparative studies and analyses of working fluids for organic rankine cycles-orc. *Master of Science Thesis] KTH School of Industrial Engineering and Management, Stockholm, Sweden*.

Odeh, S., Morrison, G., and Behnia, M., 1998. Modelling of parabolic trough direct steam generation solar collectors. *Solar energy,* 62 (6), 395-406.

Pak, B. C., and Cho, Y. I., 1998. Hydrodynamic and heat transfer study of dispersed fluids with submicron metallic oxide particles. *Experimental Heat Transfer an International Journal,* 11 (2), 151-170.

Panesar, A. S., 2012. *A study of organic rankine cycle systems with the expansion process performed by twin screw machines.* Thesis. City University London.

Pathipakka, G., and Sivashanmugam, P., 2010. Heat transfer behaviour of nanofluids in a uniformly heated circular tube fitted with helical inserts in laminar flow. *Superlattices and Microstructures,* 47 (2), 349-360.

Purohit, N., Purohit, V. A., and Purohit, K., 2016. Assessment of nanofluids for laminar convective heat transfer: A numerical study. *Engineering Science and Technology, an International Journal,* 19 (1), 574-586.

Qiu, G., 2012. Selection of working fluids for micro-chp systems with orc. *Renewable Energy,* 48, 565-570.

Qiu, G., Shao, Y., Li, J., Liu, H., and Riffat, S. B., 2012. Experimental investigation of a biomass-fired orc-based micro-chp for domestic applications. *Fuel,* 96, 374-382.

Quaschning, V., 2004. Solar thermal water heating. *Renewable Energy World,* 2 (2004), 95-99.

Quaschning, V., 2009. *Renewable energy and climate change.* Wiley.

Quoilin, S., Declaye, S., Tchanche, B. F., and Lemort, V., 2011. Thermo-economic optimization of waste heat recovery organic rankine cycles. *Applied thermal engineering,* 31 (14), 2885-2893.

Quoilin, S., and Lemort, V., 2009. Technological and economical survey of organic rankine cycle systems.

Rayegan, R., and Tao, Y., 2011. A procedure to select working fluids for solar organic rankine cycles (orcs). *Renewable Energy,* 36 (2), 659-670.

Reddy, V. S., Kaushik, S., Ranjan, K., and Tyagi, S., 2013. State-of-the-art of solar thermal power plants—a review. *Renewable and Sustainable Energy Reviews,* 27, 258-273.

Richter, C., Teske, S., and Short, R., 2009. Global concentrating solar power outlook 2009. *Amsterdam: Greenpeace*.

Romero, M., and González-Aguilar, J., 2014. Solar thermal csp technology. *Wiley Interdisciplinary Reviews: Energy and Environment,* 3 (1), 42-59.

Saadatfar, B., Fakhrai, R., and Fransson, T., 2014. Conceptual modeling of nano fluid orc for solar thermal polygeneration. *Energy Procedia,* 57, 2696-2705.

Saha, G., and Paul, M. C., 2015. Heat transfer and entropy generation of turbulent forced convection flow of nanofluids in a heated pipe. *International Communications in Heat and Mass Transfer,* 61, 26-36.

Salman, B., Mohammed, H., and Kherbeet, A. S., 2014. Numerical and experimental investigation of heat transfer enhancement in a microtube using nanofluids. *International Communications in Heat and Mass Transfer,* 59, 88-100.

Shah, M., 1982. Chart correlation for saturated boiling heat transfer: Equations and further study.

Shahinfard, S., and Beyene, A., 2013. Regression comparison of organic working mediums for low grade heat recovery operating on rankine cycle. *Journal of Power Technologies,* 93 (4), 257-270.

Siavashi, M., and Jamali, M., 2016. Heat transfer and entropy generation analysis of turbulent flow of tio 2-water nanofluid inside annuli with different radius ratios using two-phase mixture model. *Applied Thermal Engineering,* 100, 1149-1160.

Tchanche, B., Lambrinos, G., Frangoudakis, A., and Papadakis, G., 2010. Exergy analysis of micro-organic rankine power cycles for a small scale solar driven reverse osmosis desalination system. *Applied Energy,* 87 (4), 1295-1306.

Tchanche, B. F., Lambrinos, G., Frangoudakis, A., and Papadakis, G., 2011. Low-grade heat conversion into power using organic rankine cycles – a review of various applications. *Renewable and Sustainable Energy Reviews,* 15 (8), 3963-3979.

Tchanche, B. F., Papadakis, G., Lambrinos, G., and Frangoudakis, A., 2009. Fluid selection for a low-temperature solar organic rankine cycle. *Applied Thermal Engineering,* 29 (11), 2468-2476.

Tsai, W.-T., 2005. Environmental risk assessment of hydrofluoroethers (hfes). *Journal of hazardous materials,* 119 (1), 69-78.

Vélez, F., Segovia, J. J., Martín, M. C., Antolín, G., Chejne, F., and Quijano, A., 2012. A technical, economical and market review of organic rankine cycles for the conversion of low-grade heat for power generation. *Renewable and Sustainable Energy Reviews,* 16 (6), 4175-4189.

Wang, J., Zhao, L., and Wang, X., 2010. A comparative study of pure and zeotropic mixtures in low-temperature solar rankine cycle. *Applied Energy,* 87 (11), 3366-3373.

Wang, J., Zhao, L., and Wang, X., 2012. An experimental study on the recuperative low temperature solar rankine cycle using r245fa. *Applied Energy,* 94, 34-40.

Wang, M., Wang, J., Zhao, Y., Zhao, P., and Dai, Y., 2013. Thermodynamic analysis and optimization of a solar-driven regenerative organic rankine cycle (orc) based on flat-plate solar collectors. *Applied Thermal Engineering,* 50 (1), 816-825.

Wang, X., Zhao, L., Wang, J., Zhang, W., Zhao, X., and Wu, W., 2010. Performance evaluation of a low-temperature solar rankine cycle system utilizing r245fa. *Solar Energy,* 84 (3), 353-364.

Wen, D., and Ding, Y., 2004. Experimental investigation into convective heat transfer of nanofluids at the entrance region under laminar flow conditions. *International journal of heat and mass transfer,* 47 (24), 5181-5188.

Yamaguchi, H., Zhang, X., Fujima, K., Enomoto, M., and Sawada, N., 2006. Solar energy powered rankine cycle using supercritical co 2. *Applied Thermal Engineering,* 26 (17), 2345-2354.

Yang, B., Peng, X., He, Z., Guo, B., and Xing, Z., 2009. Experimental investigation on the internal working process of a co 2 rotary vane expander. *Applied Thermal Engineering,* 29 (11), 2289-2296.

Yousefi, T., Shojaeizadeh, E., Veysi, F., and Zinadini, S., 2012a. An experimental investigation on the effect of ph variation of mwcnt–h 2 o nanofluid on the efficiency of a flat-plate solar collector. *Solar Energy,* 86 (2), 771-779.

Yousefi, T., Veysi, F., Shojaeizadeh, E., and Zinadini, S., 2012b. An experimental investigation on the effect of al 2 o 3–h 2 o nanofluid on the efficiency of flat-plate solar collectors. *Renewable Energy,* 39 (1), 293-298.

Zeinali Heris, S., Kazemi-Beydokhti, A., Noie, S., and Rezvan, S., 2012. Numerical study on convective heat transfer of al2o3/water, cuo/water and cu/water nanofluids through square cross-section duct in laminar flow. *Engineering Applications of Computational Fluid Mechanics,* 6 (1), 1-14.

Zhai, H., Shi, L., and An, Q., 2014. Influence of working fluid properties on system performance and screen evaluation indicators for geothermal orc (organic rankine cycle) system. *Energy,* 74, 2-11.

Zhang, X.-R., Yamaguchi, H., and Uneno, D., 2007. Experimental study on the performance of solar rankine system using supercritical co2. *Renewable Energy,* 32 (15), 2617-2628.

Zhao, N., Yang, J., Li, H., Zhang, Z., and Li, S., 2016. Numerical investigations of laminar heat transfer and flow performance of al 2 o 3–water nanofluids in a flat tube. *International Journal of Heat and Mass Transfer,* 92, 268-282.

Zobaa, A. F., and Bansal, R. C., 2011. *Handbook of renewable energy technology.* Singapore: World Scientific.

Appendix

Appendix A: Journal papers

Paper I

Energy Conversion and Management 117 (2016) 567–576

Contents lists available at ScienceDirect

Energy Conversion and Management

journal homepage: www.elsevier.com/locate/enconman

Experimental study of thermodynamic assessment of a small scale solar thermal system

H.U. Helvaci *, Z.A. Khan

Bournemouth University, Faculty of Science and Technology, Bournemouth, Nano Corr., Energy and Modelling Research Group, BH12 5BB, UK

ARTICLE INFO

Article history:
Received 7 January 2016
Received in revised form 17 March 2016
Accepted 19 March 2016

Keywords:
Solar energy
ORC
HFE 7000
Flat plate collector
Exergy

ABSTRACT

In this study, a scaled solar thermal system, which utilises HFE 7000, an environmentally friendly organic fluid has been designed, commissioned and tested to investigate the system performance. The proposed system comprises a flat-plate solar energy collector, a rotary vane expander, a brazed type water-cooled condenser, a pump and a heat recovery unit. In the experimental system, the flat-plate collector is employed to convert HFE-7000 into high temperature superheated vapour, which is then used to drive the rotary vane expander, as well as to generate mechanical work.

Furthermore, a heat recovery unit is employed to utilise the condensation heat. This heat recovery unit consists of a domestic hot water tank which is connected to the condenser. Energy and exergy analysis have been conducted to assess the thermodynamic performance of the system. It has been found that the collector can transfer 3564.2 W heat to the working fluid (HFE 7000) which accounts for the 57.53% of the total energy on the collector surface. The rotary vane expander generates 146.74 W mechanical work with an isentropic efficiency of 58.66%. In the heat recovery unit, 23.2% of the total rejected heat (3406.48 W) from the condenser is recovered in the hot water tank and it is harnessed to heat the water temperature in the domestic hot water tank up to 22.41 °C which subsequently will be utilised for secondary applications. The net work output and the first law efficiency of the solar ORC is found to be 135.96 W and 3.81% respectively. Exergy analysis demonstrates that the most exergy destruction rate takes place in the flat plate collector (431 W), which is the thermal source of the system. Post collector, it is followed by the expander (95 W), the condenser (32.3 W) and the pump (3.8 W) respectively. Exergy analysis results also show that the second law efficiency of the solar ORC is 17.8% at reference temperature of 15 °C. Parametric study analysis reveals that both increase in the expander inlet pressure and the degree of superheat enhances the thermodynamic performance of the solar ORC.

1. Introduction

Large scale energy utilisation has become a vital concern due to the increase in the demand of energy use in the last decades. At the same time, use of conventional energy sources such as fossil fuels has brought many environmental problems. Climate change and global warming, which is the main issues resulted from the release of harmful substances into the atmosphere have been forcing us to explore alternative energy sources [1,2].

Solar energy is a free, clean and abundant alternative energy source and it can be utilised by means of solar photovoltaic (PV) and solar thermal systems [3]. Although solar PVs have become one of the most representative ways of electricity generation in rural areas, high costs of PV panels, limited efficiency and requirement of expensive batteries are the main disadvantages of such systems [4].

Medium and high temperature solar thermal systems where concentrated solar collectors such as parabolic through [5,6], linear Fresnel [7] and parabolic dish [8] are used have been suggested and developed over the last decades. However, these systems need high initial cost and complex tracking devices [9].

An organic Rankine cycle, which has the same system configuration as conventional Rankine cycle uses organic substances (refrigerants or hydrocarbons) instead of water as a working fluid [10]. Using organic fluids with a lower boiling temperature than water allows these systems to utilise low temperature heat from various renewable energy sources [11]. As a result, non-concentrated low temperature flat plate collectors can be employed in organic Rankine cycles to generate power and heat simultaneously [12].

* Corresponding author at: Faculty of Science and Technology, Fern Barrow, Talbot Campus, Bournemouth University, Poole, Dorset BH12 5BB, UK.
E-mail address: hhelvaci@bournemouth.ac.uk (H.U. Helvaci).

http://dx.doi.org/10.1016/j.enconman.2016.03.050
0196-8904/

Nomenclature

A	area (m^2)
CFCs	chlorofluorocarbons
e	specific exergy (J/kg)
$\dot{E}x$	exergy rate (W)
h	enthalpy (J/kg)
HCFCs	hydrochlorofluorocarbons
HFCs	hydrofluorocarbons
HFEs	hydrofluoroethers
L	litre
m	mass (kg)
$\dot{m}$	mass flow rate (kg/s)
I	solar radiation (W/m^2)
ORC	organic Rankine cycle
$\dot{Q}$	heat transfer rate (W)
$\dot{Q}_u$	useful heat gain (W)
PFCs	perfluorocarbons
PV	photovoltaic
RO	reverse osmosis
s	entropy (J/kg K)
t	time (s)
T	temperature (°C)
V	volume (m^3)
$\dot{W}$	work rate (W)

Subscripts

amb	ambient
col	collector
cond	condenser
dest	destruction
exp	expander
fin	final
in	inlet
int	initial
out	outlet
p	plate
rec	recovery
s	isentropic
sat	saturation
sol	solar
st	storage
u	useful
w	water
wf	working fluid
0	reference (dead) state

Greek symbols

ρ	density (kg/m^3)
η	first law efficiency
ε	second law efficiency

Various refrigerants have been used and analysed in solar organic Rankine cycles for both mechanical work and heat generation. Manolakos et al. [13–15] suggested a low-temperature solar thermal power system utilising HFC-134a for reverse osmosis (RO) desalination. The mechanical work generated in the expander of the cycle is used for the pumping purpose of the RO desalination. An experimental study of solar organic Rankine cycle using HFC-245fa was conducted by [9]. In this study, two stationary collectors which are flat-plate and evacuated tube were employed in the experiments. Collector efficiencies of evacuated tube and flat-plate were found 71.6% and 55.2% respectively. The solar thermal power system, including heat regeneration was also analysed in [16]. In this study R-245fa was used as a working fluid of the cycle and maximum thermal efficiency of 9% was obtained with heat regeneration [16]. In another study, recuperative solar thermal cycle with HFC-245fa was designed and constructed by Wang et al. [17]. It was found that the recuperator did not have any effect on the improvement of the system thermal efficiency, which was about 3.67% [17]. Not only pure refrigerants but also zeotropic mixtures were studied in solar thermal systems. Wang et al. [18] carried out an experimental study of low-temperature solar thermal system considering pure HFC-245fa, a zeotropic mixture of (HFC-245fa/HFC-152a, 0.9/0.1) and another mixture of (HFC-245fa/HFC-152a, 0.7/0.3). Since the efficiency of the collector and the system found higher in zeotropic mixtures it is concluded that zeotropic mixtures have a potential to improve the overall efficiency of such systems [18].

In addition to refrigerants, CO_2 which is a natural fluid was also examined in many solar powered supercritical cycle studies. Zhang et al. [19] carried out an experimental study to examine a solar thermal power cycle performance where supercritical CO_2 was utilised as a working fluid. They concluded that the heat collection efficiency of the collector reached 70% and the system achieved 8.78–9.45% power generation efficiency [19]. Another solar thermal power system using CO_2 was proposed and built in Yamaguchi et al. [20]. A throttling valve was used in order to simulate pressure drop in turbine and to study the system performance. They concluded that solar collector can be used for heating of CO_2 in the cycle up to 165 °C. The power generation efficiency of the cycle is estimated for 25% and the heat recovery efficiency for 65% [20].

Thermodynamic analysis considering energy and exergy methods is an essential tool to investigate not only the quantity, but also the quality of energy used in a system [21] and it is also important for designing and analysing thermal systems [22].

Many studies, including energy and exergy analysis of solar thermal power systems have been conducted by various researchers. Singh et al. [23] conducted the first and second laws analysis of a solar thermal power system integrated with parabolic through collector. It is reported that the highest energy loss occurred in the condenser whereas parabolic through collector/receiver component was found to be the source of main exergy losses in the system [23]. Exergy analysis of parabolic through collector combined with steam and organic Rankine cycle has been examined by [24]. Among the considered various refrigerants R-134a gives the best exergetic performance with an efficiency of 26% [24]. Combined exergetic and exergoeconomic analysis of an integrated solar cycle system was carried out by [25]. In this study, genetic algorithm was utilised for the optimisation procedure to minimise the investment cost of equipment and the cost of exergy destruction. Results showed that for optimum operation, total cost rate decreased by 11% [25]. Elsafi [26] applied exergy and exergoeconomic analysis methods to a commercial-size solar power plant using parabolic through collectors. Exergy and exergy costing balance equations are formulated for each component. It is reported that the highest exergy destruction was calculated for the solar field (63,319 kW) and it was followed by the condenser (4187.5 kW) [26].

Although numerous experimental and simulation studies have been reported on the thermal performance evaluation of small scale solar organic Rankine cycles, detailed thermodynamic analysis of such systems considering energy and exergy methods has

been of interest to a limited number of papers. Previously, a flat plate solar collector was numerically modelled and simulated to investigate the collector performance for two working fluids (HFC-134a and HFE-7000) under various operating conditions [27]. In this study, a scaled solar thermal cycle where the flat plate solar collector is utilised as a direct vapour generator of the system was designed and commissioned. An experimental study using working thermo-fluid (HFE-7000) was performed. To understand the performance characteristics of the solar ORC, the first and second law analyses of each component, as well as the whole system, is evaluated by using experimental data. To utilise the rejected heat from the system, the solar ORC is integrated with a heat recovery unit and the findings is represented in the energy analysis of the system.

In the exergy analysis of the solar organic Rankine cycle, exergy destruction rate and the second law efficiency of each component is investigated. Furthermore, a parametric analysis is carried out in order to evaluate the effects of expander inlet pressure and the degree of superheat on the system performance.

2. Working fluids for solar ORC

Working fluid selection is an important task in ORCs since it affects the performance of a system, as well as it is essential for environmental concerns [28]. Chlorofluorocarbons (CFCs) and hydrochlorofluorocarbons (HCFCs) are conventional refrigerants and they have high potential to deplete the ozone layer [29]. Therefore, perfluorocarbons (PFCs) and hydrofluorocarbons (HFCs) have been used as a promising alternative since they have near-zero ozone depletion potential (ODP). However, PFCs and some HFCs have a relatively high global warming potential [30]. Alternatively, hydrofluoroethers (HFEs) which have zero ozone depletion factor and low global warming potential can be used as candidates for CFCs, HCFCs and PFCs [31] and HFEs can be utilised as a working fluid in ORCs [32,33]. Table 1 shows the properties of conventional and novel organic fluids that have been used in ORCs and refrigeration cycles.

In this study, HFE-7000 is utilised as a working fluid of the solar thermal cycle as it has zero ODP, relatively low value of GWP and reasonable boiling temperature.

3. Experimental bench testing

Experimental system evaluates the performance of a small scale solar thermal technology which employs HFE 7000 as a working fluid.

3.1. Description of the system

The proposed experimental solar thermal system consists of two units: (i) Solar organic Rankine cycle unit which has main components of a flat-plate solar collector, an air motor, a plate-type heat exchanger, a liquid reservoir and a positive displacement pump. (ii) Heat recovery unit with a domestic hot water tank, as shown in Fig. 1. The test rig operates on an ORC principle where the working fluid (HFE-7000) is compressed by the pump and is sent to the flat-plate collector (Fig. 1, state 2). The solar radiation is converted to heat in the collector and it is transferred to the high pressure fluid in the collector tubes where the phase change occurs. Therefore, the collector acts as an evaporator, in other words pressurised vapour generator of the cycle. The fluid might leave the collector as liquid–vapour mixture, saturated vapour or superheated vapour depending on the operating conditions of the system (Fig. 1, state 3).

Pressurised vapour is directed to the turbine where the fluid expands and generates mechanical work. Then, the lower pressure exhaust vapour at the end of the expander goes to the condenser to reject some of its heat from the system (Fig. 1, state 4). The mains water (with an average temperature of 10–13 °C) is used to cool the working fluid and turn it into the liquid state in the condenser (Fig. 1, state 1). Then, liquefied working fluid is pumped again into high pressure to complete the cycle. As shown in Fig. 1 the condenser outlet is connected to the heat recovery unit where the domestic hot water tank is utilised to recover the energy content of rejected heat from the solar ORC.

Flat-plate collector which is formed of a glass cover, a stainless steel absorber plate and a 56 m copper tube in length is used in the experiments. A diaphragm pump which is employed in the experiments to compress the working fluid and it can provide a maximum flow rate of 3 L/min. To adjust the flow rate of the fluid by throttling on the discharge side of the pump a valve is mounted in the system. The condenser utilised in the experiments is a brazed plate heat exchanger and it is fed by mains water to cool the working fluid as mentioned previously. Twelve litre vertical liquid reservoir which provides a steady supply of the fluid was placed after the condenser. A rotary vane air motor is modified and used as an expander of the cycle. Rotary vane expanders can be utilised in ORC applications [37] since they have simpler structure, easy manufacturing and low cost [28]. The air motor used in the experiments can supply a maximum power output of 0.8 kW and maximum rotational speed of 4000 rpm. A 118 L copper-coiled hot water tank is selected to deliver the energy of the pre-heated water coming out of the condenser to the stagnant, stored water in the storage tank (Fig. 1, heat recovery unit).

3.2. Experimental method

Leak test of the system is one of the most important tasks as it affects the overall efficiency and the safety of the system. The system leak test was conducted to examine if there was any leakage somewhere in the cycle. Special attention was given to couplings, joints and the components of the cycle. Initially, a vacuum pump was connected to the system via a vacuum line to pull a vacuum in the cycle. Vacuum gauge was mounted to the system to record the pressure. The system was evacuated and left for 24 h to observe for any leakage through changes in the system pressure. As no change observed in the pressure of the system the line was shut off and the vacuum pump was disconnected. Then, the same line was connected to the working fluid cylinder and the valve was turned on for the subsequent flow of the working fluid into the cycle due to the pressure difference between the system and the working fluid cylinder. 8 kg (5.7 L) of HFE-7000 was introduced to the system. Evaluation of the amount of working fluid to be charged relies on the calculation of the volume of each component and the tube of the cycle. Since the vapour density of the fluid is relatively smaller than the liquid density, the regions in the components and the pipe where the fluid turns into vapour is neglected in the calculation. After the calculation of the volume of each component and the tube, the total volume of the system is multiplied by the fluid density to evaluate the total mass of the working fluid

Table 1
Properties of conventional and novel organic fluids.

Working fluid		$T_{boiling}$[a] (°C)	ODP	GWP	Reference
CFC	R-11	23.37	1	5800	[34]
HCFC	R-141b	31.67	0.12	725	[35]
HFC	R-245fa	14.81	0	950	[35]
HFE-7000	RE347mcc	34	0	450	[30]

[a] Fluids boiling temperature data was taken from REFPROP 9.1 programme [36] at 1 bar.

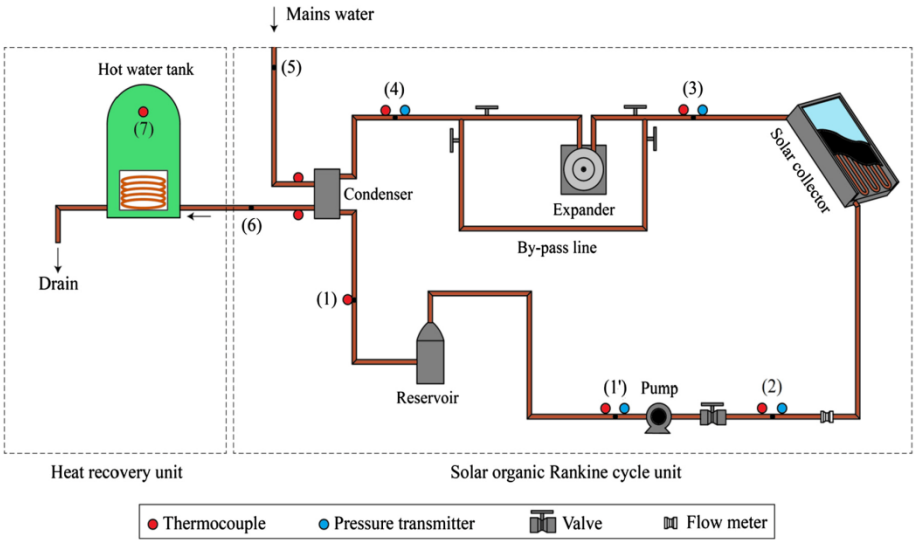

Fig. 1. Schematic layout of the solar thermal system.

[38]. Then, the condenser and the pump were turned on to circulate the water and the fluid through the system without supplying any heat input to check the system consistency and safety. The data acquisition unit was turned on to monitor and record the temperature, pressure and flow rate data. In order to supply steady radiant energy to the collector a solar simulator was utilised in the experiment. Initially, the solar simulator was switched on and the expander by-pass line was opened so the fluid reaches the condenser directly after the solar collector. Once the fluid reaches the vapour conditions the by-pass line was closed and let the fluid pass through the expander. The fluid expands in the rotary vane air motor and produces mechanical work by rotating the motor shaft. Then it is condensed by the help of cooling water in the condenser and is sent back to the solar collector.

In the data measurement system, K-type thermocouples and pressure transmitters are mounted in the experimental prototype to measure temperature and pressure values of HFE-7000 and temperature values of water at specified points as represented in Fig. 1. Thermocouples and pressure transmitters have an accuracy of ±0.18 and ±0.5% respectively. A turbine flow meter with an accuracy of 2% was used to measure the volumetric flow rate of the fluid and the measured flow rate was multiplied by the fluid density (ρ_{wf}) to calculate the mass flow rate of the working fluid. All the data is taken and recorded in a time step of 10 s and transmitted to the computer by an Agilent 34972A data acquisition unit. Although it was not shown in Fig. 1, a pyranometer is mounted in the collector to measure the average irradiance on the collector surface. The collector was marked at every 48 cm in height and at every 58 cm in width. 10 kW heat was supplied from the solar simulator and the radiation data was measured at the specified points via the pyranometer on the collector surface. Detailed representation of the measured points on the collector surface can be found in [27]. During the measurements the solar simulator was located 2 m away from the collector surface and the measured radiation was assumed to be constant at each point. According to the measurement results the calculated average radiation on the collector surface was found to be 890 W/m^2. This value of average radiation on the collector surface is in the range of solar radiation intensity which is used both in experimental and theoretical studies reported previously [9,17,20,24,39].

4. Thermodynamic analysis

Based on the measured temperature, pressure and flow rate values of the working fluid at the defined locations (Fig. 1) it is possible to gain an understanding of performance of the proposed solar thermal cycle by applying the first and second law analysis of thermodynamics. Since the proposed solar thermal system is a closed loop cycle the calculations rely on the application of mass, energy and exergy balance equations at steady state on the each component.

The balance equations in the rate form for any open system at steady state, steady-flow condition with negligible kinetic and potential energy changes are expressed in Eqs. (1)–(3) [40,41].

$$\sum \dot{m}_{in} = \sum \dot{m}_{out} \tag{1}$$

where $\dot{m}$ is the mass flow rate and the subscripts "in" and "out" represent inlet and outlet respectively.

The energy balance equation can be defined as:

$$\dot{Q} - \dot{W} = \sum \dot{m}_{out} h_{out} - \sum \dot{m}_{in} h_{in} \tag{2}$$

In Eq. (2), h is the enthalpy, $\dot{Q}$ and $\dot{W}$ are the heat and work transfer rates of the system.

The exergy balance equation is expressed as:

$$\dot{E}x_{heat} - \dot{W} + \sum \dot{E}x_{in} - \sum \dot{E}x_{out} = \sum \dot{E}x_{dest} \tag{3}$$

where $\dot{E}x$ indicates the exergy rate and the subscript "dest" represents the exergy destruction rate of the system.

In Eq. (3), $\dot{E}x_{heat}$ represents the exergy transfer rate by heat and it can be calculated as:

$$\dot{E}x_{heat} = \sum 1 - \left(\frac{T_0}{T}\right)\dot{Q}_j \tag{4}$$

and the specific exergy (kJ/kg) is given by:

Table 2
Balance equations for each component [21,41,42].

Component	Mass balance equations	Energy balance equations	Exergy balance equations
Collector	$\dot{m}_2 = \dot{m}_3 = \dot{m}_{wf}$	$\dot{Q}_u = \dot{m}_{wf} \times (h_3 - h_2)$	$\dot{E}x_{dest,col} = (\dot{E}x_2 - \dot{E}x_3) + IA_{col}\left[1 - \frac{T_0}{T_p}\right]$
Expander	$\dot{m}_3 = \dot{m}_4 = \dot{m}_{wf}$	$\dot{W}_{exp} = \dot{m}_{wf} \times (h_3 - h_4)$	$\dot{E}x_{dest,exp} = (\dot{E}x_3 - \dot{E}x_4) - \dot{W}_{exp}$
Condenser	$\dot{m}_4 = \dot{m}_1 = \dot{m}_{wf}$ $\dot{m}_5 = \dot{m}_6 = \dot{m}_w$	$\dot{Q}_{cond} = \dot{m}_{wf} \times (h_4 - h_1)$ $\dot{Q}_{cond} = \dot{m}_w \times (h_{w,out} - h_{w,in})$	$\dot{E}x_{dest,cond} = (\dot{E}x_4 - \dot{E}x_1) + (\dot{E}x_5 - \dot{E}x_6)$
Pump	$\dot{m}_{1'} = \dot{m}_2 = \dot{m}_{wf}$	$\dot{W}_{pump} = \dot{m}_{wf} \times (h_2 - h_{1'})$	$\dot{E}x_{dest,pump} = (\dot{E}x_{1'} - \dot{E}x_2) + \dot{W}_{pump}$

$$e = (h - h_0) - T_0(s - s_0) \tag{5}$$

Therefore, the total exergy rate (W) can be calculated by using the following equation:

$$\dot{E}x = \dot{m} \times e \tag{6}$$

The balance equations (mass, energy and exergy) for each component are derived with the following assumptions by using Eqs. (1)–(6) and given in Table 2.

- All the components in the system are at steady state.
- Changes in kinetic and potential energy are neglected.
- The reference-dead state has a pressure of P_0 = 1 bar = 101.325 kPa and temperature of 15 °C.

In the exergy destruction equation of the collector, the term $\left(IA_{col}\left[1 - \frac{T_0}{T_p}\right]\right)$ represents the exergy rate of the solar radiation absorbed on the collector surface where I is the incoming solar radiation, A_{col} is the collector area, T_0 and T_p are the dead state temperature and the collector plate temperature respectively [42].

Furthermore, water flow rate through the condenser is evaluated via the energy balance in the condenser. Considering the steady state conditions:

$$\dot{Q}_{cond} = \dot{m}_{wf} \times (h_4 - h_1) = \dot{m}_w \times (h_{w,out} - h_{w,in}) \tag{7}$$

and water mass flow rate can be evaluated as:

$$\dot{m}_w = \frac{\dot{Q}_{cond}}{(h_{w,out} - h_{w,in})} \tag{8}$$

where $\dot{Q}_{cond}$ represents the amount of heat rate rejected in the condenser and $h_{w,out}$ and $h_{w,in}$ represents the outlet and inlet enthalpy of the water respectively.

4.1. Energy efficiencies

First law efficiency, in other words energy efficiency of a system or system component represents the ratio of energy output to the energy input and it can be calculated as [43];

$$\eta = \frac{\textit{Desired output energy}}{\textit{Supplied energy input}} \tag{9}$$

Flat-plate collector

Collector efficiency can be defined as the ratio of useful collected heat rate of the working fluid ($\dot{Q}_u$) to the solar radiation absorbed on the collector surface (Q_{sol}).

$$\eta_{col} = \frac{\dot{Q}_u}{Q_{sol}} \tag{10}$$

where

$$Q_{sol} = I \times A_{col} \tag{11}$$

Expander

$$\eta_{exp} = \frac{h_3 - h_4}{h_3 - h_{4,s}} \tag{12}$$

Solar ORC

The thermal (first law) efficiency of the proposed solar organic Rankine cycle can be expressed as the ratio of the net work output to the useful heat gain of the working fluid and it is calculated as below:

$$\eta_{sorc} = \frac{\dot{W}_{net}}{\dot{Q}_u} = \frac{\dot{W}_{exp} - \dot{W}_{pump}}{\dot{Q}_u} \tag{13}$$

Heat recovery

Heat recovery efficiency can be expressed as the ratio of the amount of heat which is gained by the water in the hot water tank to the maximum amount of heat that can be utilised from the condenser.

$$\eta_{rec} = \frac{\dot{Q}_{st}}{\dot{Q}_{cond}} \tag{14}$$

where

$$\dot{Q}_{st} = \frac{m_{w,st} \times C_{p,w} \times (T_{w,st,final} - T_{w,st,initial})}{t_{exp}} \tag{15}$$

$$m_{w,st} = V_{st} \times \rho_w \tag{16}$$

4.2. Exergy efficiencies

Second law efficiency is defined as the ratio of the output exergy to the exergy input and it is given as:

$$\varepsilon = \frac{\textit{Exergy output}}{\textit{Exergy input}} \tag{17}$$

Flat-plate collector

Exergy efficiency of the collector is the ratio between the exergy gain of the fluid and exergy content of the incoming solar radiation and it is calculated as:

$$\varepsilon_{col} = \frac{\dot{E}x_3 - \dot{E}x_2}{IA_{col}\left(1 - \frac{T_0}{T_p}\right)} \tag{18}$$

Expander

$$\varepsilon_{exp} = \frac{\dot{W}_{exp}}{(\dot{E}x_3 - \dot{E}x_4)} \tag{19}$$

Pump

$$\varepsilon_{pump} = \frac{\dot{E}x_2 - \dot{E}x_{1'}}{\dot{W}_{pump}} \tag{20}$$

Condenser

$$\varepsilon_{cond} = \frac{\dot{E}x_6 - \dot{E}x_5}{(\dot{E}x_4 - \dot{E}x_1)} \tag{21}$$

Solar ORC

The exergy efficiency of the system is written as;

$$\varepsilon_{sorc} = \frac{\dot{W}_{net}}{\dot{E}x_{in}} \tag{22}$$

Taking the exergy of the solar radiation as an exergy input to the solar organic Rankine cycle Eq. (22) becomes;

$$\varepsilon_{sorc} = \frac{\dot{W}_{net}}{IA_{col}\left(1 - \frac{T_0}{T_p}\right)} \quad (23)$$

Furthermore, in order to calculate the relative ratio of the exergy destruction of j_{th} component to the total exergy destruction, the following expression is used:

$$RI_j = \frac{\dot{E}x_{dest,j}}{\dot{E}x_{dest,tot}} \quad (24)$$

5. Results and discussion

In performing the first and second law analysis of the small scale solar thermal system, the experimental values of temperature (°C), pressure (bar) and flow rate (kg/s) were collected in order to determine fluid state where gas refers to superheated vapour, specific enthalpy (kJ/kg), specific exergy and exergy rate associated with each of the state of the proposed cycle (Table 3). T–s diagram of the working fluid at each state is also shown in Fig. 2.

During the experiments the average value of I = 890 W/m^2 of solar radiation was supplied to the collector and the flow rate of the working fluid was held constant with an average value of 0.022 kg/s. In the analysis, the-reference dead state conditions for temperature and pressure are taken to be 288 K and 1 bar respectively. All the data monitored and analysed in this study when the expansion takes place in the expander and thermodynamic state properties of HFE 7000 were extracted from Ref. [36].

5.1. Energy analysis results

In this section the performance of the proposed solar thermal cycle through the collector efficiency, expander efficiency, heat recovery efficiency, net work output and the system thermal efficiency are examined by the measured temperature, pressure and flow rate values.

Energy rate analysis of the solar collector is shown in Table 4.

The energy received on the collector surface is calculated as 6194.4 W with the help of Eq. (11). In the collector, 57.53% of this energy is utilised to heat the working fluid from 19.1 °C at the collector inlet to 45.41 °C at the collector outlet. The working fluid temperature at the outlet of the collector is almost 4 °C higher than the corresponding saturation temperature (T_{sat} = 41 °C) of the fluid. This shows that with the constant flow rate of 0.022 kg/s, HFE-7000 was able to finish its phase change and leave the collector as a superheated vapour state (Fig. 2). Since HFE 7000 is a dry fluid according to its saturation vapour line, a small degree of superheating would not cause any risk of encountering some portion of liquid in the expander. Furthermore, higher degree of superheating at the collector outlet might lead to an excessive increase in the fluid temperature as well as the heat loss from the system to the atmosphere. Energy rate analysis of the expander can be found in Table 5. Assuming that the expander is adiabatic, according to Eq. (12) the isentropic efficiency of the expander and the work output are found to be 58.66% and 146.74 W respectively. This isentropic efficiency value is similar to the reported efficiency of rotary vane expander using HFE 7000 in [32].

As it can also be seen from Fig. 1, pressure loss through the condenser is neglected. Therefore, the outlet pressure of the expander also represents the condensing pressure of the cycle (P_{sat} = 0.66 - bar). The working fluid leaves the expander at 36.36 °C and it transfers its heat to the cooling water and leaves the condenser at 19.54 °C. According to the corresponding saturation temperature at 0.66 bar (T_{sat} = 22.93 °C), the fluid is below the saturation temperature, in other words it is sub-cooled at the outlet of the condenser. Then its temperature decreases to 18.73 °C after the liquid reservoir. Although there is a slight decrease in pressure after the liquid reservoir, it can be seen that with the temperature of 18.73 °C and a pressure of 0.57 bar, the fluid is sub-cooled at the

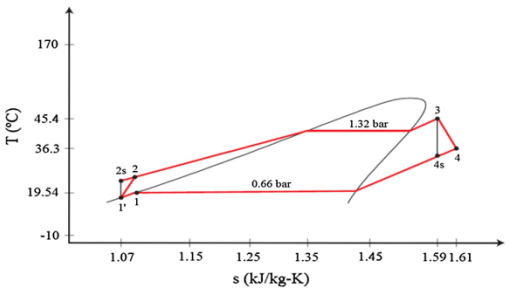

Fig. 2. T–s diagram of the experimental results.

Table 4
Energy rate analysis of the solar collector.

Parameters	Value	Unit
Energy received by the collector (Q_{sol})	6194.4	W
Useful heat gain of the fluid (Q_u)	3564.2	W
Collector energy loss[a]	2907.8	W
Collector efficiency (η_{exp})	57.53	%

[a] $Q_{sol} - Q_u$.

Table 5
Energy rate analysis of the expander.

Parameters	Value	Unit
Work output of the expander ($\dot{W}_{exp}$)	146.74	W
Isentropic efficiency of the expander (η_{exp})	58.66	%

Table 3
Thermodynamic state properties of HFE-7000 at various points.

State (No)	Fluid type	Phase	T (°C)	P (bar)	$\dot{m}$ (kg/s)	h (kJ/kg)	e (kJ/kg)	$\dot{E}x$ (W)
0	HFE-7000	Dead state	15	1	–	218.05	–	–
0	Water	Dead state	15	1	–	63.076	-	–
1	HFE-7000	Liquid	19.54	0.66	0.022	223.56	0.038	0.83
1′	HFE-7000	Liquid	18.73	0.57	0.022	222.57	0.084	1.86
2	HFE-7000	Liquid	19.1	1.86	0.022	223.06	0.402	8.84
3	HFE-7000	Gas	45.41	1.32	0.022	385.07	15.532	341.7
4	HFE-7000	Gas	36.36	0.66	0.022	378.4	4.542	99.98
5	Water	Liquid	13.47	0.66	0.06	56.63	−0.11	−6.6
6	Water	Liquid	26.88	0.66	0.06	112.75	1.002	60.12

outlet of the reservoir. This shows that there is no vapour flowing through the pump which might cause a cavitation problem otherwise. Since water-cooling system is used to reject some portion of heat from the solar ORC unit, it is found that in the condenser an average amount of 3406.48 W heat is transferred to the cooling water and increased its temperature from 13.47 °C to 26.88 °C. As mentioned above, in order to recover the dissipated heat the condenser outlet (Fig. 1, state 6) is connected to the hot water storage tank. This pre-heated water circulates within the coil of the water tank and delivers its heat energy to the stored cold water (Fig. 1, state 7) in the tank. Fig. 3 shows the cooling water inlet and outlet temperature and the temperature change of the stored water in the tank during the experiment. It is seen from Fig. 3 that at the beginning of the experiment stored water temperature was 16.65 °C and its final temperature reached 22.41 °C by the end of the experiment. This utilised heat in the hot water tank is supplied by the waste cooling water coming out of the condenser with an average temperature of 26.88 °C.

By using Eqs (14)–(16) heat gain rate of the hot water tank and the heat recovery efficiency of the system are calculated and the analysis results are given in Table 6. It is shown that 23.2% of the total rejected heat ($\dot{Q}_{cond} = 3.406$ kW) is recovered and is used to pre-heat the stored water in the hot water storage tank.

Consequently, the proposed solar ORC extracts 3564.2 W heat from the solar source and it converts 146.74 W of this heat to the mechanical work. Considering the average pump consumption rate in the analysis ($\dot{W}_{pump} = 10.78$ W), the net work output of the proposed solar ORC is found to be 135.96 W. Therefore, by using Eq. (13), the first law efficiency of the cycle is calculated as 3.81%. In the condenser, 3406.48 W of heat, which represent 95.5% of the total heat input of the cycle is rejected from the system. Then, 23.2% of this rejected heat is recovered in the domestic hot water tank for secondary uses.

5.2. Exergy analysis results

The exergy destruction rate and the exergetic efficiency values are represented in Table 7 and relative irreversibility of each component is represented in Fig. 4. It should be noted that heat recovery unit is neglected in the calculation of exergy analysis. Therefore, the causes of the exergy destruction in the solar ORC include flat-plate solar collector, expander, pump and condenser.

As it can be seen from Table 7 the highest exergy loss occurs in the collector (431 W) and this represents 76.68% of the total exergy destruction rate in the system (Fig. 4). This large amount of exergy destruction rate in the solar collector could be explained by the high difference in quality between solar radiation and the working fluid at collector operating temperature. The same trend can be found in Ref. [24,26,44] where the solar collector that represents the thermal source of the cycle is the main source of exergy destruction. The next largest exergy destruction rate appeared to be in the expander (95 W), representing 16.9% of total exergy destruction rate (Fig. 4). Then the expander is followed by condenser and pump, accounting for 32.36 W and 3.8 W respectively. The second law efficiencies of each component and the system are calculated by using Eqs. (17)–(23) and are represented in Table 7. As it can be seen from Table 7 that solar collector has the lowest second law efficiency (43.57%) due to its large exergy destruction. Another exergy efficiency value at the expander was calculated as 60.69%. This low exergetic efficiency value could be explained by the irreversibilities in the expander such as internal leakage and thermal loss [45]. This also leads a low expander isentropic efficiency which is found to be 58.66% for the present expander. Finally, according to Eq. (23) the exergy efficiency of the whole system is calculated as 17.8%. The overall exergy efficiency of the system can be improved by reducing the exergy destruction rate of the flat-plate collector and the expander as these components are the main source of the irreversibilities of the system. This will also diminish the overall exergy destruction rate of the system and will lead to an increase in the exergy efficiency of these components, as well as the whole system.

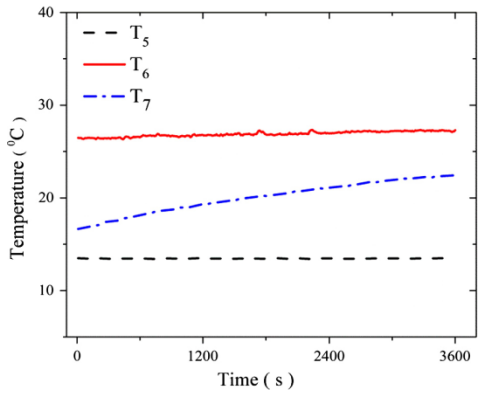

Fig. 3. Water temperature at condenser inlet, outlet and hot water tank.

Table 6
Analysis results of the heat recovery unit.

Parameters	Value	Unit
Testing time	3600	s
Initial water temperature ($T_{7,int}$)	16.65	°C
Final water temperature ($T_{7,fin}$)	22.41	°C
Total mass of water in the tank ($m_{w,st}$)	118	kg
Water specific heat capacity ($C_{p,w}$)	4.187	kJ/kg K
Total energy gain rate in the tank	2845.82	kJ
Average energy gain rate throughout the test ($\dot{Q}_{st}$)	0.79	kW
Average rejected heat rate in the condenser ($\dot{Q}_{cond}$)	3.406	kW
Heat recovery efficiency in the hot water tank (η_{rec})	23.2	%

Table 7
Exergy performance data for the cycle.

Component	$\dot{E}x_{dest}$ (W)	ε (%)
Solar collector	431	43.57
Expander	95	60.7
Condenser	32.3	67.3
Pump	3.8	64.73

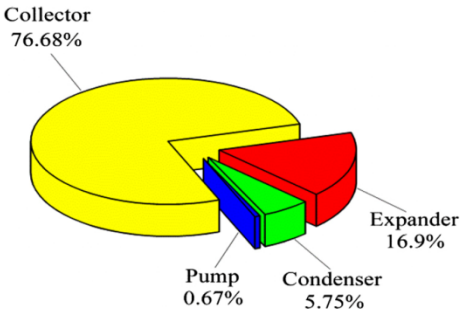

Fig. 4. Relative irreversibilities of each component.

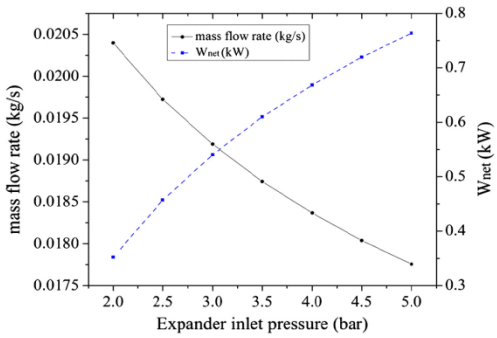

Fig. 5. Mass flow rate and net work output of the cycle versus expander inlet pressure.

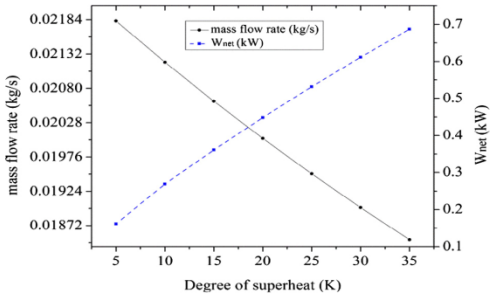

Fig. 6. Mass flow rate and net work output of the cycle versus degree of superheat.

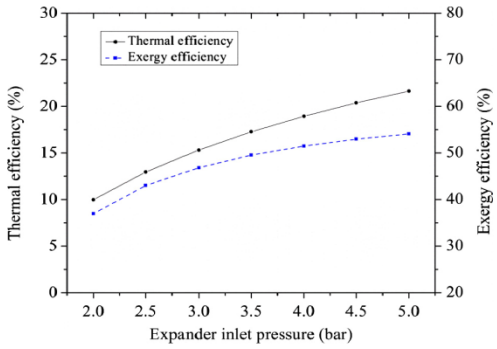

Fig. 7. Variation of the energy and exergy efficiencies of the solar ORC for various expander inlet pressure.

5.3. Parametric analysis

As a part of the analysis the effects of expander inlet pressure and the degree of superheat on the first and second law efficiency of the solar ORC are investigated. Figs. 5 and 6 demonstrate the effect of expander inlet pressure and superheat at the expander inlet on working fluid mass flow rate and the net work output of the solar ORC respectively.

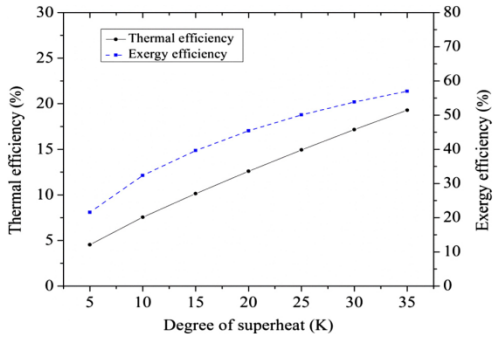

Fig. 8. Variation of the energy and exergy efficiencies of the solar ORC for various degree of superheat.

Since the incoming solar radiation and the collector efficiency were kept constant, increase in expander inlet pressure and degree of superheat reduce the working fluid mass flow rate. At the same time, increase in the both pressure and temperature leads an improvement in the enthalpy gradient at the expander which results in higher amount of net work output of the system. Fig. 7 shows the variation of the first and second law efficiency of the solar ORC with increasing expander inlet pressure.

As it can be seen from Fig. 7 that for the constant condenser pressure of 0.66 bar, when the expander inlet pressure increases from 2 bar to 5 bar, the first and second law efficiency of the system increase from 9.96% to 21.63% and from 36.95% to 54.07% respectively. As expected this trend shows that higher pressure ratio of the cycle leads to an increase in the efficiency of the system [34].

Similar trend is observed with the increasing expander inlet temperature. At the constant expander inlet pressure (1.32 bar) when the degree of superheating is increased to 35 K the thermal efficiency of the system rises and finally reaches 19.29% while the exergy efficiency reaches 56.9% (Fig. 8).

Improvements in the first and second law efficiency of the system with increasing both expander pressure and the degree of superheat could be explained by the improvement in the amount of net work output which is superior to the decrease in the flow rate of the system. However, during the parametric analysis some limitations of the cycle such as the pressure ratio of the cycle and heat losses from the collector to the ambient were neglected. For instance, in real conditions due to leakage and structural problems there should be a reasonable pressure ratio value which was stated as about 3.5 by Tchanche et al. [46]. Furthermore, it is expected that as the degree of superheating and pressure at the expander inlet increases, in other words the collector temperature increases, the higher amount of thermal losses takes place from the collector to the ambient and this would cause a decrease in the collector efficiency [27]. Therefore, it is important to conduct an optimisation study considering all the limitations mentioned above in order to define optimum operating conditions of the cycle.

6. Conclusions

In this study, a small scale solar thermal cycle which employs HFE 7000 as a working fluid is designed, commissioned and tested experimentally. The proposed cycle is comprised of solar ORC and heat recovery units. The solar ORC uses a solar flat-plate collector as an evaporator in order to supply sufficient heat to the fluid

and it acts as a direct vapour generator in the cycle. This high pressure vapour in the collector expands and generates mechanical work through the rotary vane expander. Some portion of the heat is rejected from the solar ORC in the condenser. In order to utilise this waste heat, the condenser is connected to the heat recovery unit where the domestic hot water tank is placed.

Experimental results have been discussed through the first and second law analysis of thermodynamics using mass, energy and exergy balance equations in this paper. The results reveal that the flat plate collector can provide sufficient heat to increase the working fluid temperature up to 45.41 °C and turn it into superheated vapour at the expander inlet with an average solar radiation of 890 W/m^2. In the energy analysis, average heat collection efficiency of the collector is estimated as 57.53%. The rotary vane expander which is used in the experiments generates average mechanical work of 146.74 W, with an isentropic efficiency of 58.66%. In the condenser 3.406 kW heat is rejected from the system and 23.2% of this condensation heat is re-used in the heat recovery unit. It is recovered to increase the temperature of 118 L water in the tank from 16.65 °C to 22.41 °C in 60 min. Exergy analysis results show that the maximum exergy destruction rate occurs in the flat plate collector with 431 W which also accounts for around 76.68% of the total exergy destruction rate of the solar ORC. The expander is the second highest source of the exergy destruction rate with a value of 95 W and this value represents 16.9% of the total exergy destruction rate. It is followed by the condenser (32.3 W) and the pump (3.8 W) respectively. These results highlight that more attention should be given to the flat plate collector which is the heat source of the solar ORC in order to enhance the system efficiency. The components of the cycle: flat-plate collector, expander, condenser and pump exergy efficiencies are estimated at 43.57%, 60.7%, 67.3% and 64.73% respectively. The overall energy and exergy efficiency of the solar ORC is calculated as 3.81% and 17.8% respectively. The parametric analysis study also demonstrates that an increase in expander inlet pressure and the degree of superheat have a positive impact on the first and second law efficiency of the solar ORC. Finally, these results show that small scale solar thermal systems, which utilises a flat plate collector can be used to generate not only mechanical work but also heat energy at the same time. Furthermore, environmentally friendly working fluid HFE 7000 offers a feasible alternative to be utilised in small scale solar thermal systems.

Acknowledgement

The authors acknowledge full financial and in-kind support provided by Future Energy Source (FES) Ltd., UK and are thankful to Bournemouth University for their support.

References

[1] Reddy VS, Kaushik S, Ranjan K, Tyagi S. State-of-the-art of solar thermal power plants—a review. Renew Sustain Energy Rev 2013;27:258–73.
[2] Baharoon DA, Rahman HA, Omar WZW, Fadhl SO. Historical development of concentrating solar power technologies to generate clean electricity efficiently – a review. Renew Sustain Energy Rev 2015;41:996–1027.
[3] Mekhilef S, Saidur R, Safari A. A review on solar energy use in industries. Renew Sustain Energy Rev 2011;15:1777–90.
[4] García-Rodríguez L, Blanco-Gálvez J. Solar-heated Rankine cycles for water and electricity production: POWERSOL project. Desalination 2007;212:311–8.
[5] Zarza E, Valenzuela L, Leon J, Hennecke K, Eck M, Weyers H-D, et al. Direct steam generation in parabolic troughs: final results and conclusions of the DISS project. Energy 2004;29:635–44.
[6] Fernandez-Garcia A, Zarza E, Valenzuela L, Pérez M. Parabolic-trough solar collectors and their applications. Renew Sustain Energy Rev 2010;14:1695–721.
[7] Abbas R, Martínez-Val J. Analytic optical design of linear Fresnel collectors with variable widths and shifts of mirrors. Renew Energy 2015;75:81–92.
[8] Yaqi L, Yaling H, Weiwei W. Optimization of solar-powered Stirling heat engine with finite-time thermodynamics. Renew Energy 2011;36:421–7.
[9] Wang X, Zhao L, Wang J, Zhang W, Zhao X, Wu W. Performance evaluation of a low-temperature solar Rankine cycle system utilizing R245fa. Sol Energy 2010;84:353–64.
[10] Tchanche BF, Lambrinos G, Frangoudakis A, Papadakis G. Low-grade heat conversion into power using organic Rankine cycles – a review of various applications. Renew Sustain Energy Rev 2011;15:3963–79.
[11] Rayegan R, Tao Y. A procedure to select working fluids for Solar Organic Rankine Cycles (ORCs). Renew Energy 2011;36:659–70.
[12] Marion M, Voicu I, Tiffonnet A-L. Study and optimization of a solar subcritical organic Rankine cycle. Renew Energy 2012;48:100–9.
[13] Manolakos D, Papadakis G, Mohamed ES, Kyritsis S, Bouzianas K. Design of an autonomous low-temperature solar Rankine cycle system for reverse osmosis desalination. Desalination 2005;183:73–80.
[14] Manolakos D, Papadakis G, Kyritsis S, Bouzianas K. Experimental evaluation of an autonomous low-temperature solar Rankine cycle system for reverse osmosis desalination. Desalination 2007;203:366–74.
[15] Manolakos D, Kosmadakis G, Kyritsis S, Papadakis G. On site experimental evaluation of a low-temperature solar organic Rankine cycle system for RO desalination. Sol Energy 2009;83:646–56.
[16] Bryszewska-Mazurek A, Świeboda T, Mazurek W. Performance analysis of a solar-powered organic rankine cycle engine. J Air Waste Manage Assoc 2011;61:3–6.
[17] Wang J, Zhao L, Wang X. An experimental study on the recuperative low temperature solar Rankine cycle using R245fa. Appl Energy 2012;94:34–40.
[18] Wang J, Zhao L, Wang X. A comparative study of pure and zeotropic mixtures in low-temperature solar Rankine cycle. Appl Energy 2010;87:3366–73.
[19] Zhang X-R, Yamaguchi H, Uneno D. Experimental study on the performance of solar Rankine system using supercritical CO_2. Renew Energy 2007;32:2617–28.
[20] Yamaguchi H, Zhang X, Fujima K, Enomoto M, Sawada N. Solar energy powered Rankine cycle using supercritical CO_2. Appl Therm Eng 2006;26:2345–54.
[21] Dincer I, Rosen MA. Exergy: energy, environment and sustainable development. Newnes; 2012.
[22] Helvacı HU, Akkurt GG. Thermodynamic performance evaluation of a geothermal drying system. In: Progress in exergy, energy, and the environment. Springer; 2014. p. 331–41.
[23] Singh N, Kaushik S, Misra R. Exergetic analysis of a solar thermal power system. Renew Energy 2000;19:135–43.
[24] Al-Sulaiman FA. Exergy analysis of parabolic trough solar collectors integrated with combined steam and organic Rankine cycles. Energy Convers Manage 2014;77:441–9.
[25] Baghernejad A, Yaghoubi M. Exergoeconomic analysis and optimization of an Integrated Solar Combined Cycle System (ISCCS) using genetic algorithm. Energy Convers Manage 2011;52:2193–203.
[26] Elsafi AM. Exergy and exergoeconomic analysis of sustainable direct steam generation solar power plants. Energy Convers Manage 2015;103:338–47.
[27] Helvaci H, Khan ZA. Mathematical modelling and simulation of multiphase flow in a flat plate solar energy collector. Energy Convers Manage 2015;106:139–50.
[28] Bao J, Zhao L. A review of working fluid and expander selections for organic Rankine cycle. Renew Sustain Energy Rev 2013;24:325–42.
[29] Husband W, Beyene A. Low-grade heat-driven Rankine cycle, a feasibility study. Int J Energy Res 2008;32:1373–82.
[30] Tsai W-T. Environmental risk assessment of hydrofluoroethers (HFEs). J Hazard Mater 2005;119:69–78.
[31] Sekiya A, Misaki S. The potential of hydrofluoroethers to replace CFCs, HCFCs and PFCs. J Fluorine Chem 2000;101:215–21.
[32] Qiu G, Shao Y, Li J, Liu H, Riffat SB. Experimental investigation of a biomass-fired ORC-based micro-CHP for domestic applications. Fuel 2012;96:374–82.
[33] Jradi M, Li J, Liu H, Riffat S. Micro-scale ORC-based combined heat and power system using a novel scroll expander. Int J Low-Carbon Technol 2014:ctu012.
[34] Baral S, Kim KC. Thermodynamic modeling of the solar organic Rankine cycle with selected organic working fluids for cogeneration. Distrib Gener Altern Energy J 2014;29:7–34.
[35] Wang Z, Zhou N, Guo J, Wang X. Fluid selection and parametric optimization of organic Rankine cycle using low temperature waste heat. Energy 2012;40:107–15.
[36] Lemmon E, Huber M, McLinden M. NIST reference database 23: reference fluid thermodynamic and transport properties-REFPROP, version 9.1. Standard Reference Data Program; 2013.
[37] Liu H, Qiu G, Shao Y, Daminabo F, Riffat SB. Preliminary experimental investigations of a biomass-fired micro-scale CHP with organic Rankine cycle. Int J Low-Carbon Technol 2010:ctq005.
[38] Quoilin S. Experimental study and modeling of a low temperature Rankine cycle for small scale cogeneration. University of Liege; 2007.
[39] Li Y, Wang R, Wu J, Xu Y. Experimental performance analysis on a direct-expansion solar-assisted heat pump water heater. Appl Therm Eng 2007;27:2858–68.
[40] Bejan A. Advanced engineering thermodynamics, 1997. New York: Interscience; 1996.
[41] Cengel YA, Boles MA, Kanoğlu M. Thermodynamics: an engineering approach. New York: McGraw-Hill; 2002.
[42] Dikici A, Akbulut A. Performance characteristics and energy–exergy analysis of solar-assisted heat pump system. Build Environ 2008;43:1961–72.

Paper II

Energy Conversion and Management 106 (2015) 139–150

Contents lists available at ScienceDirect

Energy Conversion and Management

journal homepage: www.elsevier.com/locate/enconman

Mathematical modelling and simulation of multiphase flow in a flat plate solar energy collector

H.U. Helvaci *, Z.A. Khan

Bournemouth University, Sustainable Design Research Centre (SDRC), Faculty of Science and Technology, Bournemouth BH12 5BB, UK

ARTICLE INFO

Article history:
Received 26 May 2015
Accepted 10 September 2015

Keywords:
Flat plate collector
Simulation
Multiphase flow
Heat transfer coefficient

ABSTRACT

Non-conventional collectors where organic fluid or refrigerant experience a phase change have many advantages over conventional collectors which have either air or relatively high temperature boiling liquid. Increase in heat transfer coefficient and system efficiency, corrosion prevention and freeze protection are the main benefits of the first type. In this study, a detailed numerical model of a flat plate collector is developed to investigate the fluid mean temperature, useful heat gain and heat transfer coefficient along the collector tube. The refrigerant HFC-134a was used in the simulation as the working fluid of the collector. The model can both predict the location where the fluid undergoes a phase change in the tube and the state at the exit under given inlet conditions. The effect of boiling on the heat transfer coefficient of the fluid is also investigated. Simulations were performed at three different mass flow rates (0.001, 0.005 and 0.01 kg/s) and three different operating pressures (4, 6 and 8 bar) to be able to see the effect of mass flow rate and pressure on plate temperature, heat loss coefficient, efficiency of the collector and the heat transfer coefficient of the fluid. The simulation results indicate that the heat transfer coefficient of the fluid increases from 153.54 $W/m^2 K$ to 610.27 $W/m^2 K$ in multiphase flow region. In the liquid single phase region, the collector efficiency rises from 60.2% to 68.8% and the heat transfer coefficient of the fluid increases from 39.24 $W/m^2 K$ to 392.31 $W/m^2 K$ with an increased flow rate whereas the collector efficiency decreases from 72.5% to 62.3% as the operating pressure increases from 4 bar to 8 bar. In order to validate the simulation model an experimental test rig was built and the experiments were performed with HFE 7000 as working thermo-fluid. A new simulation model utilizing HFE 7000 has been developed and the outlet temperature of the fluid was compared with the measured outlet temperature. Both measured and simulated results have shown close conformity.

1. Introduction

Utilization of fossil fuels has caused many problems such as the release of CO_2 to the atmosphere and its subsequent effects on our environment. This can be changed if our dependence is decreased on fossil fuels by using alternative renewable energy sources [1]. Due to its lower impacts on environment solar energy can be considered as one of the most favourable option to contribute to the energy demand with extensive applications in industry [2]. There has been an upward trend in various kinds of solar energy harvesting systems. A dynamic model of a solar pond was developed in order to investigate the effect of the sunny area ratios on the efficiency by [3]. Experimental and simulation studies on the thermal performance of a room heated with an attached sunspace were conducted by [4]. The thermal behaviour of volumetric solar receiver with double-layer of porous media and the effects of geometry of each layer on the performance was numerically studied by [5]. Dehghan et al. [6] analysed the effect of radiation heat transfer on forced convective heat transfer mechanism through cellular porous media confined by two parallel plates. The plates subjected to constant heat flux and the Darcy–Brinkman equation was utilized to model the flow through the porous medium [6]. In another study the effects of thermal radiation on the forced convection through cellular porous media considering a combined conductive–convective–radiation heat transfer model were studied by [7].

Solar collectors which convert solar energy into heat produce either hot water or air depending on the working fluid of the collector [8]. Recently, many studies have focused on increasing the efficiency of solar water heaters. An experimental study to investigate the effect of using a mixture of ethylene glycol and copper nanoparticles as a working fluid on the collector efficiency was conducted by [9]. In another study it is reported that using

* Corresponding author at: Faculty of Science and Technology, Fern Barrow, Talbot Campus, Bournemouth University, Poole, Dorset BH12 5BB, UK. Tel.: +44 7473 770009.
E-mail address: hhelvaci@bournemouth.ac.uk (H.U. Helvaci).

http://dx.doi.org/10.1016/j.enconman.2015.09.028
0196-8904/

Nomenclature

A_p	collector plate area, m^2
Bo	boiling number
C_b	bond conductance
C_p	specific heat of the working fluid, J/kg K
Co	convection number
D	tube diameter, m
D_i	tube inner diameter, m
D_o	tube outer diameter, m
f	friction factor
F	fin efficiency
F_R	collector heat removal factor
Fr	Froude number
G	mass flux, kg/m^2 s
h	heat transfer coefficient, W/m^2 K
H	enthalpy, J/kg
H_{fg}	heat of vaporization, J/kg
k	thermal conductivity, W/m K
L	Length, m
$\dot{m}$	mass flow rate, kg/s
N	dimensionless parameter
N_c	number of glass cover
Nu	Nusselt number
P	pressure, bar
Pr	Prandtl number
Q_{gain}	heat gain of the fluid, W
Q_l	heat loss, W
Q_u	useful heat, W
Q''_u	useful heat rate, W/m^2
Re	Reynolds number
S_{in}	incoming solar radiation, W/m^2
T	temperature, K
U_{back}	heat loss coefficient for the back of the collector, W/m^2 K
U_{edge}	heat loss coefficient for the edge of the collector, W/m^2 K
U_{top}	heat loss coefficient for the top of the collector, W/m^2 K
U_T	total heat loss coefficient of the collector, W/m^2 K
W	tube spacing, m
x	vapour quality

Subscripts

a	ambient
c	glass cover
col	collector
cb	convective boiling
f	fluid
g	gas
in	inlet
ins	insolation
l	liquid
m	mean
mp	multiphase
nb	nucleate boiling
out	outlet
p	plate
sat	saturation
sp	single phase
w	wind
wf	working fluid

Greek symbols

$\tau\alpha$	transmittance-absorbance product
β	collector tilt angle, °
δ	absorber plate thickness, m
ε	emissivity
ρ	density, kg/m^3
σ	Stefan–Boltzmann constant, $W/m^2 K^4$
ψ	enhancement factor
μ	dynamic viscosity, kg/m s
Φ	heat flux, W/m^2
η	efficiency, %

Al_2O_3-distillated water nanofluid in the collector increased the thermal efficiency up to 11.7% [10].

Alternatively, collectors using organic fluid or refrigerant provide higher performance than conventional collectors where water or air is used. Because organic fluid or refrigerant undergoes a phase change, this phenomenon increases the heat transfer coefficient of the fluid and leads to an increase in the system performance [11]. Reduced parasitic energy use and freeze protection are the other benefits of such collectors [12].

Collectors using organic fluid or refrigerant can be used for further applications. Evacuated solar collector was used to generate vapour in the solar Rankine system where CO_2 was utilized as the working fluid [13]. Marion et al. [14] conducted both theoretical and experimental studies to indicate the potential mechanical energy generation by using solar thermal collectors which are combined with an organic Rankine cycle (ORC). The system was simulated for three organic fluids R134a, R227ea and R365mfc and the simulation model was validated against experiments using glycol–water mixture [14]. An optimization study of a solar organic Rankine cycle was conducted by [15]. In this study authors considered various models of stationary solar collectors such as a flat-plate collector, compound parabolic collector, and evacuated tube collector. Twelve substances, including dry, wet and isentropic organic fluids were taken into account as working fluids of the system and aperture area of the collector needed per unit of mechanical power output of the cycle was considered as a comparison criteria for different operating conditions of ORC [15]. Wang et al. [16] carried out an experimental study of a low-temperature solar Rankine cycle system where flat plate collectors are used. Pure R245fa, zeotropic mixture of R245fa/R152a (0.9/0.1) and another mixture of R245fa/R152a, (0.7/0.3) were considered in the analyses [16]. An experimental study of a solar thermal system utilizing R245fa was conducted by [17]. Two stationary collectors which are evacuated tube and flat-plate collector were used in the experiments. Results showed that collector efficiencies of evacuated tube and solar collector were found 71.6% and 55.2% respectively [17].

Solar collectors using organic refrigerants also have been utilized in solar assisted heat pump systems. The thermal performance of direct expansion solar assisted heat pump system using two collector configurations which are bare collector and one cover collector were analysed in [18]. Several refrigerants were used to analyse the performance of the system. Authors reported that R-12 gives the highest performance value, followed by R-22 and R-134a [18]. Zhang et al. [19] studied the effects of refrigerant charge, solar collector area and solar collector thickness on the thermal performance of direct-expansion solar assisted heat pump system [19]. Solar assisted heat pump system for low temperature water heating application where solar collector is used as the evaporator of the heat pump was investigated by [20]. A simulation model in order to show the potential use of solar assisted heat pump system for hot water production was conducted by [21]. Authors found that the system can achieve a higher performance than conventional heat pump system [21].

Furthermore, various studies have been conducted to analyse solar collectors theoretically where the fluid undergoes a phase change.

An extended mathematical model of a boiling flat plate collector in which fluid and plate temperatures, heat transfer coefficient and vapour quality can be predicted along the collector tube was developed by [11]. Various organic fluids (R-113, n-pentane, methanol, acetone, diethyl ether) and water as a working fluid were used and the effect of transition from single phase flow to the boiling flow was taken into account in the study [11]. Results showed that no matter what working fluid was used, a higher thermal efficiency was obtained in a boiling flow as compared to single phase flow in the collector. Analysis of the boiling collector was studied by [12] where operating characteristics of condenser were also considered in their analysis. The refrigerant R-11 was utilized in a two-phase collector which operates in a thermo syphon mode. TRNSYS simulation program was used for modelling the boiling collector-condenser system which also accounted for heat losses and pressure drops in the vapour and liquid line [12].

Aziz et al. [22], conducted a numerical analysis of a solar collector which was employed as an evaporator of a heat pump cycle. In order to evaluate the size of a solar collector multiphase flow of (R-123–R134a) mixture is analysed, thermodynamic and heat transfer characteristics were calculated. The effect of various mass flow rate of the mixture, solar radiation and inlet pressure on the heat transfer coefficient and collector tube length was also taken into account. Authors concluded that both mass flow rate and solar radiation have important effects on the collector size and heat transfer coefficient of the mixture where operating pressure does not have any significant effect on the tube length of collector [22].

R134a is a hydrofluorocarbon (HFC) refrigerant and has been of interest to Sustainable Design Research Centre (SDRC), Bournemouth University in terms of industrial applications [23,24].

In this study, a detailed numerical model of a flat plate collector is developed to investigate mean temperature, useful heat gain and heat transfer coefficient of HFC-134a along the collector tube. The model can predict both the location where the fluid undergoes a phase change in the tube and the fluid exit state. The effect of mass flow rate of the fluid and operating pressure on the collector efficiency, outlet fluid temperature, absorber plate temperature and heat transfer coefficient of the fluid is also investigated. Furthermore, the model was utilized with novel-thermo fluid (HFE 7000) in order to compare the collector performance between two working fluids. Also, simulation results using HFE 7000 was validated against experimental results.

2. Collector specifications

Serpentine type flat plate collector was used to conduct this simulation and it consists of a cover, absorber, copper tube and insulation at the backend and edges of the collector. Cover (1) with 3 mm thick is used for reducing both radiation and convection loss from the collector. Absorber (2) is a coated stainless steel sheet, of which surface has dark-coloured paint for high absorption property. The thickness of the absorber plate is 1 mm. The fluid is circulated in the copper tubes (3) where the heat is gained from the absorber to the fluid. Conduction loss from the backend and edges of the collector is reduced by insulation (4). The schematic description of the collector is shown in Fig. 1.

3. Mathematical modelling

Developed analytical model of serpentine flat plate collector under a phase change is based on the model represented by [25]. The model is modified and used under following assumptions:

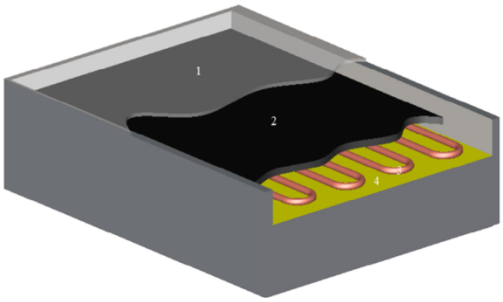

Fig. 1. Schematic of serpentine tube flat plate collector.

- Steady-state conditions.
- Absorber and glass cover thermal and radiation properties are constant (independent of temperature).
- Uniform heat flux conditions are granted instead of uniform wall temperature.
- Entry regions effects are neglected (L_{tube}/D = 7000).
- The fluid undergoes a phase-change as the average fluid temperature reaches the boiling temperature of the fluid at corresponding pressure.
- Both single and multiphase heat transfer coefficient of the fluid varies along the tube.
- Serpentine tube considered as one flat tube to calculate heat transfer coefficients for both single and multiphase flows.

3.1. Heat loss calculation

There are mainly two types of losses occur in a flat plate collector which are optical and thermal losses, respectively. Optical losses can be shown as S_{in} $(\tau\alpha)$, where $(\tau\alpha)$ is the transmittance-absorbance of the glass cover depending on the material properties. Thermal losses can be divided into three parts which are heat loss from the top of the collector U_{top}, from the back U_{back} and the edge of the collector U_{edge} respectively. During the calculations heat loss through the edges has been ignored. Heat loss from the top of the collector can take place by means of radiation and convection heat transfer mechanism from the glass cover to the atmosphere and from the absorber plate to the cover. Klein [26] generalized formula to calculate the top heat loss coefficient which is shown in Eq. (1).

$$U_{top} = \left(\frac{N_c}{\frac{C}{T_p}\left[\frac{T_p - T_a}{N_c + f}\right]^e} + \frac{1}{h_w} \right)^{-1} + \frac{\sigma (T_p + T_a)\left(T_p^2 + T_a^2\right)}{\left(\varepsilon_p + 0.00591 N_c h_w\right)^{-1} + \frac{2N_c + f - 1 + 0.133\varepsilon_p}{\varepsilon_c} - N_c} \quad (1)$$

where

$$f = (1 + 0.0889 h_w - 0.1166 h_w \varepsilon_p)(1 + 0.07866 N_c)$$

$$C = 520(1 - 0.000051\beta^2) \quad \text{for } 0^\circ < \beta < 70^\circ \text{ and if } 70^\circ < \beta < 90^\circ \text{ apply } \beta = 70^\circ$$

$$e = 0.430(1 - 100/T_p)$$

Heat losses from the back of the collector is

$$U_{back} = \frac{k_{ins}}{L_{ins}} \quad (2)$$

Therefore, total heat loss coefficient of the collector becomes

$$U_T = U_{top} + U_{back} \quad (3)$$

Absorbed solar energy on the surface of the plate can be written as

$$Q_p = A_p S_{in}(\tau\alpha) - Q_l \quad (4)$$

When plate temperature (T_p) and heat loss coefficient (U_T) are taken into account, then the absorbed solar energy on the plate surface can be calculated as;

$$Q_p = A_p\left[S_{in}(\tau\alpha) - U_T(T_p - T_a)\right] \quad (5)$$

3.2. Convective heat transfer to the fluid

Since there is incident solar energy on the absorber of the collector some portions of that will be transferred to the fluid by convection along the collector tube. This energy is called the useful energy and can be expressed as:

$$Q_u = A_p F_R\left[S_{in}(\tau\alpha) - U_T(T_{f,in} - T_a)\right] \quad (6)$$

In Eq. (6), T_p is replaced by fluid inlet temperature $T_{f,in}$ and the new term F_R which is heat removal factor is introduced and is found to be as below;

$$F_R = \frac{\dot{m}C_p}{A_p U_T}\left[1 - \exp\left(\frac{-A_p U_T F'}{\dot{m}C_p}\right)\right] \quad (7)$$

(F') is the collector efficiency factor and can be expressed as;

$$F' = \frac{(U_T)^{-1}}{W[U_T(D_o + (W - D_o)F)]^{-1} + (C_b)^{-1} + (\pi D_i h_f)^{-1}} \quad (8)$$

where C_b represents the bond conductance and it can be neglected ($1/C_b = 0$) as it is assumed to be very large.

And F is the fin efficiency is

$$F = \frac{\tanh[m(W - D_o/2)]}{m(W - D_o/2)}, \text{ where } m = \sqrt{\frac{U_T}{k\delta}} \quad (9)$$

In Eq. (8), h_f represents the convective heat transfer coefficient for both single and multi-phase conditions. The determination of heat transfer coefficient in single and multiphase flows is analysed in the following section.

3.2.1. Single-phase flow

For constant surface heat flux and fully developed single-phase laminar flow ($Re < 2300$) in a circular tube, Nusselt (Nu) number is constant and independent from Reynolds (Re) and Prandtl (Pr) numbers [27].

$$Nu = \frac{h_{sp}D}{k_{sp}} = 4.36 \quad (10)$$

For fully developed turbulent flow where $0.5 < Pr < 2000$ and $3 \times 10^3 < Re < 5 \times 10^6$ in a circular tube, Nusselt number can be obtained by Gnielinski equation which is a modification of Petukhov correlation [28].

$$Nu = \frac{\left(\frac{f}{8}\right)(Re - 1000)Pr}{1 + 12.7\left(\frac{f}{8}\right)^{0.5}(Pr^{2/3} - 1)} \quad (11)$$

3.2.2. Multiphase flow

A large number of theoretical and experimental studies have been conducted to calculate saturated flow boiling coefficient since it is important to reduce cost and gain better design of evaporators, boilers and other multiphase process components [29]. Among many studies a general and reliable correlation was investigated by [30]. However, it was limited to vertical flows. Another correlation which is valid for both horizontal and vertical flows was generated by [31]. In this study, the chart correlation for the estimation of saturated boiling heat transfer coefficient that includes a comparison with 800 data points from 18 experimental studies is represented. Due to the difficulties of graphical form of correlations researchers have presented equations which express these chart correlations [32].

Following the Shah's method the procedure to calculate two-phase heat transfer coefficient is represented in this section. The correlations mainly consist of four dimensionless parameters in order to estimate heat transfer coefficient. The Froude number is given by the following equation [31];

$$Fr_l = \frac{G^2}{\rho_l^2 g D_i} \quad (12)$$

Froude number is calculated to determine if the surface is fully wet or not. For vertical tubes the surface is fully wet independently of Froude number. However, for horizontal tubes if $Fr_l > 0.04$ the surface is fully wet otherwise ($Fr_l < 0.04$) the surface is partly dry. Once Froude number is determined then the dimensionless parameter N can be calculated for two different conditions;

3.2.3. Vertical and horizontal tubes

For vertical tubes at all conditions of Fr_l values and for horizontal tubes when $Fr_l > 0.04$ dimensionless parameter (N) equals to the convection number (Co).

3.2.4. Horizontal tubes

For horizontal tubes when $Fr_l < 0.04$, then the following relation is applicable.

$$N = 0.38 Fr_l^{-0.3}\text{Co} \quad (13)$$

The next dimensionless parameter is the convection number (Co) and this can be calculated as [31];

$$\text{Co} = \left(\frac{1}{x} - 1\right)^{0.8}\left(\frac{\rho_g}{\rho_l}\right)^{0.5} \quad (14)$$

Another parameter is the enhancement factor (ψ) and it represents the ratio of multiphase flow heat transfer coefficient (h_{mp}) to the liquid phase heat transfer coefficient (h_l). Dittus–Boelter equation is used to calculate liquid phase heat transfer coefficient in this analysis [31].

Then, the calculation is followed by the evaluation of both nucleate and convective boiling factor. For the calculation of nucleate boiling factor three applicability conditions of the dimensionless number (N) are represented below [33];

For $N > 1$

$$\psi_{nb} = 230\text{Bo}^{0.5} \quad \text{If Bo} > 0.3 \times 10^{-4}$$

$$\psi_{nb} = 1 + 46\text{Bo}^{0.5} \quad \text{If Bo} < 0.3 \times 10^{-4}$$

ψ_{nb} and Bo represents nucleate boiling factor and boiling number respectively. Bo is calculated as [31];

$$\text{Bo} = \frac{\Phi}{GH_{fg}} \quad (15)$$

where Φ is the heat flux, G is the mass flux and H_{fg} represents heat of vaporization.

Convective boiling factor ψ_{cb} is given by the following Eq. (16).

$$\psi_{cb} = 1.8N^{-0.8} \quad (16)$$

As both nucleate boiling factor ψ_{nb} and convective boiling factor ψ_{cb} are calculated, the larger value is taken as enhancement factor and is used to calculate multi phase heat transfer coefficient (h_{tmp}).

For $0.1 < N < 1$

$$\psi_{nb} = F\mathrm{Bo}^{0.5}\exp(2.74N^{-0.1}) \quad (17)$$

ψ_{cb} is determined from Eq. (16) and ψ equals to the larger value of ψ_{nb} or ψ_{cb}.

For $N < 0.1$

$$\psi_{nb} = F\mathrm{Bo}^{0.5}\exp(2.47N^{-0.15}) \quad (18)$$

ψ_{cb} is evaluated from Eq. (16) and ψ equals to the larger value of ψ_{nb} or ψ_{cb} .

The constant F is as follows [33];

Bo > 0.0011, F = 14.7.
Bo < 0.0011, F = 15.43.

4. Iteration procedure

During the research a numerical model is developed to simulate flat plate collector performance, fluid temperature and heat transfer coefficient along the tube. Collector specifications and operating parameters are shown in Tables 1 and 2.

Basically, the model relies on dividing the collector tube into small finite elements and calculating the fluid outlet temperature, plate temperature, the heat loss coefficient, the useful heat, the heat gain and the enthalpy values iteratively. As shown in Fig. 2 for each element the outlet temperature and enthalpy values are set equal to the inlet conditions of the next element till the end of the last element.

Initially, the model starts with calculating the heat loss coefficient by using Eq. (1). As it can be seen from Eq. (1) plate temperature (T_p) is necessary to determine the heat loss coefficient (U_T). Since T_p is an unknown an arbitrary value which is estimated as 5 °C higher than inlet fluid temperature is given in order to calculate U_T. Then, the model evaluates useful heat (Q_u) by introducing the calculated U_T into Eq. (6). In order to determine heat transfer coefficient, the fluid flow is defined whether it is laminar or turbulence by calculating Reynolds (Re) number. Depending on the flow type, Nusselt (Nu) number is determined and heat transfer coefficient is calculated by using Eqs. (10) and (11). Fluid thermodynamic properties such as saturation temperature (T_{sat}), thermal conductivity (k), density (ρ), specific heat (Cp), viscosity (μ) and enthalpy (H) are calculated by developed regression equations. Data for the regression analysis is taken from REFPROP 9.1 programme [34] for various temperature values. Desired properties of the fluid are estimated by introducing fluid mean temperature into the regression equations. The estimated plate temperature is used to determine initial fluid mean temperature as the outlet temperature of the fluid is not known. Initial fluid mean temperature is defined as;

$$T_{f,m} = \frac{T_p + T_{f,in}}{2} \quad (19)$$

However, calculated Q_u represents the amount of useful heat for the whole collector tube. This can be represented by Eq. (20).

$$Q_u = Q_u'' \pi D_{in} L_{tube} \quad (20)$$

where Q_u'' is the useful heat rate and πD_{in} is the surface perimeter. In other words, the useful heat rate can be obtained by dividing useful heat (Q_u) by the surface area of the collector ($\pi D_{in} L_{tube}$). To calculate heat gain for each small element the rate of useful heat is multiplied by the surface perimeter and the length of each element which is defined previously by dividing total collector length into small finite elements. Therefore, heat gain of each element can be evaluated by;

$$Q_{gain} = Q_u'' \pi D_{in} \int_0^L dx \quad (21)$$

Once the heat gain is evaluated for the first element the fluid outlet temperature is calculated by introducing Q_{gain} into Eq. (22).

$$T_{f,out} = T_{f,in} + \frac{Q_{gain}}{\dot{m} C_p} \quad (22)$$

Calculated fluid outlet temperature $T_{f,out}$ is introduced into Eq. (23) to determine new fluid mean temperature. The new mean fluid temperature can be determined as;

$$T_{f,m} = \frac{T_{f,in} + T_{f,out}}{2} \quad (23)$$

The new mean temperature calculated by Eq. (23), is used for determining the new Q_u. After calculating the new Q_u, a new plate temperature is calculated as;

$$T_p = T_{f,in} + \frac{Q_u / A_p}{F_R U_T}(1 - F_R) \quad (24)$$

Then, the algorithm re-evaluates U_T, Q_u and Q_{gain} by utilizing the new plate temperature and the new fluid mean temperature in Eqs. (3), (6) and (21). This process is repeated in the first loop until the difference between T_p and its value in the previous iteration and T_{out} and its value in the previous iteration is lower than convergence criteria. Convergence criterion of 0.01 °C was selected for the iterated indicators mentioned above and the results converge within 10 iterations.

Second loop checks if the outlet temperature of the element reaches the saturation temperature of the fluid at corresponding pressure. If the exit temperature does not provide saturation conditions then algorithm increases the number of element. In other words, the length of the tube is increased and the same calculations are performed for the next element. Once the outlet temperature reaches the saturation temperature then flow boiling occurs in the collector tube. In the flow boiling calculations same steps are followed with the exception of calculating single phase heat transfer coefficient, multiphase heat transfer coefficient is calculated. Since the fluid temperature is constant in boiling outlet enthalpy is determined as;

$$H_{f,out} = H_{f,in} + \frac{Q_{gain}}{\dot{m}} \quad (25)$$

Table 1
Collector specifications.

Collector area (m^2)	6.96
Absorber plate thermal conductivity (W/m K)	50
Absorber plate thickness (m)	0.001
Total length of tube (m)	56
Tube inner diameter (m)	0.008
Tube outer diameter (m)	0.01
Effective transmittance–absorbance product (–)	0.81

Table 2
System parameters.

Fluid inlet temperature (K)	278
Fluid mass flow rate (kg/s)	0.001–0.005–0.01
Ambient temperature (K)	275
Operating pressure (bar)	4–6–8
Incoming solar radiation (W/m^2)	500
Wind velocity (m/s)	2

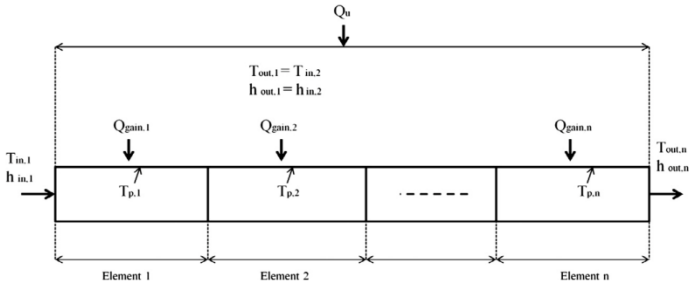

Fig. 2. Schematic of collector elements.

In boiling region vapour quality of the fluid is calculated at each element using Eq. (26).

$$x = \frac{H_{f,out} - H_l}{H_g - H_l} \tag{26}$$

where H_l and H_g represent saturated liquid and saturated vapour enthalpy of the fluid, respectively. The third loop also checks if the vapour quality reaches 1 at the end of each element. Multiphase flow calculations continue with the increase of elements since the fluid become superheated vapour ($x > 1$). At this point same calculations are performed with the single phase heat transfer coefficient which was mentioned above. The only difference is superheated vapour properties of the fluid are determined and used in the calculations.

A computer code is developed via Matlab software to perform iterative computations. Flowchart of the computer code is represented in Fig. 3.

5. Results and discussion

The simulation study is conducted with HFC-134a and its transport and thermodynamic properties can be found in [34]. Fig. 4 shows that the fluid enters to the collector at 5 °C temperature and 6 bar pressure. Its mean temperature increases along the col-

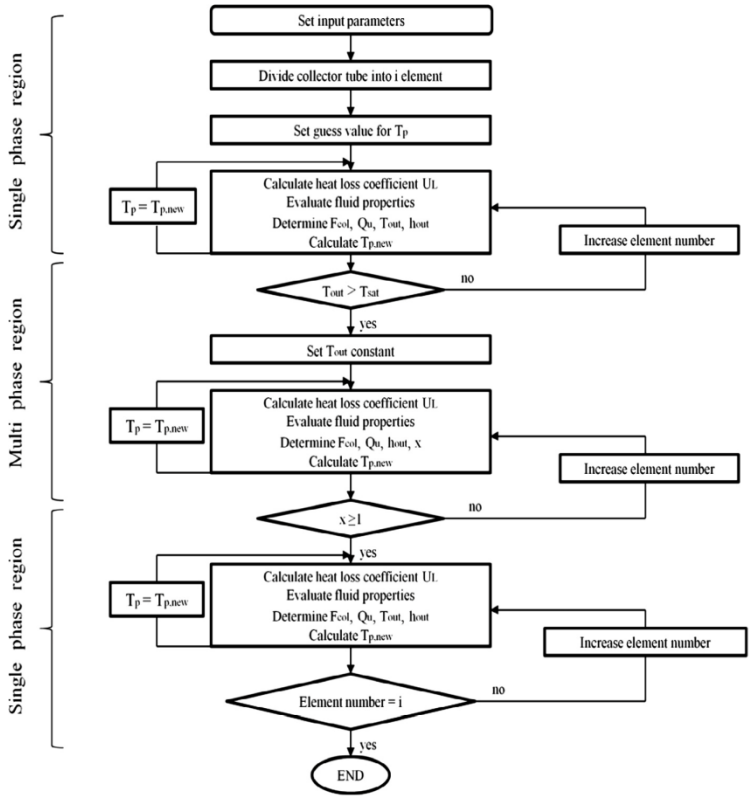

Fig. 3. Flow chart of the simulation study.

lector tube as the useful heat gain of the fluid raises. The increment in fluid mean temperature continues until it reaches the corresponding boiling temperature (22.2 °C). This region is called liquid single-phase flow which corresponds to 29% of total length of the collector tube. If the fluid reaches its saturation point, the fluid mean temperature remains constant and the fluid undergoes a phase-change. The region where saturated liquid turns into saturated vapour indicates multiphase flow or flow boiling. Boiling region occupies 58% of the tube. The heat gain of the fluid also increases during the flow boiling and this heat is used to generate vapour in the tube. Once the liquid completely turns into saturated vapour where the vapour quality equals to 1 represents the end of the boiling region. As the fluid continues gaining the heat its temperature increases again along the collector tube. This region is called vapour single-phase flow in which saturated vapour turns into superheated vapour. This phenomena proceeds till the end of the collector tube. The fluid temperature reaches 26.3 °C at the end of the tube and leaves the collector as a superheated vapour.

Fig. 5 represents the convective heat transfer coefficient of HFC-134a in both single-phase (liquid and vapour) and multiphase flows. In the liquid single phase region, the heat transfer coefficient ranged from 153.54 W/m^2 K to 173.93 W/m^2 K where as it changed from 375.2 W/m^2 K to 416.66 W/m^2 K in multiphase region. This indicates that in flow boiling the heat transfer coefficient is considerably higher than in single-phase region. Fig. 5 is generally in agreement with the studies [11,12]. In superheated vapour region, the heat transfer coefficient decreased to 73.4 W/m^2 K and remained almost constant.

The variation of flow boiling heat transfer coefficient versus vapour quality is shown in Fig. 6. Heat transfer coefficient increases from 375.2 W/m^2 K to 498.23 W/m^2 K as the vapour quality increases. The maximum heat transfer coefficient (610.27 W/m^2 K) is observed at a quality of $x = 0.8$ then it decreased gradually to 498.23 W/m^2 K.

This could be explained by the occurrence of dry out which results in a decrease in the heat transfer coefficient due to the low conductivity of dry steam [35]. Fig. 7 indicates that at constant pressure (6 bars), liquid single phase heat transfer coefficient and useful heat gain of the fluid increases with the increasing mass flow rate.

As the mass flow rate increases from 0.001 kg/s to 0.01 kg/s heat transfer coefficient and heat gain of the fluid increases from 39.24 W/m^2 K to 392.31 W/m^2 K and from 61.17 W to 535.13 W respectively. An increase in mass flow rate yields to a rise in Reynolds number, in other words a transition from laminar flow to turbulent flow in collector tubes. This results in a greater value of heat transfer coefficient and more heat which transferred to the working fluid. Instead of conventional fluid temperature absorber temperature is considered to develop efficiency equation for the collector. Collector efficiency η_{col} can be determined as follows:

$$\eta_{col} = \frac{Q_p}{S_{in}A_p} = \frac{A_p\left[S_{in}(\tau\alpha) - U_T(T_p - T_a)\right]}{S_{in}A_p} \quad (27)$$

It can be seen from Fig. 8 that the collector efficiency increases from 60.2% to 68.8% while absorber plate temperature decreases from 45.53 °C to 29.7 °C. This phenomenon indicates that the more heat is gained by the fluid the more heat which is absorbed on the absorber plate is transferred to the fluid. Increase in heat transfer from the absorber plate to the working fluid yields to a decrease

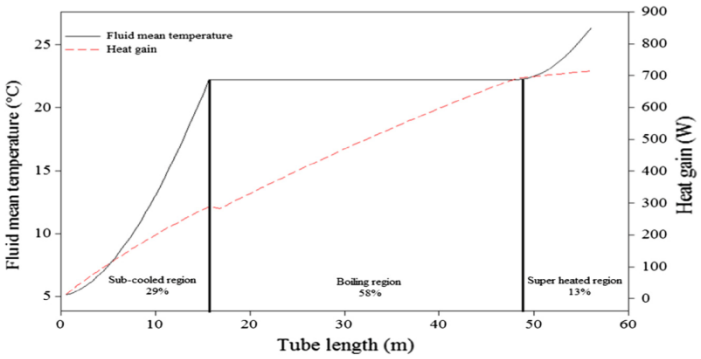

Fig. 4. Fluid mean temperature and heat gain variation along the collector tube ($P = 6$ bar, $m = 0.005$ kg/s).

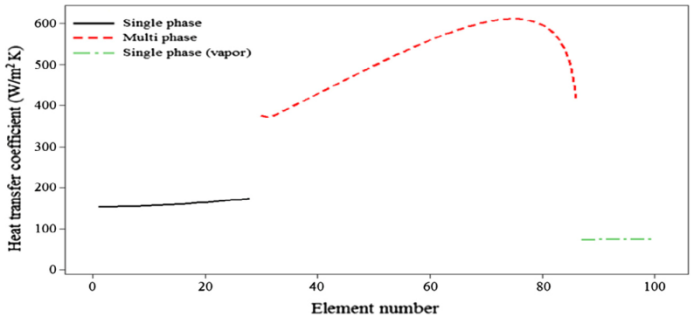

Fig. 5. Fluid heat transfer coefficient in various flow regions ($P = 6$ bar, $m = 0.005$ kg/s).

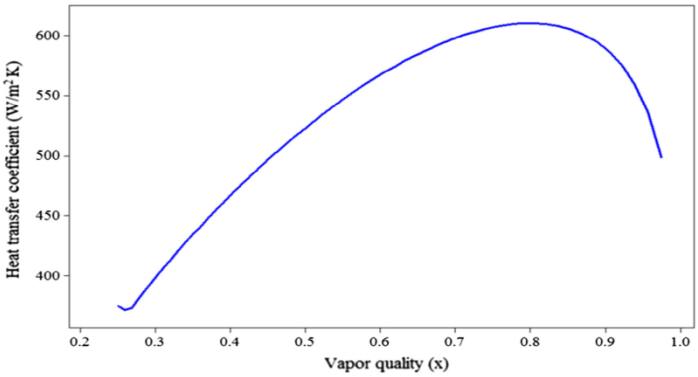

Fig. 6. Boiling heat transfer coefficient versus vapour quality (P = 6 bar, m = 0.005 kg/s).

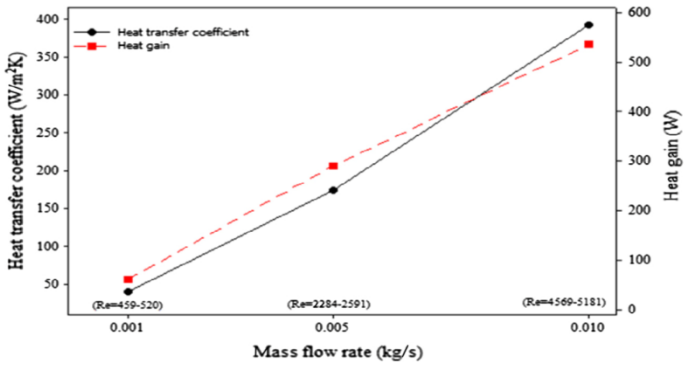

Fig. 7. Heat transfer coefficient and heat gain at various mass flow rates (P = 6 bar).

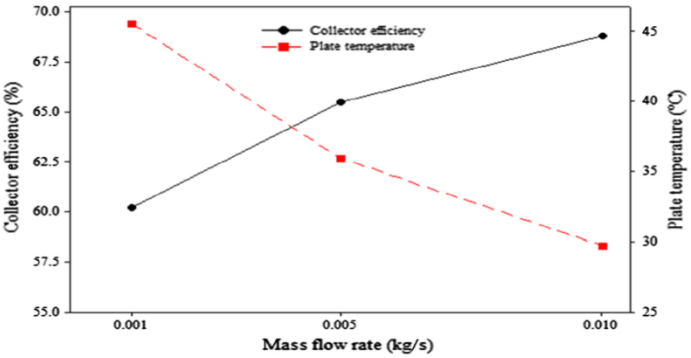

Fig. 8. Collector efficiency and plate temperature at various mass flow rates (P = 6 bar).

in the absorber plate temperature which brings less heat loss from the collector plate to the surroundings. As a result higher collector efficiency value is observed.

Fig. 9 represents the effect of inlet pressure of the fluid on the plate temperature and collector efficiency at constant mass flow rate ($\dot{m} = 0.005$ kg/s).

It can be seen from Fig. 9 that saturation temperature increases from 9.6 °C to 31.9 °C as the operating pressure of the collector increases from 4 bars to 8 bars. At saturation temperature of 9.6 °C plate temperature is found 22.1 °C whereas plate temperature is found 41.8 °C at 31.9 °C saturation temperature. Moreover, a decrease in the collector efficiency from 72.5% to 62.3% is due

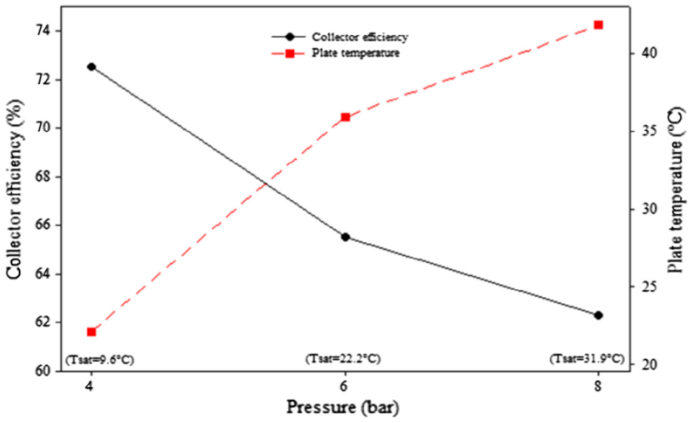

Fig. 9. Collector efficiency and plate temperature at various operating pressure (m = 0.005 kg/s).

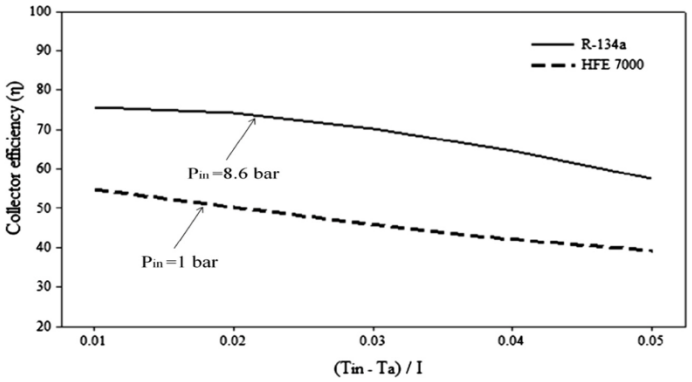

Fig. 10. Collector efficiency as a function of $(T_{in} - T_a)/I$ with R-134a and HFE-7000 for the same saturation temperature condition.

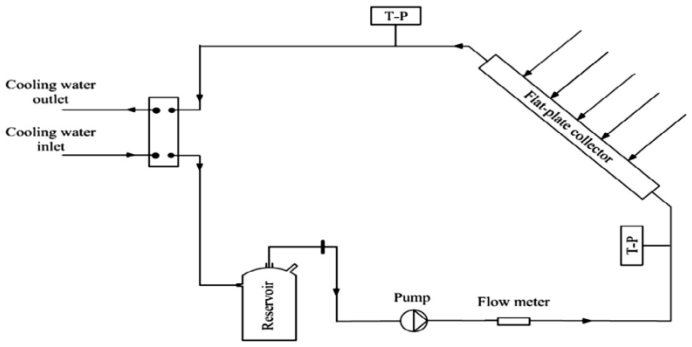

Fig. 11. Schematic of the experimental rest rig.

to the increase in the plate temperature and thus causes thermal loss from the collector.

In Fig. 10 the efficiency of the flat-plate collector using both R-134a and HFE-7000 versus reduced temperature $(T_{in} - T_a)/I$ is represented. In the analysis fluid saturation temperature for both fluids are 15 °C higher than the fluid inlet temperature at corresponding collector operating pressures. As it can be seen from Fig. 10 that for the same incident radiation (I = 500 W/m^2), mass flow rate ($\dot{m}$ = 0.005 kg/s) and inlet temperature (20 °C) R-134a gives higher collector performance than HFE-7000 in both

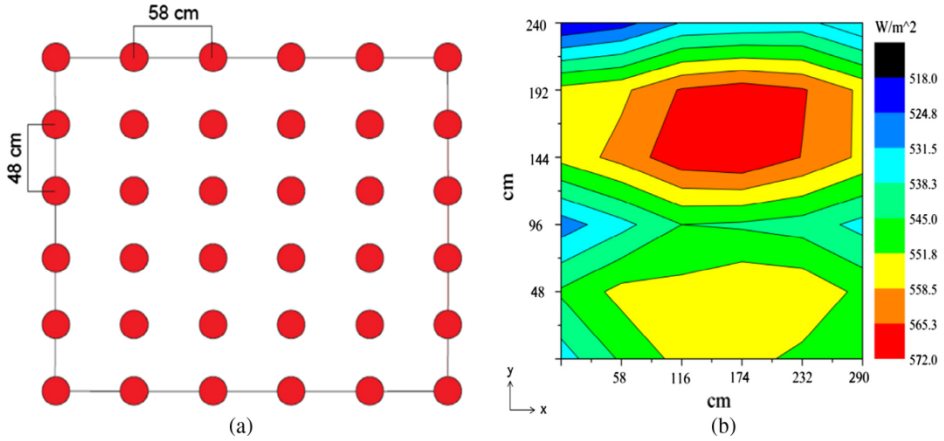

Fig. 12. (a) Measured points on the collector surface and (b) solar radiation distribution on the collector surface.

Table 3
Experimental conditions.

Parameter	Unit	Value
Collector inlet temperature	°C	28.4–47.9
Ambient temperature	°C	18
Collector inlet pressure	bar	1.4–2.1
Fluid mass flow rate	kg/s	0.012–0.013
Solar radiation	W/m^2	550

non-boiling and boiling region. This could be explained by relatively higher thermal conductivity of R-134a (k = 0.083 W/m K) than HFE-7000 (k = 0.0757 W/m K) at given conditions.

6. Experimental validation

In order to validate the proposed mathematical and numerical models an experimental test rig was designed and commissioned. The test rig consists of a flat plate collector, a circulation pump, a reservoir and a heat exchanger (Fig. 11).

The flat plate collector specifications are given in Table 1 previously. A solar simulator was employed as an artificial source of radiation to provide steady radiant energy to the collector. Solar simulator consists of 12 glare lamps and each lamp can provide 1 kW heat output. In the experiments 6 kW heat is supplied from the simulator to the collector. A pyranometer (Kipp&Zonen CMP3) was used to measure the irradiance on the collector surface. The solar simulator placed 2 m away from the collector surface during the measurements. Fig. 12(a) shows the measured points on the collector surface. It is found that the distributed heat flux ranged from 518 to 572 W/m^2 on the collector surface and the average irradiance over the collector surface (2.9×2.4 m) is 550 W/m^2 (Fig. 12(b)).

Although HFC 134a was used in the simulation study, in order to check the compatibility of the mathematical and the numerical models a novel working thermo-fluid (HFE 7000) was utilized in the experiment. The new simulation study using HFE 7000 was conducted and the fluid outlet temperature of the simulation was compared with the experimental data. The required thermodynamic and transport properties of HFE 7000 were taken from REFPROP 9.1 programme. Furthermore, HFE 7000 has a higher boiling point temperature (34 °C at 1 atm) than HFC 134a (−26 °C at 1 atm) and therefore it is easier to handle at atmospheric conditions. Initially 8 kg of HFE 7000 was charged in the system and it was compressed by the pump and sent to the collector. The absorbed heat which is converted from simulated solar radiation in the collector is transferred to the fluid via convective heat transfer mechanism. The fluid exits the collector with a higher temperature and reaches the heat exchanger. Some portion of its

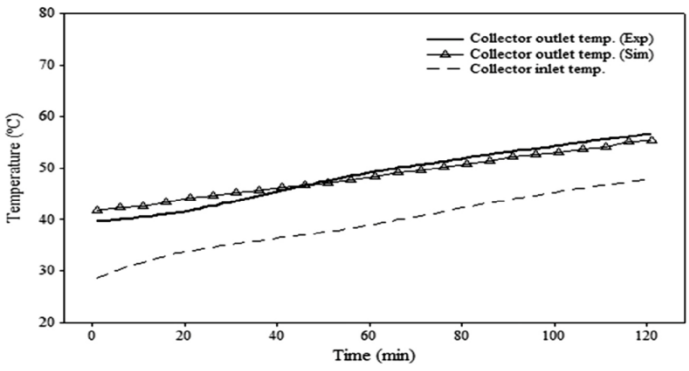

Fig. 13. Fluid temperatures at the inlet and outlet of the collector.

Table A.1
Measured parameters and their uncertainties.

Instruments	Measured parameters	Range	Uncertainty (%)
Thermocouples (°C)	Collector inlet temperature	0–100 (°C)	2.5
	Collector outlet temperature	0–100 (°C)	2
Pressure transmitters (bar)	Collector inlet pressure	0–10 (bar)	3.0
	Collector outlet pressure	0–10 (bar)	3.5
Flow meter (l/min)	Fluid flow rate	0.12–1.6 (l/min)	3.2

heat is rejected from the system and therefore its temperature decreases in the heat exchanger. Tap water is used to cool and condense the working fluid. The fluid is collected in the reservoir and is then compressed by the pump again to complete the cycle.

In order to measure temperature and pressure values of the fluid, K-type thermocouples with an accuracy of ±0.18% and pressure transmitters with an accuracy of ±0.5% are mounted at the inlet and outlet of the collector. A flow meter is placed 65 cm away from the pump to measure the volumetric flow rate of the fluid and the accuracy of the flow meter is ±2%. Temperature, pressure and flow rate data of the fluid are recorded and transmitted to a computer by a data acquisition unit. Table 3 represents the environmental and the inlet conditions of the experiment.

It can be seen from Fig. 13 that the model can predict the outlet temperature of the fluid with a small range of deviation. The deviation for the outlet temperature of the fluid between the simulation and the experimental results ranged from 0.45% to 4.9%.

7. Conclusions

A numerical model for the flat plate collector was developed to simulate the collector performance under various conditions. The derived algorithm can solve the model and can iteratively evaluate the fluid mean temperature, fluid heat gain, absorber temperature and the heat transfer coefficient of the fluid at any point along the flow direction. The model is capable of calculating single phase heat transfer coefficient, as well as the multiphase heat transfer coefficient of the fluid if its temperature surpasses its boiling temperature in the collector. The algorithm was implemented by utilizing the MATLAB programme. The model was solved with HFC-134a refrigerant. The simulation results showed that in the flow boiling region the heat transfer coefficient (375.2–416.6 W/m^2) is higher than in single phase liquid (153.54–173.93 W/m^2) and single phase vapour (73.4 W/m^2) regions. Effect of the mass flow rate and the pressure on the heat transfer coefficient, collector efficiency and heat gain of the fluid is also taken into account in the simulation study. It is found that heat transfer coefficient have shown a dependency on the flow rate of the flow. As the mass flow rate, as well as the Reynolds number of the flow increases, the flow becomes turbulent. In turbulent region higher heat transfer coefficient is obtained than laminar region which leads to an increase in the heat gain of the fluid and the efficiency of the collector. Analysis of the simulation results also showed that operating pressure, in other words saturation pressure of the fluid has an effect on the collector efficiency. In higher saturation pressure condition in the collector saturation temperature becomes further from the inlet fluid temperature and the efficiency of the collector decreases. Furthermore, the collector efficiency with two working fluids (R-134a and HFE-7000) is compared for the same inlet conditions. It is found that R-134a gives higher collector efficiency due to its superior properties compared to the HFE-7000 at given conditions. An experimental test rig was built in order to validate the simulation model against experimental results. HFE-7000 was utilized in the experiment and the simulation results for HFE-7000 show good agreement with the experimental results.

Acknowledgment

This research is funded by Future Energy Source (FES) Ltd, UK. The authors acknowledge in-kind support provided by Mr Brian Camfield and Mr Tony Camfield.

Appendix A. Uncertainty analysis

In order to evaluate the accuracy and the reliability of the measured parameters an uncertainty analysis is conducted. The measured instruments and their uncertainties are shown in Table A.1.

References

[1] Baharoon DA, Rahman HA, Omar WZW, Fadhl SO. Historical development of concentrating solar power technologies to generate clean electricity efficiently – a review. Renew Sustain Energy Rev 2015;41:996–1027.
[2] Villicana-Ortiz E, Gutierrez-Trashorras AJ, Paredes-Sanchez JP, Xiberta-Bernat J. Solar energy potential in the coastal zone of the Gulf of Mexico. Renewable Energy 2015;81:534–42.
[3] Bozkurt I, Karakilcik M. The effect of sunny area ratios on the thermal performance of solar ponds. Energy Convers Manage 2015;91:323–32.
[4] Owrak M, Aminy M, Jamal-Abad MT, Dehghan M. Experiments and simulations on the thermal performance of a sunspace attached to a room including heat-storing porous bed and water tanks. Build Environ 2015;92:142–51.
[5] Chen X, Xia XL, Meng X-L, Dong X-H. Thermal performance analysis on a volumetric solar receiver with double-layer ceramic foam. Energy Convers Manage 2015;97:282–9.
[6] Dehghan M, Rahmani Y, Ganji DD, Saedodin S, Valipour MS, Rashidi S. Convection–radiation heat transfer in solar heat exchangers filled with a porous medium: Homotopy perturbation method versus numerical analysis. Renewable Energy 2015;74:448–55.
[7] Dehghan M, Mahmoudi Y, Valipour MS, Saedodin S. Combined conduction–convection–radiation heat transfer of slip flow inside a micro-channel filled with a porous material. Transp Porous Media 2015;108:413–36.
[8] Kalogirou SA. Solar thermal collectors and applications. Prog Energy Combust Sci 2004;30:231–95.
[9] Zamzamian A, Keyanpourrad M, Kianineyestani M, Jamal-Abad MT. An experimental study on the effect of Cu-synthesized/EG nanofluid on the efficiency of flat-plate solar collectors. Renewable Energy 2014;71:658–64.
[10] Colangelo G, Favale E, Miglietta P, De Risi A, Milanese M, Laforgia D. Experimental test of an innovative high concentration nanofluid solar collector. Appl Energy 2015;154:874–81.
[11] Abramzon B, Yaron I, Borde I. An analysis of a flat-plate solar collector with internal boiling. J Sol Energy Eng 1983;105:454–60.
[12] Price H, Klein S, Beckman W. Analysis of boiling flat-plate collectors. J Sol Energy Eng 1986;108:150–7.
[13] Zhang X-R, Yamaguchi H, Uneno D. Experimental study on the performance of solar Rankine system using supercritical CO_2. Renewable Energy 2007;32:2617–28.
[14] Marion M, Voicu I, Tiffonnet A-L. Study and optimization of a solar subcritical organic Rankine cycle. Renewable Energy 2012;48:100–9.
[15] Delgado-Torres AM, García-Rodríguez L. Analysis and optimization of the low-temperature solar organic Rankine cycle (ORC). Energy Convers Manage 2010;51:2846–56.
[16] Wang J, Zhao L, Wang X. A comparative study of pure and zeotropic mixtures in low-temperature solar Rankine cycle. Appl Energy 2010;87:3366–73.
[17] Wang X, Zhao L, Wang J, Zhang W, Zhao X, Wu W. Performance evaluation of a low-temperature solar Rankine cycle system utilizing R245fa. Sol Energy 2010;84:353–64.
[18] Gorozabel Chata FB, Chaturvedi SK, Almogbel A. Analysis of a direct expansion solar assisted heat pump using different refrigerants. Energy Convers Manage 2005;46:2614–24.
[19] Zhang D, Wu QB, Li JP, Kong XQ. Effects of refrigerant charge and structural parameters on the performance of a direct-expansion solar-assisted heat pump system. Appl Therm Eng 2014;73:522–8.

[20] Chaturvedi SK, Gagrani VD, Abdel-Salam TM. Solar-assisted heat pump – a sustainable system for low-temperature water heating applications. Energy Convers Manage 2014;77:550–7.
[21] Chow TT, Pei G, Fong KF, Lin Z, Chan ALS, He M. Modeling and application of direct-expansion solar-assisted heat pump for water heating in subtropical Hong Kong. Appl Energy 2010;87:643–9.
[22] Aziz W, Chaturvedi S, Kheireddine A. Thermodynamic analysis of two-component, two-phase flow in solar collectors with application to a direct-expansion solar-assisted heat pump. Energy 1999;24:247–59.
[23] Khan ZA, Hadfield M, Tobe S, Wang Y. Ceramic rolling elements with ring crack defects – a residual stress approach. Mater Sci Eng, A 2005;404:221–6.
[24] Khan ZA, Hadfield M, Wang Y. Pressurised chamber design for conducting rolling contact experiments with liquid refrigerant lubrication. Mater Des 2005;26:680–9.
[25] Duffie JA, Beckman WA. Solar engineering of thermal processes. John Wiley & Sons; 2013.
[26] Klein S. Calculation of flat-plate collector loss coefficients. Sol Energy 1975;17:79–80.
[27] Cengel Y. Heat transfer: a practical approach. Columbus, OH: McGraw Hill; 2003.
[28] Incropera FP. Fundamentals of heat and mass transfer. John Wiley & Sons; 2011.
[29] Kandlikar SG. A general correlation for saturated two-phase flow boiling heat transfer inside horizontal and vertical tubes. J Heat Transfer 1990;112:219–28.
[30] Chen JC. Correlation for boiling heat transfer to saturated fluids in convective flow. Ind Eng Chem Process Des Dev 1966;5:322–9.
[31] Shah MM. A new correlation for heat transfer during boiling flow through pipes. Ashrae Trans 1976;82:66–86.
[32] Shah M. Chart correlation for saturated boiling heat transfer: equations and further study. 1982.
[33] Collier JG, Thome JR. Convective boiling and condensation. Oxford University Press; 1994.
[34] Lemmon E, Huber M, McLinden M. N. REFPROP. Standard reference database 23. REFPROP, NIST, Version. 9.1; 2013.
[35] Odeh S, Morrison G, Behnia M. Modelling of parabolic trough direct steam generation solar collectors. Sol Energy 1998;62:395–406.

Paper III

Energy Conversion and Management 138 (2017) 493–510

Contents lists available at ScienceDirect

Energy Conversion and Management

journal homepage: www.elsevier.com/locate/enconman

Thermodynamic modelling and analysis of a solar organic Rankine cycle employing thermofluids

H.U. Helvaci *, Z.A. Khan

Bournemouth University, Nano Corr, Energy and Modelling, Faculty of Science and Technology, Bournemouth BH12 5BB, UK

ARTICLE INFO

Article history:
Received 2 November 2016
Received in revised form 2 February 2017
Accepted 6 February 2017

Keywords:
Solar thermal energy
Saturated organic Rankine cycle
Vane expander
Thermofluids

ABSTRACT

This paper presents thermodynamic modelling and simulation study of a small scale saturated solar organic Rankine cycle (ORC) which consists of a stationary, flat plate solar energy collector that is utilised as a vapour generator, a vane expander, a water-cooled condenser and a pump. Simulations are conducted under constant condensing temperature/pressure and various cycle pressure ratios (PR) for 24 organic thermofluids including Hydrocarbons (HCs), Hydrofluorocarbons (HFCs), Perfluorocarbons (PFCs), Hydrofluoroethers (HFEs) and Hydrofluoroolefins (HFOs). Special attention is given to the influence of PR and fluids' physical properties on the solar ORC performance as well as fluids' environmental and safety impacts including global warming potential (GWP), flammability and toxicity. The simulation results indicate that when the same fluid is considered, pressure ratio of the cycle leads to various operating conditions such as collector (evaporating) pressure which results in various collector, expander and cycle efficiency. For instance, increasing the pressure ratio of the cycle enhances the net work output and the thermal efficiency of the cycle, whereas it decreases the flat plate collector efficiency. The results also indicate that the proposed system produces the maximum net work output of 210.45 W with a thermal efficiency of 9.64% by using 1-butene. Furthermore, *trans*-2-butene, *cis*-2-butene, R600, R600a, R601, R601a and neopentane (HC), R227ea and R236fa (HFC), RC318 (PFC) and R1234ze (HFO) show promising solar ORC thermal performances. However, the flammability problem of HCs and global warming potential issue of HFCs and PFCs limit their applications, owing to the safety and environmental concerns.

On the other hand, in terms of the environmental impact, thermofluids such as RE347mcc, RE245fa2 (HFEs) and R1234ze, R1233zd (HFOs) offer an attractive alternative, yet they were neither the most efficient, nor generated the highest amount of net work output. This paper provides thermofluids' selection guidelines to achieve maximum efficiency within solar thermal energy technologies while keeping environmental impacts into considerations.

1. Introduction

The World has been facing numerous environmental problems such as air pollution, ozone layer depletion, acid rain and global warming, mainly due to increasing consumption of fossil fuels [1]. Extracting fossil fuels in the future will become gradually challenging. Increasing demands of energy from non-renewable sources remain unsustainable. Therefore utilising renewable energy sources as an alternative has been of great importance for domestic heating and electricity generation [2,3].

Renewable energy sources such as solar thermal, geothermal, biomass and waste heat can be categorised as low-grade temperature energy sources and they have potential in reducing consumption of fossil fuels [4,5]. However, conventional Rankine cycle is not an economical and efficient alternative for the conversion of heat from renewable energy sources [4]. A conventional Rankine cycle employing organic compounds rather than water is called as organic Rankine cycle (ORC) and it is the most accepted technology for converting low-grade heat energy source into mechanical work [6].

A considerable amount of research has been conducted on the installation of solar ORCs where non-stationary flat plate collectors are used as a heat source of the cycle. Experimental study on the performance of such systems with a selected pure fluid including various types of organic compounds such as HFCs (R134a, R245fa), HFEs (HFE 7000) and inorganic compounds (CO_2) has been conducted. Manolakos et al. conducted an experimental study on a low-grade solar ORC using pure R-134a as the working fluid.

* Corresponding author at: Faculty of Science and Technology, Fern Barrow, Talbot Campus, Bournemouth University, Poole, Dorset, BH12 5BB, UK.
E-mail address: hhelvaci@bournemouth.ac.uk (H.U. Helvaci).

http://dx.doi.org/10.1016/j.enconman.2017.02.011
0196-8904/

Nomenclature

A	area, m^2
Bo	boiling number
C	constant
C_b	bond conductance
C_p	specific heat, J/kg K
Co	convection number
d	radius of the stator to the centre of the rotor
D	diameter, m
e	eccentricity, m
f	friction factor
F	fin efficiency
F'	collector efficiency factor
F_R	heat removal factor
Fr	Froude number
G	mass flux, kg/m^2 s
h_{sp}	single phase heat transfer coefficient, W/m^2 K
h_{tp}	two phase heat transfer coefficient, W/m^2 K
$h_{nc,B}$	nucleate boiling factor
$h_{c,B}$	convective boiling factor
h	enthalpy, J/kg
h_{fg}	heat of vaporisation, J/kg
k	thermal conductivity, W/m K
k_{ratio}	heat capacity ratio
$\dot{m}$	mass flow rate, kg/s
M	molecular weight, g/mol
N	dimensionless parameter
n	number of vanes
Nu	Nusselt number
ORC	organic Rankine cycle
P	Pressure, bar
PR	pressure ratio
Pr	Prandtl number
r	radius, m
$r_{v,built\text{-}in}$	built-in ratio of the expander
Re	Reynolds number
S	solar radiation, W/m^2
T	temperature, °C
U	heat loss coefficient, W/m^2 K
$\dot{Q}$	heat, W
v	velocity, m/s
V	volume, m^3
W	tube spacing
$\dot{W}$	work, kW
x	vapour quality

Subscripts

a	ambient
col	collector
$cond$	condensation
$crit$	critical
cw	cooling water
cyc	cycle
dsg	designed
$evap$	evaporation
exh	exhaust
exp	expander
f	fluid
g	vapour
i	inner
in	inlet, incoming
int	intake
is	isentropic
l	liquid
lat	latent
max	maximum
mec	mechanical
nbp	normal boiling point
o	outer
out	outlet
ov	over
p	plate
pp	pinch point
rot	rotor
s	isentropic
snb	sensible
sp	single phase
$stat$	stator
t	top
tp	two phase
T	total
u	useful
ud	under
wf	working fluid

Greek symbols

υ	kinematic viscosity, m^2/s
v	specific volume, m^3/kg
ϕ	heat flux, W/m^2
ρ	density, kg/m^3
$\varkappa$	angle between the vanes, deg
θ	angle of a specific vane from the origin

The generated mechanical work is utilised for reverse osmosis (RO) desalination [7–9]. Wang et al. designed and constructed a solar sourced ORC, where R245fa is used as the working fluid of the system. They reported that 1.64 kW average shaft output was obtained from the new designed R245fa expander [10]. Another experimental study of a small scale solar ORC using R245fa is established by [11]. The effect of a recuperator for the constant flow rate condition was analysed in their study, and it was concluded that the recuperator does not lead to an increase in the thermal efficiency of the system [11]. Yamaguchi et al. conducted an experimental study on supercritical solar ORCs, using CO_2 [12]. Another solar ORC, utilising inorganic fluid (CO_2) was also investigated in Ref. [13]. In both studies it is concluded that CO_2 offers a feasible alternative to be used in solar thermal power applications.

On the other hand, selection of the most suitable working fluid for solar ORCs and optimisation of the system for various operating conditions, including both simulation and experimental studies has attracted many researchers. Rayegan [14] compared 117 organic fluids on the basis of their effects on thermal efficiency, net power output and exergetic efficiency of the solar ORC. They claimed that fluids with higher critical temperature were considered to be the best [14]. Torres [15] presented a theoretical study of solar ORC where solar collector is used as thermal energy source of the cycle. In their analysis, they considered four different models of stationary solar collectors with twelve substances, including organic (HCs and HFCs) and inorganic (ammonia) fluids. Aperture area needed per unit of mechanical power output was set as a comparison criteria and it was generalised that dry fluids need lower

values of the unit aperture area than wet fluids. Marion et al. carried out both theoretical and experimental analyses to show the potential of generating mechanical energy by combining a solar thermal flat plate collector with an organic Rankine cycle. The cycle was simulated by using three organic fluids which were R134a, R227ea and R365mfc. In order to investigate the optimum operating conditions, a parametric optimisation was conducted. It was found that R365mfc gives the highest performance and it is followed by R134a and R227ea. They also reported that net mechanical power work generation highly depends on the working fluid flow rate [16]. A mathematical model was presented to simulate a solar-sourced regenerative ORC by [17]. In their study they performed a parametric analysis of the system by using different working fluids. They also presented an optimisation study where the daily average efficiency was set as the objective function. It was reported that R245fa and R123 was recommended as the most suitable fluids for the proposed system. They also claimed that turbine inlet pressure and condensation temperature have an effect on the system performance [17]. Another working fluid selection study was conducted by [18]. They modelled the solar organic Rankine cycle with fifteen organic fluids and evaluated the thermodynamic performance of the system for each case. It was reported that R134a and R245fa are the most suitable working fluids [18]. In another study of working fluid selection for solar ORC, R134a was found to be the most appropriate working fluid [19]. It is also concluded that although hydrocarbons such as R600, R600a and R290 show good performance characteristics they need safety measures due to their high flammable nature.

Previously, a theoretical and simulation study of multiphase flow (single and two-phase) in a flat plate collector was conducted and the effect of single and two-phase flows on the heat transfer coefficients, as well as the collector performance was investigated for two working fluids (R134a and HFE 7000) [20]. In the current study, the previous work is extended by modelling a small scale solar ORC, where the flat plate collector is connected directly to the cycle. The simulation analysis of the cycle, using 24 working fluids is conducted under various pressure ratio points. Special attention is given to the effect of the system pressure ratio on the collector efficiency, expander efficiency, net work output of the cycle and the cycle efficiency. Investigation of the most suitable working fluid for a small scale solar ORC is also discussed in terms of its thermo-physical and environmental properties. This research is also expected to demonstrate the potential of solar ORCs where flat-plate collectors can be either mounted on or integrated into a roof of a commercial or residential building to generate mechanical and heat energy simultaneously by utilising environmentally friendly thermo-fluids.

2. Mathematical modelling

2.1. Solar organic Rankine cycle

The proposed small scale saturated solar ORC is made up of four components which are a solar collector, a pump, a condenser and an expander (Fig. 1).

In the proposed system, the solar collector is utilised as an evaporator of the cycle where pressurised vapour is directly generated. This configuration is called 'Direct vapour generation' (DVG) and has been studied and recommended by various researchers [15,16] due to its advantage of eliminating additional heat exchanger (evaporator) which would cause extra cost and heat losses. As represented in Fig. 1, the liquid working fluid is pressurised by the pump and is then sent to the flat plate collector (1 → 2). In the collector, solar radiations are converted to thermal energy and this energy is then transferred to the working fluid. The working fluid

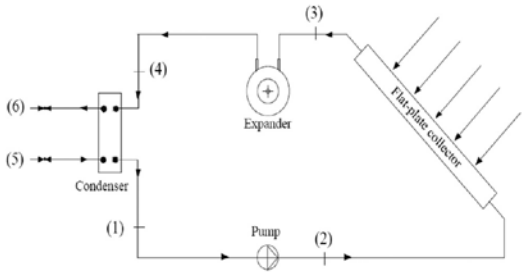

Fig. 1. A schematic diagram of the proposed solar ORC.

is preheated and evaporated within the collector tube (2 → 3). Then, the pressurised saturated vapour reaches the expander and turns the expander shaft to generate mechanical energy. This mechanical work could be used to produce electricity when the expander shaft is connected to a generator (3 → 4). In the condenser, low pressure exhaust vapour coming from the expander is condensed to saturated liquid with a constant pressure (4 → 1). The working fluid is cooled by cold water as it circulates through the condenser (5 → 6). Finally, the working fluid is pumped back to the collector to start a new cycle (1 → 2). The thermodynamic process of the saturated organic Rankine cycle on T-s diagram is represented in Fig. 2.

Each component of the system is modelled by considering the following assumptions:

- The system is considered as a steady state.
- Pressure drops in the collector, condenser and the pipelines have been neglected.

2.2. Flat plate collector

The serpentine flat plate collector is previously modelled and represented comprehensively in [20]. The collector consists of a glass cover, absorber plate, copper tube and insulation as it is shown in Fig. 3.

As the incoming solar radiation travels through the glass cover (1) some portion of this heat is lost to the atmosphere and the remaining is absorbed on the absorber plate (2). Solar energy on the absorber plate surface is calculated as;

$$\dot{Q}_p = A_p[S_{in}(\tau\alpha) - U_T(T_p - T_a)] \quad (1)$$

where A_p is the collector plate area, S_{in} is the incoming solar radiation on the collector and $(\tau\alpha)$ is the transmittance-absorbance product. U_T represents the total heat loss coefficient, T_p and T_a represent

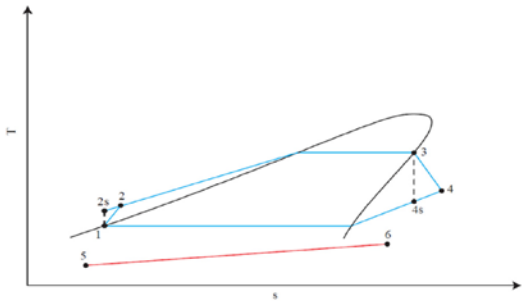

Fig. 2. A typical T-s diagram of saturated ORC (for HFE 7000).

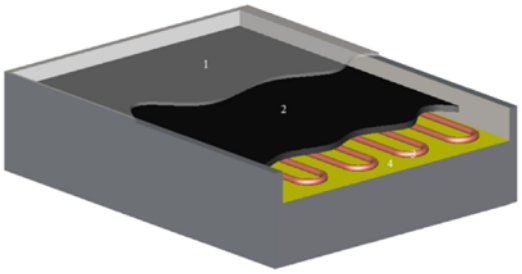

Fig. 3. Schematic of the serpentine tube flat plate collector [20].

the plate and ambient temperature respectively. Since the heat loss through the edges has been neglected in this study, the total heat loss coefficient is found to be below:

$$U_T = U_{top} + U_{back} \tag{2}$$

U_{top} and U_{back} can be calculated by the formula developed by Klein [21].

Absorbed solar energy on the collector plate (2) is transferred to the working fluid as it circulates along the collector tube (3). This is called "useful energy gain" of the fluid and it is estimated as;

$$\dot{Q}_u = A_p F_R[S_{in}(\tau\alpha) - U_T(T_{f,in} - T_a)] \tag{3}$$

where F_R represents the collector heat removal factor and $T_{f,in}$ represents the working fluid collector inlet temperature.

Collector heat removal factor is found to be as below:

$$F_R = \frac{\dot{m}C_p}{A_p U_T}\left[1 - \exp\left(-\frac{A_p U_T F'}{\dot{m}C_p}\right)\right] \tag{4}$$

In Eq. (4), F' is the collector efficiency factor and it can be calculated as:

$$F' = \frac{(U_T)^{-1}}{W[U_T(D_0 + (W - D_0)F)]^{-1} + (C_b)^{-1} + (\pi D_i h_f)^{-1}} \tag{5}$$

where W is tube spacing, D_o and D_i is the outer and inner tube diameter respectively. C_b represents the bond conductance and it is neglected ($1/C_b = 0$) in the calculation.

F is the fin efficiency and it is determined by Eq. (6):

$$F = \frac{\tanh[m(W - D_0/2)]}{m(W - D_0/2)}, \quad \text{where} \quad m = \sqrt{\frac{U_T}{k\delta}} \tag{6}$$

In Eq. (5), h_f represents the convective heat transfer coefficient of the fluid in the collector tube. As mentioned previously, the flat plate collector is utilised as an evaporator of the solar thermal cycle where the phase change of the fluid takes place. Therefore, the convective heat transfer coefficient (h_f) is evaluated for both single and two phase flows separately in the model.

2.2.1. Single-phase flow

The heat transfer coefficient in the single phase region for fully developed laminar flow and for fully developed turbulent flow are calculated respectively as follows [22]:

$$Nu = 4.36 \quad \text{where } Re < 2300 \tag{7}$$

$$Nu = \frac{\left(\frac{f}{8}\right)(Re - 1000)Pr}{1 + 12.7\left(\frac{f}{8}\right)^{0.5}(Pr^{2/3} - 1)}$$
$$\text{where } (3 \times 103 < Re < 5 \times 106), (0.5 < Pr < 2000) \tag{8}$$

In the calculations the Reynolds number is estimated as:

$$Re = \frac{VD}{\upsilon} \tag{9}$$

and the Prandtl number is defined as:

$$Pr = \frac{\rho \upsilon C_p}{k} \tag{10}$$

where v is the flow velocity, υ is the kinematic viscosity, ρ is the density, C_p is the specific heat of the working fluid and k is the thermal conductivity.

The single phase heat transfer coefficient of the working fluid in the collector tube is calculated with the following equation:

$$h_{sp} = Nu\frac{k}{D} \tag{11}$$

2.2.2. Two-phase flow

Calculation of two-phase flow heat transfer coefficient (h_{tp}) is based on the model represented by Shah [23]. The model consists of two distinct boiling mechanisms (nucleate and convective) relies on the calculation of a range of dimensionless parameters.

The dimensionless parameter (N) is calculated according to the conditions of Froude number Fr_l.

$$Fr_l = Froude\ number = \frac{G^2}{\rho^2 gD} \tag{12}$$

where

$$Frl < 0.04 \quad N = 0.38(Fr_l)^{-0.3}Co \tag{13}$$

$$Frl > 0.04 \quad N = Co \tag{14}$$

Convection number is calculated as follows;

$$Co = \text{Convection number} = \left(\frac{1}{x} - 1\right)^{0.8}\left(\frac{\rho_g}{\rho_l}\right)^{0.5} \tag{15}$$

Then, nucleate boiling ($h_{nc,B}$) and convective boiling ($h_{c,B}$) factors are determined at the following cases;

Case 1 (N > 1)

$$h_{nc,B} = (230Bo^{0.5}) \times h_l \quad \text{where Bo} > 0.0003 \tag{16a}$$

$$h_{nc,B} = (1 + 46Bo^{0.5}) \times h_l \quad \text{where Bo} < 0.0003 \tag{16b}$$

$$h_{c,B} = (1.8N^{0.8}) \times h_l \tag{16c}$$

Case 2 (1 > N > 0.1)

$$h_{nc,B} = (CBo^{0.5}) \times \exp(0.47N^{-0.1}) \times h_l \tag{17a}$$

$$h_{c,B} = (1.8N^{0.8}) \times h_l \tag{17b}$$

Case 3 (N < 0.1)

$$h_{nc,B} = (CBo^{0.5}) \times \exp(2.47N^{-0.15}) \times h_l \tag{18a}$$

$$h_{c,B} = (1.8N^{0.8}) \times h_l \tag{18b}$$

In all three cases, h_l represents the liquid phase heat transfer coefficient and it is calculated by using Dittus-Boelter equation.

The constant C is calculated by using the following equations:

$$Bo > 0.0011 \quad C = 14.7 \tag{19a}$$

$$Bo < 0.0011 \quad C = 15.43 \tag{19b}$$

where

$$Bo = Boiling\ number = \frac{\phi}{Gh_{fg}} \tag{20}$$

Finally, for each case the nucleate boiling and convective boiling factors are calculated and the larger value is selected. In other words, the larger represents the boiling mechanism and is taken as two-phase flow heat transfer coefficient.

2.3. Expander

The expander is mathematically modelled in the current study, was tested experimentally in a small scale solar organic Rankine cycle using HFE 7000 refrigerant in [24]. The mathematical modelling is divided into two parts which are geometrical and thermodynamic analyses respectively. The former is developed in order to determine the design characteristics and the built-in volume ratio of the expander, whereas the latter is built up to evaluate the expander expansion losses (under or over expansion) where the effect of the operating conditions of the system is taken into account.

The multi-vane expander mainly consists of a stator (cylinder), a rotor and four vanes Fig. 4. The rotor is mounted eccentrically in the stator, has radial slots where the vanes are positioned. As the working fluid enters the expander through the inlet port, the rotor as well as the vanes move and compose a working chamber. Due to the continuous rotational movement of the rotor, the area of the working chamber increases until the working fluid begins flowing toward the outlet port. Since then, the area of the working chamber starts to decrease and eventually the vanes close the working chamber. When the fluid begins filling the chamber again after the minimum area of the working chamber is reached, the cycle of the expander is completed [25].

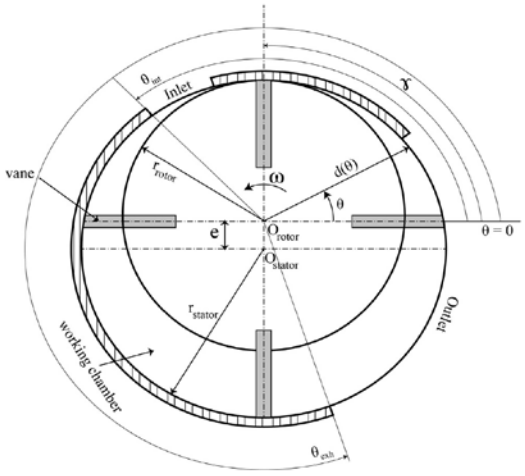

Fig. 4. Schematic of the multi-vane expander.

In order to evaluate the volume of a working chamber as a function of angular displacement, initially, the radius of the stator to the centre of the rotor is calculated by using the following formula;

$$d(\theta) = -e \times \sin\theta + \sqrt{(r_{stat})^2 - (e \times \cos\theta)^2} \tag{21}$$

The area of a working chamber can be evaluated if the geometrical parameters of the expander such as stator radius (r_{stat}), rotor radius (r_{rot}), eccentricity (e) and number of the vanes (n) are known.

$$A(\theta) = \frac{1}{2}\int_{\theta}^{\theta+\frac{2\pi}{n}} (d^2 - r_{rot}^2)\,d\theta \tag{22}$$

The volume of a working chamber can be given as;

$$V(\theta) = A \times L_{stat} \tag{23}$$

Volume ratio or built-in ratio of an expander can be defined as the ratio between the volume of the working chambers at the end and at the beginning of an expansion process [26]. The volume of the working chambers can be calculated by introducing the intake (θ_{int}) and the exhaust (θ_{exh}) angles into the Eq. (22) and (23). Thus, built-in ratio is calculated by using the formula below;

$$r_{v,built\text{-}in} = \frac{V_{out}}{V_{in}} \tag{24}$$

Following the built-in ratio of the expander, expander designed pressure ratio can be calculated as [27];

$$PR_{dsg} = \frac{P_{exp,in}}{P_{exp,out,dsg}} = (r_{v,built\text{-}in})^{k_{ratio}} \tag{25}$$

where k represents the heat capacity ratio of the fluid.

As it is stated in [28,29] that during the expansion process, under-expansion occurs if the designed pressure ratio imposed by the expander is lower than the operating pressure ratio of the system whereas over-expansion happens when the designed pressure ratio is higher than the operating pressure ratio. The operating pressure ratio of the system is the pressure ratio of the collector outlet/expander inlet and expander outlet/condenser inlet.

$$PR_{cyc} = \frac{P_{exp,in}}{P_{exp,out}} \tag{26}$$

Fig. 5 represents the isentropic expansion process on a P-V diagram for both under and over expansion cases [29].

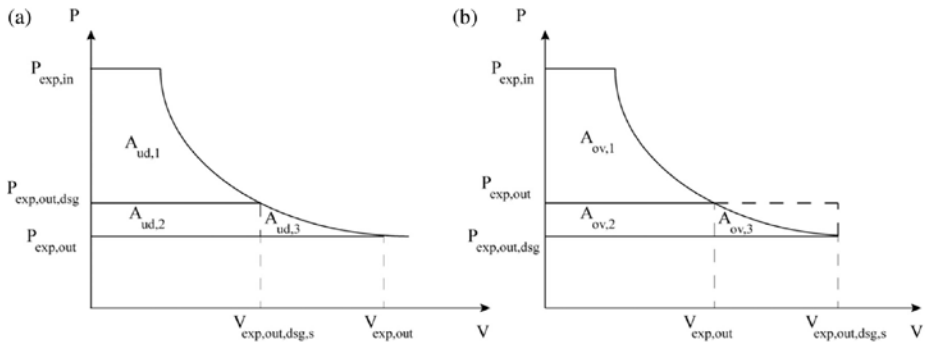

Fig. 5. Isentropic expansion process (a) under expansion, (b) over expansion.

Then, the work during the expansion process can be calculated according to the areas represented in Fig. 5.

2.3.1. Under-expansion

$$\dot{W}_{exp,ud} = A_{ud,1} + A_{ud,2} = \dot{m}_{wf} \times \left(\left(h_{exp,in} - h_{\substack{exp,out \\ dsg,s}} \right) \times 10^{-3} + \left(v_{\substack{exp,out \\ dsg,s}} \times \left(P_{\substack{exp,out \\ dsg}} - P_{exp,out} \right) \right) \times 10^{-2} \right) \times \eta_{mec} \quad (27)$$

The efficiency of the expander for under-expansion case is calculated as;

$$\eta_{exp,ud} = \frac{\dot{W}_{exp,ud} \times 10^3}{\dot{m}_{wf} \times (h_{exp,in} - h_{exp,out,is})} \quad (28)$$

2.3.2. Over-expansion

$$\dot{W}_{exp,ov} = (A_{ov,1} + A_{ov,2}) - (A_{ov,2} + A_{ov,3}) = \dot{m}_{wf} \times \left(\left(h_{exp,in} - h_{\substack{exp,out \\ dsg,s}} \right) \times 10^{-3} - \left(v_{\substack{exp,out \\ dsg,s}} \times \left(P_{\substack{exp,out \\ dsg}} - P_{exp,out} \right) \right) \times 10^{-2} \right) \times \eta_{mec} \quad (29)$$

The efficiency of the expander for over-expansion case is calculated as;

$$\eta_{exp,ov} = \frac{\dot{W}_{exp,ov} \times 10^3}{\dot{m}_{wf} \times (h_{exp,in} - h_{exp,out,is})} \quad (30)$$

In Eq. (27) and (29), $h_{exp,in}$ and $h_{exp,out,dsg,s}$ represent the enthalpy at the expander inlet and expander designed outlet isentropic enthalpy respectively. $P_{exp,out,dsg}$ and $P_{exp,out}$ are the designed expander outlet pressure and expander outlet pressure at operating conditions respectively. $v_{exp,out,dsg,s}$ and η_{mec} indicates expander designed outlet isentropic specific volume and the mechanical efficiency of the expander respectively. Expander mechanical efficiency, which represents the frictional, leakage and heat dissipation losses is assumed to be 0.7 [25].

To validate the expander simulation, the model is utilised by using the same expander input conditions as those in [24]; $T_{exp,in}$ = 45.41 °C, $P_{exp,in}$ = 1.32 bar and $\dot{m}_{wf}$ = 0.022 kg/s. A good agreement between the simulation and experimental results are obtained (Table 1).

Table 1
Expander model validation results.

Conditions	Current study	[24]
$T_{exp,in}$ (°C)	45.41	45.41
$T_{exp,out}$ (°C)	36.36	36.36
$P_{exp,in}$ (bar)	1.32	1.32
$P_{exp,out}$ (bar)	0.66	0.66
$\dot{m}_{wf}$ (kg/s)	0.022	0.022
$\dot{W}_{exp}$ (W)	130.3	146.74

2.4. Condenser

The modelled condenser is a water-cooled heat exchanger in which the cooling water circulates to condense working fluid at desired conditions. The condenser is divided into 2 zones during the analysis, which are sensible heat and latent heat rejection respectively. As it is previously mentioned, the working fluid leaves the condenser as saturated liquid at corresponding temperature. The total amount of condensation heat can be calculated as the sum of the sensible and latent heat rejection of the working fluid in the condenser.

$$\dot{Q}_{cond} = \dot{m}_{wf} \times \left(h_{exp,out} - h_{\substack{g@cond \\ temp}} \right) + \dot{m}_{wf} \times \left(h_{\substack{g@cond \\ temp.}} - h_{\substack{l@cond \\ temp.}} \right) \quad (31)$$

The first and the second terms of the right hand side of Eq. (31) represent the sensible and latent heat rejection respectively.

In the condenser modelling, the pinch point temperature (ΔT_{pp}) which is the smallest difference between the working fluid and cooling water temperature is imposed (Fig. 6) [30]. The pinch point (point pp) takes place at where the working fluid starts to condense and the pinch point difference at this point is assumed to be 5 °C.

$$T_{cond} - T_{cw,pp} \geq \Delta T_{pp} \quad (32)$$

Latent heat rejection represents the enthalpy change of the working fluid from the pinch point to the end of the condenser. This latent heat is equal to the amount of heat that increased the cooling water temperature from the inlet to the pinch point.

$$\dot{m}_{wf} \times \left(h_{\substack{g@cond \\ temp}} - h_{\substack{l@cond \\ temp}} \right) = \dot{m}_{cw} \times C_{p,cw} \times (T_{cw,pp} - T_{cw,in}) \quad (33)$$

As the condensation temperature and the minimum pinch point temperature are defined as 25 °C and 5 °C respectively, the cooling water pinch point temperature and the cooling water mass flow rate can be evaluated by utilising Eq. (33) iteratively.

Then, the cooling water outlet temperature is calculated by using the formula below;

$$\dot{Q}_{cond} = \dot{m}_{cw} \times C_{p,cw} \times (T_{cw,out} - T_{cw,in}) \quad (34)$$

2.5. Pump

The consumed work by the pump is determined by the following equation [31].

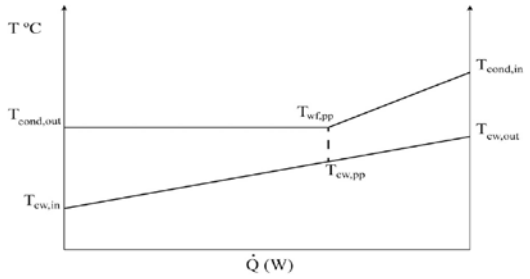

Fig. 6. Temperature profiles and the pinch point in the condenser.

Table 2
Operating conditions of the saturated solar ORC.

Parameter	Unit	Value
Incoming solar radiation	W/m^2	800
Condensation temperature	°C	25
Ambient temperature	°C	15
Cooling water inlet temperature	°C	12
Pump isentropic efficiency	–	0.6
Expander mechanical efficiency	–	0.7
Pressure ratio of the cycle	–	1.5–6

$$\dot{W}_{pump} = \frac{\dot{m}_{wf}(v_{pump,in}) \times (P_{evap} - P_{cond}) \times 10^{-2}}{\eta_{pump,s}} \quad (35)$$

where v is the specific volume of the working fluid, P is the pressure and $\eta_{pump,is}$ is the pump isentropic efficiency. It is important to note that in Eq. (35), the specific volume at the inlet of the pump is used instead of the average of the specific volume at the inlet and outlet of the pump as the difference is small.

3. Numerical process

The simulation model which utilises the developed Matlab computer code is explained in terms of the iteration procedure of the components as well as the whole system in this section. The proposed solar ORC model consists of specific sub-codes which are developed to simulate each component according to the defined input, output and fixed variables. Each component calculates output variables which are utilised as input variables of another component as each sub-code is connected to each other. In the simulations, the component specifications, the condensing temperature, the ambient and the cooling water temperature, the pump isentropic efficiency, the expander mechanical efficiency and the incoming solar radiation were kept constant whereas the pressure ratio of the cycle was the only selected control variable of the cycle. Properties of each fluid at various operating conditions were taken from REFPROP 9.1 [32] which was developed by the National Institute of Standards and Technology was run in parallel with the computer code. Operating conditions of the system are given in Table 2.

As the condensing temperature is set constant at 25 °C, the corresponding condensing pressure at saturated conditions can be determined. The system operating pressure ratio represents the ratio between the evaporation and the condensation pressure. Thus, the evaporating pressure of each fluid at saturated conditions is determined for each pressure ratio value.

Initially, the fluid properties at given operating conditions is taken from REFPROP (Table 3).

As all the necessary fluid data is derived by the computer code, the simulation starts with the determination of the specific pump work by using the following equation;

$$\dot{w}_{pump} = \frac{v_{pump,in} \times (P_{evap} - P_{cond}) \times 10^{-2}}{\eta_{pump,s}} \quad (\mathrm{kJ/kg}) \quad (36)$$

Table 4
Collector specifications.

Collector area (m^2)	6.96
Absorber plate thermal conductivity (W/m K)	50
Absorber plate thickness (m)	0.001
Total length of tube (m)	56
Tube inner diameter (m)	0.008
Tube outer diameter (m)	0.01
Effective transmittance-absorbance product (–)	0.81

Thus, the collector inlet enthalpy can be calculated as the pump inlet enthalpy and the pump specific work is known.

$$h_{col,in} = (\dot{w}_{pump} \times 10^3) + h_{pump,in} \quad (\mathrm{J/kg}) \quad (37)$$

According to the calculated collector inlet enthalpy and given collector (evaporation) pressure, the collector inlet temperature is identified and sent to the computer code.

3.1. Flat plate collector

Previously, a numerical model of the serpentine flat plate collector was developed and experimentally validated [20]. The collector specifications which are also used in this study are given in Table 4.

In the model, the collector tube was considered as a single flat tube and was divided into small finite elements. Then, the outlet temperature of the fluid, collector plate temperature, useful heat gain and the collector heat loss at the end of each element and also at the collector outlet was evaluated iteratively for given fluid inlet temperature and fluid mass flow rate. In this study, the same approach is followed by the difference of investigating the mass flow rate for given collector inlet and collector outlet temperature (as the cycle is saturated). Basically, the collector iteration model consists of two parts which are single phase and two phase flow calculations. Single phase flow represents the region from the fluid temperature at the collector inlet to its saturation temperature at corresponding saturation pressure. Two phase flow indicates the region between saturated liquid and saturated vapour points of the fluid. Initially, the simulation considers only the first element in the single phase region and the rest of the elements in the two phase region. Then, after each iteration, the model increases the number of elements in the single phase region until the desired criteria is satisfied. Fig. 7 demonstrates the elements and their regions (single or two phase) at two various iteration steps.

At the start, the flow rate of fluid as well as at which element the fluid goes into the saturated region is not known. Therefore, an arbitrary value of the fluid mass flow rate for the first element which represents the single phase flow region is given. Then, in order to calculate the fluid heat transfer coefficient in the single phase region, the flow type is determined whether it is laminar or turbulent by using Eq. (7) and (8). In the inner loop, the heat loss coefficient is calculated with the given initial plate temperature (T_p) value. (T_p value is considered as 5 °C higher than the fluid inlet

Table 3
Fluid data taken from REFPROP at given operating conditions.

Fluid data	
Fluid evaporation temperature at corresponding P_{evap}	Fluid sat. liquid enthalpy at corresponding P_{evap}
Fluid sat. liquid density at corresponding P_{evap}	Fluid sat. vapour enthalpy at corresponding P_{evap}
Fluid sat. liquid density at corresponding P_{evap}	Fluid condensation pressure at 25 °C
Fluid sat. vapour density at corresponding P_{evap}	Fluid saturated liquid enthalpy at 25 °C
Fluid sat. liquid conductivity at corresponding P_{evap}	Fluid saturated vapour enthalpy at 25 °C
Fluid sat. liquid viscosity at corresponding P_{evap}	Fluid saturated liquid specific volume at 25 °C
Fluid sat. vapour viscosity at corresponding P_{evap}	

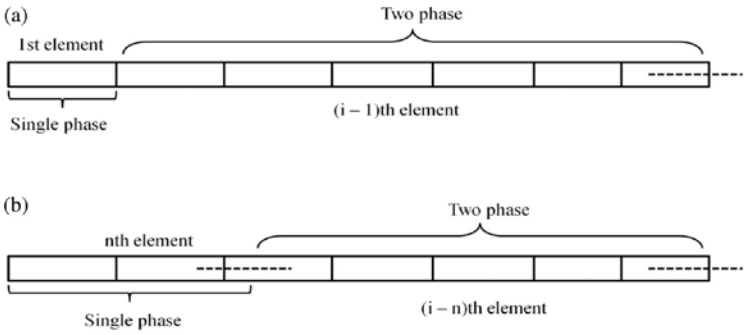

Fig. 7. Simulation iteration steps (a) first iteration, (b) xth iteration.

temperature for the first iteration) [20]. After the calculation of collector heat loss coefficient, the useful gain of the fluid Q_u is evaluated by using Eq. (3). With the calculated value of Q_u, the new plate temperature is evaluated by using the following equation;

$$T_p = T_{col,in} + \frac{\frac{\dot{Q}_u}{A_p}}{F_R U_T}(1 - F_R) \tag{38}$$

This process is repeated until the difference of two consecutive values of T_p is less than 0.01 °C. When the condition of T_p is satisfied in the inner loop, the last value of the useful heat gain of the fluid represents the amount of the heat for the whole collector tube and it can be shown as;

$$\dot{Q}_u = Q''_u \pi D_{in} L_{tube} \tag{39}$$

where Q''_u represents the useful heat rate, πD_{in} and L_{tube} indicate the surface perimeter and the length of the collector tube. Then, the heat gain of each element is calculated by using the formula below;

$$\dot{Q}_{gain} = Q''_{us} \pi D_{in} \int_0^L dx \tag{40}$$

In Eq. (40), dx is the length of each element which is obtained by dividing the whole collector tube into 'n' number of small elements. Using Eq. (40), the length of the first element is multiplied by useful heat rate and surface perimeter to evaluate the heat gain of the first element. As the collector inlet temperature and the saturation temperature of the fluid is known, the amount of the sensible heat transfer can be calculated as;

$$\dot{Q}_{snb} = \dot{m}_{wf,sp} \times C_p \times (T_{evap} - T_{col,in}) \tag{41}$$

Then, the mass flow rate for single phase flow is calculated as the sensible heat transfer is equal to the heat gain of the first element.

$$\dot{m}_{wf,sp} = \frac{\dot{Q}_{gain,sp}}{C_p \times (T_{evap} - T_{col,in})} \tag{42}$$

New calculated mass flow rate value of the fluid in the single phase region indicates that the first iteration assumes that the fluid undergoes a phase change in other words reaches its saturation points after the first element with the calculated mass flow rate. Then, the second loop starts where the two phase flow calculations are performed. In this loop, again the heat loss coefficient is evaluated by using the latest calculated T_p value. The useful heat gain of the fluid is evaluated (Eq. (3)) with another arbitrary value of the fluid mass flow rate for two phase region. Similar to the single phase part of the code, the new plate temperature is evaluated with the calculated value of useful heat (Eq. (38)). The process is repeated until the same convergence criterion is met (0.01 °C). Then, the heat gain of the fluid for the rest of the collector elements is calculated again by using Eq. (39). Differently from the first part, useful heat rate and surface perimeter are multiplied by another figure which equals to the length of the first element subtracted from the total length of the tube. Then, similar to the sensible heat, the amount of the latent heat transfer can be calculated as;

$$\dot{Q}_{lat} = \dot{m}_{wf,tp} \times (h_g - h_l) \tag{43}$$

and the mass flow rate for the two phase region;

$$\dot{m}_{wf,tp} = \frac{\dot{Q}_{gain,tp}}{(h_g - h_l)} \tag{44}$$

At the end of the second loop, the model checks if the difference between $\dot{m}_{wf,sp}$ and $\dot{m}_{wf,tp}$ is less than 0.0001. If the condition does not meet the convergence criterion (0.0001), the model increases the number of elements for the single phase part region and the same calculations are performed. This is continued until the condition satisfies the convergence. This point represents the element where the flow reaches the saturation point with corresponding mass flow rate. Finally, the collector efficiency is determined as;

$$\eta_{col} = \frac{\dot{m}_{wf} \times [(C_p(T_{evap} - T_{col,in}) + (h_g - h_l))]}{S \times A_{col}} \tag{45}$$

The flow chart of the simulation model is represented in Fig. 8.

3.2. Expander

The iteration begins with setting the parameters and the inputs of the expander. The parameters of the expander, inputs and outputs of the expander model are given in Table 5. Then the expander built-in ratio and expander designed outlet pressure are calculated by using Eq. (24) and (25). As it is previously mentioned, the fluid at the inlet of the expander is saturated vapour at corresponding evaporation pressure. This means the entropy at the outlet of the expander is equal to the entropy at the inlet of the expander as long as the expansion process is isentropic. Therefore, at the given entropy and expander designed outlet pressure, expander designed outlet isentropic enthalpy and isentropic specific volume can be calculated.

As all the unknowns in Eq. (27)–(30) are evaluated, now the model compares the designed and system operating pressure ratio values. Then, the mechanical work generated in the expander and the expander efficiencies are calculated according to the conditions of under and over expansion. The flow chart of the expander model is given in Fig. 9.

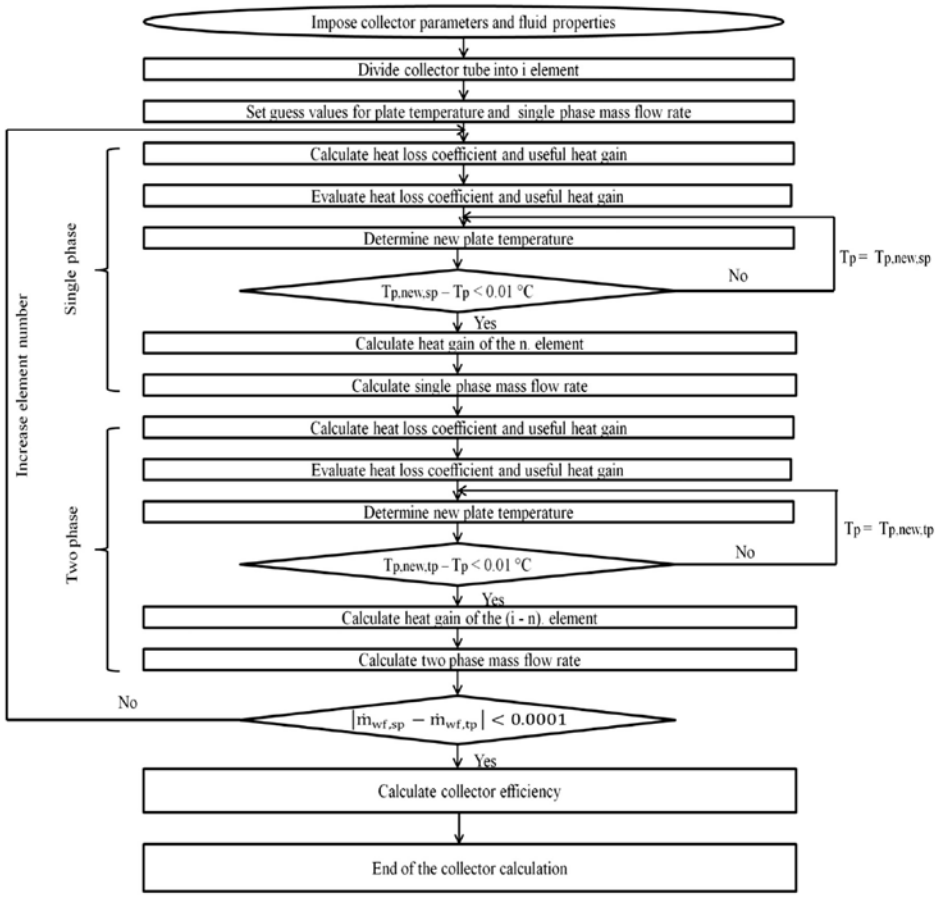

Fig. 8. Flow chart of the simulation model.

Table 5
Expander model specifications.

Parameters	Inputs	Outputs
Rotor radius, (r_{rot})	Inlet pressure, ($P_{exp,in}$)	Built-in volume ratio, ($r_{v,built-in}$)
Stator radius, (r_{stat})	Outlet pressure, ($P_{exp,out}$)	Expander designed outlet pressure, ($P_{exp,out,dsg}$)
Eccentricity, (e)		Expander designed outlet isentropic enthalpy, ($H_{exp,out,dsg,s}$)
Intake angle, (θ_{int})		Expander designed outlet isentropic specific volume, ($v_{exp,out,dsg,s}$)
Exhaust angle, (θ_{exh})		Expander mechanical work, ($\dot{W}_{exp}$)
Expander mechanical efficiency, (η_{mec})		Expander efficiency, (η_{exp})

3.3. Condenser

In the condenser simulations, cooling water mass flow rate and outlet temperature are aimed to be determined. Initially, pinch point condition in the code is set as;

$$25 - T_{cw,pp} \geqslant 5\ ^{\circ}C \quad (46)$$

This is to evaluate the cooling water mass flow rate. Then, with the given initial cooling water mass flow rate (0.001 kg/s), cooling water pinch point temperature is calculated by using Eq. (33) iteratively where the mass flow rate is increased by 0.001 intervals until the condition (Eq. (46)) is satisfied. This point provides the real value of the cooling water mass flow rate and cooling water pinch point temperature. Thereafter, the cooling water outlet temperature is evaluated with the use of Eq. (34) as the cooling water mass flow rate is determined previously. It is important to note that Eq. (31) is valid as long as the fluid leaves the expander as superheated vapour. However, if the fluid falls in the saturation region after the expansion process, the first term of the right hand side of Eq. (31) which represents the sensible heat rejection is omitted and the following equation is utilised to calculate the total amount of the condensation heat.

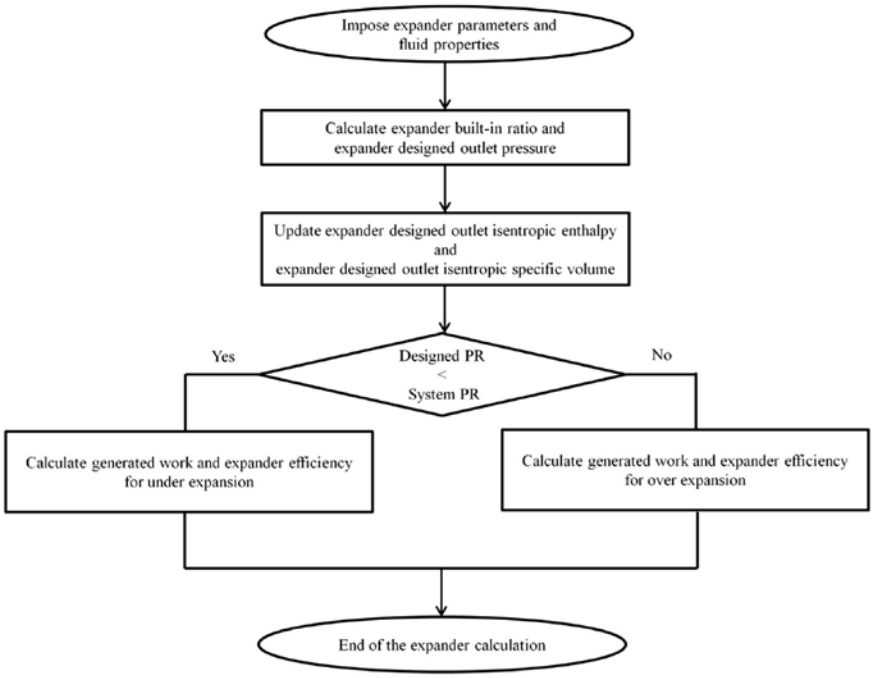

Fig. 9. Flow chart of the expander simulation model.

$$\dot{Q}_{cond} = \dot{m}_{wf} \times \left(h_{exp,out} - h_{\substack{l@cond \\ temp}} \right) \quad (47)$$

As the sensible heat rejection does not occur, the smallest difference between the working fluid and cooling water temperature takes place at the point where the cooling water leaves the condenser. Therefore, Eq. (33) can be rewritten as:

$$\dot{m}_{wf} \times \left(h_{exp,out} - h_{\substack{l@cond \\ temp}} \right) = \dot{m}_{cw} \times C_{p,cw} \times (T_{cw,out} - T_{cw,in}) \quad (48)$$

Then, Eq. (48) is solved iteratively with the same condition (Eq. (46)) to calculate the cooling water mass flow rate and outlet temperature.

3.4. The saturated solar ORC

The model of the whole solar ORC is developed by interconnecting all the components with the given input parameters. The performance analysis of the cycle is evaluated through the performance parameters.

The first performance parameter is the net work output of the system and it is defined as;

$$\dot{W}_{net} = \dot{W}_{exp} - \dot{W}_{pump} \quad (49)$$

The other parameter is the solar ORC efficiency and it is calculated as;

$$\eta_{SORC} = \frac{\dot{W}_{net} \times 10^3}{\dot{Q}_{gain}} \quad (50)$$

3.5. Simulation model constraints

The boundary conditions of the saturated solar ORC model are listed below;

- Superheating at the expander inlet and sub-cooling at the condenser outlet are zero, in other words working fluid leaves the collector as saturated vapour and leaves the condenser as saturated liquid in order to reduce total irreversibility of the cycle [33].
- The saturated solar ORC is simulated at constant condensing temperature of 25 °C
- As the fluids undergo a phase change in the collector, the maximum pressure of the cycle is limited to 1.5 MPa (15 bar) due to the leakage and safety concerns of the maximum flat plate collector pressure in domestic applications.
- Minimum condenser pressure should be higher than 0.05 bar [34].
- Pump isentropic efficiency is 0.6 [35].

3.6. Fluid pre-selection

In order to narrow down the list of the potential candidates to be used in the proposed solar ORC, some of the compounds were eliminated, according to their environmental parameter (ODP) and their corresponding saturation pressure at 25 °C in the condenser.

Several Hydrocarbons and Siloxanes have been discarded from the analysis due to having corresponding condensation pressure less than 0.05 bar at 25 °C (Table 6).

Ozone depletion potential (ODP) states compound's potential to contribute ozone degradation is one of the vital environmental factors for working fluid selection [34,36]. Due to their high ODP val-

Table 6
Fluids with a condensation pressure less than 0.05 bar.

Fluid	Condensation pressure at 25 °C (bar)
D4	0.0012
Decane	0.001
Dodecane	0.0001
Ethyl benzene	0.012
MDM	0.004
MD2 M	0.0005
MD3 M	0.00006
m-xylene	0.011
Nonane	0.005
Octane	0.018
p-xylene	0.011
Toluene	0.037

ues Chlorofluorocarbons (CFCs) and hydrochlorofluorocarbons (HCFCs) are discarded from the analysis. Thus, the fluids belong to Hydrocarbons (HCs), Hydrofluorocarbons (HFCs), Perfluorocarbons (PFCs), Hydrofluoroolefins (HFOs) and Hydrofluoroethers (HFEs) are considered and analysed in this study and 24 fluids given in Table 7 are considered as potential candidates.

4. Results and discussion

In this section, the simulation results of the proposed saturated solar ORC at various pressure ratio, using 24 working fluids are presented. It is well known that the net work output and the thermal efficiency of an ORC increase with the increasing difference of condenser and evaporator pressure and temperature. However, as it is previously stated, the flat plate collector is utilised as the evaporator (heat source) of the cycle in this study and the collector efficiency, in other words the amount of the heat that is recovered by the working fluid in the collector is highly related to the collector temperature due to the heat losses to the atmosphere as the collector efficiency is not set constant. Furthermore, unlike many studies in the literature, turbine/expander efficiency was not fixed and it varied as the expander inlet pressure changes due to the different behaviour of expansion (under/over) losses in the expander. Therefore, special attention is given to the collector and expander characteristics under various pressure ratio values of the system when the whole system is analysed in this section.

As it is stated previously, the maximum collector pressure is set to 15 bars. However, fluids such as R-134a, R-152a, R-227ea, R-236fa, RC-318, 1-butene, R-600a and RE-170 have an

Table 7
Properties of the investigated fluids [32].

Fluid	Alt. name	Type	T_{crit} (°C)	P_{crit} (bar)	$T_{boiling}$ (°C)[a]	Molar Mass (kg/kmol)
Trans-2-butene		HC	155.46	40.27	0.88	56.106
Cis-2-butene		HC	162.6	42.25	3.72	56.106
1-butene		HC	146.14	40.05	−6.31	56.10
Isobutane	R600a	HC	134.66	36.29	−11.74	58.122
Butane	R600	HC	151.98	37.96	−0.49	58.122
Neopentane		HC	160.59	31.96	9.5	72.149
Isopentane	R601a	HC	187.2	33.78	27.83	72.149
Pentane	R601	HC	196.55	33.7	36.06	72.149
Isohexane		HC	224.55	30.4	60.21	86.175
Hexane		HC	234.67	30.34	68.71	86.175
Cyclohexane		HC	280.45	40.805	80.71	84.159
1,1,1,2-tetrafluoroethane	R134a	HFC	101.06	40.593	−26.07	102.03
1,1-difluoroethane	R152a	HFC	113.26	45.168	−24.02	66.05
1,1,1,2,3,3,3-heptafluoropropane	R227ea	HFC	101.75	29.25	−16.34	170.03
1,1,1,2,3,3-hexafluoropropane	R236ea	HFC	139.29	34.2	6.17	152.04
1,1,1,3,3,3-hexafluoropropane	R236fa	HFC	124.92	32.0	−1.49	152.04
1,1,1,3,3-pentafluoropropane	R245fa	HFC	154.01	36.51	15.14	134.05
1,1,2,2,3-pentafluoropropane	R245ca	HFC	174.42	39.40	25.26	134.05
Octafluorocyclobutane	RC318	PFC	115.23	27.775	−5.97	200.03
Methyl-heptafluoropropyl-ether	RE347mcc	HFE	164.55	24.762	34.19	200.05
2,2,2-trifluoroethyl-difluoromethyl-ether	RE245fa2	HFE	171.73	34.33	29.25	150.05
2,3,3,3-Tetrafluoropropene	R1234yf	HFO	94.7	33.82	−29.45	114.04
Trans-1,3,3,3-tetrafluoropropene	R1234ze	HFO	109.36	36.34	−18.97	114.04
Trans-1-chloro-3,3,3-trifluoropropene	R1233zd	HFO	165.6	35.70	18.32	130.5

[a] Normal boiling temperature at 1 bar.

Table 8
Fluid corresponding evaporation pressures at various pressure ratio values.

Fluid	Pressure ratio										
	P_{cond} at 25 °C (bar)	1.5	2	2.5	3	3.5	4	4.5	5	5.5	6
1-butene	2.95	4.43	5.91	7.39	8.87	10.35	11.83	13.31	14.79	**16.27**	**17.75**
R-600a	3.49	5.23	6.98	8.72	10.47	12.21	13.96	15.71	**17.45**	**19.20**	**20.94**
R-134a	6.62	9.93	13.2	**16.56**	**19.87**	**23.18**	**26.49**	**29.80**	**33.12**	**36.43**	**39.74**
R-152a	5.93	8.90	11.8	14.84	**17.81**	**20.78**	**23.75**	**26.71**	**29.68**	**32.65**	**35.62**
R-227ea	4.52	6.78	9.05	11.31	13.57	15.84	**18.10**	**20.36**	**22.63**	**24.89**	**27.15**
R-236fa	2.7	4.05	5.41	6.76	8.11	9.47	10.82	12.17	13.52	14.88	**16.23**
RC-318	3.11	4.66	6.22	7.77	9.33	10.88	12.44	13.99	15.55	**17.10**	**18.66**
R1234yf	6.79	10.1	13.5	**16.9**	**20.3**	**23.78**	**27.18**	**30.5**	–	–	–
R1234ze	4.96	7.44	9.92	12.4	14.88	**17.36**	**19.85**	**22.33**	**24.81**	**27.29**	**29.77**

The numbers in bold represent the pressure points greater than 1.5 MPa ± 0.75.

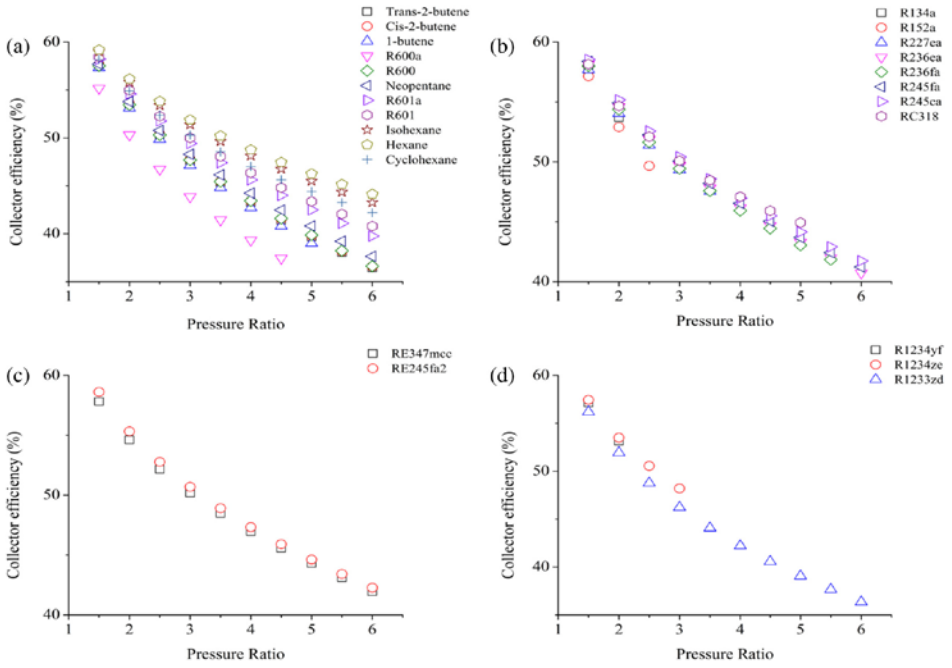

Fig. 10. Collector efficiency (a) HCs, (b) HFC-PFCs, (c) HFEs, (d) HFOs.

evaporation/collector pressure greater than 1.5 MPa at some pressure ratio points. This is due to their low saturation temperature behaviour. In the analysis, only the cases where the evaporation pressure is less than 1.5 MPa ± 0.75 is taken into account for these fluids (Table 8).

4.1. Collector analysis

The efficiency of the collector for each fluid category (HC, HCF, PFC, HFE and HFO) at various pressure ratios is represented in Fig. 10. It can be seen that the collector efficiency decreases independently of the fluid category as the pressure ratio of the system increases. This can be explained by the fact that the higher pressure ratio leads to an increase in the saturation pressure, as well as saturation temperature in the collector (saturated ORC). As a result, higher collector temperature causes greater heat loss from the collector to the ambient [16,20].

Fig. 11 shows the collector heat loss and the saturation temperature of the fluids R600a, R236ea, RE245fa2 and R1234ze as an example. In general, the collector efficiency for all the investigated fluids varied between 59.19% and 37.44% and the highest and the lowest efficiency value is obtained from Hexane and R-600a which ranged from 59.19% to 44.12% and 55.18% to 37.44% respectively.

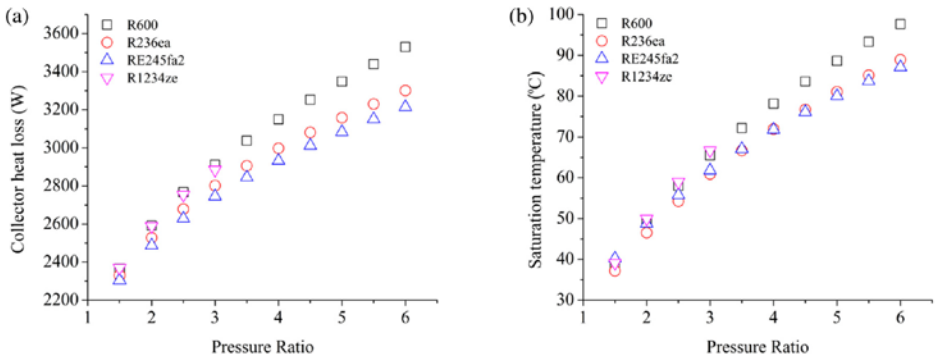

Fig. 11. Collector heat loss and saturation temperature with pressure ratio.

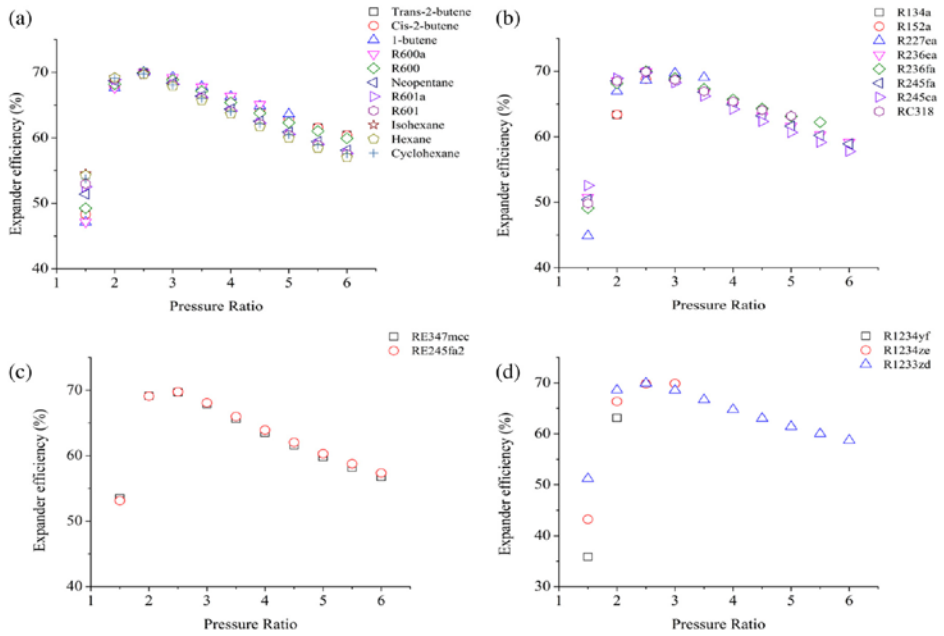

Fig. 12. Expander efficiency under various pressure ratio (a) HCs, (b) HFC-PFCs, (c) HFEs, (d) HFOs.

4.2. Expander analysis

In this section, the vane expander efficiency is analysed in terms of investigating the relation between the expander designed pressure ratio PR_{dsg} and the system pressure ratio PR_{cyc}. It can be seen from Fig. 12 that for each investigated fluid, the maximum expander efficiency occurred at the pressure ratio of 2.5 which also represents the designed expander pressure ratio (PR_{cyc}). The only exception was R134a and R1234yf where the pressure ratio of 2 provides the highest efficiency due to their saturation pressure limitation.

For instance, the efficiency of R600 was to be 49.26% at pressure ratio of 1.5 which is lower than its designed pressure ratio and results in over-expansion. Then, the efficiency increases to 68.2% as the pressure ratio rises to 2 and the efficiency reaches its maximum (69.98%) at PR of 2.5. After η_{exp} achieves the maximum value, it decreases gradually with the increasing pressure ratio. This is because further increase in PR causes the expander to operate under the under-expansion zone.

The minimum expander efficiency (35.61%) is obtained from the pressure ratio of 1.5 with R134a and the maximum expander efficiency (70.1%) is observed for the pressure ratio of 2.5 with 1-butene among the considered fluids. It is important to note that the analysis shows that the design parameters of a vane expander and the operating parameters of the cycle has a significant influence on the expander performance as it is also stated by [25,29]. It is also worth mentioning that all the investigated fluids except HFC-152a left the expander as a superheated vapour which shows that there is no risk of encountering any liquid droplet in the expander. The only exception was HFC-152a which was in the superheated vapour region at the pressure ratio of 1.5, then fell into the saturated region and had vapour quality of 0.997, 0.988 and 0.982 at the pressure ratio of 2, 2.5 and 3 respectively. Thereby, superheating might be necessary when utilising HFC-152a in order to avoid liquid formation in the expander.

Table 9
Calculated cooling water mass flow rate and outlet temperature at pressure ratio of 1.5.

Fluid	Cooling water mass flow rate (kg/s)	Cooling water inlet temperature (°C)	Cooling water outlet temperature (°C)
Trans-2-butene	0.091	12	20.21
Cis-2-butene	0.092	12	20.11
1-butene	0.091	12	20.16
R600a	0.087	12	20.25
R600	0.091	12	20.14
Neopentane	0.09	12	20.33
R601a	0.092	12	20.16
R601	0.093	12	20.14
Isohexane	0.094	12	20.18
Hexane	0.094	12	20.2
Cyclohexane	0.094	12	19.99
R134a	0.093	12	20.13
R152a	0.093	12	20
R227ea	0.09	12	20.39
R236ea	0.092	12	20.22
R236fa	0.092	12	20.23
R245fa	0.093	12	20.18
R245ca	0.093	12	20.18
RC318	0.09	12	20.45
RE347mcc	0.091	12	20.43
RE245fa2	0.093	12	20.23
R1234yf	0.091	12	19.01
R1234ze	0.091	12	20.24
R1233zd	0.09	12	18.65

4.3. Condenser analysis

It was previously mentioned that the heat rejection from the proposed cycle was carried out in the condenser. The working fluid was cooled by water which has an inlet temperature of 12 °C. The amount of the calculated condensation heat varied between

1729 W and 3223.96 W. Thus, this amount of heat was transferred from the system to the cooling water which subsequently increased the water temperature at the outlet of the condenser. The cooling water mass flow rate and the cooling water temperature at the exit of the condenser was calculated for each considered fluid. The results at pressure ratio of 1.5 are represented in Table 9. As it can be seen from Table 9 that the cooling water mass flow rate varied from 0.087 kg/s to 0.094 kg/s and the cooling water outlet temperature varied between 18.65 °C and 20.45 °C. Furthermore, the increased temperature of cooling water at the collector outlet can be utilised for secondary uses. For instance, the cooling water flow can be directed to a hot water tank to recover some portion of its heat [24].

4.4. Solar ORC analysis

In this section the net work output of the cycle with the thermal efficiency of the solar ORC is investigated. Fig. 13 shows the net work output of the cycle for each investigated fluid. It can be observed that the net work output of the cycle augments initially, reaches its peak and remains almost constant with the increasing pressure ratio for 1-butene, R600a, hexane, Isohexane, Cyclohexane, R236fa, R245fa and RE245fa2.

The reason for this behaviour can be explained by the decrease in the mass flow rate of the cycle and increase in the consumed pump work. The former is due to the rise in the pressure ratio of the system at a constant condensation pressure, which augments the difference between the collector and condenser pressure that represent the highest and the lowest points of the cycle respectively. This results in an increase in the enthalpy difference between the two points and causes the mass flow rate to decrease due to the energy balance of the cycle. Fig. 14 represents the mass flow rate of four working fluids versus pressure ratio as an example.

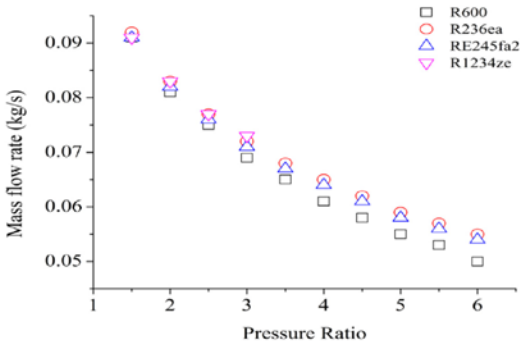

Fig. 14. Mass flow rate of R600, R236ea, RE245fa2 and R1234ze versus pressure ratio.

It can be observed that initially, the effect of the increase in the enthalpy drop across the expander is higher than the decrease in the mass flow rate and the increase in the consumed pump work. However, after a certain point of the pressure ratio the increase in the enthalpy drop does not dominate the decrease in the mass flow rate and the rise in the consumed pump work. This is even more pronounced for the fluids such as *trans*-2-butene, *cis*-2-butene, R600, neo-pentane, R601a, R236ea, R245ca, RE347mcc and R1233zd where the net work output starts to decline beyond the pressure ratio of the maximum net work output. The same trend can be found in [17,30]. On the other hand, fluids such as R134a,

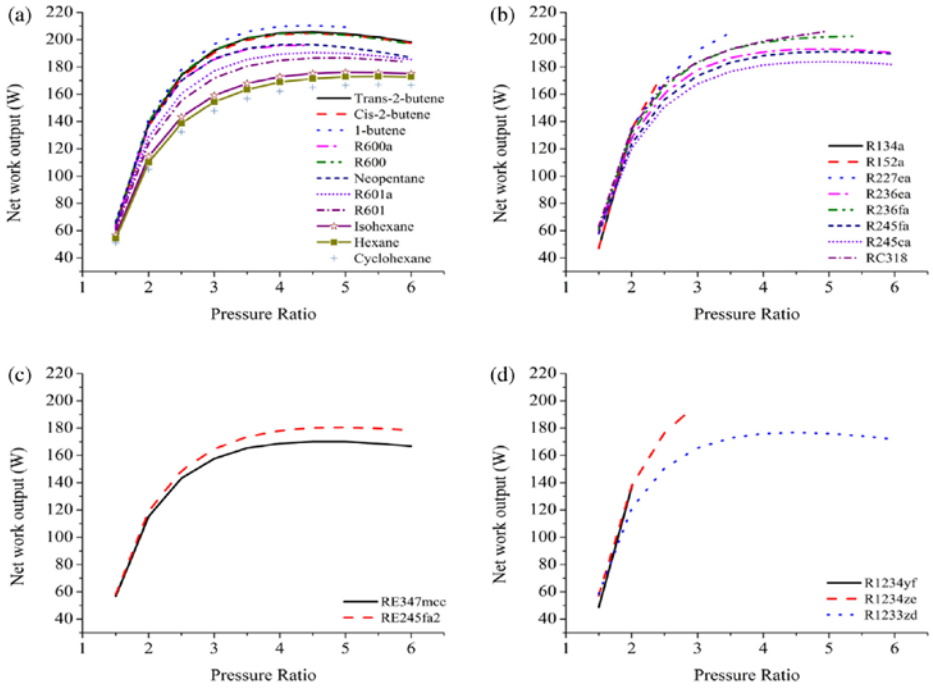

Fig. 13. Net work output versus pressure ratio for (a) HCs, (b) HFC-PFCs, (c) HFEs, (d) HFOs.

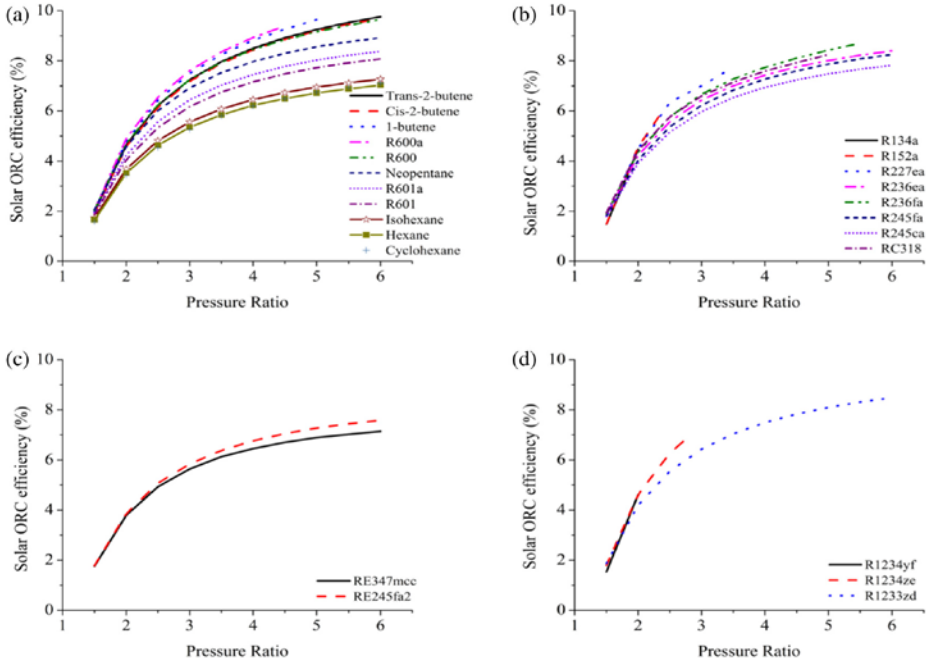

Fig. 15. Solar ORC efficiency varies with pressure ratio for (a) HCs, (b) HFC-PFCs, (c) HFEs, (d) HFOs.

R152a, R227ea, RC318, R1234yf, R1234ze shows an increasing tendency with the rising pressure ratio owing to the limitations of their saturation pressure points higher than 15 bars.

Another parameter which is investigated in this section is the thermal efficiency of the solar ORC. As it is stated by [14] it is important to consider net work output along with the thermal efficiency when comparing various working fluids. It is apparent from Fig. 15 that the cycle efficiency increases with increasing pressure ratio for each investigated fluid. Similar trend can be found in [19].

This behaviour is different from the net work output of the cycle as it is demonstrated previously in Fig. 13. The reason for the upward trend of cycle efficiency when there is a maximum point for the net work output is the decrease in the amount of the heat gained by the fluid in the collector. Similar results were reported in [33] for R134a refrigerant. The highest cycle efficiency is obtained by *trans*-2-butene (9.76%) and *cis*-2-butene (9.69%) among the investigated fluids.

Figs. 13 and 15 represents that generally, HCs provide higher net work output and cycle efficiency compared to the others thermofluids and among the hydrocarbons, *trans*-2-butene, *cis*-2-butene, 1-butene, R600 and R600a gives the highest results. For HCFs, HFEs and HFOs R227ea, R236fa, RC318 and R1234ze generate more net power output, whereas R227ea, R236ea, R236fa and RC318 provide higher thermal efficiency.

It is important to note that the net mechanical work output of R236ea (60.57–190.39 W) is found to be less than R227ea (58.18–205.06 W) and RC318 (62.94–206.34 W). However, the cycle efficiency of R236ea (1.87–8.4%) is greater that of R227ea (1.81–7.75%) and RC318 (1.94–8.25). This can be explained by the fact that R236ea provides less collector efficiency (58.15–40.72%) compared to R227ea (57.69–47.57%) and RC318 (58.16–44.93%). In other words, less amount of useful heat is transferred to R236ea owing to its higher saturation (collector) temperature. According to Eq. (50), the higher cycle efficiency of R236ea shows an interesting potential of converting the heat energy into the mechanical work.

In addition to the thermal efficiency of the proposed solar ORC, the overall efficiency which represents the ratio of the net power output of the cycle to the incoming solar radiation is calculated as:

$$\eta_{sys} = \frac{\dot{W}_{net}}{SA_{col}} \tag{51}$$

The overall efficiency shows similar trend with the net work output of the solar ORC (Fig. 16). The highest overall efficiency is obtained by 1-butene (3.78%) and this is followed by *trans*-2-butene (3.69%) and *cis*-2-butene (3.72%).

4.5. Environmental and safety impacts

In this section, the environmental impact of the fluids in terms of the contribution to the global warming and the safety characteristics of the fluids such as flammability and toxicity are discussed and the properties of the fluids are given in Table 10. It can be seen from Table 10 that some refrigerants such as HFCs and PFC have considerably high global warming potential. As an example, R236fa and RC318 have GWP of 6300 and 10,300 respectively. On the other hand, HFEs, HFOs and HCs have a negligible global warming potential [37–39]. Another environmental concern of the fluids is the flammability and toxicity. Hydrocarbons are more flammable compared to the other fluid categories such as HFCs, HFEs and HFOs.

4.6. Overall analysis of the thermofluids

In general, as it is stated by several researchers there is no fluid which can satisfy all the conditions such as providing high thermal

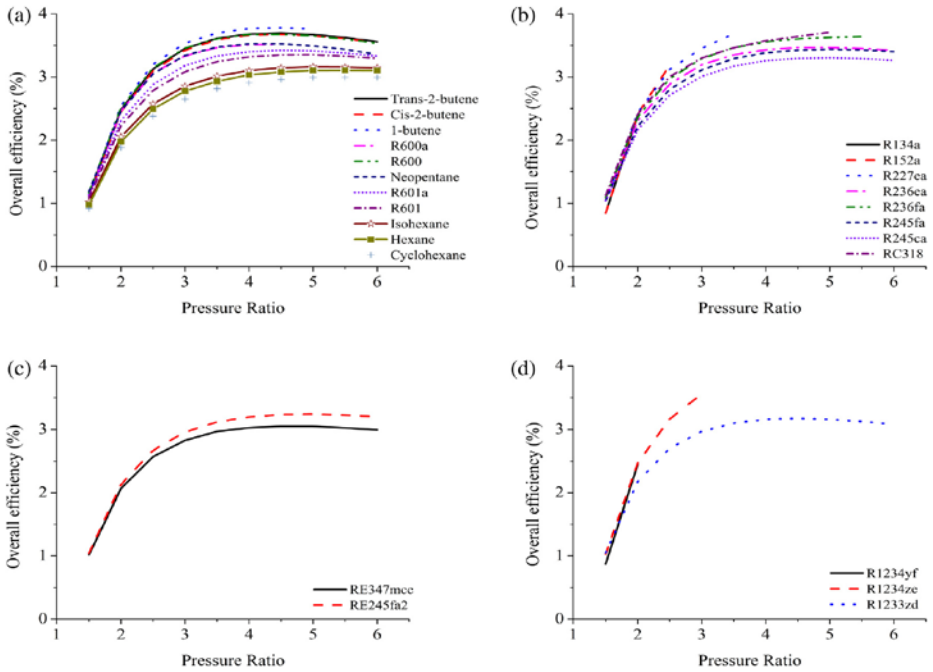

Fig. 16. Overall efficiency varies with pressure ratio for (a) HCs, (b) HFC-PFCs, (c) HFEs, (d) HFOs.

Table 10
Environmental and safety data of the considered fluids.

Fluid	Alt. name	Type	GWP	Safety
Trans-2-butene		HC	~20 [33]	–
Cis-2-butene		HC	~20 [33]	–
1-butene		HC	~20 [33]	–
Isobutane	R600a	HC	~20 [33]	A3 [19]
Butane	R600	HC	~20 [33]	A3 [19]
Neopentane		HC	~20 [33]	–
Isopentane	R601a	HC	~20 [33]	A3 [40]
Pentane	R601	HC	~20 [33]	A3 [41]
Isohexane		HC	~20 [33]	–
Hexane		HC	~20 [33]	–
Cyclohexane		HC	~20 [33]	A3 [19]
1,1,1,2-tetrafluoroethane	R134a	HFC	1370 [33]	A1 [19]
1,1-difluoroethane	R152a	HFC	133 [33]	A2 [19]
1,1,1,2,3,3,3-heptafluoropropane	R227ea	HFC	3500 [42]	A1 [18]
1,1,1,2,3,3-hexafluoropropane	R236ea	HFC	1410 [33]	–
1,1,1,3,3,3-hexafluoropropane	R236fa	HFC	6300 [42]	A1 [43]
1,1,1,3,3-pentafluoropropane	R245fa	HFC	1050 [33]	B1 [18]
1,1,2,2,3-pentafluoropropane	R245ca	HFC	726 [33]	–
Octafluorocyclobutane	RC318	PFC	10,300 [35]	A1 [19]
Methyl-heptafluoropropyl-ether	RE347mcc	HFE	450 [44]	Non-flammable [44]
2,2,2-trifluoroethyl-difluoromethyl-ether	RE245fa2	HFE	659 [45]	–
2,3,3,3-Tetrafluoropropene	R1234yf	HFO	4 [46]	A2L [35]
Trans-1,3,3,3-tetrafluoropropene	R1234ze	HFO	6 [47]	A2L [35]
Trans-1-chloro-3,3,3-trifluoropropene	R1233zd	HFO	7 [48]	A1 [48]

A: Lower toxicity, B: Higher toxicity, 1: Non-flammable, 2: Lower flammability 3: Higher flammability.

efficiency and net work output, having reasonable saturation points and low GWP and being non-flammable [19,28].

The selection of the most suitable thermofluid for the proposed solar ORC depends on the decision criteria. For instance, R600a, R600 and cyclohexane show high thermal efficiency and net work output but they have flammability problems. Furthermore, R236fa, R227ea have high GWP, R134a, R152a, R1234yf, R1234ze represents high saturation pressure, and R245fa has toxicity issue. One

way to restrain the flammability and GWP of the compounds is blending them with other compounds that have lower flammability and GWP.

In addition to the environmental benefits, the system performance could also be improved by using a mixture as the limitations on the cycle operating conditions and thermodynamic and physical properties are enhanced [49,50]. Lastly, the selected fluid should not be corrosive to eliminate major corrosion problems in the cycle components in terms of the durability of the system.

5. Conclusion

A small scale solar ORC has been modelled thermodynamically and the cycle simulations with 24 working fluids are studied in this research. In the simulation analyses, the effect of each working fluid on each component as well as the whole cycle at various pressure ratios of the cycle is investigated.

The simulation results reveal that pressure ratio, in other words evaporating pressure of the cycle, has a significant effect on the collector and expander efficiency and therefore, on the net work output and thermal efficiency of the cycle.

The simulation results also showed that in general, HCs such as *trans*-2-butene, *cis*-2-butene, 1-butene, R600a, R600, R601, R601a, neopentane, HFCs such as R227ea, R236fa, and RC318 (PFC) and R1234ze (HFO) yield higher values of net work output of the cycle.

Furthermore, the working fluid plays a key role in the operation of the solar ORC. For instance, fluids with relatively low boiling temperature, such as R134a, R152a, R227ea, R1234yf, and R1234ze, lead to an increase in the evaporation pressure that might limit their application in the collector. The other important parameter is the environmental impacts of the thermo-fluids. For example, although the HCs provide high solar ORC performance, one of the disadvantages of hydrocarbons is their high flammability. In addition to the flammability issue of the fluids, toxicity for R245fa and global warming potential for RC318, R134a and R236fai are the other environmental limitations of these fluids. On the other hand, although, HFEs (RE347mcc and RE245fa2) and HFOs (R1234yf andR1233zd) offer a moderate system performance, they are viable thermo-fluids for the proposed solar ORC based on their thermo-physical characteristics, low GWP and safety issues.

Finally, it is suggested that a mixture of two components can be used in order to eliminate the problems such as flammability, toxicity and global warming potential that might occur when pure components are utilised in the solar ORC.

Acknowledgment

The authors would like to acknowledge financial and in-kind support provided by Future Energy Source (FES) Ltd UK to conduct this research.

References

[1] Qiu G. Selection of working fluids for micro-CHP systems with ORC. Renew Energy 2012;48:565–70.
[2] Boyle G, Everett B, Ramage J, University TO. Energy systems and sustainability. Oxford: Oxford University Press; 2003.
[3] Mekhilef S, Saidur R, Safari A. A review on solar energy use in industries. Renew Sustain Energy Rev 2011;15:1777–90.
[4] Chen H, Goswami DY, Stefanakos EK. A review of thermodynamic cycles and working fluids for the conversion of low-grade heat. Renew Sustain Energy Rev 2010;14:3059–67.
[5] He C, Liu C, Gao H, Xie H, Li Y, Wu S, et al. The optimal evaporation temperature and working fluids for subcritical organic Rankine cycle. Energy 2012;38:136–43.
[6] Roy J, Misra A. Parametric optimization and performance analysis of a regenerative organic Rankine cycle using R-123 for waste heat recovery. Energy 2012;39:227–35.
[7] Manolakos D, Papadakis G, Mohamed ES, Kyritsis S, Bouzianas K. Design of an autonomous low-temperature solar Rankine cycle system for reverse osmosis desalination. Desalination 2005;183:73–80.
[8] Manolakos D, Papadakis G, Kyritsis S, Bouzianas K. Experimental evaluation of an autonomous low-temperature solar Rankine cycle system for reverse osmosis desalination. Desalination 2007;203:366–74.
[9] Manolakos D, Kosmadakis G, Kyritsis S, Papadakis G. On site experimental evaluation of a low-temperature solar organic Rankine cycle system for RO desalination. Sol Energy 2009;83:646–56.
[10] Wang X, Zhao L, Wang J, Zhang W, Zhao X, Wu W. Performance evaluation of a low-temperature solar Rankine cycle system utilizing R245fa. Sol Energy 2010;84:353–64.
[11] Wang J, Zhao L, Wang X. An experimental study on the recuperative low temperature solar Rankine cycle using R245fa. Appl Energy 2012;94:34–40.
[12] Yamaguchi H, Zhang X, Fujima K, Enomoto M, Sawada N. Solar energy powered Rankine cycle using supercritical CO 2. Appl Therm Eng 2006;26:2345–54.
[13] Zhang X-R, Yamaguchi H, Uneno D. Experimental study on the performance of solar Rankine system using supercritical CO2. Renew Energy 2007;32:2617–28.
[14] Rayegan R, Tao Y. A procedure to select working fluids for Solar organic Rankine cycles (ORCs). Renew Energy 2011;36:659–70.
[15] Delgado-Torres AM, García-Rodríguez L. Analysis and optimization of the low-temperature solar organic Rankine cycle (ORC). Energy Convers Manage 2010;51:2846–56.
[16] Marion M, Voicu I, Tiffonnet A-L. Study and optimization of a solar subcritical organic Rankine cycle. Renew Energy 2012;48:100–9.
[17] Wang M, Wang J, Zhao Y, Zhao P, Dai Y. Thermodynamic analysis and optimization of a solar-driven regenerative organic Rankine cycle (ORC) based on flat-plate solar collectors. Appl Therm Eng 2013;50:816–25.
[18] Baral S, Kim KC. Thermodynamic modeling of the solar organic Rankine cycle with selected organic working fluids for cogeneration. Distrib Gener Altern Energy J 2014;29:7–34.
[19] Tchanche BF, Papadakis G, Lambrinos G, Frangoudakis A. Fluid selection for a low-temperature solar organic Rankine cycle. Appl Therm Eng 2009;29:2468–76.
[20] Helvaci H, Khan ZA. Mathematical modelling and simulation of multiphase flow in a flat plate solar energy collector. Energy Convers Manage 2015;106:139–50.
[21] Klein S. Calculation of flat-plate collector loss coefficients. Sol Energy 1975;17:79–80.
[22] Incropera FP. Fundamentals of heat and mass transfer. John Wiley & Sons; 2011.
[23] Shah M. Chart correlation for saturated boiling heat transfer: equations and further study; 1982.
[24] Helvaci HU, Khan ZA. Experimental study of thermodynamic assessment of a small scale solar thermal system. Energy Convers Manage 2016;117:567–76.
[25] Kolasiński P. The Influence of the heat source temperature on the multivane expander output power in an organic Rankine cycle (ORC) system. Energies 2015;8:3351–69.
[26] Quoilin S. Sustainable energy conversion through the use of organic Rankine cycles for waste heat recovery and solar applications. Belgium: University of Liège; 2011.
[27] Gnutek Z, Kolasiński P. The application of rotary vane expanders in organic Rankine cycle systems—thermodynamic description and experimental results. J Eng Gas Turbines Power 2013;135:061901.
[28] Quoilin S, Declaye S, Tchanche BF, Lemort V. Thermo-economic optimization of waste heat recovery organic Rankine cycles. Appl Therm Eng 2011;31:2885–93.
[29] Kim YM, Shin DG, Kim CG. Optimization of design pressure ratio of positive displacement expander for vehicle engine waste heat recovery. Energies 2014;7:6105–17.
[30] Wang J, Yan Z, Wang M, Ma S, Dai Y. Thermodynamic analysis and optimization of an (organic Rankine cycle) ORC using low grade heat source. Energy 2013;49:356–65.
[31] Liu Q, Shen A, Duan Y. Parametric optimization and performance analyses of geothermal organic Rankine cycles using R600a/R601a mixtures as working fluids. Appl Energy 2015;148:410–20.
[32] Lemmon E, Huber M, McLinden M. NIST reference database 23: reference fluid thermodynamic and transport properties-REFPROP, version 9.1. Standard reference data program; 2013.
[33] Zhai H, Shi L, An Q. Influence of working fluid properties on system performance and screen evaluation indicators for geothermal ORC (organic Rankine cycle) system. Energy 2014;74:2–11.
[34] Bao J, Zhao L. A review of working fluid and expander selections for organic Rankine cycle. Renew Sustain Energy Rev 2013;24:325–42.
[35] Vivian J, Manente G, Lazzaretto A. A general framework to select working fluid and configuration of ORCs for low-to-medium temperature heat sources. Appl Energy 2015;156:727–46.
[36] Husband W, Beyene A. Low-grade heat-driven Rankine cycle, a feasibility study. Int J Energy Res 2008;32:1373–82.
[37] Helvaci H, Khan ZA. Heat transfer and entropy generation analysis of HFE 7000 based nanorefrigerants. Int J Heat Mass Transf 2017;104:318–27.

[38] Granryd E. Hydrocarbons as refrigerants—an overview. Int J Refrig 2001;24:15–24.
[39] Invernizzi CM, Iora P, Preßinger M, Manzolini G. HFOs as substitute for R-134a as working fluids in ORC power plants: a thermodynamic assessment and thermal stability analysis. Appl Therm Eng 2016;103:790–7.
[40] Designation N. Safety classification of refrigerants. ASHRAE Standard, ANSI/ASHRAE; 1993.
[41] Juhasz JR, Simoni LD. A review of potential working fluids for low temperature organic rankine cycles in waste heat recovery. In: 3rd international seminar on ORC, Brussels, Belgium. p. 12–4.
[42] Wang Z, Zhou N, Guo J, Wang X. Fluid selection and parametric optimization of organic Rankine cycle using low temperature waste heat. Energy 2012;40:107–15.
[43] Kosmadakis G, Manolakos D, Kyritsis S, Papadakis G. Comparative thermodynamic study of refrigerants to select the best for use in the high-temperature stage of a two-stage organic Rankine cycle for RO desalination. Desalination 2009;243:74–94.
[44] Tsai W-T. Environmental risk assessment of hydrofluoroethers (HFEs). J Hazard Mater 2005;119:69–78.
[45] Striebig B, Ogundipe AA, Papadakis M. Engineering applications in sustainable design and development. Nelson Education; 2015.
[46] Ayachi F, Ksayer EB, Zoughaib A, Neveu P. ORC optimization for medium grade heat recovery. Energy 2014;68:47–56.
[47] Feidt M, Kheiri A, Pelloux-Prayer S. Performance optimization of low-temperature power generation by supercritical ORCs (organic Rankine cycles) using low GWP (global warming potential) working fluids. Energy 2014;67:513–26.
[48] Molés F, Navarro-Esbrí J, Peris B, Mota-Babiloni A, Barragán-Cervera Á, Kontomaris KK. Low GWP alternatives to HFC-245fa in organic Rankine cycles for low temperature heat recovery: HCFO-1233zd-E and HFO-1336mzz-Z. Appl Therm Eng 2014;71:204–12.
[49] Wang J, Zhao L, Wang X. A comparative study of pure and zeotropic mixtures in low-temperature solar Rankine cycle. Appl Energy 2010;87:3366–73.
[50] Song J, Gu C-W. Analysis of ORC (organic Rankine cycle) systems with pure hydrocarbons and mixtures of hydrocarbon and retardant for engine waste heat recovery. Appl Therm Eng 2015;89:693–702.

Paper IV

Proceedings of the ASME 2017 Power and Energy Conference
PowerEnergy2017
June 26-30, 2017, Charlotte, North Carolina, USA

PowerEnergy2017-3194

A THORETICAL AND EXPERIMENTAL STUDY OF HFE-7000 IN A SMALL SCALE SOLAR ORGANIC RANKINE CYCLE AS A THERMOFLUID

Huseyin Utku Helvaci
Nano Corr, Energy and Modelling Research Group
Bournemouth University
Bournemouth, UK

Zulfiqar Ahmad Khan
Nano Corr, Energy and Modelling Research Group
Bournemouth University
Bournemouth, UK

ABSTRACT

Renewable energy technologies and sources have been playing a key role in reducing reliance on fossil fuels and significantly reducing CO_2 emissions and its footprint. EU initiative of generating 50% of the energy needs through sustainable sources by 2050 needs a direct response in terms of providing applied solutions to realize this target on time. Solar energy is one of the major and abundantly renewable energy sources which are free and clean. Solar energy can be utilized by means of solar Photovoltaic (PV) or solar collectors. Concentrating solar collectors supply thermal energy from medium to high grade where as non-concentrating collectors (flat plate) delivers low-grade thermal energy. The use of thermofluids with boiling temperatures lower than the water, allows the operation of low grade solar thermal systems on an Organic Rankine Cycle (ORC) to generate both mechanical and heat energy. At the same time, the selection of appropriate thermofluid is an important process and has a significant effect both on the system performance and the environment. Conventional thermofluids such as Chlorofluorocarbons (CFCs) and Hydrochlorofluorocarbons (HCFCs) have high ozone depletion (ODP) and high global warming (GWP) potential. It is therefore important to investigate novel and environmentally friendly thermofluids to address environmental impacts as global warming and ozone layer depletion. Hydrofluoroethers (HFEs) are non-ozone depleting substances and they have relatively low GWP. Therefore, HFEs can be used as a replacement for CFCs and HCFCs. In this study, a solar ORC is designed and commissioned to use HFE 7000 as a thermofluid. The proposed system consists of a flat-plate solar collector, a vane expander, a condenser and a pump where the collector and the expander are used as the heat source and prime mover of the cycle respectively. The performance of the system is determined through energy analysis. Then, a mathematical model of the cycle is developed to perform the simulations using HFE-7000 at various expander pressure. Experimental data indicated that the efficiency and the net mechanical work output of the cycle was found to be 3.81% and 135.96 W respectively. The simulation results showed that increasing the pressure ratio of the cycle decreased the amount of the heat that is transferred to HFE 7000 in the collector due to the increased heat loss from the collector to the environment. Furthermore, net output of the system followed a linear augmentation as the pressure ratio of the system increased. In conclusion, both the experimental and theoretical research indicates that HFE 7000 offers a viable alternative to be used efficiently in small scale solar ORCs to generate mechanical and heat energy.

INTRODUCTION

Renewable energy sources such as solar energy can be classified as a low-grade temperature heat source and it is crucial to utilize low-grade heat sources in terms of meeting the World electricity demand [1]. Organic Rankine cycle (ORC) has the same configuration as the conventional Rankine cycle with the exception of working fluid that is used in the cycle [2]. Organic compounds with lower boiling temperature allow ORCs to utilize low-grade temperature heat sources efficiently [3]. Solar sourced ORC which consists of solar collectors such as evacuated tube (ETC), flat-plate (FPC) and parabolic trough collectors (PTC) combined with ORC unit can generate heat with temperature ranging from 80-150 ℃ to generate mechanical power [4].

An important number of experimental studies have been conducted to convert solar thermal energy into mechanical, as well as electric power by using solar sourced ORCs. Manolakos et al. conducted an experimental study to investigate the performance of a solar ORC employing HFC-134a for reverse osmosis desalination [5-7]. A solar ORC considering FPC and ETC was investigated in [8]. In their study, HFC-245fa refrigerant was used as a working fluid and the collector efficiencies were found to be 55.2% and 71.6% respectively. A thermal efficiency of a solar ORC, including heat regeneration

with the working fluid of HFC-245fa was found to be 9% in [9]. In addition to HFC-134a and HFC-245fa, CO_2 was also utilized as a working fluid in several solar ORC applications. For instance, Zhang et al. analyzed the performance of supercritical solar ORC, using CO_2 [10]. They revealed that the cycle efficiency was found to be 8.78-9.45%. Another solar ORC system, using CO_2 was examined by [11]. They reported that the solar collector generated heat with temperature of 165 °C and the cycle efficiency was 25%. In order to address the variability nature of solar energy sensible heat storage (SHS) system has been used in solar ORCs [12]. For instance, a dynamic simulation study of flat-plate collectors based solar ORC system using an oil storage tank was conducted by [12]. Another solar ORC analysis, including SHS was performed in Ref. [13]. Wang et al. presented a regenerative solar ORC, where a thermal storage system was utilized to store the collected heat in the system [14]. In addition to SHSs, latent heat storage (LHS) systems can also be applied to solar thermal power applications [15, 16].

Selection of an appropriate working fluid is an important process as it has a crucial effect on the performance of ORCs. In addition to this, environmental and safety impacts of a fluid such as ozone depletion potential (ODP), global warming potential (GWP), flammability and toxicity should be considered. Therefore, working fluid selection studies for a small scale solar ORC have been conducted by several researchers [17]. A theoretical study of a solar ORC, where solar collector was employed as thermal energy source of the ORC was conducted by [18]. In their study, twelve thermofluids including hydrocarbons (HCs), Hydrofluorocarbons (HFCs) and ammonia were analyzed. A theoretical and experimental analysis of a solar ORC with FPC using HFC-134a, HFC-227ea and HFC-365mfc was performed by [19]. The results showed that HFC-365mfc was the most efficient fluid. Rayegan simulated a solar ORC, using 117 organic compounds. It was claimed that compounds with higher critical temperature are better options for ORC applications [3]. In another simulation study of a solar thermal power cycle, HFC-245fa and HFC-134a were recommended to be utilized as the working fluids of the cycle [20].

It is stated that for an efficient ORC application in terms of obtaining maximum power output from a heat source, the challenge lies in choosing an appropriate working fluid and defining the cycle parameters according to the selected fluid [21]. A small scale solar ORC, where a flat-plate collector was employed as the direct heat source was constructed and the experimental tests of the cycle were conducted in order to evaluate the performance characteristics of the cycle through energy analysis in this study. As the working fluid of the cycle, new generation HFE-7000 refrigerant was utilized. Then, the solar ORC was mathematically modeled to simulate the cycle using the same working fluid (HFE-7000). The simulations were performed under various expander pressures to determine its effect on the collector, the expander and the whole cycle performance. Finally, the optimum expander pressure that provides the maximum amount of net work output of the cycle was evaluated.

NOMENCLATURE

Nomenclature

A	area, m^2	f	fluid
C_p	specific heat, J/kg K	g	vapor
D	diameter, m	i	Inner
e	eccentricity, m	in	inlet, incoming
F	fin efficiency	int	intake
F_R	heat removal factor	l	liquid
h	heat transfer coefficient, W/m^2K	mec	mechanical
H	Enthalpy, J/kg	o	outer
H_{fg}	Heat of vaporization, J/kg	out	outlet
k	thermal conductivity, W/m K	ov	over
$\dot{m}$	Mass flow rate, kg/s	p	plate
n	number of vanes	rot	rotor
r	radius, m	s	isentropic
S	solar radiation, W/m^2	sp	single phase
T	temperature, °C	$stat$	stator
U	heat loss coefficient, W/m^2K	tp	two phase
Q	heat, W	T	total
V	Volume, m^3	u	useful
W	work, kW	ud	under
		wf	working fluid

Subscripts

		Greek symbols	
a	Ambient	$\tau\alpha$	transmittance - absorbance product
col	Collector	δ	absorber plate thickness, mm
$cond$	Condensation	v	specific volume, m^3/kg
dsg	designed	θ	angle of a specific vane from the origin
$evap$	evaporation	η	efficiency
exh	exhaust		
exp	expander		

EXPERIMENTAL

A solar organic Rankine cycle test rig, utilizing HFE-7000 was built and commissioned to evaluate the cycle performance in this section. HFE-7000 refrigerant which is a Hydrofluoroether (HFE) is a non-ozone depleting refrigerant. It also has relatively low GWP [22]. The proposed system consists of a collector, a vane expander, a condenser, a liquid reservoir and a pump (Figure 1). The cycle operates on four main processes which are:

- compression of the liquid HFE-7000 from low pressure to high pressure (Figure 1, state 2)

- conversion of solar radiation into heat and heat addition to the working fluid in the collector (Figure 1, state 3)
- Expansion of HFE-7000 in the expander and generation of mechanical energy (Figure 1, state 4)
- Heat rejection and condensation of the working fluid in the condenser (Figure 1, state 1)

The specifications of each component of the solar ORC can be found in Ref. [23].

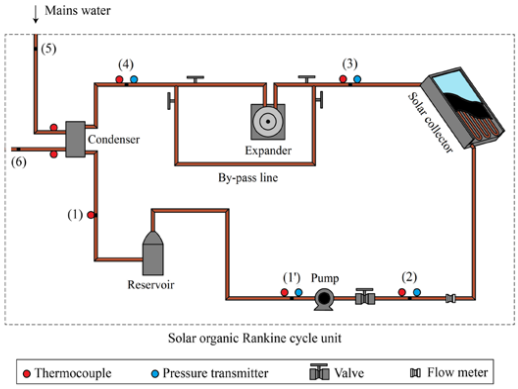

Figure 1 Schematic diagram of the solar ORC [23]

Initially, the leak test of the system was conducted prior to the system experiments to observe if there was any leakage somewhere in the system. As the cycle did not show any sign of leakage, 8 kg (5.7 L) of working fluid was introduced into the cycle through the liquid reservoir. Then, the pump and the condenser were turned on to let the water and HFE-7000 circulates in the system with no heat input. This was performed to check the reliability of the system. Then, the data acquisition unit and the solar simulator were turned on to initiate the experiment. During the experiments, a solar simulator was used to provide a stable energy to the cycle. Initially, the expander by-pass line of the expander was on to avoid any liquid going through the expander. As the HFE-7000 temperature and pressures were monitored, the by-pass line of the expander was closed when the liquid reached the vapor conditions. Thus, the vapor expands in the expander and generates mechanical energy by rotating the expander shaft. Finally, post the expander, the fluid condensed in the condenser and was pumped to the flat-plate collector to complete the cycle. The experimental methodology, including the locations of the thermocouples and pressure transmitters, specification of the flow meter is comprehensively reported in Ref. [23]. During the experiment, an average radiation of 890 W/m2 was supplied on the collector surface. A detailed description of the measurement of the radiation on the surface of the collector by using a pyranometer can be found in Ref. [23].

THEORY

Flat-plate collector:

Previously, the serpentine tube flat-plate collector which is utilized in this study was modeled and validated against experimental data in Ref. [24]. Initially, the solar energy on the absorber plate (Q_p) and the useful energy (Q_u) are calculated by using the formulas below;

$$Q_p = A_p\left(S_{in}(\tau\alpha) - U_T\left(T_p - T_a\right)\right) \quad (1)$$

$$Q_u = A_p F_R\left(S_{in}(\tau\alpha) - U_T\left(T_{f,in} - T_a\right)\right) \quad (2)$$

A_p, S_{in} and $\tau\alpha$ represent the collector area, incoming solar radiation and transmittance-absorbance product respectively. The collector heat balance is shown in Figure 2.

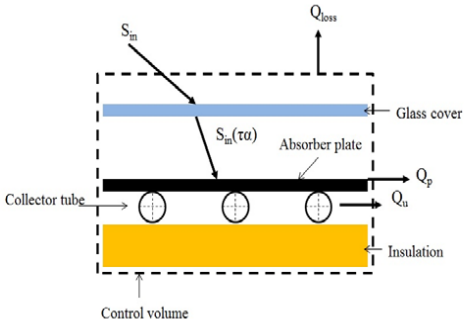

Figure 2 Collector heat balance

Therefore, the first product of the right hand side of Eq. (1-2) indicates the solar radiation travelling through the glass cover where some portion of the heat is lost to the ambient. U_T is the total heat loss coefficient and it consists of the top and the back heat losses. The calculation of the total heat transfer coefficient was explained by Klein [25]. It is important to note that the edge heat transfer loss was neglected in this study. Then, some portion of the energy that is absorbed on the collector surface is also lost to the atmosphere through the convection losses and the remaining is transferred to the working fluid. The amount of the heat that is transferred to the working fluid is called *'useful energy'* and it is calculated by using Eq. (2). The difference between Eq. (1) and Eq. (2) is that instead of the plate temperature T_p, fluid inlet temperature $T_{f,in}$ is taken into account to calculate the heat transfer losses with the addition of the collector heat removal factor (F_R). Equation (3) estimates the heat removal factor as:

$$F_R = \frac{\dot{m} C_p}{A_p U_T}\left(1 - exp\left(-\frac{A_p U_T F'}{\dot{m} C_p}\right)\right) \quad (3)$$

where F' represents the collector efficiency factor and it is calculated by Equation (4);

$$F' = \frac{(U_T)^{-1}}{W(U_T(D_o + (W - D_o)F))^{-1} + (C_b)^{-1} + (\pi D_i h_f)^{-1}} \quad (4)$$

where F indicates the fin efficiency.

$$F = \frac{tanh(m(W - D_o/2))}{m(W - D_o/2)}; \qquad m = \sqrt{\frac{U_T}{k\delta}} \quad (5)$$

In Equation (4), h_f represents the heat transfer coefficient of the working fluid and it is estimated under two cases which are single phase and two-phase flow. The calculation of the heat transfer coefficient was explained comprehensively in Ref. [24].

Vane expander:

In the mathematical modelling of the expander, initially, the built-in volume ratio, which is the ratio of the working chambers' volumes at the end and of the expansion process and at the beginning of the expansion process was evaluated according to the geometrical characteristics of the expander [26]. The following formula was used to calculate the radius of the stator to the center of the rotor:

$$d(\theta) = -e \times sin\theta + \sqrt{(r_{stat})^2 - (e \times cos\theta)^2} \quad (6)$$

where r and e represent the eccentricity and radius. The volume of the working chamber as a function of the angular movement was calculated by using the formula below:

$$V(\theta) = A(\theta) \times L_{stat} \quad (7)$$

where $A(\theta)$ is the area of the working chamber and it can be determined as:

$$A(\theta) = \frac{1}{2} \int_{\theta}^{\theta + \frac{2\pi}{n}} (d(\theta)^2 - r_{rot}{}^2) d(\theta) \quad (8)$$

As the radius of the stator (r_{stat}) and the rotor (r_{rot}), length of the stator (L_{stat}), the eccentricity (e), intake (θ_{int}) and exhaust angles (θ_{exh}) are the known parameters, expander built-in volume ratio can be evaluated by using the formula below:

$$r_v = \frac{V_{exh}}{V_{int}} \quad (9)$$

In order to calculate the expander under and over- expansion losses, the designed pressure ratio of the expander was estimated as [27]:

$$PR_{dsg} = (r_v)^k \quad (10)$$

Under-expansion occurs if the operating pressure of the cycle ($P_{exp,in}/P_{exp,out}$) is greater than the designed pressure ratio of the expander, otherwise over-expansion arises. As the designed pressure ratio was calculated (Eq. 10), the work output and the losses of the expander under the under-expansion and over-expansion cases can be determined as [28]:

$$W_{exp,ud} = \dot{m}_{wf} \times \left(\begin{matrix} (H_{exp,in} - H_{exp,out,dsg,s}) \\ + (v_{exp,out} \times (P_{exp,out,dsg} - P_{exp,out})) \times 100 \end{matrix} \right) \times \eta_{mec} \quad (11)$$

$$W_{exp,ov} = \dot{m}_{wf} \times \left(\begin{matrix} (H_{exp,in} - H_{exp,out,dsg,s}) \\ - (v_{exp,out} \times (P_{exp,out,dsg} - P_{exp,out})) \times 100 \end{matrix} \right) \times \eta_{mec} \quad (12)$$

where H and v are the enthalpy and specific volume of the working fluid. η_{mec} represents the mechanical efficiency of the expander after frictional and heat transfer losses of the expander. In this study, the mechanical efficiency of the expander was taken as 0.7 [29].

Condenser:

The amount of the heat that is rejected from the condenser was calculated by using the following formula:

$$Q_{cond} = \dot{m}_{wf} \times (H_{cond,in} - H_{g,cond}) + \dot{m}_{wf} (H_{g,cond} - H_{l,cond}) \quad (13)$$

Pump:

The consumed work in the pump was estimated as follows:

$$W_{pump} = \frac{\dot{m}_{wf} \times v_{pump,in} \times (P_{evap} - P_{cond})}{\eta_{pump,s}} \quad (14)$$

$\eta_{pump,s}$ represents the isentropic pump efficiency and it was taken as 0.6.

Simulation procedure:

A computer code was developed in Matlab environment in order to simulate the proposed solar ORC. The fluid properties were taken from REFPROP 9.1 [30]. It is important to note that as HFE-7000 is a dry fluid, the system was modeled as a saturated cycle in other words, the fluid is saturated vapor and saturated liquid at the outlet of the collector and the condenser respectively. The pressure losses within the collector and the condenser were neglected. The simulations were performed at constant condensing temperature of 25 °C and various collector/expander pressure (1.06 - 4.27 bar). As it was mentioned that the pressure losses were assumed to be zero, corresponding saturation pressure at 25 °C represents the condensing pressure of the cycle. Similarly, corresponding temperature at collector/expander pressure indicates the evaporating temperature of the cycle. The simulation procedure starts with the calculation of the fluid properties at the collector inlet. As the fluid is saturated liquid at 25 °C at the condenser outlet, the enthalpy at the collector inlet was calculated by using the formula below:

$$H_{col,in} = w_{pump} + (H_{cond,out} \times 1000) \quad (15)$$

where w_{pump} represents the specific pump work and it can be determined as:

$$w_{pump} = \frac{v_{pump,in} \times (P_{evap} - P_{cond})}{\eta_{pump,s}} \quad (16)$$

The collector inlet temperature can be evaluated as the collector inlet enthalpy and the collector pressure are known. The numerical procedure was based on dividing the collector tube into small elements and determining the fluid outlet

temperature, collector plate temperature, the working fluid heat gain and the collector heat loss at the end of each element, as well as the collector outlet by using the known fluid temperature at the collector inlet and the fluid mass flow rate. The fluid entered the collector as a sub-cooled liquid and it gained energy as it circulated in the collector tube. The single-phase flow calculations were applied as the fluid remains in the sub-cooled region. When the fluid temperature reached the corresponding saturation temperature, then the two-phase flow calculations were utilized in the analysis. As the fluid vapor quality reached 1 before the end of the collector tube, the single phase flow calculations were applied again. Therefore, the fluid left the collector as a super-heated vapor at the evaluated temperature. However, in this study, the collector inlet and outlet temperatures and the collector inlet and outlet enthalpies are the known parameters as it was assumed that the fluid leaves the collector as saturated vapor at the corresponding collector pressure whereas the flow rate of the working fluid is an unknown parameter. Therefore, it is crucial to determine at which element the fluid reaches the saturation points to apply corresponding flow calculations (single or two-phase flow). Initially, the collector tube was considered as two regions which are single-phase and two-phase. In order to determine the transition element where the fluid goes into the saturated region, the iteration begins by assuming that the fluid reaches the saturation conditions after the first element. This means that, if it is assumed that the tube was divided into 'j' elements, the single phase region covers 1 element, whereas the two-phase region covers j-1 elements. Then, the mass flow rate was calculated iteratively for both the single-phase and two-phase regions:

$$\dot{m}_{wf,sp} = \frac{Q_{gain,sp}}{\left(H_{col,in} - H_l\right)} \tag{17}$$

$$\dot{m}_{wf,tp} = \frac{Q_{gain,tp}}{\left(H_g - H_l\right)} \tag{18}$$

The iteration continued until the following criterion was satisfied:

$$\left|\dot{m}_{wf,sp} - \dot{m}_{wf,tp}\right| \le 0.0001 \tag{19}$$

This point represents the number of elements where HFE-7000 reached saturation condition. The collector specifications, the description of the iterative method for the fluid and plate temperature calculations, heat gain of the fluid and the collector heat loss determinations were described comprehensively in Ref. [24]. Once the, working fluid mass flow rate was calculated, the expander calculations were started to determine the built-in volume ratio and the expander designed outlet pressure with the help of Eq. (9-10). Then, the code evaluated the mechanical work of the expander according to its operating case (under or over expansion) by using Eq. (11-12). Post expander, the amount of the rejected heat and the consumed pump work was determined by using Eq. (13-14) respectively. The simulation conditions were given in Table 1.

Table 1 Parameters of the solar ORC simulations

Parameter	Value
Solar radiation (S_{in})	800 W/m^2
Condenser temperature (T_{cond})	25 °C
Ambient temperature (T_a)	15 °C
Expander pressure (P_{exp})	1.068 - 4.271 bar
Expander mechanical efficiency (η_{mec})	0.7
Pump isentropic efficiency (η_{pump})	0.6

Performance indicators:

The efficiency of the collector, the expander and the solar ORC were evaluated according to the equations below:

$$\eta_{col} = \frac{\dot{m}_{wf}\left(\left(C_p\left(T_{evap} - T_{col,in}\right)\right) + \left(H_g - H_l\right)\right)}{S_{in} \times A_{col}} \tag{20}$$

$$\eta_{exp} = \frac{W_{exp,isd}}{\dot{m}_{wf} \times \left(H_{exp,in} - H_{exp,out,s}\right)}$$

or

$$\eta_{exp} = \frac{W_{exp,av}}{\dot{m}_{wf} \times \left(H_{exp,in} - H_{exp,out,s}\right)} \tag{21}$$

$$\eta_{SORC} = \frac{W_{net}}{Q_{gain}} \tag{22}$$

where W_{net} is the net work output of the solar ORC and it was estimated as:

$$W_{net} = W_{exp} - W_{pump} \tag{23}$$

RESULTS AND DISCUSSION

Experimental results:

The working fluid flow rate was held constant at 0.022 kg/s during the experiments and all the thermodynamic properties of HFE-7000 at various states were taken from REFPROP 9.1 [30]. The temperature, pressure and enthalpy values of HFE-7000 at various states are given in Table 2.

Table 2 State properties of HFE-7000 and water [23]

State (No)	Phase	$\dot{m}$ (kg/s)	T (°C)	P (bar)	h (kJ/kg)
1	Liquid	0.022	19.54	0.66	223.56
1'	Liquid	0.022	18.73	0.57	222.57
2	Liquid	0.022	19.1	1.86	223.06
3	Gas	0.022	45.41	1.32	385.07
4	Gas	0.022	36.36	0.66	378.4
5	Liquid	0.06	13.47	0.66	56.63
6	Liquid	0.06	26.88	0.66	112.75

It can be seen that HFE-7000 entered the collector at 1.86 bar and 19.1 °C as a sub-cooled liquid. Then, its temperature increased to 45.41 °C and whereas its pressure decreased to 1.32 bar due to the friction losses in the collector. According to the corresponding temperature and pressure values, the fluid left the collector as a superheated vapor and flows through the expander. In the expander, HFE-7000 expanded and its temperature and pressure reduced to 36.36 °C and 0.66 bar respectively. This is where the mechanical energy was generated by rotating the expander shaft. All the state points of HFE-7000 are represented on a T-s diagram Figure 3.

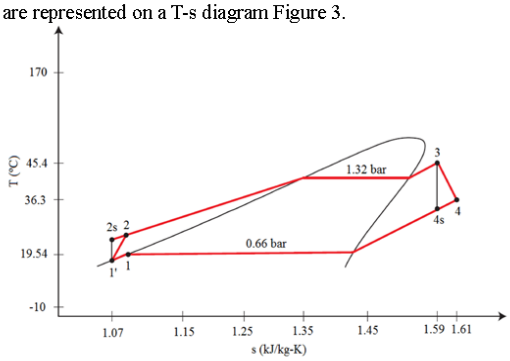

Figure 3 T-s diagram of HFE-7000 at various points [23]

Table 3 indicates that in the experiment, the collector received a 6194.4 W energy on its surface and 57.53% of this energy was transferred to the fluid as the useful heat gain of the fluid. The expander generated 146.74 W mechanical energy with an isentropic efficiency of 58.66 %. The similar efficiency value for a vane expander was reported in Ref. [31]. Finally, the net work output of the cycle was calculated as 135.96 W (W_{pump}= 10.78 W) and the thermal efficiency of the cycle was found to be 3.81% (Table 3).

Table 3 Collector and expander analysis [23]

Component	Parameter	Value
Flat-plate collector	Incoming solar radiation	6194.4 (W)
	Collector useful heat gain	3564.2 (W)
	Collector efficiency	57.53 (%)
Expander	Expander work output	146.74 (W)
	Expander efficiency	58.66 (%)
Solar ORC	Net work output	135.96 (W)
	Thermal efficiency	3.81 (%)

Simulation results:

Figure 4 shows the variation of the collector efficiency, collector heat gain, the collector temperature and collector heat loss with the expander pressure. As it can be observed that collector efficiency and collector heat gain decreased from 57.81% and 3219W to 41.95% and 2335.9W respectively as the expander pressure rose from 1.068 bar to 4.271 bar.

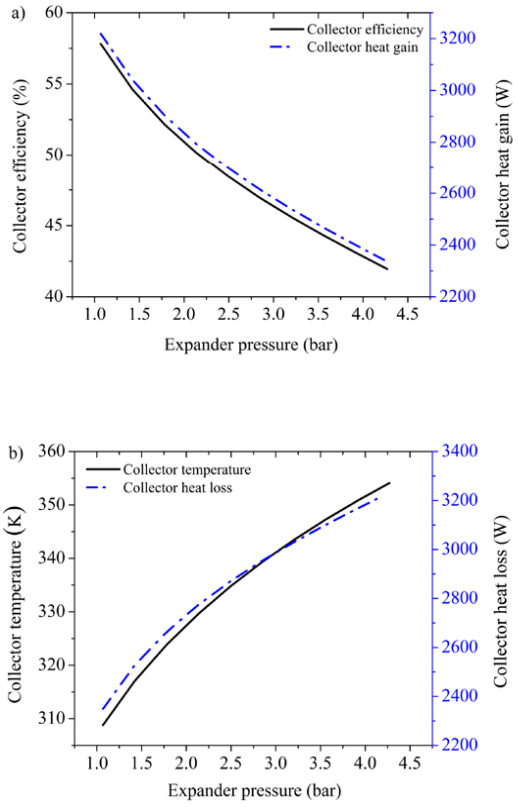

Figure 4 Collector analysis a) efficiency - heat gain b) temperature - heat loss

This can be explained by the fact that the increase in the expander inlet pressure in other words, in the collector pressure (the cycle is saturated) increased the fluid saturation points which resulted in a higher saturation temperature of the fluid, as well as a higher collector temperature. Due to the heat transfer losses from the collector to the ambient, the collector temperature and the collector heat losses augmented correspondingly as it can be seen from Figure 4. Similar findings were reported in Ref. [24].

The efficiency of the expander versus expander pressure is represented in Figure 5. The expander efficiency was 53.48% at 1.068 bar of expander pressure. This value increased to 69.13% as the expander pressure rose to 1.424 bar. These two expander pressure values fell on the left side of the dashed line which represents the over expansion case of the expander. Then, the expander efficiency reached its maximum value (69.67%) at expander pressure of 1.78 bar. This is where the expander

begins operating in under expansion case. After this point, the expander pressure decreased to 56.76% with the further increase in the expander pressure (Figure 5).

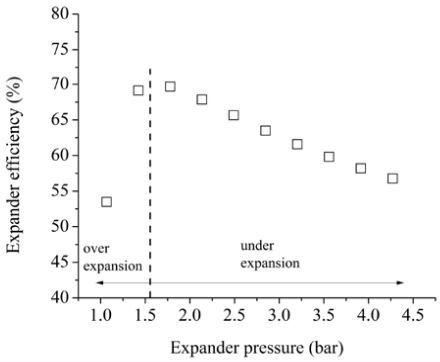

Figure 5 Expander efficiency versus expander pressure

Figure 6 represents the generated net work and the solar ORC thermal efficiency. The net work of the cycle rose from 56.78 W to 170.08 W as the expander pressure increased from 1.068 bar to 3.55 bar. This is also where the net work output reached its maximum point.

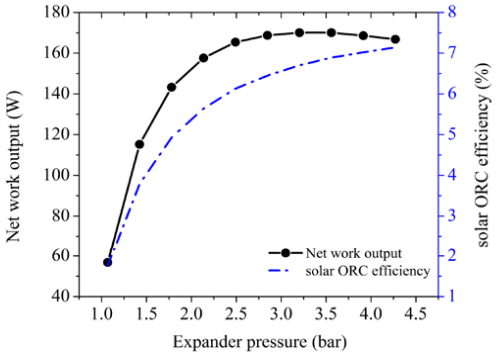

Figure 6 Solar ORC net work output and thermal efficiency

This augmentation can be explained by the fact that as the condenser temperature/pressure is constant, the increase in the expander pressure caused a higher enthalpy drop in the expander which resulted in an higher net work output of the cycle. Although, the pump work was augmented and the flow rate of HFE-7000 decreased with the increase in the pressure, the negative effects of the increased pump work and diminished flow rate was smaller than the increase in the amount of the enthalpy drop. However, this trend has changed since the expander pressure increased from 3.55 bar to 4.27 bar as the net work output decreased to 166.8 W. On the other hand, the thermal efficiency of the solar ORC continued to increase, yet the generated net work of the cycle did not enhance after the expander pressure of 3.55 bar. This is due to the drop in the amount of useful heat gain, which caused a gradual increase in the thermal efficiency of the cycle. Therefore, it is important to consider the thermal efficiency and the net work output of the cycle together where the collector (the direct heat source of the cycle) varies with the operating conditions such as expander pressure of the cycle.

Table 4 Optimization results of HFE-7000

Parameter	Value
Expander pressure (bar)	3.04
Collector efficiency (%)	46.16
Expander efficiency (%)	62.67
Cycle efficiency (%)	6.62
Net work output (W)	**170.43**

Regression analysis was conducted to predict net work output of the system, according to the expander pressure. The regression equation and the fitted line of the equation is represented in Figure 7. Optimization analysis was also performed to determine the optimum expander pressure value that provides the highest amount of the generated net work of the cycle. The optimization results were presented in Table 4. Optimization analysis indicated that the proposed cycle could generate 170.43 W of net work output with the thermal efficiency of 6.62% at 3.04 expander pressure.

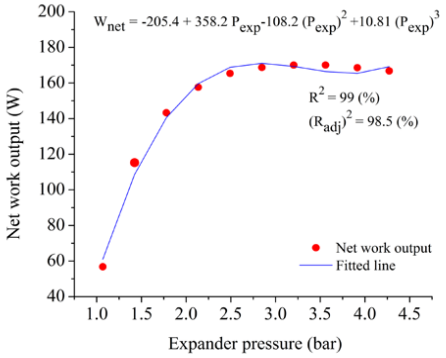

Figure 7 Fitted line plot

CONCLUSION

A small scale solar organic Rankine cycle was constructed and tested in this study. The cycle consists of a collector, an expander, a condenser and a pump. HFE-7000 was chosen as the working fluid of the cycle. Then, the system was numerically modeled as a saturated solar ORC and the simulations of the cycle were performed at a constant condenser temperature and various expander pressures. The experimental results showed that the flat-plate collector transferred 3564.2W heat to the working fluid with the efficiency of 57.53%. The

expander efficiency was found to be 58.66%. The proposed solar ORC provided 135.96W with a thermal efficiency of 3.81%. It was found from the simulation results that the expander pressure has a significant effect on the flat-plate collector, vane expander, as well as the cycle performance. For instance, increasing the expander pressure, which resulted in a rise in the collector saturation pressure/temperature, augmented the heat losses from the collector. Thus, the collector efficiency decreased with the increasing expander pressure (41.95%). Similarly, the variation in the expander pressure caused the expander to operate under two expansion cases (under and over expansion) which resulted in various expander efficiencies (53.48-69.67%). Therefore, the net work output of the cycle varied from 56.78W to 170.08W as the expander pressure increased from 1.068 bar to 4.271. The optimization analysis showed that the cycle generated the highest amount of the net work output (170.43W) at the expander pressure of 3.04 bar and the corresponding cycle efficiency was found to be 6.62. In overall, both the experimental and simulation results revealed that HFE-7000 provides a moderate cycle performance and offers a viable alternative to be utilized in such cycles.

ACKNOWLEDGMENTS

The authors would like to acknowledge financial and in-kind support provided by Bournemouth University, UK and Future Energy Sources (FES) Ltd. UK to conduct this research.

REFERENCES

[1] Chen, H., Goswami, D. Y., and Stefanakos, E. K., 2010, "A review of thermodynamic cycles and working fluids for the conversion of low-grade heat," Renewable and sustainable energy reviews, 14(9), pp. 3059-3067.
[2] Tchanche, B. F., Lambrinos, G., Frangoudakis, A., and Papadakis, G., 2011, "Low-grade heat conversion into power using organic Rankine cycles–a review of various applications," Renewable and Sustainable Energy Reviews, 15(8), pp. 3963-3979.
[3] Rayegan, R., and Tao, Y., 2011, "A procedure to select working fluids for Solar Organic Rankine Cycles (ORCs)," Renewable Energy, 36(2), pp. 659-670.
[4] Mavrou, P., Papadopoulos, A. I., Stijepovic, M. Z., Seferlis, P., Linke, P., and Voutetakis, S., 2015, "Novel and conventional working fluid mixtures for solar Rankine cycles: Performance assessment and multi-criteria selection," Applied Thermal Engineering, 75, pp. 384-396.
[5] Manolakos, D., Papadakis, G., Mohamed, E. S., Kyritsis, S., and Bouzianas, K., 2005, "Design of an autonomous low-temperature solar Rankine cycle system for reverse osmosis desalination," Desalination, 183(1), pp. 73-80.
[6] Manolakos, D., Papadakis, G., Kyritsis, S., and Bouzianas, K., 2007, "Experimental evaluation of an autonomous low-temperature solar Rankine cycle system for reverse osmosis desalination," Desalination, 203(1), pp. 366-374.
[7] Manolakos, D., Kosmadakis, G., Kyritsis, S., and Papadakis, G., 2009, "On site experimental evaluation of a low-temperature solar organic Rankine cycle system for RO desalination," Solar Energy, 83(5), pp. 646-656.
[8] Wang, X., Zhao, L., Wang, J., Zhang, W., Zhao, X., and Wu, W., 2010, "Performance evaluation of a low-temperature solar Rankine cycle system utilizing R245fa," Solar Energy, 84(3), pp. 353-364.
[9] Bryszewska-Mazurek, A., Świeboda, T., and Mazurek, W., 2011, "Performance Analysis of a Solar-Powered Organic Rankine Cycle Engine," Journal of the Air & Waste Management Association, 61(1), pp. 3-6.
[10] Zhang, X.-R., Yamaguchi, H., and Uneno, D., 2007, "Experimental study on the performance of solar Rankine system using supercritical CO2," Renewable Energy, 32(15), pp. 2617-2628.
[11] Yamaguchi, H., Zhang, X., Fujima, K., Enomoto, M., and Sawada, N., 2006, "Solar energy powered Rankine cycle using supercritical CO 2," Applied Thermal Engineering, 26(17), pp. 2345-2354.
[12] Calise, F., d'Accadia, M. D., Vicidomini, M., and Scarpellino, M., 2015, "Design and simulation of a prototype of a small-scale solar CHP system based on evacuated flat-plate solar collectors and Organic Rankine Cycle," Energy Conversion and Management, 90, pp. 347-363.
[13] Freeman, J., Hellgardt, K., and Markides, C. N., 2015, "An assessment of solar-powered organic Rankine cycle systems for combined heating and power in UK domestic applications," Applied Energy, 138, pp. 605-620.
[14] Wang, J., Yan, Z., Wang, M., Ma, S., and Dai, Y., 2013, "Thermodynamic analysis and optimization of an (organic Rankine cycle) ORC using low grade heat source," Energy, 49, pp. 356-365.
[15] Khan, Z., Khan, Z., and Ghafoor, A., 2016, "A review of performance enhancement of PCM based latent heat storage system within the context of materials, thermal stability and compatibility," Energy Conversion and Management, 115, pp. 132-158.
[16] Khan, Z., Khan, Z., and Tabeshf, K., 2016, "Parametric investigations to enhance thermal performance of paraffin through a novel geometrical configuration of shell and tube latent thermal storage system," Energy Conversion and Management, 127, pp. 355-365.
[17] Aljundi, I. H., 2011, "Effect of dry hydrocarbons and critical point temperature on the efficiencies of organic Rankine cycle," Renewable Energy, 36(4), pp. 1196-1202.
[18] Delgado-Torres, A. M., and García-Rodríguez, L., 2010, "Analysis and optimization of the low-temperature solar organic Rankine cycle (ORC)," Energy Conversion and Management, 51(12), pp. 2846-2856.
[19] Marion, M., Voicu, I., and Tiffonnet, A.-L., 2012, "Study and optimization of a solar subcritical organic Rankine cycle," Renewable Energy, 48, pp. 100-109.
[20] Baral, S., and Kim, K. C., 2014, "Thermodynamic modeling of the solar organic Rankine cycle with selected organic working fluids for cogeneration," Distributed Generation & Alternative Energy Journal, 29(3), pp. 7-34.

[21] Vivian, J., Manente, G., and Lazzaretto, A., 2015, "A general framework to select working fluid and configuration of ORCs for low-to-medium temperature heat sources," Applied Energy, 156, pp. 727-746.
[22] Helvaci, H., and Khan, Z. A., 2017, "Heat transfer and entropy generation analysis of HFE 7000 based nanorefrigerants," International Journal of Heat and Mass Transfer, 104, pp. 318-327.
[23] Helvaci, H. U., and Khan, Z. A., 2016, "Experimental study of thermodynamic assessment of a small scale solar thermal system," Energy Conversion and Management, 117, pp. 567-576.
[24] Helvaci, H., and Khan, Z. A., 2015, "Mathematical modelling and simulation of multiphase flow in a flat plate solar energy collector," Energy Conversion and Management, 106, pp. 139-150.
[25] Klein, S., 1975, "Calculation of flat-plate collector loss coefficients," Solar Energy, 17(1), pp. 79-80.
[26] Quoilin, S., 2011, "Sustainable Energy Conversion Through the Use of Organic Rankine Cycles for Waste Heat Recovery and Solar Applications," University of Liège (Belgium.
[27] Gnutek, Z., and Kolasiński, P., 2013, "The application of rotary vane expanders in organic rankine cycle systems—thermodynamic description and experimental results," Journal of Engineering for Gas Turbines and Power, 135(6), p. 061901.
[28] Kim, Y. M., Shin, D. G., and Kim, C. G., 2014, "Optimization of design pressure ratio of positive displacement expander for vehicle engine waste heat recovery," Energies, 7(9), pp. 6105-6117.
[29] Kolasiński, P., 2015, "The Influence of the Heat Source Temperature on the Multivane Expander Output Power in an Organic Rankine Cycle (ORC) System," Energies, 8(5), pp. 3351-3369.
[30] Lemmon, E., Huber, M., and McLinden, M., 2013, "NIST reference database 23: reference fluid thermodynamic and transport properties-REFPROP, version 9.1," Standard Reference Data Program.
[31] Qiu, G., Shao, Y., Li, J., Liu, H., and Riffat, S. B., 2012, "Experimental investigation of a biomass-fired ORC-based micro-CHP for domestic applications," Fuel, 96, pp. 374-382.

Paper V

International Journal of Heat and Mass Transfer 104 (2017) 318–327

Contents lists available at ScienceDirect

International Journal of Heat and Mass Transfer

journal homepage: www.elsevier.com/locate/ijhmt

Heat transfer and entropy generation analysis of HFE 7000 based nanorefrigerants

H.U. Helvaci *, Z.A. Khan

Bournemouth University, NanoCorr, Energy and Modelling (NCEM), Faculty of Science and Technology, Bournemouth BH12 5BB, UK

ARTICLE INFO

Article history:
Received 9 June 2016
Received in revised form 16 August 2016
Accepted 17 August 2016

Keywords:
CFD
Nanofluid
Heat transfer coefficient
Pressure loss
Entropy generation

ABSTRACT

In this study, two dimensional numerical simulations of forced convection flow of HFE 7000 based nanofluids in a horizontal circular tube subjected to a constant and uniform heat flux in laminar flow were performed by using single phase homogeneous model. Four different nanofluids considered in the present study are Al_2O_3, CuO, SiO_2 and MgO nanoparticles dispersed in pure HFE 7000. The simulations were performed with particle volumetric concentrations of 0, 1, 4 and 6% and Reynolds number of 400, 800, 1200 and 1600. Most of the previous studies on the forced convective flow of nanofluids have been investigated through hydrodynamic and heat transfer analysis. Therefore, there is limited number of numerical studies which include both heat transfer and entropy generation investigations of the convective flow of nanofluids. The objective of the present work is to study the influence of each dispersed particles, their volume concentrations and Reynolds number on the hydrodynamic and thermal characteristics as well as the entropy generation of the flow. In addition, experimental data for Al_2O_3–water nanofluid was compared with the simulation model and high level agreement was found between the simulation and experimental results. The numerical results reveal that the average heat transfer coefficient augments with an increase in Reynolds number and the volume concentration for all the above considered nanofluids. It is found that the highest increase in the average heat transfer coefficient is obtained at the highest volume concentration ratio (6%) for each nanofluids. The increase in the average heat transfer coefficient is found to be 17.5% for MgO-HFE 7000 nanofluid, followed by Al_2O_3-HFE 7000 (16.9%), CuO-HFE 7000 (15.1%) and SiO_2-HFE 7000 (14.6%). However, the results show that the enhancement in heat transfer coefficient is accompanied by the increase in pressure drop, which is about (9.3–28.2%). Furthermore, the results demonstrate that total entropy generation reduces with the rising Reynolds number and particle volume concentration for each nanofluid. Therefore, the use of HFE 7000 based MgO, Al_2O_3, CuO and SiO_2 nanofluids in the laminar flow regime is beneficial and enhances the thermal performance.

1. Introduction

The low thermal conductivity of traditional fluids for instance, water, mineral oil and ethylene glycol is one of the obstacles to higher compactness and efficiency of heat exchangers [1] and it is crucial to develop more efficient heat transfer fluids with substantially higher thermal conductivity [2]. Therefore, micro/millimetre-sized solid particles which have considerably higher thermal conductivity than those fluids have been suspended in them to cause an enhancement in the thermal conductivity [3,4]. However, significant problems such as abrasion and clogging were observed when particles of the order of millimetres and micrometres are suspended in a liquid.

Alternatively, nano-sized particles suspended in conventional fluids can provide an improvement in the performance of these fluids. Such novel liquid suspensions that consist of solid particles at nanometric scale are called *nanofluids* and have become popular in terms of its utilisation in various practices such as heat transfer, thermal energy storage and industrial cooling [5,6]. Nanofluids have superior heat transfer performance than conventional fluids because of the improved effective thermal conductivity of the fluid [7]. As a consequence, several studies have been conducted on the investigation of thermo-physical properties of nanofluids, particularly the effective thermal conductivity and viscosity [8–13]. Superior thermal conductivity and viscosity of nanofluids in comparison to the base fluids were reported in the above studies. However, in

* Corresponding author at: Faculty of Science and Technology, Fern Barrow, Talbot Campus, Bournemouth University, Poole, Dorset BH12 5BB, UK.
E-mail address: hhelvaci@bournemouth.ac.uk (H.U. Helvaci).

http://dx.doi.org/10.1016/j.ijheatmasstransfer.2016.08.053
0017-9310/

Nomenclature

A	area, m^2
C_p	specific heat, J/kg K
D	diameter, m
f	friction factor
GWP	global warming potential
h	heat transfer coefficient, $W/(m^2 K)$
HFE	hydrofluoroether
k	thermal conductivity, W/m K
L	length, m
Nu	Nusselt number
ODP	ozone depletion potential
R	radius of the tube, m
P	pressure, Pa
q''	heat flux, W/m^2
Re	Reynolds umber
S	entropy, W/K
T	temperature, K
u	Velocity in axial direction, m/s
$\dot{W}$	work rate, W

Subscripts

amb	ambient
ave	average
bf	base fluid
f	fluid
fr	frictional
gen	generation
in	inlet
m	mean
nf	nanofluid
out	outlet
s	nanoparticle
th	thermal
tot	total
w	wall

Greek symbols

ρ	density, kg/m^3
η	first law efficiency
ε	second law efficiency
μ	dynamic viscosity, kg/m s
ϕ	particle volume concentration (%)

addition to the thermo-physical properties, forced convection (laminar and turbulent flow) heat transfer characteristics of nanofluids need to be investigated as it is important for their practical applications [14]. One of the earliest experimental work on forced convection of nanofluids was conducted by Xuan and Li [7]. In their study, Cu–water nanofluid was used to examine the heat transfer process of the nanofluid. They obtained higher heat transfer performance for the nanofluid compared to that of the base liquid. Another experimental study was conducted by Wen et al. [15] where the effect of the laminar flow of water–Al_2O_3 nanofluid was analysed. They stated that the heat transfer rate rose by addition of nanoparticles, especially at the entrance region of the tube. The relation between the heat transfer coefficient and nanoparticle size and Peclet number was studied by Heris et al. [16] for Al_2O_3–water and CuO–water nanofluids in a circular tube. It was found that the heat transfer coefficient soared with increasing particle size and Peclet number for both nanofluids.

In addition to experimental studies, numerical analysis of forced convection of nanofluids has been of interest to many researchers. Numerical analysis in the literature consists of two different approaches for evaluating the heat transfer correlations of nanofluids which are single phase (homogenous) and two-phase (mixture) models. In the former model, nanofluid is assumed as a single fluid rather than a solid–fluid mixture and it is also assumed that there is no motion slip between particles and fluid. Moraveji et al. [17] numerically studied the convective heat transfer coefficient of Al_2O_3 nanofluid along a tube using single phase model. It was observed that the heat transfer coefficient rose with increasing nanoparticle volume fraction ratio and the Reynolds number. Demir et al. [18] investigated the forced convection flow of nanofluids in a horizontal tube subjected to constant wall temperature. They utilised homogeneous model with two-dimensional equations in order to study the effects of TiO_2 and Al_2O_3 nanoparticles and Reynolds number on the convective heat transfer coefficient, Nusselt number and pressure drop. The results revealed that nanofluids with a higher volume ratio showed a higher improvement of heat transfer rate. Salman et al. [19] investigated the laminar forced convective flow of water based Al_2O_3 and SiO_2 nanofluids numerically. The results indicated that SiO_2–water and Al_2O_3–water nanofluids have better heat transfer properties compared to pure water.

In order to take the effect of nanoparticle chaotic movements into account in single phase model, thermal dispersion approach is proposed by several researchers [20–22]. These researchers also concluded that increasing particle volume concentration enhances the heat transfer rate. Furthermore, the mixture model approach where the interactions between the particle and fluid are considered is also proposed in several numerical analyses in the literature [23–26].

As previously mentioned suspending nano-scale particles in a base fluid enhances the thermal conductivity but also increases the viscosity. An augmentation in the thermal conductivity leads a better heat transfer rate, whereas an increase in the viscosity leads an enhancement in pressure drop. Consequently, the addition of the particles changes the thermophysical properties of a fluid as well as the irreversibility of a system [27]. Entropy generation demonstrates the irreversibility of a system thus, it is important to minimise the entropy generation to obtain better working conditions [28,29]. As a result, entropy generation analysis has been considered in nanofluid flow analysis in order to find the optimum working conditions by several researchers [27,30–37]. For instance, Moghaddami et al. [31] studied the estimation of the entropy generation of Al_2O_3 particles suspended in water and ethylene glycol in a circular tube for both laminar and turbulent flows. They revealed that the entropy generation is diminished by the addition of the particles at any Reynolds number for laminar flow. However, for turbulent flow it is stated that utilising the nanoparticles in the base fluid is beneficial only at Reynolds number smaller than 40,000. Biancoa et al. [28] studied the numerical entropy generation of Al_2O_3–water nanofluids under the turbulent forced convection flow for fixed Reynolds number, mass flow rate and velocity. Their numerical outcomes reveal that at constant velocity condition, lower concentration of nanoparticles can minimise the total entropy generation. In another study, Saha et al. [33] evaluated the entropy generation of water based TiO_2 and Al_2O_3 nanofluids for turbulent flow in a heated pipe. It was found that

there is an optimum Reynolds number where the entropy generation is minimised. They also showed that the use of TiO_2 nanofluid is more beneficial than Al_2O_3 nanofluid.

Hydrofluoroethers (HFEs) which are the new generation refrigerants have zero Ozone Depletion Potential (ODP) and relatively low Global Warming Potential (GWP). Therefore, they have been used in various applications as a replacement to conventional refrigerants such as Chlorofluorocarbons (CFCs) and hydrochlorofluorocarbons (HCFCs) [38]. In addition to that HFE 7100 based nanofluids have been of interest to various researchers in terms of convective heat transfer analysis [39–41]. Previously, HFE 7000 (RE 347mcc) refrigerant has been studied both experimentally and numerically in terms of its utilisation in various solar thermal applications [42,43]. In this study, laminar forced convection flow characteristics of HFE 7000 (RE 347mcc) based Al_2O_3, SiO_2, CuO and MgO nanofluids in a horizontal tube under constant heat flux is analysed numerically. Single phase homogeneous approach is applied in order to investigate the effects of Reynolds number and particle volume concentration ratio on both the heat transfer coefficient and the pressure drop of each nanofluid. Furthermore, the entropy generation analysis is provided for each nanofluid flow to specify the most beneficial nanofluid with optimum working conditions that minimises the total entropy generation of the flow.

2. Problem definition

In this study, two dimensional, steady state, laminar flow in a circular tube, subjected to constant heat flux is investigated. The geometry of the considered problem is represented in Fig. 1. As it can be seen from the figure, the computational domain consists of a tube with a length of 1.2 m and a diameter of 0.00475 m. In the analysis, only the top half of the tube is considered as the flow is presumed to be symmetrical. In the simulations, 1000 W/m^2 constant heat is supplied on the upper wall of the tube. Also, the base and nanofluids enters the tube at temperature of 283 K and the pressure of 1 bar. This inlet temperature is chosen due to the HFE 7000 saturation pressure–temperature conditions.

3. Numerical analysis

The defined problem is solved using single phase approach where the base fluid HFE 7000 (RE 347mcc) and the particles are assumed to be in equilibrium and there is no relative velocity between the two of them.

3.1. Mathematical modelling

The following equations (continuity, momentum and energy) for laminar, incompressible flow can be expressed as follows:

Continuity equation:

$$\nabla \cdot (\rho_{nf} V) = 0 \tag{1}$$

Momentum equation:

$$\nabla \cdot (\rho_{nf} VV) = -\nabla P + \nabla \cdot (\mu_{nf} \nabla V) \tag{2}$$

Energy equation:

$$\nabla(\rho_{nf} V C_p T) = \nabla(k_{nf} \nabla T) \tag{3}$$

3.2. Thermo-physical properties of nanofluids

The thermal and physical properties of nanofluids are investigated using the formulas below:

The density of nanofluid can be calculated by the equation developed by Pak and Chao [44]:

$$\rho_{nf} = \phi \rho_s + (1-\phi)\rho_{bf} \tag{4}$$

where ϕ is the nanoparticle volume concentration, ρ_s and ρ_{bf} are the nanoparticle and base fluid densities respectively.

Mass-averaged calculation of specific heat which is based on heat capacity concept of nanofluid is shown below [29]:

$$C_{p,nf} = \frac{\phi(\rho C_p)_s + (1-\phi)(\rho C_p)_{bf}}{\phi \rho_s + (1-\phi)\rho_{bf}} \tag{5}$$

where $C_{p,s}$ and $C_{p,bf}$ are particles and base fluid heat capacity respectively.

Effective thermal conductivity of nanofluid is obtained in the following form [45]:

$$k_{nf} = k_{bf} \frac{[k_s + (n-1)k_{bf} + (n-1)\phi(k_s - k_{bf})]}{[k_s + (n-1)k_{bf} - \phi(k_s - k_{bf})]} \tag{6}$$

where k_{bf} and k_s are the thermal conductivities of the base fluid and solid particles and $n = 3$ for spherical solid particles.

Dynamic viscosity of nanofluid is estimated by using Einstein's equation which is based on kinetic theory [46]:

$$\mu_{nf} = \mu_{bf}(1 + 2.5\phi) \tag{7}$$

In Eq. (7), μ_{nf} and μ_{bf} are the dynamic viscosity of the nanofluid and base fluid respectively.

The thermo-physical properties of two base fluids (water and HFE 7000) and the particles used in this study are given in Table 1.

3.3. Boundary conditions

In order to solve the governing equations given above, the appropriate boundary conditions are applied and expressed as follows;

Uniform velocity boundary condition depending on the value of the flow Reynolds number and inlet temperature are defined at the inlet of the tube.

$$u(0,r) = U, \quad v(0,r) = 0$$
$$T(0,r) = T_{in}$$

No-slip boundary conditions at the wall ($r = D/2$) is imposed. Therefore, the velocity at the upper wall becomes;

$$u(x,R) = v(x,R) = 0$$

The upper surface of the tube is subjected to a constant heat flux and it is expressed as;

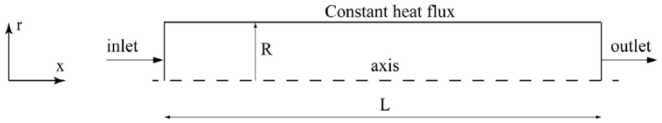

Fig. 1. Schematic of the flow domain under consideration.

Table 1
Thermo-physical properties of the base fluids (water and HFE 7000) and the nanoparticles.

Fluid/particle	Density (kg/m^3)	Specific heat (J/kg K)	Thermal conductivity (W/m K)	Viscosity (kg/m s)	Reference
Pure water	998.2	4182	0.6	0.001003	[47]
HFE 7000*	1446.1	1204.6	0.079	0.00058	[48]
Al_2O_3	3970	765	40	–	[49]
SiO_2	2200	703	1.2	–	[19]
MgO	3560	955	45	–	[47]
CuO	6500	535.6	20	–	[50]

* The data is taken at 1 bar and 283 K.

$$-k_{nf}\left.\frac{\partial T}{\partial r}\right|_{r=R} = q''$$

Finally, at the exit section of the tube pressure outlet condition is applied.

4. Numerical procedure

In this study, the governing equations (continuity, momentum and energy) with appropriate boundary conditions are solved by employing the finite volume solver Fluent 6.3.26 [51]. Second order upwind scheme is applied for solving the convective and diffusive terms. The SIMPLE algorithm is used to model pressure–velocity coupling. The residue of 10^{-6} is defined as convergence criteria for all the dependent variables as mass, velocity and energy.

4.1. Data reduction

The local heat transfer coefficient is expressed as:

$$h(x) = \frac{q''}{T(x)_w - T(x)_{f,m}} \tag{8}$$

where $T(x)_w$ represents the wall temperature at a given location (x) along the tube and it is calculated as:

$$T(x,R) = T(x)_w \tag{9}$$

where x represents any given axial position along the tube and R is the radius of the tube.

$T(x)_{f,m}$ is the fluid mean temperature at any (x), which can be found via integration:

$$T(x)_{f,m} = \frac{\int_0^R urTdr}{\int_0^R urdr} \tag{10}$$

where u is the velocity in axial (x) direction.

The average convective heat transfer coefficient is calculated as:

$$h_{ave} = \frac{1}{L}\int_0^L h(x)dx \tag{11}$$

In addition to heat transfer coefficient, the total entropy generation rate of the fluid flow is evaluated in order to determine the benefits of using nanofluid in terms of thermodynamic analysis. The total entropy generation rate of a flow in a circular tube which consists of two parts: (i) thermal entropy generation (ii) frictional entropy generation is calculated as follows [33]:

$$S_{tot} = \frac{(q'')^2\pi D^2 L}{NukT_{ave}^2} + \frac{32\dot{m}^3 fL}{\pi^2\rho^2 T_{ave}D^5} \tag{12}$$

In Eq. (12), the first term of the left hand side represents the thermal entropy generation and the second term represents the frictional entropy generation.

In the first term, D indicates the diameter of the tube, Nu is the Nusselt number, k and T_{avg} are the thermal conductivity and the average temperature of fluid.

Average Nusselt number and fluid temperature are given by:

$$Nu_{ave} = \frac{h_{ave}D}{k} \tag{13}$$

$$T_{ave} = \frac{T_{in} - T_{out}}{ln\left(\frac{T_{in}}{T_{out}}\right)} \tag{14}$$

In the second term $\dot{m}$ is the mass flow rate, f and ρ represent the friction factor and the density of fluid respectively.

Friction factor (f) can be calculated using the following equation:

$$f = \frac{2\cdot\Delta P\cdot D}{\rho\cdot V^2\cdot L} \tag{15}$$

4.2. Grid independency test

A grid independency test is conducted to guarantee the accuracy of the numerical results. Five different sets of uniform grids have been used to check for grid independency. The tests were carried out for both pure water and HFE 7000 at Re = 800 and Re = 1600 for each of the grids. Table 2 shows the comparison of the results for each fluid. It can be seen that the value of the heat transfer coefficient converges as the number of grid cells increases. Grid 4 shows little difference (0.25% for water and 0.41% for HFE 7000) from the results obtained for Grid 4. Therefore, in the present study, Grid 4 is utilised for the numerical analysis.

It is also important to ensure the appropriate grid cell size in order to obtain accurate simulation results. Therefore, y^+ value for Grid 4 is calculated and given in Table 3 at each Reynolds number. As it can be seen from Table 3 that y^+ in the laminar flow region at any Reynolds number remains less than 11.63 for Grid 4 [52,53].

4.3. Validation of the computational model

Due to the absence of experimental and numerical studies for HFE 7000 based nanofluids, the experimental data of the local heat transfer coefficients of pure water and Al_2O_3/water nanofluid in laminar developing region represented by [54] was compared to the corresponding numerical results in order to validate the accuracy of the model. In the experimental work [54], a test rig was set-up in order to investigate the heat transfer characteristics of Al_2O_3/water nanofluid with particle sizes of 45 nm and 150 nm in a straight tube under constant heat flux conditions. The experimental test loop comprises a pump, a heated test section, a cooling sec-

Table 2
Grid independency test results.

Grid number	Number of cells in x direction	Number of cells in y direction	h (pure water)	h (pure HFE 7000)
Re = 800				
1	250	5	755.384	125.05
2	500	10	728.2	116.41
3	1000	20	720.32	114.63
4	**2000**	**40**	**718.47**	**114.16**
5	3000	40	719.26	114.21
Re = 1600				
1	250	5	1120.64	158.05
2	500	10	1032.7	146.14
3	1000	20	1011.44	142.68
4	**2000**	**40**	**1006.25**	**141.86**
5	3000	40	1007.34	142

Table 3
y^+ values versus Reynolds number.

Reynolds number	Grid 4 (2000 × 40)
400	1.32
800	2.43
1200	3.47
1600	4.46

tion and a collecting tank. In the test section a straight tube with 4.75 mm inner diameter and 1200 mm long was utilised and constant heat flux was provided by wounding a Nickel-chrome wire that can give maximum power of 200 W along the tube.

Fig. 2 shows the comparison of the experimental heat transfer coefficient for both pure water and Al_2O_3/water nanofluid (with the particle diameter of 45 nm and the volume concentration ratio of 4%) at Re = 1580 and Re = 1588 versus simulation results. It should be noted that the effect of various particle size was not considered in this study and the simulation results are only compared with the experimental results of Al_2O_3/water nanofluid with particle diameter of 45 nm as it is widely accepted that solid particles which have a diameter less than 100 nm can be easily fluidised and be treated as a single fluid.

As it is shown in Fig. 2, the axial variation of the heat transfer coefficient using numerical results is in good agreement with the experimental data. The maximum discrepancy between the experimental data and numerical model is found to be 12%. As the heat transfer enhancement is highly related to the accuracy of the effective properties of nanofluid, namely thermal conductivity in homogenous model, several factors such as particle size, temperature dependent properties, random movement of particles and thermal dispersion, which might have an impact on the accurate determination of the effective thermal conductivity could be attributed to the reason of the deviation between the simulation and the experimental results [7,55].

5. Results and discussion

In this section, the simulations of Al_2O_3-HFE 7000, CuO-HFE 7000, SiO_2-HFE 7000 and MgO-HFE 7000 nanofluids at various Reynolds numbers (Re = 400–1600) and particle volume fraction (ϕ = 1–6%) under constant heat flux conditions were conducted and the effect of Reynolds number and particle volume concentration ratio of the nanofluids on the flow and heat transfer characteristics as well as the entropy generation is represented and discussed.

5.1. Temperature profiles

Fig. 3 shows the axial bulk and wall temperature distributions of Al_2O_3-HFE 7000 nanofluids at Re = 800 and at ϕ = 0, 1, 4, 6%. It can be observed that increasing nanoparticle concentration decreases the temperature differences between the wall and bulk temperature of nanofluids. A similar trend is obtained in Ref. [40] for Al_2O_3-HFE 7100 with ϕ = 0 and 5%. This behaviour of the wall and bulk temperatures shows the beneficial effects of the nanofluids in terms of having superior thermal properties in comparison to that of the base fluid which leads higher heat transfer coefficients consequently.

The effect of particle volume concentration on the temperature distribution of Al_2O_3-HFE 7000 nanofluids at Re = 800 is also represented in Fig. 4.

5.2. Convective heat transfer coefficient

Fig. 5 illustrates the heat transfer coefficient of the investigated nanofluids and the base fluid at various Reynolds numbers and volumetric concentration ratio. It can be observed from Fig. 5 that in general, the average heat transfer coefficient of each nanofluid is greater than the base fluid at any volumetric ratio and Reynolds number. The heat transfer coefficients of four nanofluids rise as the volume concentration ratio increases in the laminar flow regime. This is reasonable because the higher volume concentration ratios of nanoparticles lead a higher thermal conductivity in nanofluid than the conventional fluid which results in higher thermal-energy transfer. Similar findings were reported by previous researchers [17,25,36]. Among all the investigated nanofluids, MgO-HFE 7000 shows the highest heat transfer enhancement, at any given Reynolds number and particle volume fraction. For example, at Re = 400 and ϕ = 6% for the MgO-HFE 7000 nanofluid the enhancement in the heat transfer coefficient is approximately 17.5%, whereas for Al_2O_3-HFE 7000, CuO-HFE 7000 and SiO_2-HFE 7000, it is found to be 16.9%, 15.1% and 14.6% respectively.

This could be explained by the superior physical properties such as thermal conductivity of MgO compared to the other particles (Table 1). As it is reported previously, in the single phase laminar flow model, the enhancement in the heat transfer coefficient of nanofluid is proportional to the increase in thermal conductivity

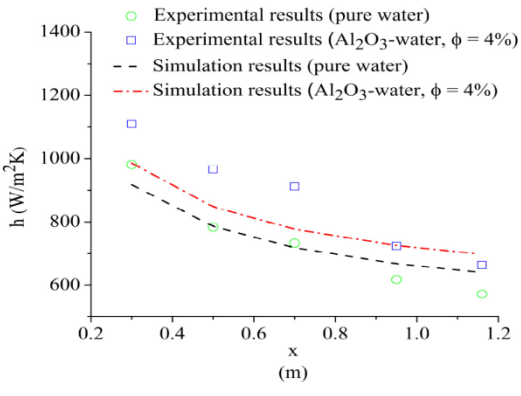

Fig. 2. Comparison between the simulated and experimental results.

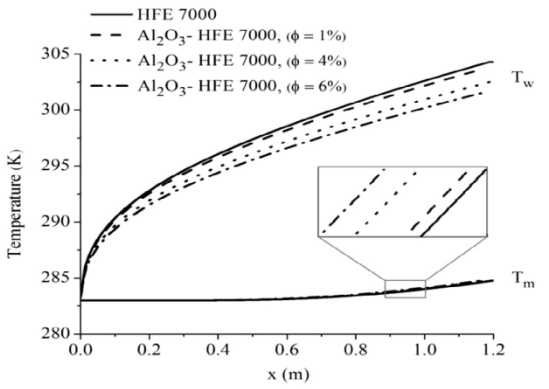

Fig. 3. Axial distribution of wall and fluid temperature of Al_2O_3 nanofluid at various volume concentrations.

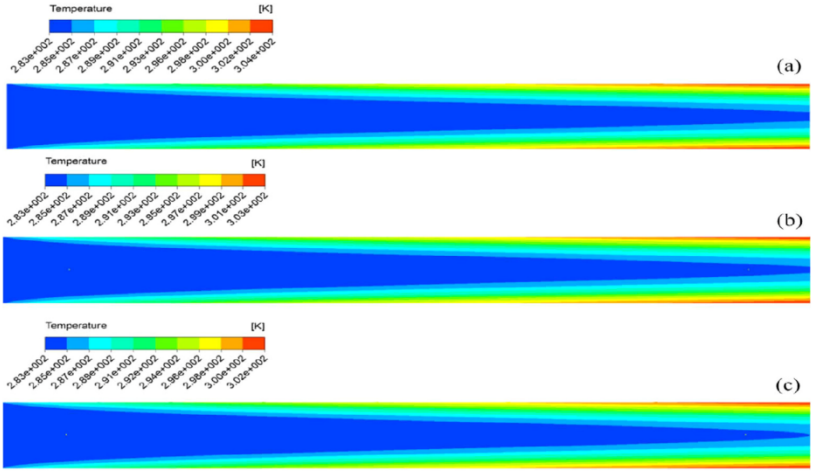

Fig. 4. Temperature distribution of Al_2O_3-HFE 7000 nanofluids along the tube at (a) 1% volume concentration, (b) 4% volume concentration, (c) 6% volume concentration.

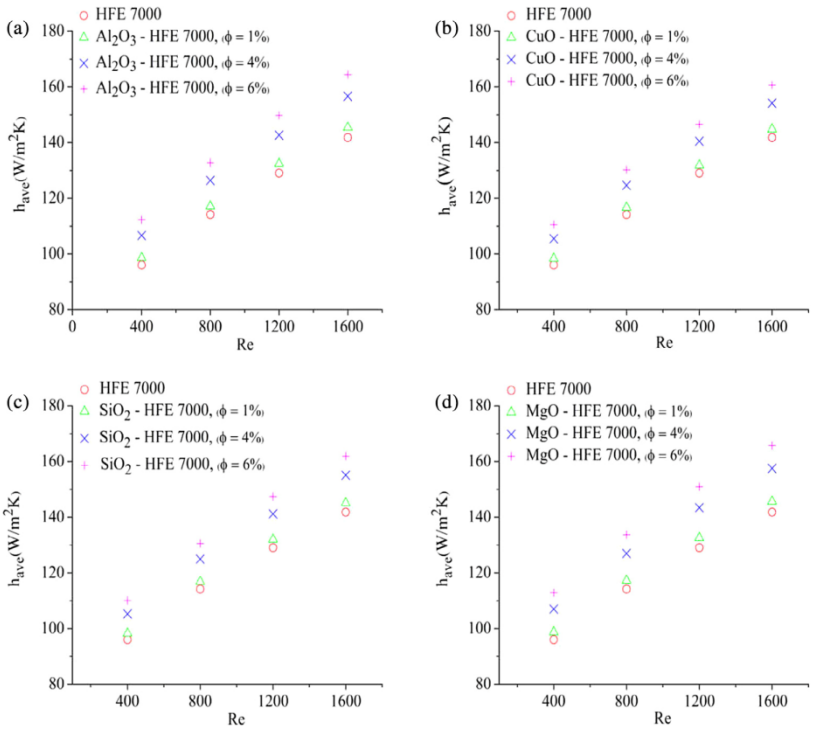

Fig. 5. Variation of the heat transfer coefficients at different Reynolds number for (a) Al_2O_3-HFE 7000, (b) CuO-HFE 7000, (c) SiO_2-HFE 7000, (d) MgO-HFE 7000.

of corresponding nanofluid [55]. This dependency of the heat transfer mechanism on the nanofluid effective properties might cause single-phase model to under-predict the heat transfer enhancement [24]. Alternatively, two phase models can be utilised in order to evaluate the heat transfer characteristics of nanofluids. However, they are more complicated and need higher computational cost [37]. In order to compare both the experimental results with the current model and two-phase models, it is necessary to conduct further theoretical study including two-phase models and experimental work.

5.3. Pressure drop analysis

It is also important to study the flow characteristics of nanofluids such as pressure drop in order to investigate their potential for practical applications [56]. Pressure drop within the tube at different Reynolds number and the volume concentration is demonstrated in Fig. 6.

It is shown that pressure drop increases as the Reynolds number grows from 400 to 1600 and volume concentration from 1% to 6% for each nanofluid. The obtained results reveal that at Re = 1600 and ϕ = 6%, SiO_2-HFE 7000 nanofluid caused the highest enhancement in pressure drop (28.2%) among the four nanofluids. It is followed by MgO-HFE 7000 (21.5%), Al_2O_3-HFE 7000 (19.7%) and CuO-HFE 7000 (9.3%). This is due to the fact that nanofluids become more viscous at higher volume concentration ratios which in turn results in higher pressure drop [18].

5.4. Entropy generation analysis

Entropy generation of the considered nanofluids in terms of irreversibility that was caused by thermal and frictional gradients with Reynolds number from 400 to 1600 and at four different volume fractions (0%, 1%, 4% and 6%) is demonstrated in Figs. 7 and 8.

It is visible from Figs. 7 and 8 that the growth in Reynolds number for both the base fluid and the nanofluids diminishes the thermal irreversibility whereas enhances the frictional entropy generation.

The reason for that is the higher Reynolds number leads to a growth in the heat transfer coefficient. However, the higher velocity profile of the fluids at higher Reynolds number improves entropy generation due to the friction [33]. Similarly, the opposite trend between the thermal and frictional irreversibility for volume fraction can be found in Figs. 7 and 8. Namely, the thermal entropy generation diminishes with increasing volume concentration ratio. This can be explained by the fact that higher particle volume fraction leads higher nanofluid effective thermal conductivity and better heat transfer mechanism between the wall and the fluid which corresponds a decline in thermal dissipation and an improvement in the heat transfer mechanism. On the contrary, frictional entropy generation is increased with the volume concentration ratio. This is due to the growth of the viscosity of nanofluids as the nanoparticle volume fraction increases [28]. As it can be seen from Figs. 7 and 8 the magnitude of the thermal irreversibility is relatively higher than the irreversibility due to the friction.

In order to define the thermodynamic performance of the flow in terms of the second law efficiency the ratio of the total entropy generation of nanofluid to that of base fluid ($S_{gen,ratio}$) is defined as follows [35].

$$S_{gen,ratio} = \frac{S_{gen,tot,nf}}{S_{gen,tot,bf}} \tag{16}$$

where $S_{gen,tot,nf}$ and $S_{gen,tot,bf}$ represent the total entropy generation of the nanofluid and the base fluid respectively. As it is stated in Eq. (16), $S_{gen,ratio}$ equals to 1 for pure HFE 7000 (ϕ = 0%) which shows that there is no contribution to entropy generation. Therefore, the lower the value of $S_{gen,ratio}$ the better the thermodynamic performance of the flow.

Fig. 9 indicates the entropy generation ratio of the investigated nanofluids for the volume concentration ratios. It can be highlighted from the figure that each nanofluid at any volume fraction has a lower value of the entropy generation rate in comparison to that of the base fluid ($S_{gen,ratio}$ = 1) which indicates the advantage of adding nanoparticles in terms of a reduction in total entropy generation. Additionally, the entropy generation rate decreases with increasing volume concentration and the decrease is more pro-

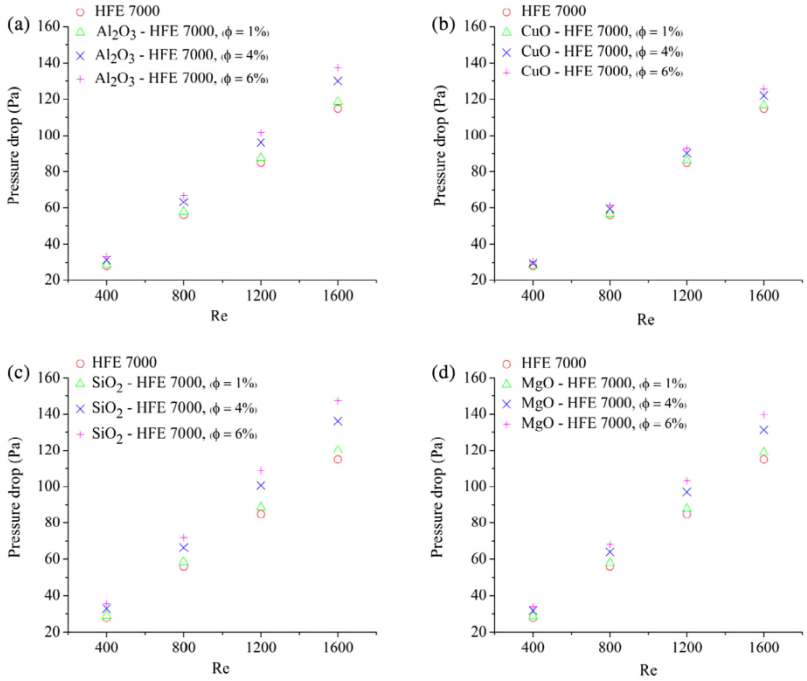

Fig. 6. Variation of pressure drop at different Reynolds number for (a) Al_2O_3-HFE 7000, (b) CuO-HFE 7000, (c) SiO_2-HFE 7000, (d) MgO-HFE 7000.

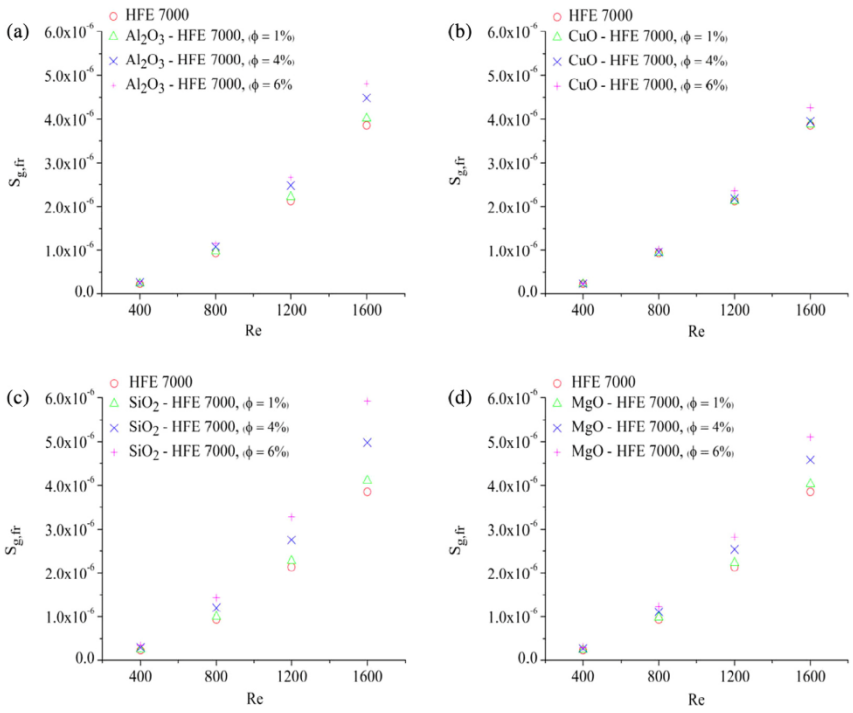

Fig. 7. Variation of frictional entropy generation at different Reynolds number for (a) Al_2O_3-HFE 7000, (b) CuO-HFE 7000, (c) SiO_2-HFE 7000, (d) MgO-HFE 7000.

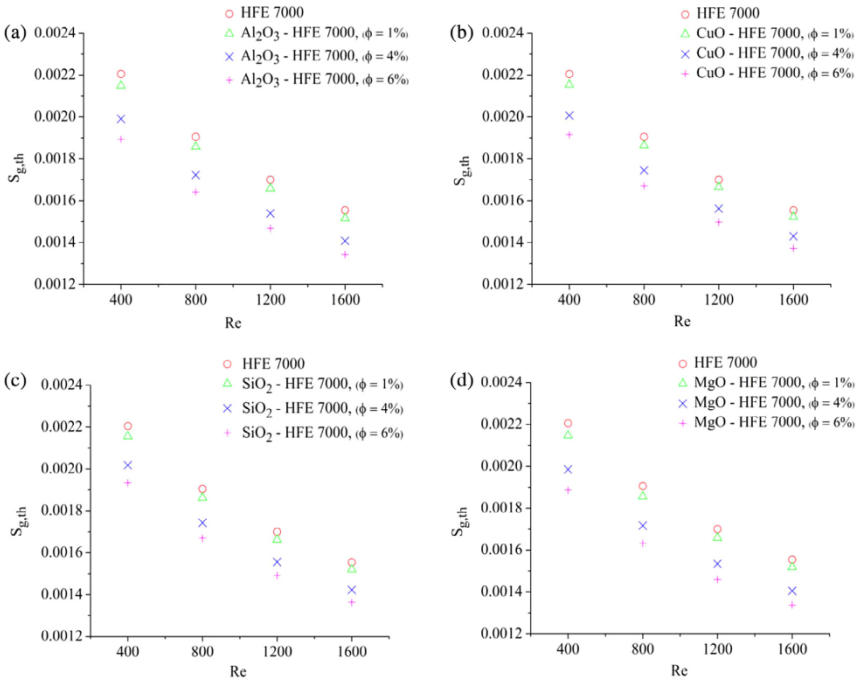

Fig. 8. Variation of thermal entropy generation at different Reynolds number for (a) Al_2O_3-HFE 7000, (b) CuO-HFE 7000, (c) SiO_2-HFE 7000, (d) MgO-HFE 7000.

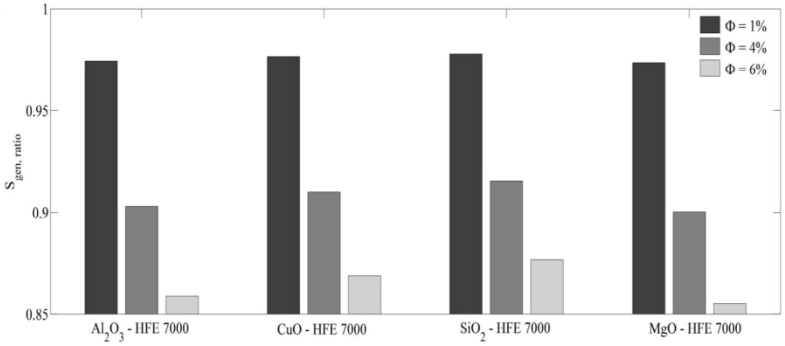

Fig. 9. Entropy generation ratio of the nanofluids at Re = 800.

nounced at 6% volume concentration ratio. For instance, the entropy generation rate drops from 0.97 to 0.85 and from 0.97 to 0.87 for MgO-HFE 7000 and SiO_2-HFE 7000 respectively as the volume concentration rises from 1% to 6%. This trend can be explained by the fact that higher volume concentration determines a reduction in thermal entropy generation. Although there is an opposite trend between the frictional and thermal entropy generation (Figs. 7 and 8) the effect of the former is relatively small compared to the latter. Thus, the overall behaviour of the total entropy generation is dominated by the thermal effects. Similar results were reported by [27,31,34] for Al_2O_3–water nanofluid. As a result, it can be concluded that the utilisation of Al_2O_3-HFE 7000, CuO-HFE 7000, SiO_2-HFE 7000 and MgO-HFE 7000 nanofluids is beneficial where the total entropy generation is dominated by the contribution of thermal irreversibility.

5.5. Correlations

Non-linear regression analysis is applied to the simulation results to derive the following correlations which can predict the average Nusselt number and friction factor for each investigated nanofluid. The evaluated equations are valid for $400 \leqslant Re \leqslant 1600$ and $0\% \leqslant \phi \leqslant 6\%$. The average Nusselt number is modelled as a function of Reynolds number, Prandtl number and volumetric concentration ratio whereas friction factor as a function of Reynolds number and volumetric concentration ratio.

Nusselt number

$$Al_2O_3\text{-HFE 7000}: \quad Nu_{ave} = 0.576(Re\ Pr)^{0.28}(1+\phi)^{3.016} \tag{17}$$

$$CuO\text{-HFE 7000}: \quad Nu_{ave} = 0.591(Re\ Pr)^{0.278}(1+\phi)^{2.658} \tag{18}$$

$$SiO_2\text{-HFE 7000}: \quad Nu_{ave} = 0.567(Re\ Pr)^{0.282}(1+\phi)^{2.737} \tag{19}$$

$$MgO\text{-HFE 7000}: \quad Nu_{ave} = 0.571(Re\ Pr)^{0.281}(1+\phi)^{3.143} \tag{20}$$

Friction factor

$$Al_2O_3\text{-HFE 7000}: \quad f = 48.492Re^{-0.984}(1+\phi)^{0.033} \tag{21}$$

$$CuO\text{-HFE 7000}: \quad f = 48.197Re^{-0.984}(1+\phi)^{0.899} \tag{22}$$

$$SiO_2\text{-HFE 7000}: \quad f = 48.696Re^{-0.984}(1+\phi)^{0.401} \tag{23}$$

$$MgO\text{-HFE 7000}: \quad f = 48.056Re^{-0.983}(1+\phi)^{0.398} \tag{24}$$

The maximum deviation between the simulated and the predicted results are found to be 1.74% and 3% for Nusselt number and friction factor of CuO-HFE 7000 nanofluid respectively.

6. Conclusions

This paper investigates the convective heat transfer, pressure drop and entropy generation characteristics of HFE-7000 based Al_2O_3, CuO, SiO_2 and MgO nanofluids, using the single phase approach in a circular tube with constant heat flux boundary conditions in laminar flow region. It was found that the inclusion of nanoparticles (Al_2O_3, CuO, SiO_2 and MgO) increased the heat transfer coefficient (2.1–17.5%). This augmentation is attributed to the enhancement in the thermal conductivity of nanofluids. However, heat transfer enhancement is accompanied by increasing viscosity as well as an increase in pressure drop (1.5–28.2%). The enhancement in heat transfer and pressure drop found to be more pronounced with the increase in particle concentration and Reynolds number. Entropy generation results also demonstrated that when operating with constant Reynolds number, the thermal entropy generation tends to decrease whereas the frictional entropy generation tends to increase for each investigated nanofluid. However, using nanofluids caused a lower total entropy generation due to the superior contribution of thermal entropy generation compared to the frictional entropy generation. It can be concluded that in the laminar flow regime, for any Reynolds number adding nanoparticles of Al_2O_3, CuO, SiO_2 and MgO into the HFE 7000 is beneficial where the contribution of fluid friction is adequately less than the contribution of heat transfer to the total entropy generation of the flow. Finally, the current research provides a guideline to heat transfer applications on nano additives for enhanced thermal efficiency of solar thermal systems. Overall, this contribution will bring significant impacts to renewable energy technology research and development where novel and environmentally friendly thermo-fluids have been deployed.

Acknowledgement

The authors would like to acknowledge and thank Future Energy Source (FES) Ltd for providing full funding and technological support to conduct this research.

References

[1] W. Duangthongsuk, S. Wongwises, Heat transfer enhancement and pressure drop characteristics of TiO_2–water nanofluid in a double-tube counter flow heat exchanger, Int. J. Heat Mass Transfer 52 (7) (2009) 2059–2067.
[2] A. Behzadmehr, M. Saffar-Avval, N. Galanis, Prediction of turbulent forced convection of a nanofluid in a tube with uniform heat flux using a two phase approach, Int. J. Heat Fluid Flow 28 (2) (2007) 211–219.
[3] M. Chandrasekar, S. Suresh, Experiments to explore the mechanisms of heat transfer in nanocrystalline alumina/water nanofluid under laminar and turbulent flow conditions, Exp. Heat Transfer 24 (3) (2011) 234–256.

[4] M. Hejazian, M.K. Moraveji, A. Beheshti, Comparative study of Euler and mixture models for turbulent flow of Al_2O_3 nanofluid inside a horizontal tube, Int. Commun. Heat Mass Transfer 52 (2014) 152–158.
[5] Z. Khan, Z. Khan, A. Ghafoor, A review of performance enhancement of PCM based latent heat storage system within the context of materials, thermal stability and compatibility, Energy Convers. Manage. 115 (2016) 132–158.
[6] W. Minkowycz, E.M. Sparrow, J.P. Abraham, Nanoparticle Heat Transfer and Fluid Flow, CRC Press, 2012.
[7] Y. Xuan, Q. Li, Heat transfer enhancement of nanofluids, Int. J. Heat Fluid Flow 21 (1) (2000) 58–64.
[8] J.A. Eastman, S. Choi, S. Li, W. Yu, L. Thompson, Anomalously increased effective thermal conductivities of ethylene glycol-based nanofluids containing copper nanoparticles, Appl. Phys. Lett. 78 (6) (2001) 718–720.
[9] M. Assael, C.-F. Chen, I. Metaxa, W. Wakeham, Thermal conductivity of suspensions of carbon nanotubes in water, Int. J. Thermophys. 25 (4) (2004) 971–985.
[10] J.-H. Lee, K.S. Hwang, S.P. Jang, B.H. Lee, J.H. Kim, S.U. Choi, C.J. Choi, Effective viscosities and thermal conductivities of aqueous nanofluids containing low volume concentrations of Al_2O_3 nanoparticles, Int. J. Heat Mass Transfer 51 (11) (2008) 2651–2656.
[11] L. Godson, B. Raja, D.M. Lal, S. Wongwises, Experimental investigation on the thermal conductivity and viscosity of silver-deionized water nanofluid, Exp. Heat Transfer 23 (4) (2010) 317–332.
[12] W. Yu, H. Xie, L. Chen, Y. Li, Investigation on the thermal transport properties of ethylene glycol-based nanofluids containing copper nanoparticles, Powder Technol. 197 (3) (2010) 218–221.
[13] P. Sharma, I.-H. Baek, T. Cho, S. Park, K.B. Lee, Enhancement of thermal conductivity of ethylene glycol based silver nanofluids, Powder Technol. 208 (1) (2011) 7–19.
[14] S. Kakaç, A. Pramuanjaroenkij, Single-phase and two-phase treatments of convective heat transfer enhancement with nanofluids – A state-of-the-art review, Int. J. Therm. Sci. 100 (2016) 75–97.
[15] D. Wen, Y. Ding, Experimental investigation into convective heat transfer of nanofluids at the entrance region under laminar flow conditions, Int. J. Heat Mass Transfer 47 (24) (2004) 5181–5188.
[16] S. Zeinali Heris, S.G. Etemad, M. Nasr Esfahany, Experimental investigation of oxide nanofluids laminar flow convective heat transfer, Int. Commun. Heat Mass Transfer 33 (4) (2006) 529–535.
[17] M.K. Moraveji, M. Darabi, S.M.H. Haddad, R. Davarnejad, Modeling of convective heat transfer of a nanofluid in the developing region of tube flow with computational fluid dynamics, Int. Commun. Heat Mass Transfer 38 (9) (2011) 1291–1295.
[18] H. Demir, A. Dalkilic, N. Kürekci, W. Duangthongsuk, S. Wongwises, Numerical investigation on the single phase forced convection heat transfer characteristics of TiO_2 nanofluids in a double-tube counter flow heat exchanger, Int. Commun. Heat Mass Transfer 38 (2) (2011) 218–228.
[19] B. Salman, H. Mohammed, A.S. Kherbeet, Numerical and experimental investigation of heat transfer enhancement in a microtube using nanofluids, Int. Commun. Heat Mass Transfer 59 (2014) 88–100.
[20] S. Zeinali Heris, A. Kazemi-Beydokhti, S. Noie, S. Rezvan, Numerical study on convective heat transfer of Al_2O_3/water, CuO/water and Cu/water nanofluids through square cross-section duct in laminar flow, Eng. Appl. Comput. Fluid Mech. 6 (1) (2012) 1–14.
[21] S.Z. Heris, M.N. Esfahany, G. Etemad, Numerical investigation of nanofluid laminar convective heat transfer through a circular tube, Numer. Heat Transfer, Part A: Appl. 52 (11) (2007) 1043–1058.
[22] S. Göktepe, K. Atalık, H. Ertürk, Comparison of single and two-phase models for nanofluid convection at the entrance of a uniformly heated tube, Int. J. Therm. Sci. 80 (2014) 83–92.
[23] M.H. Fard, M.N. Esfahany, M. Talaie, Numerical study of convective heat transfer of nanofluids in a circular tube two-phase model versus single-phase model, Int. Commun. Heat Mass Transfer 37 (1) (2010) 91–97.
[24] M. Kalteh, A. Abbassi, M. Saffar-Avval, J. Harting, Eulerian–Eulerian two-phase numerical simulation of nanofluid laminar forced convection in a microchannel, Int. J. Heat Fluid Flow 32 (1) (2011) 107–116.
[25] M.K. Moraveji, R.M. Ardehali, CFD modeling (comparing single and two-phase approaches) on thermal performance of Al_2O_3/water nanofluid in mini-channel heat sink, Int. Commun. Heat Mass Transfer 44 (2013) 157–164.
[26] Y.-J. Chen, Y.-Y. Li, Z.-H. Liu, Numerical simulations of forced convection heat transfer and flow characteristics of nanofluids in small tubes using two-phase models, Int. J. Heat Mass Transfer 78 (2014) 993–1003.
[27] M. Moghaddami, S. Shahidi, M. Siavashi, Entropy generation analysis of nanofluid flow in turbulent and laminar regimes, J. Comput. Theor. Nanosci. 9 (10) (2012) 1586–1595.
[28] V. Biancoa, O. Mancab, S. Nardini, Entropy generation analysis of turbulent convection flow of Al_2O_3–water nanofluid in a circular tube subjected to constant wall heat flux, Energy Convers. Manage. 77 (2014) 306–314.
[29] O. Mahian, A. Kianifar, C. Kleinstreuer, A.-N. Moh'd A, I. Pop, A.Z. Sahin, S. Wongwises, A review of entropy generation in nanofluid flow, Int. J. Heat Mass Transfer 65 (2013) 514–532.
[30] P.K. Singh, K. Anoop, T. Sundararajan, S.K. Das, Entropy generation due to flow and heat transfer in nanofluids, Int. J. Heat Mass Transfer 53 (21) (2010) 4757–4767.
[31] M. Moghaddami, A. Mohammadzade, S.A.V. Esfehani, Second law analysis of nanofluid flow, Energy Convers. Manage. 52 (2) (2011) 1397–1405.
[32] A. Shalchi-Tabrizi, H.R. Seyf, Analysis of entropy generation and convective heat transfer of Al_2O_3 nanofluid flow in a tangential micro heat sink, Int. J. Heat Mass Transfer 55 (15) (2012) 4366–4375.
[33] G. Saha, M.C. Paul, Heat transfer and entropy generation of turbulent forced convection flow of nanofluids in a heated pipe, Int. Commun. Heat Mass Transfer 61 (2015) 26–36.
[34] N. Zhao, J. Yang, H. Li, Z. Zhang, S. Li, Numerical investigations of laminar heat transfer and flow performance of Al_2O_3–water nanofluids in a flat tube, Int. J. Heat Mass Transfer 92 (2016) 268–282.
[35] M. Siavashi, M. Jamali, Heat transfer and entropy generation analysis of turbulent flow of TiO_2–water nanofluid inside annuli with different radius ratios using two-phase mixture model, Appl. Therm. Eng. 100 (2016) 1149–1160.
[36] N. Purohit, V.A. Purohit, K. Purohit, Assessment of nanofluids for laminar convective heat transfer: A numerical study, Eng. Sci. Technol., Int. J. (2015).
[37] A. Ebrahimi, F. Rikhtegar, A. Sabaghan, E. Roohi, Heat transfer and entropy generation in a microchannel with longitudinal vortex generators using nanofluids, Energy 101 (2016) 190–201.
[38] W.-T. Tsai, Environmental risk assessment of hydrofluoroethers (HFEs), J. Hazard. Mater. 119 (1) (2005) 69–78.
[39] J. Lee, I. Mudawar, Assessment of the effectiveness of nanofluids for single-phase and two-phase heat transfer in micro-channels, Int. J. Heat Mass Transfer 50 (3) (2007) 452–463.
[40] T. Bergman, Effect of reduced specific heats of nanofluids on single phase, laminar internal forced convection, Int. J. Heat Mass Transfer 52 (5) (2009) 1240–1244.
[41] R. Ellahi, M. Hassan, A. Zeeshan, A.A. Khan, The shape effects of nanoparticles suspended in HFE-7100 over wedge with entropy generation and mixed convection, Appl. Nanosci. (2015) 1–11.
[42] H. Helvaci, Z.A. Khan, Mathematical modelling and simulation of multiphase flow in a flat plate solar energy collector, Energy Convers. Manage. 106 (2015) 139–150.
[43] H.U. Helvaci, Z.A. Khan, Experimental study of thermodynamic assessment of a small scale solar thermal system, Energy Convers. Manage. 117 (2016) 567–576.
[44] B.C. Pak, Y.I. Cho, Hydrodynamic and heat transfer study of dispersed fluids with submicron metallic oxide particles, Exp. Heat Transfer, Int. J. 11 (2) (1998) 151–170.
[45] R. Hamilton, O. Crosser, Thermal conductivity of heterogeneous two-component systems, Ind. Eng. Chem. Fundam. 1 (3) (1962) 187–191.
[46] A. Einstein, Eine neue bestimmung der moleküldimensionen, Ann. Phys. 324 (2) (1906) 289–306.
[47] R. Davarnejad, M. Jamshidzadeh, CFD modeling of heat transfer performance of MgO–water nanofluid under turbulent flow, Eng. Sci. Technol., Int. J. 18 (4) (2015) 536–542.
[48] E. Lemmon, M. Huber, M. McLinden, NIST reference database 23: reference fluid thermodynamic and transport properties-REFPROP, version 9.1, 2013. Standard Reference Data Program.
[49] G. Pathipakka, P. Sivashanmugam, Heat transfer behaviour of nanofluids in a uniformly heated circular tube fitted with helical inserts in laminar flow, Superlattices Microstruct. 47 (2) (2010) 349–360.
[50] R. Nasrin, M. Alim, Performance of nanofluids on heat transfer in a wavy solar collector, Int. J. Eng. Sci. Technol. 5 (3) (2013) 58–77.
[51] A.F.U.s. Guide, Release 15.0, ANSYS Inc: Canonsburg, PA, 2013.
[52] H.K. Versteeg, W. Malalasekera, An Introduction to Computational Fluid Dynamics: The Finite Volume Method, Pearson Education, 2007.
[53] H. Ingason, Y.Z. Li, A. Lönnermark, Tunnel Fire Dynamics, Springer, 2014.
[54] K. Anoop, T. Sundararajan, S.K. Das, Effect of particle size on the convective heat transfer in nanofluid in the developing region, Int. J. Heat Mass Transfer 52 (9) (2009) 2189–2195.
[55] V. Bianco, F. Chiacchio, O. Manca, S. Nardini, Numerical investigation of nanofluids forced convection in circular tubes, Appl. Therm. Eng. 29 (17) (2009) 3632–3642.
[56] M. Heyhat, F. Kowsary, A. Rashidi, M. Momenpour, A. Amrollahi, Experimental investigation of laminar convective heat transfer and pressure drop of water-based Al_2O_3 nanofluids in fully developed flow regime, Exp. Thermal Fluid Sci. 44 (2013) 483–489.

Appendix B: Properties of the considered fluids

Fluid	Alt. Name	Type	T_{crit} (ºC)	P_{crit} (bar)	$T_{boiling}$ (ºC)*	Molar Mass (kg/kmol)
Trans-2-butene		HC	155.46	40.27	0.88	56.106
Cis-2-butene		HC	162.6	42.25	3.72	56.106
1-butene		HC	146.14	40.05	-6.31	56.10
Isobutane	R600a	HC	134.66	36.29	-11.74	58.122
Butane	R600	HC	151.98	37.96	-0.49	58.122
Neopentane		HC	160.59	31.96	9.5	72.149
Isopentane	R601a	HC	187.2	33.78	27.83	72.149
Pentane	R601	HC	196.55	33.7	36.06	72.149
Isohexane		HC	224.55	30.4	60.21	86.175
Hexane		HC	234.67	30.34	68.71	86.175
Cyclohexane		HC	280.45	40.805	80.71	84.159
1,1,1,2-tetrafluoroethane	R134a	HFC	101.06	40.593	-26.07	102.03
1,1-difluoroethane	R152a	HFC	113.26	45.168	-24.02	66.05
1,1,1,2,3,3,3-heptafluoropropane	R227ea	HFC	101.75	29.25	-16.34	170.03
1,1,1,2,3,3-hexafluoropropane	R236ea	HFC	139.29	34.2	6.17	152.04
1,1,1,3,3,3-hexafluoropropane	R236fa	HFC	124.92	32.0	-1.49	152.04
1,1,1,3,3-pentafluoropropane	R245fa	HFC	154.01	36.51	15.14	134.05
1,1,2,2,3-pentafluoropropane	R245ca	HFC	174.42	39.40	25.26	134.05
Octafluorocyclobutane	RC318	PFC	115.23	27.775	-5.97	200.03
Methyl-heptafluoropropyl-ether	RE347mcc	HFE	164.55	24.762	34.19	200.05
2,2,2-trifluoroethyl-difluoromethyl-ether	RE245fa2	HFE	171.73	34.33	29.25	150.05
2,3,3,3-Tetrafluoropropene	R1234yf	HFO	94.7	33.82	-29.45	114.04
Trans-1,3,3,3-tetrafluoropropene	R1234ze	HFO	109.36	36.34	-18.97	114.04
Trans-1-chloro-3,3,3-trifluoropropene	R1233zd	HFO	165.6	35.70	18.32	130.5

Appendix C: Cycle conditions at maximum net work output for each fluid

Fluid	Pressure ratio	η_{col} (%)	η_{exp} (%)	Net work output (W)	η_{SORC} (%)
Trans-2-butene	4.5	41.41	64.22	**205.58**	8.92
Cis-2-butene	4.5	41.51	64.27	**204.69**	8.86
1-butene	4.5	40.8	64.86	**210.45**	9.64
R600a	4.5	37.44	65.1	**195.82**	9.39
R600	4.5	41.59	63.78	**204.80**	8.84
Neo-pentane	4	44.23	64.39	**196.35**	7.97
R601a	4.5	44	62.24	**190.51**	7.78
R601	5	43.37	60.45	**186.62**	7.73
Isohexane	5	45.5	60.45	**176.12**	6.95
Hexane	5.5	45.15	58.42	**173.07**	6.88
Cyclohexane	5.5	43.25	58.96	**166.98**	6.93
R134a	2	53.69	63.33	**133.39**	4.46
R152a	2.5	49.66	68.78	**177.54**	6.42
R227ea	2.5	51.4	74.62	**210.02**	7.34
R236ea	5	43.29	61.63	**193.12**	8.01
R236fa	5.5	41.83	62.21	**202.69**	8.7
R245fa	5	43.69	61.62	**191.38**	7.87
R245ca	5	44.15	60.65	**183.81**	7.48
RC318	5	44.93	63.17	**206.34**	8.25
RE347mcc	5	44.31	59.8	**170.08**	6.89
RE245fa2	5	44.62	60.3	**180.49**	7.27
R1234yf	2	53.15	63.13	**136.36**	4.61
R1234ze	3	48.2	69.88	**197.68**	7.37
R1233zd	4.5	40.56	63.02	**176.83**	7.83